The eruptions of Örfajökull 1362 (Iceland) and Lanzarote 1730-36 (Canary Islands) : sulphur emissions and volcanology

Thesis

The eruptions of Öræfajökull 1362 (Iceland) and Lanzarote 1730-36 (Canary Islands): Sulphur emissions and volcanology

A thesis presented for the degree of

Doctor of Philosophy

By

Kirti Sharma

B.Sc. (Hons) University of Manchester, United Kingdom
M.S. University of Hawaii at Manoa, Honolulu, USA

Department of Earth Sciences
The Open University

December 2005

Abstract

This thesis presents new data on the volcanology, erupted volumes, and sulphur emissions of the AD 1362 Öræfajökull eruption and the AD 1730-36 Lanzarote eruption, and relates these findings to their atmospheric and environmental impacts. The Öræfajökull eruption was an explosive Plinian event with high eruption columns (~30 km) that produced an extensive tephra-fall and a small pyroclastic flow deposit (~2 km^3 total volume). In contrast, the Lanzarote eruption was a long-lasting basaltic fissure eruption involving Hawaiian and Strombolian fire fountain activity (eruption plumes 8-16 km high) generating a scoria fall deposit and lava flows (~5 km^3 total volume).

Chapter 1 introduces the effects of volcanic gas release, and highlights the importance of SO_2. In chapter 2, I provide a critical assessment of the petrologic method used to estimate the sulphur release from a volcanic eruption. The petrologic method uses the difference in sulphur concentrations between melt inclusions and matrix glasses, measured by electron microprobe, scaled to the mass of erupted magma, and corrected for the magma crystal content. I show that it provides estimates for sulphur degassing from non-arc, basaltic, reduced magmas that are similar to independent satellite measurements (TOMS). Using this technique, the AD 1362 Öræfajökull eruption is estimated to have released only ~0.6 Mt of SO_2 into the stratosphere – supported by lack of an ice core acidity peak. The major environmental hazard resulting from this eruption was large volumes of pumice and ash injected into the upper atmosphere and its subsequent fallout over a wide area (chapter 3). The Lanzarote eruption released at least 45 Mt of SO_2. This was determined using a new technique based on the correlation between S and incompatible element (K, P, Ti) ratios (S/*I*); knowing this ratio the original S content of a degassed liquid can be calculated from its concentration of *I*. The release of SO_2 from the Lanzarote eruption is shown to have caused significant climatic perturbations – as demonstrated in the climate proxy record (chapter 4).

Acknowledgements

First and foremost I wish to thank my main supervisor Steve Blake for all his help and support during the completion of this thesis. He initiated this study under the title of "Fire and Brimstone". Together with my second supervisor, Steve Self, who suggested the eruptions of Öræfajökull 1362 and Lanzarote 1730-36 as topics for this study, the two Steves' have been a wonderful source of ideas and information!

I would also like to thank my examiners, Dr Ian Parkinson and Professor Lionel Wilson for a nice viva, and their comments which have greatly improved this thesis.

I wish to acknowledge the assistance of the following people during this thesis work. For help with the work in Chapter 2: Frank Trusdell (USGS Hawaii Volcano Observatory) for samples of the Mauna Loa 1984 eruption products; Morihisa Hamada (Japan) for both samples and glass and mineral geochemistry data from Izu-Oshima volcano; Janet Sumner for providing information and samples from the Izu-Oshima eruption and Arlin Krueger (UMBC) who provided the up-to-date TOMS estimates. For the work included in Chapter 3 Gudrun Larsen and Thor Thordarson are thanked for spending time assessing my Icelandic datasets, and for valuable information about the volcanology of Iceland, particularly regarding Öræfajökull. Juan Carlos Carracedo and Eduardo Rodriguez Badiola are thanked for the wealth of information, maps, and books provided about the 1730-36 Lanzarote eruption. I also wish to thank Louise Thomas for use of her Lanzarote samples and thin sections, Jose-Luis Palma for his translation of the Spanish contemporary accounts of the Lanzarote eruption and Linda McArdell for useful Lanzarote geological history documentation, maps, and photographs. Caco Cortes, Eliza Calder, Ralf Gertisser, Nico Fournier, Marie-Noelle Guilbaud, Anne Jay, Jose-Luis, and Luke Wooller are thanked for many useful volcanology, petrology, geochemistry, and general science discussions which have contributed to improving this thesis. I owe an immense "thank you" to Carl Thornber, Christina Heliker, Arnold Okamura (and various other past and present staff members from the USGS Hawaii Volcano Observatory), and especially Frank Trusdell for their unending love, support, and friendship. I also thank Frank for "nurturing" my interest in volcanoes while on the Mauna Loa mapping

project and teaching me many 'life lessons' – some of which still come in handy today! Carl is also thanked for his help with all things olivine!

Analytical work for this thesis would not have been completed without the help of the following people – Andy Tindle (OU electron microprobe facility), John Watson (OU XRF facility), Sarah Sephton (FTIR spectroscopy), and Andrea di Muro (IPGP, Paris) for ion chromatography analyses of the Öræfajökull pumice. Michelle Higgins, Kay Green, and Mike Henty are thanked for expert sample preparation. I am also extremely grateful to the following people who contributed microprobe glass standards and analytical advice – Ian Ridley (USGS Denver), Eugene Jarosewich (Smithsonian Institute), John Fournelle (University of Wisconsin), Mike Garcia (University of Hawaii), Christian Lacasse, Mike Davis, and Greg Meeker (USGS Denver). Dave Plant (NERC microprobe facility, University of Manchester) is also thanked for assistance with the microprobe work completed at Manchester.

I also wish to thank John Taylor and Andy Lloyd in the OU cartography department for their help with preparing conference presentations and manuscript figures, John Holbrook and Liz Lomas are thanked for their prompt assistance and wealth of information at all times, and Brandon Cook, Craig Millard for IT support. Many thanks also go to the Volcano Dynamics Group at the OU – especially John Murray for afternoon tea and Ashea for keeping us all in check.

Finally, I wish to acknowledge my parents and family, who have supported my volcanology obsession over the past 10 years – without their love and support I could not have achieved any of this!

TABLE OF CONTENTS

Chapter 4
The AD 1730-36 Lanzarote eruption, Canary Islands: Volcanology, SO_2 release and atmospheric mass loading

LIST OF FIGURES

Chapter 1
Introduction

Chapter 2
SO_2 emissions from basaltic eruptions and the excess sulphur issue

Chapter 3
The AD 1362 eruption of Oraefajokull, SE Iceland: Physical volcanology and volatile degassing

Chapter 4
The AD 1730-36 Lanzarote eruption, Canary Islands: Volcanology, SO_2 release and atmospheric mass loading

Page

LIST OF TABLES

Chapter 1
Introduction

Chapter 2
SO_2 emissions from basaltic eruptions and the excess sulphur issue

Chapter 3
The AD 1362 eruption of Öræfajökull, SE Iceland: Physical volcanology and volatile degassing

Chapter 4
The AD 1730-36 Lanzarote eruption, Canary Islands: Volcanology, SO_2 release and atmospheric mass loading

Chapter 1: Introduction

Volcanic eruptions can have profound atmospheric and environmental effects. The injection of magmatic volatiles (e.g., SO_2, Cl, F, H_2O, CO_2) into the atmosphere and the explosive eruption of large volumes of fine ash are the two most important processes that need to be assessed when considering the widespread environmental and societal impact of volcanism.

This thesis is aimed at understanding how the eruption variables (especially eruption style, height of erupting column, mass of gas released, and volatile composition of magma) influence the resulting environmental and atmospheric effects. In this chapter, I will first provide a general introduction to the atmospheric impact of volcanism, followed by a brief discussion on how volcanological studies can help us further understand the nature of volcanic volatile emissions.

1.1 Causes and effects of volcanic volatile emissions

1.1.1 Volcanic volatiles

Volcanic volatile emissions are one of the most important short-lived natural atmospheric perturbations that can influence the Earth's radiation budget, surface temperatures, and circulation patterns. Ash- and volatile-rich volcanic eruption plumes which can result in atmospheric and environmental perturbations are generated during two main types of volcanic eruption:

1. Brief explosive eruptions (usually lasting hours to days) of intermediate to silicic magma, that generate Plinian pyroclastic fall and flow deposits from high (25-40 km) eruption columns laden with ash and volcanic volatiles (e.g., Mount Pinatubo, Philippines 1991). These mainly impact the upper atmosphere (stratosphere) directly.

2. Long-lived fissure eruptions (usually lasting days to years), typically of basaltic magma, concentrated along extensive (≥ 5 km long) fissures, generating Hawaiian to Strombolian fire-fountains and associated fall deposits and lava flows. The associated eruption plumes can be up to 10-16 km high and rich in magmatic volatiles (e.g., Laki, Iceland 1783-84). These eruptions impact the atmosphere from the Earth's surface to the lower stratosphere.

The injection of volcanic gas into the stratosphere is known to act as a forcing function for climate, as the volcanic aerosols generated from the gas have the potential to remain in the stratosphere for several years, thus affecting the energy balance of the atmosphere (Jakosky 1986; Robock 2000). The potential climatic impact of volcanic aerosols on the troposphere is less well understood (Graf et al. 1997). The impact of volcanic emissions on the atmosphere is dependent on a number of volcanological and meteorological conditions (e.g., Halmer et al. 2002):

1. The level (height) in the atmosphere that receives the gas emission (related to the explosivity, or intensity, and duration of a volcanic eruption (e.g., Walker 1980))

2. Mass of gas released (related to the chemical composition, initial volatile content of the magma, and mass of magma erupted)
3. Location of the volcano (latitude and altitude)
4. Atmospheric conditions (e.g., temperature, humidity, wind conditions, seasonal weather patterns)

Studies of major explosive volcanic eruptions show that mass eruption rate is the main factor that controls the intensity and height of the erupting column (e.g., Wilson et al. 1978; Sparks 1986; Carey and Sigurdsson 1989), thus determining how high volcanic gas and ash particles are injected into the atmosphere, i.e. tropospheric versus stratospheric injections (Table 1.1). A moderate percentage of historic Northern hemisphere volcanism has been restricted to tropospheric injection. However, the tropopause is lower at high latitudes, and recent studies show (e.g., Hansen and Nazarenko 2004) that surface forcing is twice as effective at high latitudes; i.e. high latitude volcanic eruptions with a given magnitude are expected to change global surface temperatures by twice as much, (see also Hansen et al. 1997).

Table 1.1 Summary of significant historic volcanic eruptions that generated a considerable atmospheric and climatic impact. (Based on Rampino and Self (1984), with additional data from Thordarson and Self (1996), Self et al. (1996), Thordarson et al. (2001) and Self et al. (2004)).

Eruption	Volume of magma (km^3)	Plume height (km)	H_2SO_4 aerosol yield (g)	Atmospheric effects [NH ΔT (°C)]*
Tambora 1815	≥50	>40	5×10^{13}	-0.4-0.7
Krakatau 1883	≥10	>40	3×10^{12}	-0.3
Santa Maria 1902	~9	>30	$\leq 2\times10^{13}$‡	-0.4
Katmai 1912	15	>27	$\leq 2\times10^{13}$‡	-0.2
Agung 1963	0.3-0.6	>18	3×10^{12}	-0.3
El Chichon 1982	0.3-0.35	26	7×10^{10}	-0.4
Pinatubo 1991	5	≤42	9×10^{13}	≤ -0.6
Laki 1783-84	12.6[a]	10-13	2×10^{14}	-1.0
Eldgja 934 AD	19.6	5-15	4.5×10^{14}	-1.2

*Northern Hemisphere surface temperature difference from the long-term average in 1-3 years following the eruption
‡H_2SO_4 aerosol yield estimated from atmospheric optical depth measurements
[a]Tephra volume = 0.3 km^3, lava volume = 12.3 km^3

1.1.2 Volcanic aerosols

The release of volcanic volatiles affects atmospheric and climate systems in the following way: magmatic volatile species carried in volcanic eruption plumes undergo photochemical oxidation reactions with both atmospheric water and water within the eruption cloud system to generate acidic aerosols (e.g., H_2SO_4, HCl, HF). In high-intensity volcanic eruptions these chemical reactions mainly occur in the stratosphere as the residence time in the plume is too short; for most explosive eruptions the time for plume rise from the crater to the stratosphere is less than ten minutes (Textor et al. 2004). Gaseous SO_2, on reaching stratospheric levels, is converted into sulphate (H_2SO_4) aerosol within ~30 days (Zhao et al. 1995; Coffey 1996). Once upper atmospheric levels are reached by the convecting plumes, the aerosol particles

nucleate, forming widely dispersed aerosol clouds, increasing the optical depth (a measure of the degree of opacity of the stratosphere to sunlight transmission) of the stratosphere (e.g., Rampino and Self 1982, 1984; Stothers et al. 1984; Textor et al. 2004). Volcanic aerosols can remain aloft at upper atmospheric levels for some time, with isolated volcanic eruptions potentially causing climate forcing on timescales of 1-3 years. Furthermore, repeated volcanic activity that is able to continuously replenish atmospheric aerosols can change this forcing timescale to decades (Sato et al. 1993).

Volcanogenic aerosols can alter atmospheric chemistry and structure, and thus affect the climate in several different ways (Figure 1.1). Sulphate aerosols can effectively alter the Earth's radiation balance; shortwave scattering of incoming solar radiation from aerosols results in surface and lower atmospheric (troposphere) cooling, whereas absorption of long wave radiation leads to upper atmosphere (stratosphere) warming. Both processes affect stratospheric stability, troposphere-stratosphere interchange, and tropospheric dynamics.

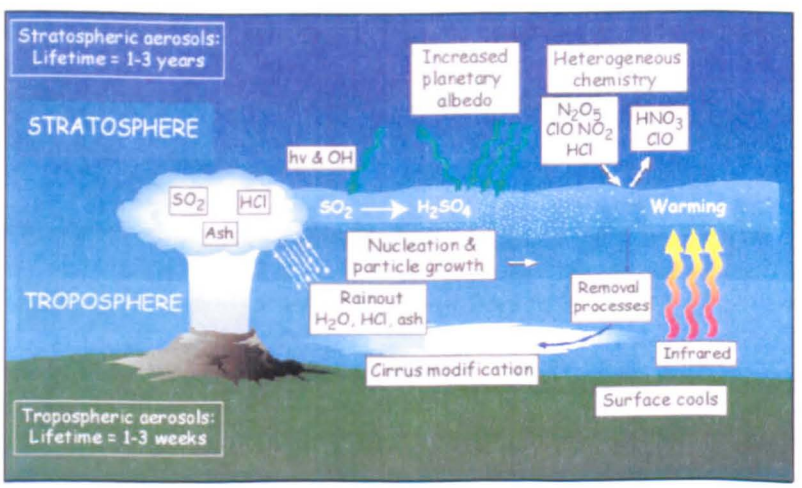

Figure 1.1 Schematic representation of the atmospheric effects caused by explosive volcanic eruptions. Modified from McCormick et al. (1995) and Textor et al. (2004).

Aerosol particles can also act as cloud condensation nuclei for upper tropospheric cirrus clouds, modifying the microphysical structure, water content, lifetime, and thus the radiative properties of clouds (Twomey 1974; Bay et al. 2004). An increased number of cloud condensation nuclei and therefore cloud droplets can lead to an increased albedo of clouds, which further enhances surface cooling (Textor et al. 2004).

Volcanic aerosols can also catalyze chemical reactions involving halogen species (e.g., Cl) leading to the depletion of the stratospheric ozone layer. Sulphate aerosol particle surfaces act as sites for heterogeneous reactions which convert stable chlorine compounds (HCl, HOCl, $ClNO_3$) into photo-chemically active chlorine species (ClO, Cl_2) that initiate ozone destruction (e.g., Hofmann and Solomon 1989). Ozone depletion leads to an increase in the amount of harmful ultraviolet radiation reaching the Earth's surface. The direct injection of magmatic halogen species into the stratosphere could result in catastrophic ozone depletion. This, however, has been thought unlikely as erupted HCl is highly water soluble and is efficiently scavenged by water droplets in the eruption column, and returned to Earth as precipitation (Tabazadeh and Turco 1993). This may not always be the case, if chlorine is released by different reactions in the stratosphere (Textor et al. 2004).

The 1991 eruption of Mount Pinatubo in the Philippines (15° 08' N 120° 21' E) provided atmospheric scientists with a real-time natural laboratory, from which detailed observations of the processes described above emerged. The eruption released ~17 Mt of SO_2 into the stratosphere (McCormick et al. 1995); approximately half of this was converted to sulphuric acid aerosols by ~21-28 days after the eruption (Self et al. 1996). The Pinatubo aerosol cloud spread rapidly around the Earth in ~3 weeks, and was subsequently dispersed into both

hemispheres, attaining global coverage ~1 year after the eruption (Trepte et al. 1993). The aerosol cloud decreased the amount of net radiation reaching the Earth's surface, and produced a climate forcing that was strong enough to offset present global warming trends (e.g., resulting from anthropogenic CO_2 emissions). This resulted in ~0.5-0.6 °C surface cooling in the Northern Hemisphere – and a global cooling of 0.4 °C over large parts of the Earth in 1992-93 (Self et al. 1996). Aerosol particles also contributed to an unprecedented increase in the Southern Hemisphere "ozone hole" in 1992, with ozone abundances reaching their lowest levels on record (2-3% lower than in any earlier year), (Self et al. 1996).

1.1.3 Tropospheric aerosols

The release of volcanic volatiles into lower tropospheric levels is also an important process. Graf et al. (1997) estimated that volcanic activity contributes ~36% to the tropospheric sulphur burden. Fissure-fed volcanic activity is the dominant source for tropospheric volcanic emissions, with eruption plumes above fire fountains injecting volatiles into the upper troposphere, and smaller plumes generated during lava flow emplacement injecting gas to lower levels in the troposphere. Aerosol residence times are much shorter in the troposphere than in the stratosphere. However, as most fissure-fed eruptions last from weeks to months (and in some cases possible years), high tropospheric aerosol concentrations can be maintained by sequential eruptive episodes, as was evident during the 1783-84 Laki eruption (Thordarson and Self 2003).

Volcanogenic aerosols injected into the upper troposphere can cause climate perturbations similar to those initiated by larger stratospheric injections – e.g., blocking of solar radiation leading to surface cooling. However, tropospheric injections can also create other

environmental and atmospheric perturbations. On a local scale, low-level plumes carrying fine ash and corrosive and poisonous volcanic gases (e.g., SO_2, F) can have serious effects on ecosystems, with rainout from volcanic eruption columns producing acidic rainfall that can burn holes in plants – therefore damaging crop yields and vegetation as well as causing burns and wounds on animals.

A tropospheric aerosol cloud, developed under conditions described above during fissure-fed volcanism, can lead to the creation of "dry fogs" – veils of aerosol particles (sulphuric acid droplets nucleating on fine ash grains) that are widely dispersed by vigorous tropospheric winds (Stothers 1999). The climatic effects of volcanic dry fogs are usually encountered in the first winter following the eruption – with severe, cold winters recorded. However, hemispheric cooling can persist for 2-5 years after the eruption onset, leading to summer cooling and winter warming phenomena (Robock 2000). As these climatic perturbations can occur for up to five years following the eruption of the source volcano, there is adequate opportunity for crop failure and disease epidemics to develop on a large scale (Stothers et al. 1999).

Just as the 1991 Pinatubo eruption helped advance scientific knowledge regarding stratospheric processes, the 1783-84 Icelandic eruption of Laki provided an excellent opportunity to study the atmospheric effects resulting from a sustained, largely tropospheric volatile injection. The Laki eruption released ~ 122 Mt of SO_2 into the upper troposphere and lower stratosphere, generating ~200 Mt of sulphate aerosol; ~ 88% of this aerosol total was removed as acidic precipitation causing the volcanic pollution and "dry fog" that affected Europe in 1783 (Thordarson and Self 2003). The tropospheric haze that originated from the

Laki 1783 eruption caused the most significant natural air-pollution event of the past two millennia (Stothers 1996). This persistent dry fog was observed across much of Europe during the summer of 1783 and was also recorded as far afield as Iraq, Japan, Alaska, and the coast of Newfoundland (Stothers 1996; Jacoby et al. 1999). Grattan et al. (1998) describe several environmental phenomena that accompanied the dry fog, e.g., intense smell of sulphur, severe damage to vegetation (corn and other crops burnt and withered away), and the veiling of the Sun and Moon. Durand and Grattan (1999) also discuss the impact of the dry fog on human health conditions (as recorded in contemporary historical records). The main effect of a volcanogenic dry fog on human health is manifested in respiratory conditions, increase in asthma and asthma-related illnesses (e.g., bronchial infections). Other conditions resulting from the dry fog enveloping Europe range from minor illnesses including headaches, loss of appetite, stinging eyes, lips, skin, and general malaise and sickness due to the acrid sulphurous fumes (Thordarson and Self 2003) to more severe complaints such as lung disease and even death (Durand and Grattan 1999). Acidic precipitation also led to the deposition of fluorine on agricultural land which caused chronic fluorosis, leading to lethal sickness in grazing livestock, resulting in the eventual death of ~60% of the livestock in less than a year (Thordarson et al. 1996).

1.1.4 Volcanic ash

In addition to volatile pollution, volcanic tephra, produced as a result of explosive activity in both of the above eruption scenarios, and subsequently injected into the atmosphere also poses a detrimental environmental threat. Eruptions that can loft volcanic ash to heights of 15 km or more pose a major hazard to commercial aircraft (Casadevall and Krohn 1995). Fallout from volcanic eruption clouds can also trigger local impacts on infrastructure, land, agriculture and

human health, e.g., large volumes of ash can bury and destroy buildings, cover agricultural land and subsequently destroy crop yields, and cause human health problems, e.g., respiratory complaints (e.g., Durand and Grattan 1999; Witham and Oppenheimer 2005; Horwell et al. 2003).

Excluding the impact on aviation traffic, the above direct effects of volcanic ash fall, although serious in nature, tend to be restricted to areas immediately surrounding the erupting volcano (maximum distances of approximately tens of kilometres). Areas further away from the volcanic source are affected only by the long-range atmospheric transport of fine ash (over hundreds to thousands of kilometres) and subsequent distal fall out. Ash is efficiently removed by sedimentation from the stratosphere within one to two months after the eruption (Pinto et al. 1989), and is therefore unlikely to have a major impact on atmospheric systems, although limited impacts on local weather conditions and ecosystems, resulting from rainout close to the volcanic source, may be possible.

1.2 Methods used to estimate volcanic volatile release

Accurately quantifying volatile emissions is critical when assessing the environmental and climatic impact of volcanism. Several methods are currently in place to estimate recent volcanic volatile emissions. These range from field based techniques such as correlation spectroscopy COSPEC (Sutton et al. 2001), open-path Fourier Transform Infrared Spectroscopy (FTIR) (e.g., Francis et al. 2000), to geochemical models of volatile solubility that help predict volatile concentrations with respect to magma compositions (e.g., Scaillet et al. 2004). In recent years (1979 onwards), instruments carried on satellites launched into

Earth orbit e.g., Total Ozone Mapping Spectrometer (TOMS), Advanced Very High Resolution Radiometer (AVHRR), Tiros Operational Vertical Sounder (TOVS), and the advancement in remote sensing techniques have led to the creation of a high resolution data series of SO_2 emissions from recently active volcanoes (e.g., Krueger et al. 1995; Carn et al. 2003; Wen and Rose 1994; Prata et al. 2004).

It is necessary to quantify volatile emissions from older eruptive events. Only a limited number of techniques are available. The most common approach that has been developed is the petrologic method (e.g., Devine et al. 1984; Palais and Sigurdsson 1989). The petrologic method involves using the difference between the magma's pre-eruptive and degassed volatile contents scaled to the mass of magma erupted and corrected for crystal content, to obtain the mass of gas (e.g., SO_2, Cl, F, CO_2, H_2O) released to the atmosphere. Finally, independent, so-called proxy methods, e.g., ice core sulphate records, tree-ring climate records, stratospheric aerosol optical depth measurements (a measure of the degree of opacity of the stratosphere to sunlight transmission) (e.g., Zielinski 1995; 2000 Jones et al. 1995, Stothers 1986) can also be used to estimate the mass aerosol loading from a given eruption, from which SO_2 emission estimates can be back-tracked out (e.g., Hammer et al. 1980; Zielinski 1995).

Each method of estimating the volcanic SO_2 release has advantages to its use but also some limitations. For example, satellite monitoring provides good spatial coverage when tracking SO_2 plumes from explosive eruptions with stratosphere-reaching eruption columns; however resolution is reduced for lower-level eruption plumes. Also, recent studies (e.g., Westrich and Gerlach 1992; Wallace 2001, 2004) have noted that satellite measurements of SO_2 emissions from arc eruptions (e.g., Mount Pinatubo 1991; El Chichon 1982) are one to two orders of

magnitude greater than petrologic estimates of the sulphur release. This discrepancy has been attributed to the presence of a sulphur-rich volatile phase at depth in the magma system whereby sulphur is sequestered into a separate fluid phase, which is then erupted along with the remaining sulphur-poor magma. This so-called "excess sulphur" issue (e.g., Westrich and Gerlach 1992) is investigated critically in Chapter 2 of this thesis.

1.3 Aims and Objectives

The eruptions of Pinatubo and Laki provide well-studied examples that link eruption style, magma chemistry, mass of SO_2, and local atmospheric conditions to climatic cooling and environmental impacts. However, a more complete range of examples is needed to fully understand the link between volcanism and the environment. For several historic explosive Plinian-style eruptions these links have been studied in detail e.g., Huaynaputina AD 1600 (De Silva and Zielinski 1998), Tambora 1815 (Self et al. 2004), Krakatau 1883 (Mandeville et al. 1996) and Agung 1963 (Self and King 1996). However, there is still valuable information to gain - especially from older Plinian events that do not have corresponding proxy or instrumental climate data. In contrast, the links between eruption mechanisms and atmospheric effects of fissure eruptions are less well understood and these also deserve to be studied.

In this thesis, besides refining the methods used to determine sulphur dioxide releases from analyses of eruption products, I have selected two different eruptions for study – the 1730-36 eruption of Lanzarote, Canary Islands, and the 1362 eruption of Öræfajökull, Iceland. Both of these eruptions were significant volcanic events of the past 1000 years. The Lanzarote

eruption was a large fire-fountain-fed eruption, similar to the 1783 Laki event, whereas the Öræfajökull eruption, a typical Plinian event, has some similarities to the 1991 Pinatubo eruption. Both eruptions might have had a possible impact on the UK environment, and future eruptions from Iceland and the Canaries may also affect the UK, therefore warranting detailed studies.

Before any quantitative assessments on the atmospheric and climatic effects of these eruptions can be made, a critical evaluation of the techniques used to calculate the volatile degassing needs to be undertaken. With this in mind, in Chapter 2, I present an appraisal of the petrologic method and its use for estimating volcanic sulphur emissions for basaltic volcanism. Comparing petrologic method data with corresponding satellite measurements of SO_2 flux for a series of volcanic eruptions allows us to evaluate its use in certain situations. This type of study is important as the petrologic method provides the only means of using direct analysis of eruption products to obtain SO_2 degassing budgets. In addition, this method is the only way in which the SO_2 release from older volcanic eruptions (before the era of satellite-borne gas detecting spectrometers) can be estimated.

Chapters 3 and 4 go on to examine the volatile degassing and environmental and atmospheric impact of the AD 1362 Öræfajökull eruption and the AD 1730-36 Lanzarote eruption. In order to derive conclusions regarding the atmospheric and climatic effects of these eruptions, I have conducted a detailed assessment of the physical volcanology of both eruptions to calculate column heights, dispersal mechanisms, and volume. Glass and mineral geochemistry is then obtained and used to constrain the magmatic conditions and to quantify the amount of sulphur released. Combining the volcanological information with the estimates

of volatile release allows a clear picture of the environmental impact to be constructed in each case. I also examine the relationship between magmatic conditions (e.g., melt composition, oxygen fugacity) and the amount of sulphur available for eruption – this is a necessary component of this study as magmatic conditions, e.g., oxygen fugacity and the bulk melt composition, exercise a large control on the concentration of sulphur in evolving magmatic liquids.

Finally, in Chapter 5, I present the main conclusions arising from this study and present ideas on further research directions.

Chapter 2: SO_2 emissions from basaltic eruptions, and the excess sulphur issue

A version of sections 2.1 to 2.7 of this chapter has been published in Geophysical Research Letters (2004):

Sharma K, Blake S, Self S, Krueger AJ (2004) SO_2 emissions from basaltic eruptions and the excess sulphur issue. Geophys Res Lett 31: L13612 doi: 10.1029/2004GL019688.

Abstract

Volcanic SO_2 emissions affect environmental conditions on Earth. Where no direct measurements of SO_2 in the atmosphere are available, a petrologic method of assessing sulphur release from the magma must be used. However, in studies of arc-derived eruptions, satellite-based measurements of SO_2 emissions are one to two orders of magnitude greater than those calculated petrologically, implying that a separate gas phase in the magma chamber may be responsible for this excess sulphur. We test here whether this applies in other tectonic settings. For Icelandic and Hawaiian basalts, results indicate that petrologic SO_2 estimates are comparable to TOMS satellite-borne measurements of SO_2 detected in eruption plumes. Thus, for non-arc basalts, the petrologic method gives reliable estimates of SO_2 released. The implied absence of excess sulphur in non-arc basaltic magmas is a reflection of source magma conditions, notably lower fO_2 and volatile contents than arc magmas, inhibiting the exsolution of a sulphur-rich gas prior to eruption.

Keywords: *volcanic SO_2, TOMS, petrologic method, basaltic eruption*

2.1 Introduction

Volcanic SO_2 emissions can have significant effects on the Earth's atmosphere and biosphere (see Chapter 1). Evaluating the amounts and mechanisms of SO_2 release is thus crucial in predicting the environmental consequences of volcanism.

The amount of SO_2 emitted by volcanic eruptions can be determined using a variety of techniques. Two techniques currently in use are the petrological method (e.g., Devine et al. 1984) and satellite measurements of SO_2 releases (TOMS) (Carn et al. 2003). Comparisons between TOMS SO_2 measurements and petrologic SO_2 estimations for six arc eruptions (Figure 2.1) of varying compositions (basaltic to dacitic) show that the TOMS SO_2 values exceed values estimated petrologically by one to two orders of magnitude. Westrich and Gerlach (1992) and Wallace (2001; 2003) have suggested that this discrepancy can be attributed to a separate sulphur-bearing volatile phase accumulating at depth in the magma system prior to eruption – so-called "excess sulphur". Estimates of sulphur release from major basaltic eruptions, e.g. flood basalts, using the petrologic method may therefore be greatly underestimated. Because comparisons between petrologic estimates of sulphur release for basaltic eruptions with independent SO_2 measurements (e.g., satellite data) are lacking, the significance of such petrologic results is uncertain. In this paper we investigate whether there is evidence for excess sulphur in non-arc basaltic volcanism using improved petrologic estimates and satellite data.

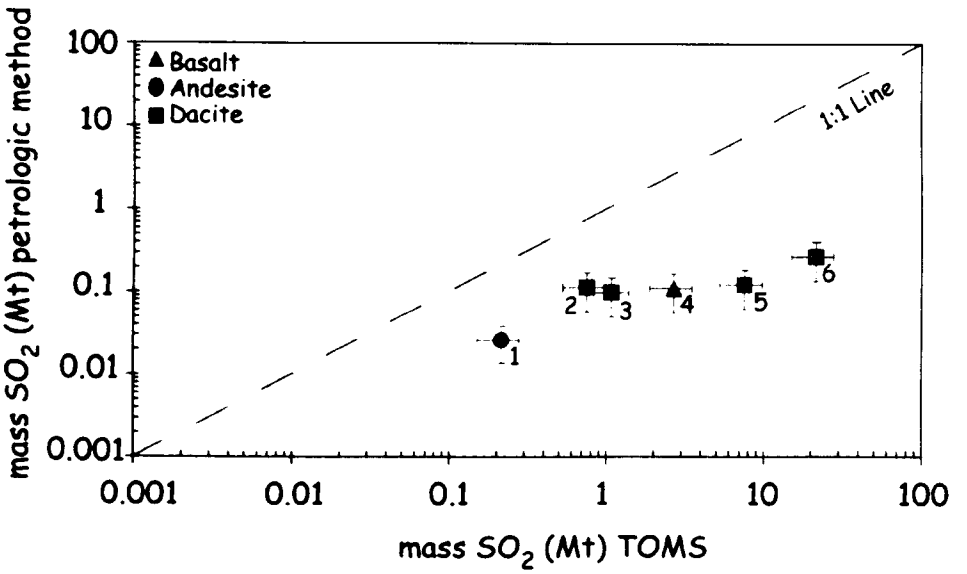

Figure 2.1 TOMS SO_2 measurements versus petrologic estimates for SO_2 for six arc eruptions (Redoubt 1989 (1), (Gerlach et al. 1994); Nevado del Ruiz 1985 (2), (Sigurdsson et al. 1990); Mount St Helens 1980 (3), (Gerlach and McGee 1994); Galunggung 1982 (4), (De Hoog et al. 2001); El Chichon 1982 (5), (Luhr et al. 1984); & Pinatubo 1991 (6), (Westrich and Gerlach 1992)). TOMS data for the 6 arc eruptions are from Bluth et al. (1997) except for Galunggung which is from Bluth et al. (1994). Error bars on the arc petrologic SO_2 values are ± 50%; estimated error on TOMS measurements is ± 30%.

2.2 The petrologic method

The petrologic method assumes that glass inclusions in magmatic phenocrysts represent volatile-bearing liquid trapped during crystal growth in the magma chamber. If there is no S-bearing gas in the magma chamber, then the sole source of the degassed S is the melt phase of the magma. The mass of sulphur released is then given by the difference in concentration of S between inclusions (C_{inc}) and the degassed matrix glass (C_{matrix}) of the volcanic rock, multiplied by the mass of erupted liquid, (Devine et al. 1984). In the cases to be considered in this paper, SO_2 detected by TOMS originated from the explosive release of magma that generated scoria with little or no syn- or post-eruptive crystallization, therefore the mass of erupted liquid is M_v ($1 - W_{xtls}$) where M_v is the mass of volcanic rock and W_{xtls} is the mass fraction of crystals. The petrologic method therefore estimates the mass of S released as:

$$M_S = \frac{M_l (1 - W_{xtls})[C_{inc} - C_{matrix}]}{100} \qquad [1]$$

Taking account of the molecular weight differences between S and SO_2, the mass of SO_2 released is $2M_S$.

The petrologic method does not account for other sources of sulphur that may contribute to the total SO_2 emitted during the eruption. The breakdown of S-bearing mineral phases (e.g., anhydrite), fumarolic or hydrothermal sulphur, and the presence of a S-rich gas phase may supply additional sulphur.

2.3 Satellite measurements of SO_2 emissions

The TOMS dataset provides a 22-year-old record of measurements of SO_2 released into the atmosphere by over 200 eruptive events (Figure 2.2) (Carn et al. 2003; http://www.skye.gsfc.nasa.gov/archives.html). The instrument measures back-scattered solar UV radiation in six different wavelength bands; an iterative algorithm is used with radiative transfer tables to retrieve the amount of SO_2 (Krueger et al. 1995). The latest instrument and algorithm in use (version 7) has a minimum detection limit of ~5 kt and SO_2 estimates have errors in the range of ± 10–30%. Errors near the lower end of this range are associated with eruption plumes containing little or no volcanic ash.

TOMS measures the total mass of SO_2 in entire eruption clouds once per day near local noon. This mass is the erupted mass less the amount lost by conversion to sulphate. The erupted mass of SO_2 in brief explosive eruptions is determined by extrapolating daily cloud totals back to the time of eruption. However, for continuing effusive eruptions, the daily

total contains new SO_2 released since the previous satellite overpass and old SO_2 remaining from earlier days. Summing of daily totals can produce an overestimate of total eruption mass. Winds sometimes make it possible to identify the older SO_2 cloud by spatial separation. With low wind speeds the loss rate, which varies by a factor of 30 from the surface to the stratosphere, must be explicitly considered in evaluating total eruption mass (Krueger et al. 1996).

2.4 Sampling and analytical setup

Lava and tephra samples were collected and analysed from four non-arc mafic eruptions with well-constrained magma volumes and TOMS data: Krafla 1984, Mauna Loa 1984, Hekla 1980, and Hekla 2000. Samples from an arc eruption – the 1986 eruption of Izu-Oshima volcano, Japan (basaltic-andesite magma composition) were also analysed.

Lava and tephra samples were crushed and sieved into small size fractions from which matrix glass shards and crystals were picked. Major element and sulphur analyses of matrix glasses and olivine- and plagioclase-hosted glass inclusions (Figure 2.4) were conducted at The Open University on a Cameca SX-100 electron microprobe, using a 20 kV accelerating voltage, 20 nA beam current and a 10-20 μm diameter beam. The glass inclusions range in size from 30 to 100 μm and are crystal-free, homogenous glasses. Care was taken to avoid inclusions containing bubbles or fractures. Microlite-free areas of matrix glass were chosen for analysis. Major element peak counting times ranged from 25-60 seconds (K, Mn = 25 s; Ca, Mg, Na, Si = 40 s; Ti, Al, Fe, P = 60 s) and two-sided background count times were half the peak time for each element. Natural glass and mineral standards were used for calibration and a PAP-ZAF correction was applied to all analyses.

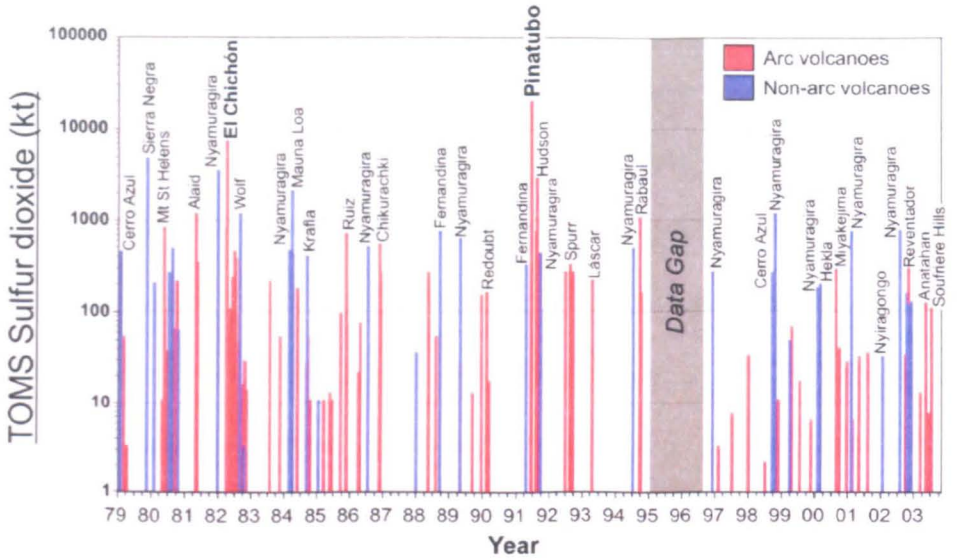

Figure 2.2 Time series showing sulphur dioxide emissions (measured in kilotons (1 kt = 1×10^{-3} Mt), as detected by various TOMS instruments (courtesy of http://www.skye.gsfc.nasa.gov/archives.html).

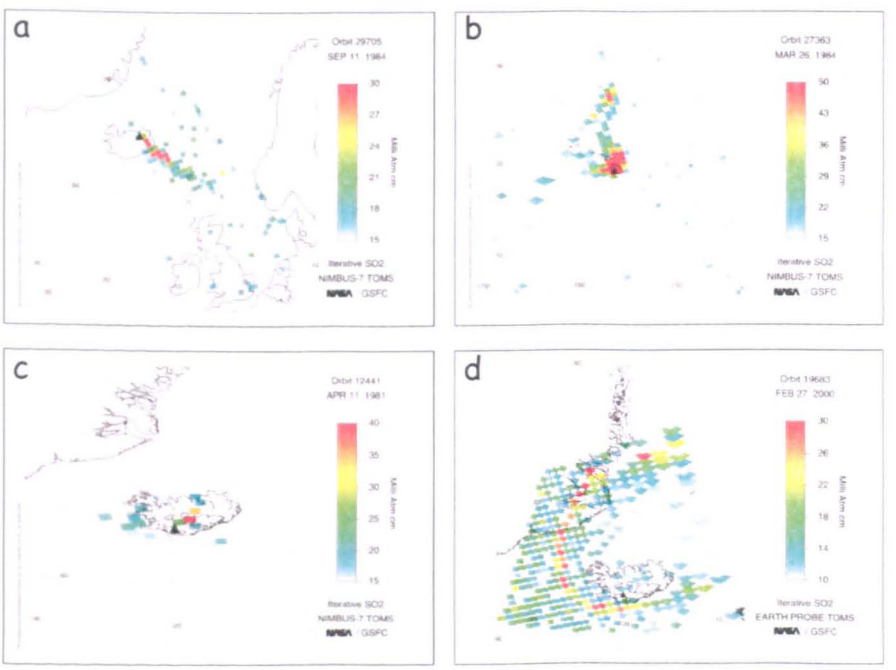

Figure 2.3 Selected TOMS (Total Ozone Mapping Spectrometer) images of tracked SO_2 plumes from four non-arc volcanic eruptions (discussed in text). A shows an image of the 1984 Krafla sulphur-bearing plume as seen on day 4 (September 11) of the eruption. B shows the 1984 Mauna Loa SO_2 plume on day 5 of the eruption. C shows the plume from the Hekla 1981 eruption, image from August 11. D shows the Hekla 2000 SO_2 plume as seen by TOMS on the first day of the eruption. Red and orange areas indicate the largest concentrations of SO_2. (Source: http://skye.gsfc.nasa.gov/Images/Volcanoes/).

Two sigma precision based upon replicate analyses of the glass standard VG-2 (Juan de Fuca Ridge glass) over a period of several months is <1% for major elements and <4% for minor elements (e.g., P, Mn, K) (Appendix A7). These values are comparable to the two sigma precision estimated using counting statistics. All reported analyses are the average of 3-10 spots. For sulphur analyses the peak counting time was increased to 80 s and troilite was used as a calibration standard. The minimum detection limit for S is 78 ppm. Replicate analyses of VG-2 gave 1480 ± 50 (2σ) ppm S (n = 180), in good agreement with values reported in previous studies, e.g., De Hoog et al. (2001) (see table 2.1).

Table 2.1 Comparison and precision of reproducibility, for S analyses of basaltic glass standard VG-2 (USNM 111240/52). Standard deviation in all cases is 2σ, n = number of analyses.

VG-2 Juan de Fuca Ridge glass	n	S (ppm)	Beam current (nA)	Peak count time (s)
Dixon et al. (1991)	19	1340 ± 160	10	80
Thordarson et al. (1996)	139	1365 ± 29	80	400
Davis et al. (2003)	56	1489 ± 26	80	400
De Hoog et al. (2001)	19	1441 ± 83	25	80
This study	120	1480 ± 50	20	80

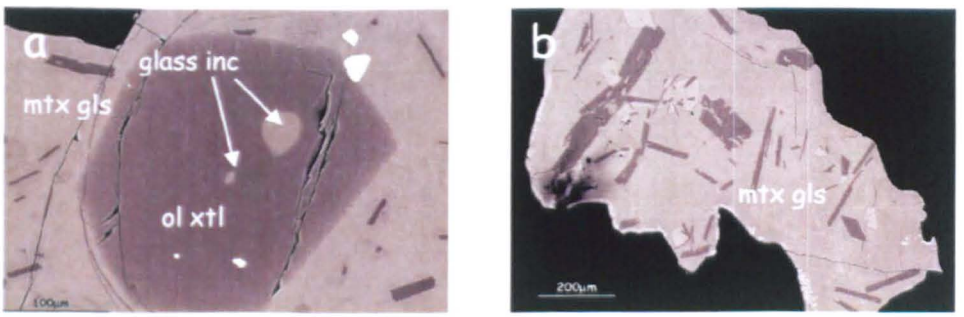

Figure 2.4 Back-scatter electron images (BSE) of representative material analysed. (a) olivine crystal with glass inclusions. (b) matrix glass shard with small amounts of microlite size crystals.

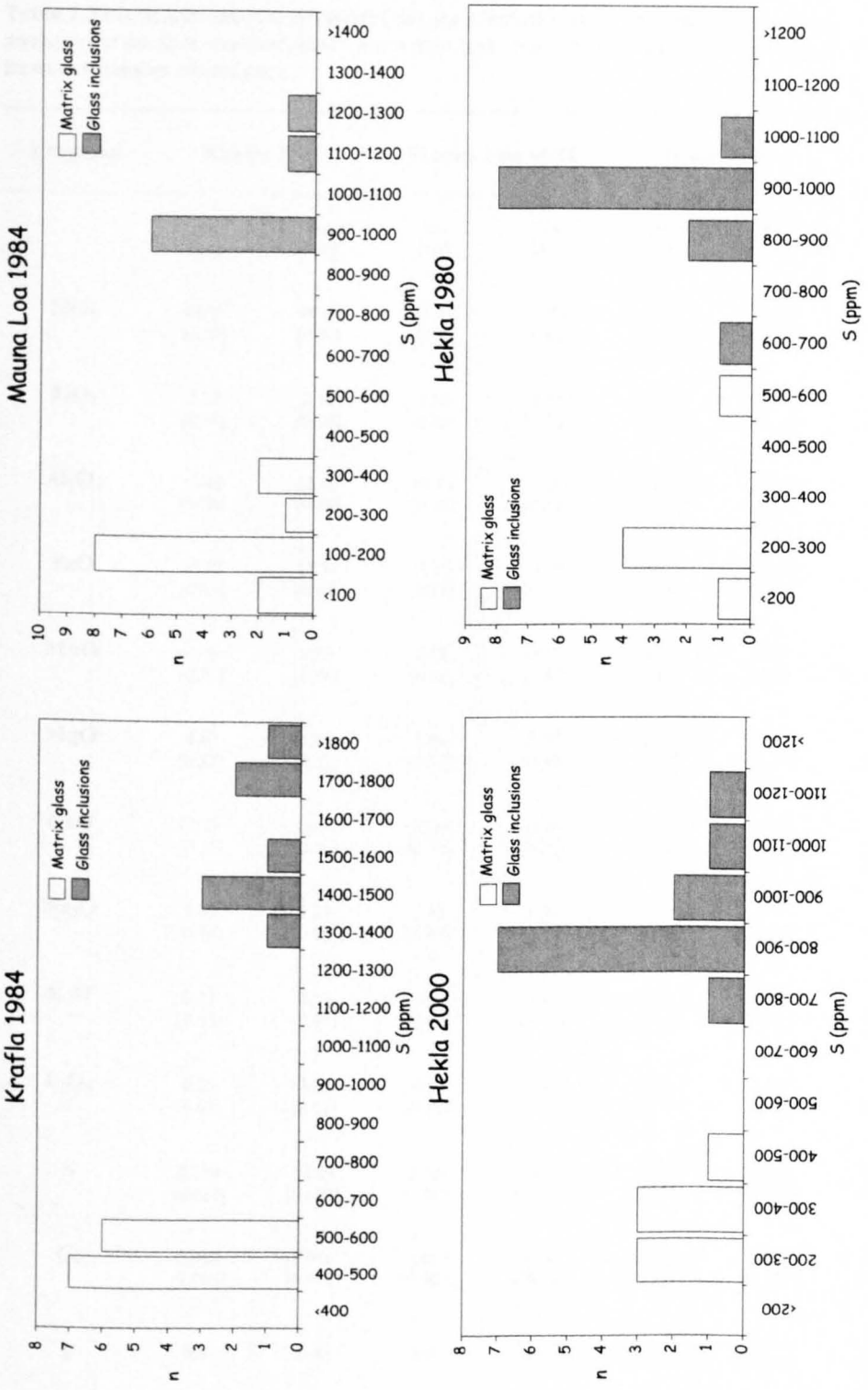

Figure 2.5 Histograms of matrix glass and glass inclusion sulphur concentrations (ppm) for the four eruptions described within text.

Table 2.2 Mean and standard deviation (1σ) glass inclusion (inc) and matrix glass (mg) analyses for the four eruptions described within text. b.d. = below microprobe detection limit; n = number of analyses.

Eruption	Krafla 1984		Mauna Loa 1984		Hekla 1980		Hekla 2000	
	Inc [1σ]	Mg [1σ]	Inc [1σ]	Mg [1σ]	Inc [1σ]	Mg [1σ]	Inc [1σ]	Mg [1σ]
SiO_2	49.95 [0.50]	49.94 [0.59]	51.27 [0.61]	51.44 [0.58]	55.79 [0.68]	55.43 [0.42]	56.73 [0.81]	55.58 [0.69]
TiO_2	2.27 [0.09]	2.32 [0.10]	2.30 [0.05]	2.32 [0.05]	2.06 [0.13]	2.02 [0.11]	2.01 [0.13]	2.10 [0.10]
Al_2O_3	13.40 [0.26]	12.65 [0.38]	13.56 [0.30]	13.36 [0.14]	14.71 [0.34]	15.09 [0.68]	14.58 [0.55]	14.55 [0.94]
FeO	14.97 [0.43]	15.34 [0.48]	11.53 [0.19]	11.63 [0.21]	11.17 [0.38]	11.25 [0.88]	11.07 [0.38]	11.90 [1.04]
MnO	0.26 [0.01]	0.25 [0.01]	0.17 [0.01]	0.17 [0.01]	0.27 [0.02]	0.27 [0.02]	0.27 [0.01]	0.28 [0.03]
MgO	4.42 [0.32]	5.15 [0.32]	5.83 [0.18]	5.98 [0.16]	2.65 [0.19]	2.74 [0.19]	2.73 [0.12]	2.69 [0.08]
CaO	10.29 [0.27]	10.01 [0.16]	10.24 [0.14]	10.29 [0.10]	6.53 [0.47]	6.82 [0.19]	6.25 [0.27]	6.70 [0.24]
Na_2O	2.61 [0.10]	2.29 [0.28]	2.36 [0.05]	2.30 [0.06]	2.95 [0.26]	3.57 [0.35]	3.02 [0.32]	3.52 [0.38]
K_2O	0.37 [0.03]	0.37 [0.02]	0.43 [0.02]	0.42 [0.01]	1.33 [0.15]	1.25 [0.10]	1.41 [0.12]	1.28 [0.20]
P_2O_5	0.25 [0.02]	0.25 [0.01]	0.27 [0.01]	0.27 [0.01]	1.01 [0.04]	1.00 [0.05]	0.98 [0.08]	1.04 [0.09]
S	0.159 [0.017]	0.049 [0.007]	0.101 [0.011]	0.016 [0.008]	0.091 [0.008]	0.034 [0.010]	0.090 [0.009]	0.031 [0.007]
Cl	0.018 [0.005]	0.016 [0.003]	0.007 [0.002]	0.008 [0.002]	0.041 [0.008]	0.037 [0.007]	0.042 [0.005]	0.038 [0.008]
F	b.d.	b.d.	b.d.	b.d.	0.072 [0.019]	0.077 [0.012]	0.067 [0.021]	0.072 [0.027]
Total	99.12	98.68	98.18	98.21	98.77	99.62	99.35	99.35
n	8	13	8	13	12	7	12	7

2.5 Results

Histograms showing sulphur data for all matrix glasses and glass inclusions from the non-arc eruptions are presented in Figure 2.5, and mean representative glass chemistry are listed in Table 2.2. In all cases the matrix glass sulphur concentrations are lower than the sulphur measured in glass inclusions.

To estimate the mass of SO_2 released through melt degassing using the petrologic method, only glass inclusions with the same major element composition as the matrix glass were used, thereby ensuring that the selected inclusions represent non-degassed equivalents of the degassed matrix liquids, as is assumed in the derivation of the petrologic method. Glass inclusions were statistically chosen by calculating the Euclidean distance function, D (in standard deviation units), between the normalized (100% volatile-free) major element composition of each inclusion and the mean normalized matrix glass composition. For each inclusion we calculated

$$D = \sqrt{\sum \left[\frac{x_i - \mu_i}{\sigma_i} \right]^2} \qquad [2]$$

where x_i is the wt% of the ith oxide in an inclusion, and μ_i and σ_i are the mean and standard deviation wt% of the ith oxide in the matrix glass. This type of test has been widely used to geochemically correlate different geological samples (e.g., Perkins et al. 1995; Dunbar et al. 2003). In computing the value of D, we include the 10 major elements; values ≤ 6.3 indicate that the inclusion is statistically identical to the mean matrix glass composition at the 95% confidence level. Only these statistically similar inclusions (D values ≤ 6.3) were averaged to obtain C_{inc} for the petrologic calculations (Table 2.2, Appendix A2-A6).

Density values in Table 2.3 (for conversion of eruption volume to magma mass) were taken from Gronvold et al. (1983) for Hekla (unless otherwise stated). In the case of scoria and lava samples from Krafla and Mauna Loa, volumes were measured using a simple water displacement method. Dividing the weight by the volume yielded the density which was proportioned according to the ratio of lava to scoria in the eruption products. Crystal mass fractions were measured by point counting of representative back-scatter electron images, except for Hekla 1980 (Gronvold et al. 1983) and Mauna Loa (Lockwood et al. 1987). Table 2.3 summarizes the sulphur, magma mass, and crystal fraction data for the studied eruptions. The error on the petrologic method estimate was calculated using the formula outlined in Appendix A1.

2.5.1 Krafla 1984

The 1984 eruption of Krafla began on September 4 with the opening of a fissure segment 6 km north of Leirhnjúkur; within 1 hour the fissure reached its full length of 8.5 km (GVN Bulletin 1984). Fire-fountaining characterized the start of the eruption but within 24 hours this activity waned and steady lava flow emplacement began. The eruption lasted ~2 weeks and a total bulk volume of 0.134 km^3 of tholeiitic basalt was erupted (Rossi 1997). TOMS detected a 0.1 Mt SO_2- rich plume produced during the first day of eruption; this plume later moved ESE towards Norway. Then, one week into the eruption, TOMS instruments detected additional amounts of SO_2 in plumes from Krafla. Sulphur dioxide plumes were tracked for 11 days and the total amount of SO_2 emitted to the atmosphere as detected by TOMS is 0.4 + 0.04/-0.15 Mt; in this case the errors are not symmetric about the mean (Bluth et al. 1993). Pre-eruptive sulphur concentrations range from 1380-1850 ppm with a mean value of 1590 ppm. Degassed sulphur values are between 400-500 ppm. The petrologic estimate of SO_2 released to the atmosphere through melt degassing is 0.64 ± 0.19 Mt. Lava matrix glasses show sulphur concentrations similar to those of scoria matrix

glasses implying that significant degassing did not take place during lava flow emplacement.

2.5.2 Mauna Loa 1984

The 1984 Mauna Loa eruption began on March 25 with a 12-hr summit eruption before activity migrated to the North East Rift Zone where fire fountains 10-50 m high prevailed, forming channel-fed lava flows. Eruptive activity lasted 23 days and the total volume of erupted tholeiitic lava was 0.22 km^3 (Lipman and Banks 1987). TOMS instruments detected an SO_2-rich plume from the volcano during 16 days of activity. The total amount of SO_2 emitted to the atmosphere was 1.0 ± 0.2 Mt as detected by TOMS and 0.85 ± 0.26 Mt calculated petrologically. The petrologic value is based on pre-eruptive sulphur contents of ~1000 ppm and degassed sulphur values of ~160 ppm.

2.5.3 Hekla 1980

The 3-day Hekla eruption of 1980 began on August 17 with simultaneous plinian and lava extrusion phases, producing basaltic-andesite fall deposits and lava flows. A 15-km-high eruption column quickly formed and deposited 0.06 km^3 of tephra in 5 to 6 hours, mainly during the first two hours. Lava (0.12 km^3) was erupted from an 8-km-long fissure cutting through the Hekla ridge (Gronvold et al. 1983). Although this was a moderately short Hekla eruption, the SO_2 cloud was relatively long-lived. Satellites tracked the plume for 6 days, with 0.5 ± 0.10 Mt of SO_2 (Carn et al. 2003) measured in the atmosphere by TOMS. The average pre-eruptive sulphur concentration is ~900 ppm and degassed sulphur values are ~300 ppm, giving a petrologic estimate of 0.36 ± 0.12 Mt of released SO_2.

2.5.4 Hekla 2000

The eruption of Hekla in 2000 began on February 26 with the opening of a 6-km-long fissure along the SW flank of the Hekla ridge. Initial activity in the central part of the fissure generated a sub-Plinian eruption column 11-12 km high. Following this, effusive activity began with the emplacement of lava flows interspersed with strombolian fire-fountain activity and phreatomagmatic explosions along the length of the fissure (Ólafsdóttir et al. 2002). The eruption intensity rapidly decreased after 5 days but activity lasted for 11 days. The total volume of basaltic-andesite magma erupted was 0.18 km^3, 0.01 km^3 of which was the tephra layer deposited in the first 12 hours of eruption (Haraldsson et al. 2002). TOMS images from 27 February show a narrow plume arcing away from Hekla before moving north towards Greenland and, finally, east over Norway. At the end of the eruption (29 February), the plume drifted east in a band along the Russian and Norwegian coasts of the Barents Sea (GVN Bulletin 2000). TOMS instruments tracked an SO_2 plume for 3 days. The total amount of SO_2 released to the atmosphere was 0.1 ± 0.05 Mt. A mean value around 900 ppm for pre-eruptive sulphur and ~300 ppm for the degassed sulphur yields a petrologic estimate of 0.48 ± 0.14 Mt SO_2 released through magma degassing.

2.5.5 Izu-Oshima 1986

The Izu-Oshima eruption is selected for analysis in order to provide a TOMS/petrologic comparison for a recent basaltic-andesitic arc eruption. The 1986 eruption of Izu-Oshima occurred in two phases. Phase 1 began on November 15 with intermittent fire fountaining. Magma quickly filled the summit crater forming a lava lake. Eventual overspill from this lake generated coalesced lava flows. On November 21 phase two of the eruption started with the opening of a 1-km-long fissure on the crater floor. Resultant explosive activity generated a 16-km-high sub-plinian eruption column (Hayakawa and Shirao 1988).

Alternating Strombolian fountaining and sub-plinian explosive activity produced a thick, vesicular air-fall scoria deposit, spatter and clastogenic lava flows (Sumner 1997). A total of 0.04 km^3 of basaltic-andesite magma was erupted, (0.014 km^3 scoria and 0.022 km^3 lava) (Nagaoka 1988). Pre-eruptive and degassed sulphur concentrations average 300 ppm and 86 ppm respectively, giving a petrologic estimate of 0.031 ± 0.02 Mt SO_2. Although TOMS detected minor amounts of SO_2 in the Izu-Oshima eruption plume on November 19, retrieval errors are too large for any meaningful estimate to be deduced. In the absence of reliable TOMS data, we are thus unable to use the petrologic/TOMS comparison from this eruption for quantitative analysis. The Izu-Oshima geochemistry dataset is presented in appendix A6.

Table 2.3 lists results for all analyzed eruptions, and Figure 2.6 compares the two types of SO_2 measurements for the eruptions listed here and for 6 arc eruptions (listed in Figure 2.1) where both data types are available.

Table 2.3 Summary of the data used in the petrologic method for calculating volcanic SO_2 release, together with the petrologic SO_2 estimate. Also shown are TOMS total SO_2 measurements for these eruptions and calculated oxygen fugacity data. Density values used to convert erupted volume (km^3) to magma mass are given in square brackets. Bulk density of Hekla 2000 tephra was provided by G. Larsen (unpublished data, 2002). Errors on C_{inc} and C_{matrix} measurements are 1σ, & errors associated with petrologic SO_2 values are 2σ. [n] = no. of analyses.

Eruption	C_{inc} [n]	C_{matrix} [n]	Mass (kg) [Density kg/m^3]	W_{xtls}	Petrologic SO_2 (Mt)	TOMS SO_2 (Mt)	Log fO_2 [ΔNNO]
Krafla 1984	0.159 ± 0.017 [8]	0.049 ± 0.007 [13]	2.95×10^{11} [2200]	0.02	0.64 ± 0.19	0.4 + 0.04/- 0.15*	-8.4 [0.3]
Mauna Loa 1984	0.101 ± 0.011 [8]	0.016 ± 0.008 [13]	5.06×10^{11} [2300]	0.01	0.85 ± 0.26	1.0 ± 0.20	-8.5 [-0.1]
Hekla 1980	0.091 ± 0.008 [12]	0.034 ± 0.017 [7]	3.22×10^{11} [700[a], 2400[b]]	0.03	0.36 ± 0.12	0.50 ± 0.10	-9.5 [-0.4]
Hekla 2000	0.090 ± 0.009 [12]	0.031 ± 0.007 [7]	4.14×10^{11} [600[a], 2400[b]]	0.01	0.48 ± 0.14	0.10 ± 0.05	-9.4 [-0.3]

[a] indicates tephra/scoria bulk density,
[b] indicates lava density
* TOMS error not symmetric about the mean

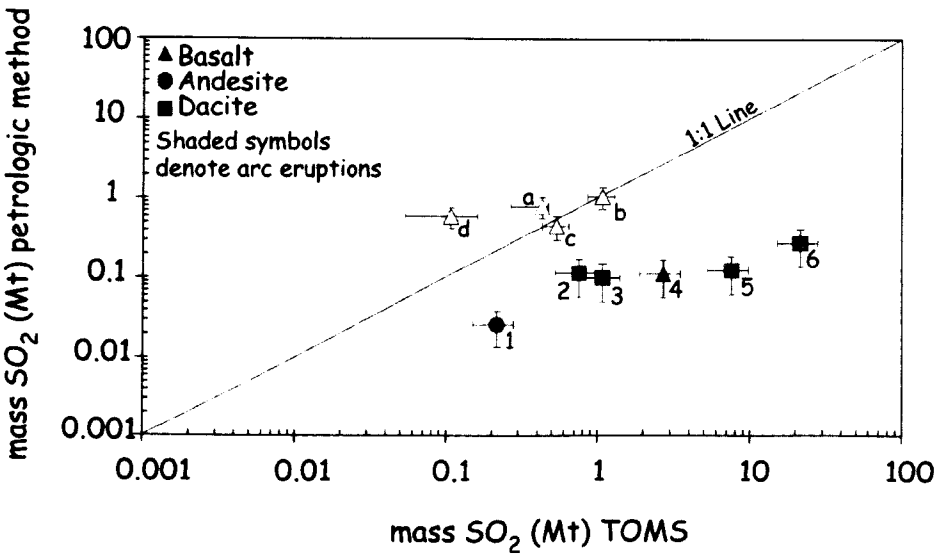

Figure 2.6 TOMS SO_2 measurements vs. calculated petrologic SO_2 for the 4 eruptions described here, Krafla 1984 (a), Mauna Loa 1984 (b), Hekla 1980 (c), & Hekla 2000 (d). Also shown are data from the 6 arc eruptions described in figure 2.1. Error bars on the non-arc petrologic SO_2 measurements are calculated 2σ errors.

2.6 Discussion

As we see from Figure 2.6, the TOMS SO_2 measurements for the non-arc eruptions are comparable to the petrologic estimations of SO_2: all of the data falls close to or on a 1:1 correlation line, indicating that there was no excess S-rich gas phase present in the underlying magma systems prior to eruption. This may be a possible reflection of the magma source conditions and tectonic setting. Data here suggest that magma composition plays little part in the separation of sulphur into an excess gas phase. The arc eruptions vary in bulk composition from basaltic (Galunggung) to dacitic (Mt. St Helens, Pinatubo), yet all have excess sulphur. The common factor connecting them is their location in an arc setting.

For Hekla 2000, the petrologic SO_2 value is however slightly higher than the SO_2 detected by TOMS. One explanation for this is that a large amount of sulphur was released through

lava degassing during the later stages of the eruption, generating low-altitude SO_2 plumes undetectable by TOMS. However, a more likely scenario is that TOMS did not detect part of the SO_2 plume. TOMS estimates are based on the scattering of solar UV radiation; thus the high-latitude location of Hekla combined with the low solar energy during the polar winter may have contributed to the low TOMS value for the 2000 eruption (Rose et al. 2004).

Magma source conditions typically found in arcs (such as higher H_2O contents and fO_2) may be the crucial factor in the pre-eruption sequestering of sulphur from the melt into an excess S-bearing fluid phase. For the arc eruptions listed in Figure 2.6, $\log fO_2$ values were obtained from the literature. For the Icelandic and Hawaiian eruptions, $\log fO_2$ values in Table 2.3 were calculated using the model of Sugawara (2001). This model uses equilibrium plagioclase and olivine compositions together with temperature and pressure values to compute $\log fO_2$, to an accuracy of $\pm$ 0.8 log units. The program can be found at http://www.geo.titech.ac.jp/takahashilab/staff/toru/sugawara.html. We express fO_2 in relation to the NNO buffer (Ni-NiO reaction), with ΔNNO defined as the $\log fO_2$ value of the magma minus the $\log fO_2$ value of the NNO buffer at the same temperature (Carmichael and Ghiorso 1990), (Figure 2.7).

When ΔNNO is plotted against the ratio TOMS SO_2/petrologic SO_2, – a measure of excess S (Fig. 2.8), we find that the data form two distinct fields. The six arc eruptions plot with high excess sulphur ratios and positive ΔNNO values. The non-arc eruptions fall within the lower sector of the graph showing low excess S ratios and low positive and negative ΔNNO values. This trend is independent of magma composition.

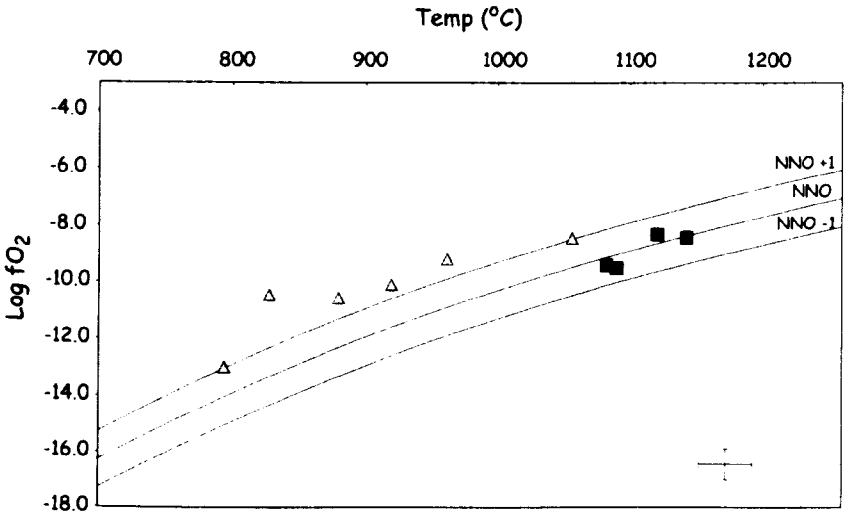

Figure 2.7 Log fO_2 versus temperature. Squares represent non-arc eruptions and triangles denote arc eruptions. Solid lines mark position of the Ni-NiO buffer (NNO). 2σ error bar shown for reference.

Figure 2.8 indicates that oxygen fugacity (fO_2) and thus tectonic setting has a greater influence than magma composition on the presence of excess S. Oxygen fugacity exerts a control on the solubility and partitioning of species with different oxidation states, e.g., Fe, S. Low fO_2 conditions indicate a reducing environment and may stabilize an immiscible sulphide phase. High fO_2 conditions indicate more oxidizing environments and may stabilize a SO_2- bearing gas phase, such that oxidized magmas release pre-existing SO_2 gas in addition to SO_2 exsolved from the melt during the eruption. Experimental studies of sulphur partitioning between melt and fluid imply that under certain conditions sulphur maybe strongly partitioned into the gas phase relative to the silicate melt (Scaillet et al. 2003). Scaillet et al. (1998) demonstrate that this partitioning strongly depends on redox conditions (Figure 2.8b). Oxidized magmas (high fO_2) have a greater tendency to sequester sulphur into a fluid/gas phase at depth because thermodynamic equilibrium requires significant fugacities of S-bearing species (SO_2, H_2S) under these conditions. Reduced magmas (low fO_2) have low sulphur partition coefficients, such that nearly all the sulphur remains in the melt and does not get partitioned into a fluid phase because nearly all of the sulphur is taken up in a stable S-bearing solid phase. Based on the comparison

between TOMS SO_2 and petrologic SO_2 data, the transition between oxidised S-rich fluid phase and reduced S-poor fluid phase occurs over a relatively narrow range – magmas that erupt excess sulphur are more oxidized than $\log fO_2 \sim -9.8$ (ΔNNO ~0.5) (Figure 2.8b).

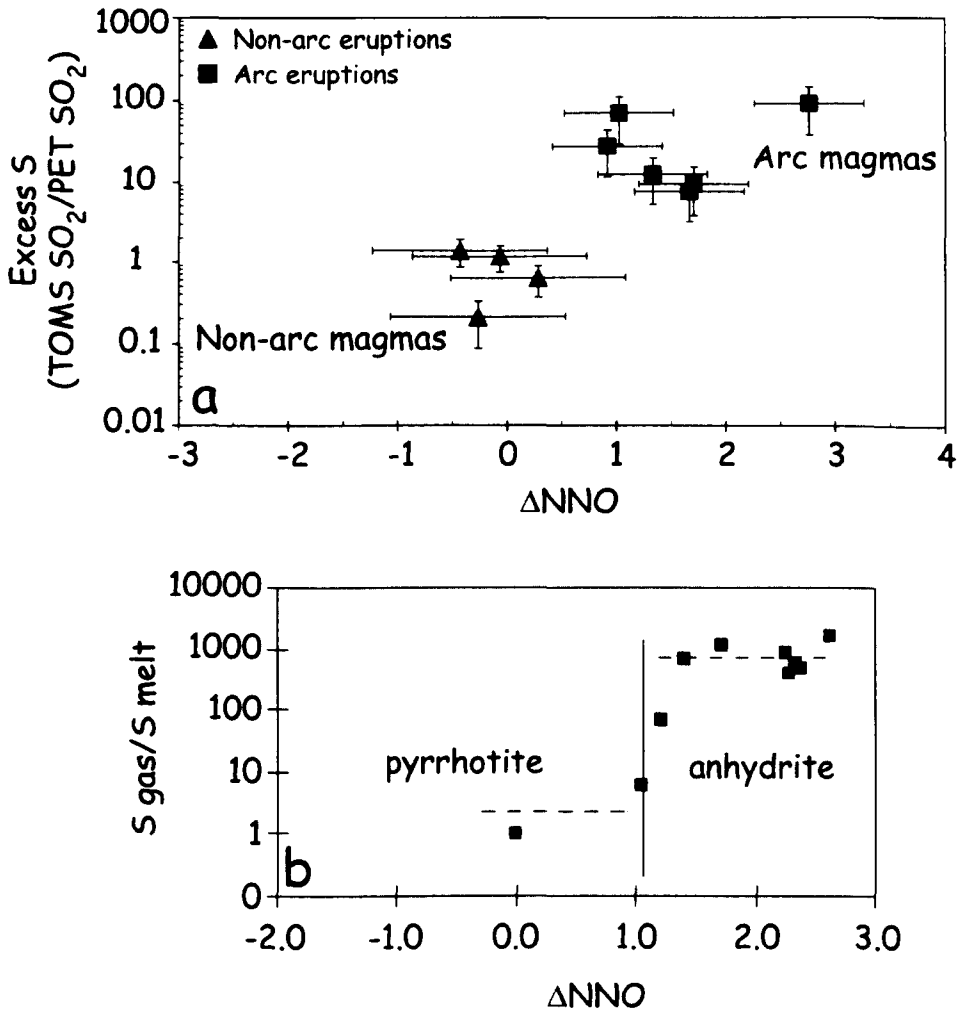

Figure 2.8 (a) ΔNNO versus TOMS SO_2/Petrologic SO_2 (a measure of excess S). (b) ΔNNO versus S gas/S melt (wt %). Diagram (b) shows experimentally-determined partition coefficient of sulphur between gas and silicate melt as a function of fO_2 (after Scaillet et al. 2003).

2.7 Conclusions

Using a petrological approach in which inclusions that are statistically similar to the initial matrix composition were selected, it is shown that for the recent eruptions of Mauna Loa, Krafla and Hekla the petrologic estimates of SO_2 are within error of the TOMS SO_2 measurements, indicating that if there was any fluid phase present at depth in these magma systems prior to eruption it was sulphur-poor. The lack of a separate S-rich gas phase reflects the links between fO_2, melt H_2O content, magma source conditions (tectonic setting) and sulphur solubility. Oxidized, water-rich arc magmas have an excess S-rich gas phase prior to eruption whereas more reduced H_2O-poor non-arc magmas do not. One exception to this may be non-arc CO_2-rich alkali basalts. As CO_2 will inevitably promote fluid saturation at depth, it is quite possible that these magmas could generate a S-rich gas phase depending on their oxidation state.

The results have shown that a petrological approach for calculating SO_2 released through melt degassing is a reliable method for quantifying SO_2 releases from tholeiitic to transitional basaltic magmas, in contrast to the situation in many arc eruptions. This result is also supported by the similarity between the petrologic estimates of SO_2 release from the AD 1783 eruption of Laki (tholeiite with ΔNNO of -0.3) and independent estimates of the mass of sulphate aerosol loading from this eruption (Thordarson et al. 1996). While the Laki case involves indirect methods of assessing the sulphate burden, the large mass of SO_2 released (~120 Mt) makes the comparison reasonably robust. I therefore conclude that petrologic estimates of SO_2 emissions from ancient basaltic eruptions, e.g., flood basalts, are likely to be realistic values.

2.8 Evaluation of the petrologic method

As discussed in Chapter 1, methods of accurately estimating SO_2 yield from volcanic eruptions are required. This chapter shows that the classic petrologic method (which assumes that the only source of SO_2 is melt degassing) replicates independent (TOMS) measurements of SO_2 release for ocean island basalts (Mauna Loa and Krafla – tholeiite; and Hekla – basalt to basaltic-andesite) with $fO_2 \leq -9.5$ ($\approx\Delta$NNO). This is in contrast to arc basalts (e.g., Galunggung) to dacites (e.g., Mount St Helens, Pinatubo) with higher H_2O and fO_2, which involve an excess sulphur phase. Using these results I suggest the following approach to estimate volcanic SO_2 releases from a petrological or geochemical standpoint:

A: Glass inclusion and matrix glass data readily available

1. For basalts with $fO_2 \leq 9.5$ where there is little or no gas in the magma chamber, or if any gas is present then because of low oxygen fugacities, gas is S-poor, one would use the 'classic' petrologic method (e.g., Devine et al. (1984), this study), where $M_S = M_{liq}\,[C_{inc} - C_{matrix}]$ – for matrix glass and glass inclusions forming in the same liquid composition (determined via statistical selection of glass inclusions).
2. For other magma compositions – dacites to rhyolites which may contain a small gas phase in the magma chamber – one could use the techniques devised by Scaillet et al. (2003) whereby one assumes the percentage of gas in the chamber and the gas/melt partition coefficient of S based on redox conditions and magma compositions (Figure 2.8b). The petrologic estimate of SO_2 release is calculated in the usual way and is then corrected for the presence of a S-rich gas.

B: Where glass inclusion data are not readily available, e.g., absence of glass inclusions, or if inclusions are partially degassed, the following can be considered to enable calculation of pre-eruptive S:

1. For a magma that is saturated with respect to sulphur, one can use the sulphide saturation (or sulphur solubility) limit to estimate the total dissolved S content of the melt. The formation of sulphide minerals will remove both Cu and S from a melt, so sulphide saturation limits can be determined using sulphide mineral chemistry; or in the absence of sulphide precipitation, the correlation between Cu and a highly incompatible trace element (e.g., Zr) can be used as an index of sulphide fractionation, e.g., the fractional crystallization of a magma under-saturated with respect to sulphide should show highly incompatible behaviour of Cu; where Cu is behaving as a compatible element, one would expect fractionation of a sulphide saturated magma. The correlation between major elements, e.g., FeO and S (e.g., Mathez 1976; Wallace and Carmichael 1992) has been successfully used in basalts of MORB composition. Thordarson et al. (2003) used the correlation between the FeO/TiO_2 ratio and S to calculate pre-eruptive S concentrations for Icelandic tholeiites.
2. For a magma that is not sulphide saturated, e.g., where Cu is highly incompatible, estimates of the melt S/K_2O ratio or other incompatible element in conjunction with information on magmatic conditions can be used to calculate pre-eruption sulphur. An example of this approach is developed in chapter 4.

All of these methods can be used to estimate sulphur yields of volcanic eruptions of various fO_2 and melt compositions. However, rigorous testing of these techniques and application to differing volcanic systems will allow me to apply better quantitative

constraints to the use of the petrologic method. In subsequent chapters of this thesis I use these approaches when calculating eruption sulphur budgets.

The AD 1362 Öræfajökull eruption, S.E. Iceland: Physical volcanology and volatile release

Abstract

I present here results from a study of the rhyolitic AD 1362 eruption of Öræfajökull volcano, Iceland, based on the sequence of pyroclastic deposits at 10 proximal locations around the south side of the volcano. Öræfajökull is an ice-clad stratovolcano in south central Iceland which has an ice-filled caldera (4-5 km diameter) of uncertain origin. During the 1362 eruption, large areas of farmland and villages were inundated by Plinian fallout, lahars, and perhaps pyroclastic flows, leading to the desolation of an important region in early Iceland. The deposits can be tied to the historic accounts of the eruption summarized in the classic work of Thorarinsson (1958). The eruption took place in June 1362 and proceeded in three main fallout phases and a pyroclastic flow phase that all together lasted a few days.

An initial phase of phreatomagmatic eruptive activity produced a volumetrically minor, coarse ash-fall deposit (unit *A*) with a bi-lobate dispersal. This was followed by a second phreatomagmatic to phreatoplinian phase of activity that deposited more fine ash beds (unit *B*), dispersed to the SSE. Phases *A* and *B* were followed by the climactic Plinian phase of the eruption which lasted ~11-13 hours and produced unit *C*, a coarse grained, pumice-clast-dominated fall deposit in the proximal region. Following the intense Plinian activity, pyroclastic flow activity occurred forming a poorly sorted pyroclastic flow deposit, unit *D*, presently of very limited thickness and exposed distribution. Much of Eastern Iceland is also covered with a very fine distal ash deposit, dispersed to the NE. This is possibly fine ash deposited from umbrella cloud margins, the distal representation of the Plinian fallout. A total bulk fall deposit volume of ~ 2.3 km^3 is calculated. Pyroclastic flow volumes have been crudely estimated to be < 0.1 km^3. Maximum clast size data suggests stratospheric eruption columns ~30 km high, reaching the stratosphere, and mass discharge rates of ~ 10^8 kg/s.

The erupted units are all rhyolite with little change in the magma composition as the eruption progressed with time. Traces of basaltic-dacitic juvenile material are found intermingled with the rhyolite pumice within unit *C*. Although the 1362 eruption was a highly-explosive event the syn-eruptive SO_2 release was minor, on the order ~1.2-1.7 Mt, as estimated petrologically. This result is supported by Greenland ice-core acidity peak data which also suggest a very small SO_2 release. Therefore, despite the low tropopause position over Iceland (~10 km) and the generation of a ~30-km-high eruption column, only a small amount of sulphate aerosol (~3 Mt) was generated. This small sulphur release reflects the low sulphur solubility in the 1362 rhyolitic melt. Similarly, pre-eruptive and degassed halogen concentrations (Cl, F) indicate that these volatiles did not efficiently degas during the eruption. The widespread impact of the Öræfajökull 1362 eruption was perhaps restricted to pumice fall across Eastern Iceland, and pyroclastic flow hazards locally, with injection of volcanic ash and dust particles into the upper atmosphere the main environmental consequence.

Keywords *Öræfajökull, Plinian eruption, sulphur degassing, atmospheric impact*

3.1 Introduction

Öræfajökull is an ice-capped stratovolcano located in south-east Iceland (64.00° N, 16.65° W), on the southern margin of the Vatnajökull icecap, which in turn forms the eastern margin of the young volcanic belt that extends through Iceland from the SW to the NNE. The volcanic edifice rises ~2000 m above sea level, the summit being ~10 km NW of the Atlantic Ocean shoreline, and is primarily composed of sub-glacial pillow lavas, tuffs and breccias, basaltic and andesitic lava flows and rhyolite intrusives and extrusives, intercalated with interglacial sediments (Thorarinsson 1958; Stevenson et al. 2006). The summit is truncated by a 4 - 5 km diameter ice-filled caldera of unknown origin and age. Several peaks (nunataks), most of them remnants of old lava domes, rise above the ice marking the margins of the caldera wall. The highest nunatak (and the highest point in Iceland), Hvannadalshnjúkur, at 2119 m is a pristine rhyolite lava dome that possibly occupies the 1362 eruptive vent site (Th. Thordarson, pers. comm. 2005). In historical times there have been two explosive eruptions of Öræfajökull, a small basaltic-andesite eruption in AD 1727-1728, and the larger rhyolitic eruption of AD 1362 (Thorarinsson 1958; Prestvik 1979; 1982).

Öræfajökull erupted violently in 1362, with historical evidence suggesting that the eruption started around June 5 (Thorarinsson 1958). By all accounts this was a large, explosive eruption that produced much ash, and devastated the local area. The explosive activity was accompanied and followed by major jökulhlaups (glacier outburst floods), carrying pumice and gravels that demolished the remaining settlements on the lowlands and caused further fatalities. Contemporary reports, summarized in the classic work by Thorarinsson (1958) describe "*blocks of hot pumice and ash raining down, on the small farm community of*

Öræfi, with such monstrous fury as to lay waste to the whole of Litlaherad[1]*, causing desolation for some 100 miles. Winds swept ash and pumice into drifts that obliterated buildings, and caused darkness so intense that roads could not be seen at midday".* Where there had previously been an expanse of water on the south side of the volcano, glacier bursts triggered by the volcanic activity carried large quantities of gravel, rock and pyroclastic material, and formed a sandur plain, an unstable braid-plain composed mainly of volcanic gravel-dominated material.

The 1362 eruption is thought to be the largest rhyolite eruption to occur in Iceland during historic times (Thorarinsson 1958). Fine ash was dispersed as far afield as Greenland, ~1300 km from source, and Scandinavia, ~ 1220 km from source, and parts of the UK, as shown on Figure 3.1 (Persson 1971; Palais et al. 1991; Hall and Pilcher 2002). Thorarinsson (1958) made a map of the widespread ash fall deposit across Eastern Iceland, and Larsen et al. (1999) revised the dispersal axis of this map slightly (her Figure 3). Although the main explosive phases apparently lasted for only a few days, historical accounts report that eruptive activity probably continued until the Autumn of 1362 (Thorarinsson 1958). This latter activity possibly involved the growth of the rhyolite dome Hvannadalshnjúkur at the 1362 vent site.

As described in Chapter 1, the release of volcanic gas during eruptive activity and the injection of volcanic ash into the atmosphere is of major importance to the scale of subsequent environmental effects. Therefore, one of the main priorities of this work is to estimate the sulphur budget of this event and assess the environmental impact of the eruption. In order to obtain estimates of the sulphur release, detailed volcanological information is needed to interpret eruption mechanisms. I therefore present a first

[1] the coastal area around Öræfajökull

interpretation of the eruption sequence and deposits based on sections through the pyroclastic deposits in the medial to proximal area around the volcano. Although the 1362 eruption involved rhyolitic magma, which usually contains little dissolved sulphur, the high FeO content (3-4 wt%) of the 1362 magma suggests that it may have had a slightly higher sulphur solubility limit.

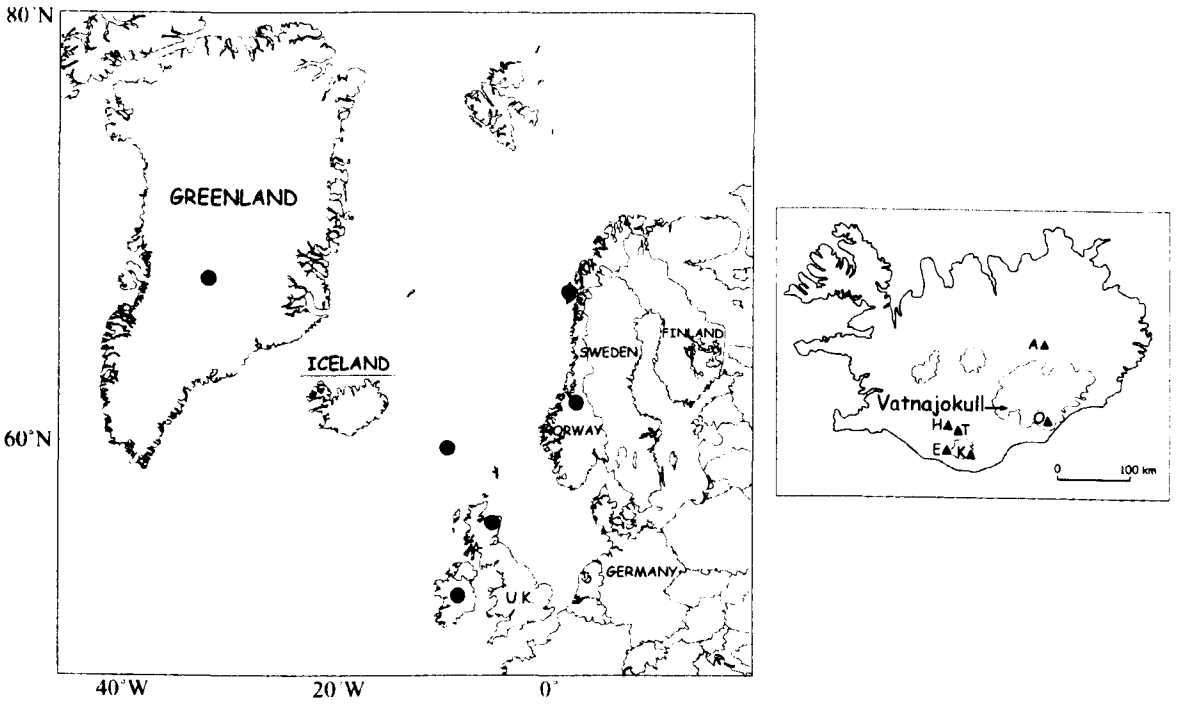

Figure 3.1 Map of Europe indicating locations where ash fall from AD 1362 event has been found. Volcanic glass shards correlated to the 1362 eruption have been discovered in south Ireland (Hall and Pilcher 2002), Norway, and Scandinavia (J Pilcher, pers. comm. 2004), and Greenland (Palais et al. 1991). Inset map shows location of Öræfajökull in Iceland. Triangles mark active silicic volcanoes of Eastern Volcanic Zone (EVZ): Ö = Öræfajökull, K = Katla, T = Torfajökull, H = Hekla, E = Eyjafjallajökull, A = Askja. Grey shaded areas denote main ice caps.

This chapter is divided into three main parts – with each part containing background information, results, and interpretation. First I present detailed descriptions of the proximal stratigraphy and primary deposits and their grain size characteristics of the 1362 eruption. Using this information, I calculate eruptive parameters, e.g., deposit volume, eruption column heights, and dispersal characteristics. I also attempt to link the distal ash deposit described by Thorarinsson with the proximal deposit sequence. In part 2, I show

data on the bulk, glass, and mineral composition of the eruptive units and estimate intensive parameters for the erupting magma. Finally, I present the first detailed account of volatile degassing, in particular for sulphur, from the 1362 eruption, and assess the potential atmospheric and environmental impact of the eruption.

3.2 Deposit stratigraphy and descriptions

The deposits from the 1362 eruption are only patchily preserved in the proximal region. This area of Iceland is a highly erosive environment and most of the 1362 deposits have been stripped away from the steep glacial valleys and ridges that cut the flanks of the volcano. Wind erosion over time has all but removed the 1362 fallout from most areas. The volcano summit, including the vent area, is also ice-capped, precluding the preservation of any ultra-proximal sections. The northern to eastern part of the proximal-medial fallout dispersal was also on ice and the deposits have presumably been removed or modified by runoff and glacier movements. However, tephrostratigraphic studies have found the 1362 tephra layer (commonly used as a marker horizon) in outlet glaciers on north-western Vatnajökull (Larsen et al. 1998). Nevertheless there are several moderately well-preserved, accessible exposures located on the lower, ice-free southern flanks of the volcano. Ten sections that provide control on the proximal deposit stratigraphy were studied and logged in detail (locations are marked on Figure 3.2; detailed location descriptions can be found in Appendix B1), and extra details are provided by information from occasional incomplete exposures. We have not attempted to re-map the distal deposit.

We identify three main fall units (*A* to *C*), see Figure 3.3, and a pyroclastic flow unit (*D*). Each unit contains one or more sub-units, but it must be noted that the sub-unit divisions,

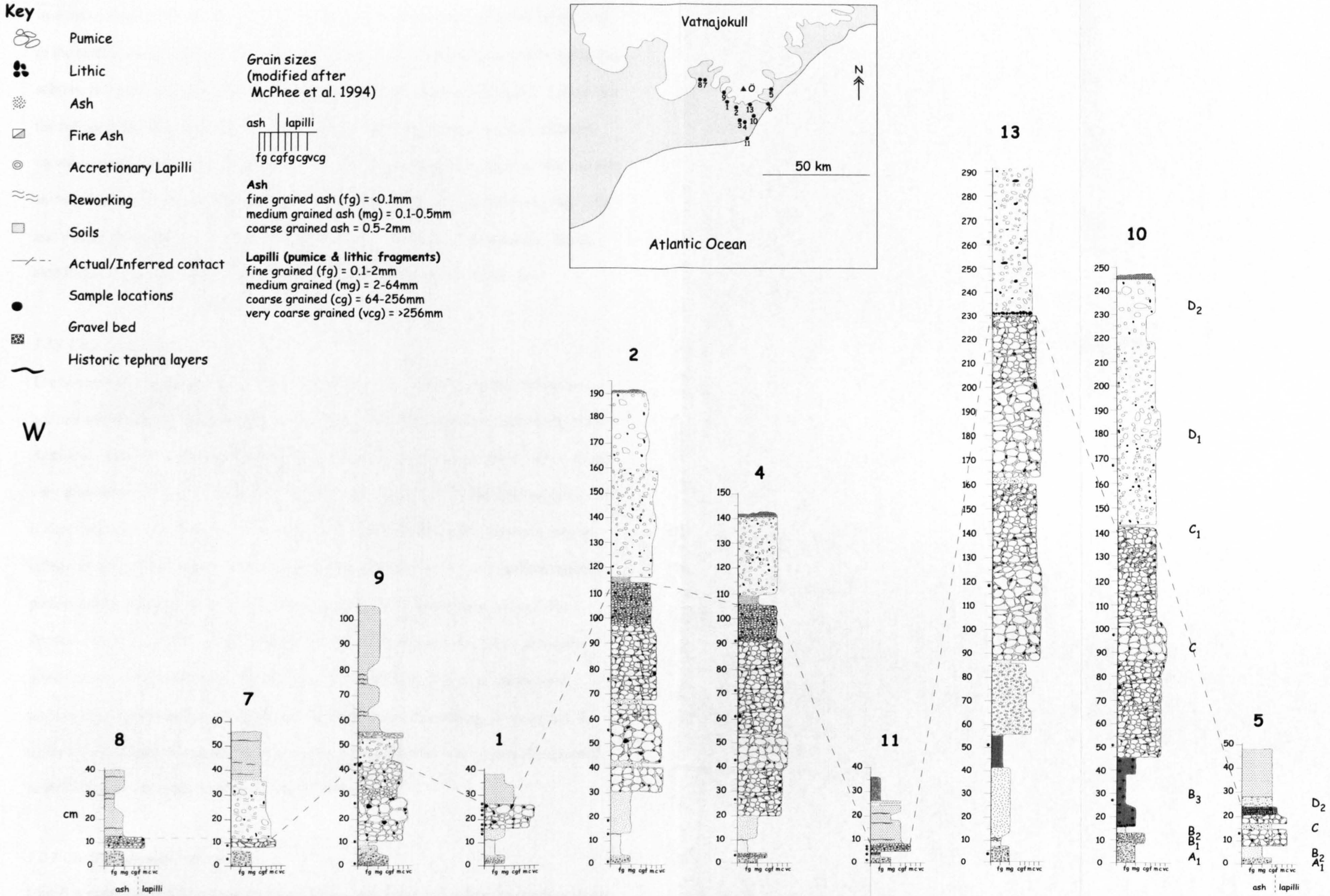

Figure 3.2 Stratigraphic sections through Öræfajökull 1362 (Ö1362) deposits. Sections are all from proximal locations on the south flank of the volcano. Index map shows the approximate location of each section (black circles with location number) and the volcano's summit (red triangle). Height of stratigraphic sections is given in cm; grain size variations (horizontal axis) are measured using modified version of grain size scale devised by McPhie et al. (1994). Dashed line on sections marks top of Plinian fall deposit (unit *C*). Unit designations are listed alongside sections 5 and 10.

in *A* and *B* especially, represent a simplification of a more complex set of fall layers. Due to the patchy preservation of these fall units, a more detailed subdivision will be difficult to achieve and was not made during this study. Stratigraphic sections in Figure 3.2 show that the fall units decrease in thickness at various rates with distance from source, reflecting varying eruption intensities. All major fall units thin more rapidly to the west than towards easterly directions. The mapped dispersal of the fallout units *A-C* are shown on Fig. 3.4a, and will be discussed in a later section. In this work, grain size terms used (e.g., lapilli, ash) follow the normal definitions used in McPhie et al. (1994), see Figure 3.3.

3.2.1 Unit A (sub-units – A_1, A_2)

The lowermost depositional unit of the 1362 eruption is composed of a fine-to coarse-grained ash bed, up to 14 cm thick in total (Figure 3.4a). Two sub-units can be identified, A_1 and A_2. Sub-unit A_1 is a locally distributed (found at two localities only), thin (~ 1 cm), very fine white ash layer. Where present it forms the basal layer of the 1362 sequence. A_2 is dominantly a medium- to coarse-grained ash and lapilli bed, mainly brown to grey in colour, but often displaying a yellowish tinge, containing small (0.1 to 1 cm) intercalated pumice and lithic lapilli; unit A_2 is also often stratified into thinner layers (Fig 3.3b). Pumice clasts in unit *A* are small, elongate and have tubular vesicles. Lithic clasts are mostly chips of fragmented, altered obsidian. The top of unit *A* is often eroded and missing in proximal sections. However, at localities where the unit top is preserved, the upper 1-2 cm is often a distinct "millet-seed" layer of extremely well-sorted fine-grained, rounded, coarse ash-grade pumice (0.5 to 2.5 mm).

3.2.2 Unit B (sub-units – B_1, B_2)

Unit *B* is distinguished from unit *A* by its differing grain size and colour; two sub-units are recognised – B_1 and B_2. B_1 is a fine-grained, grey ash bed, up to 8 cm thick. Lenses containing lapilli-size obsidian chips and small crystals can be found distributed irregularly

within the bed. Overlying B_1 in most proximal sections is sub-unit B_2, a medium-grained white to grey ash bed, up to 30 cm thick, containing scattered small (0.5-1 cm) pumice and lithic lapilli. The base of B_2 contains extremely fine-grained white or grey, thin (0.1 to 0.5-cm-thick) ash horizons interbedded within the coarser ash beds (Figure 3.3b).

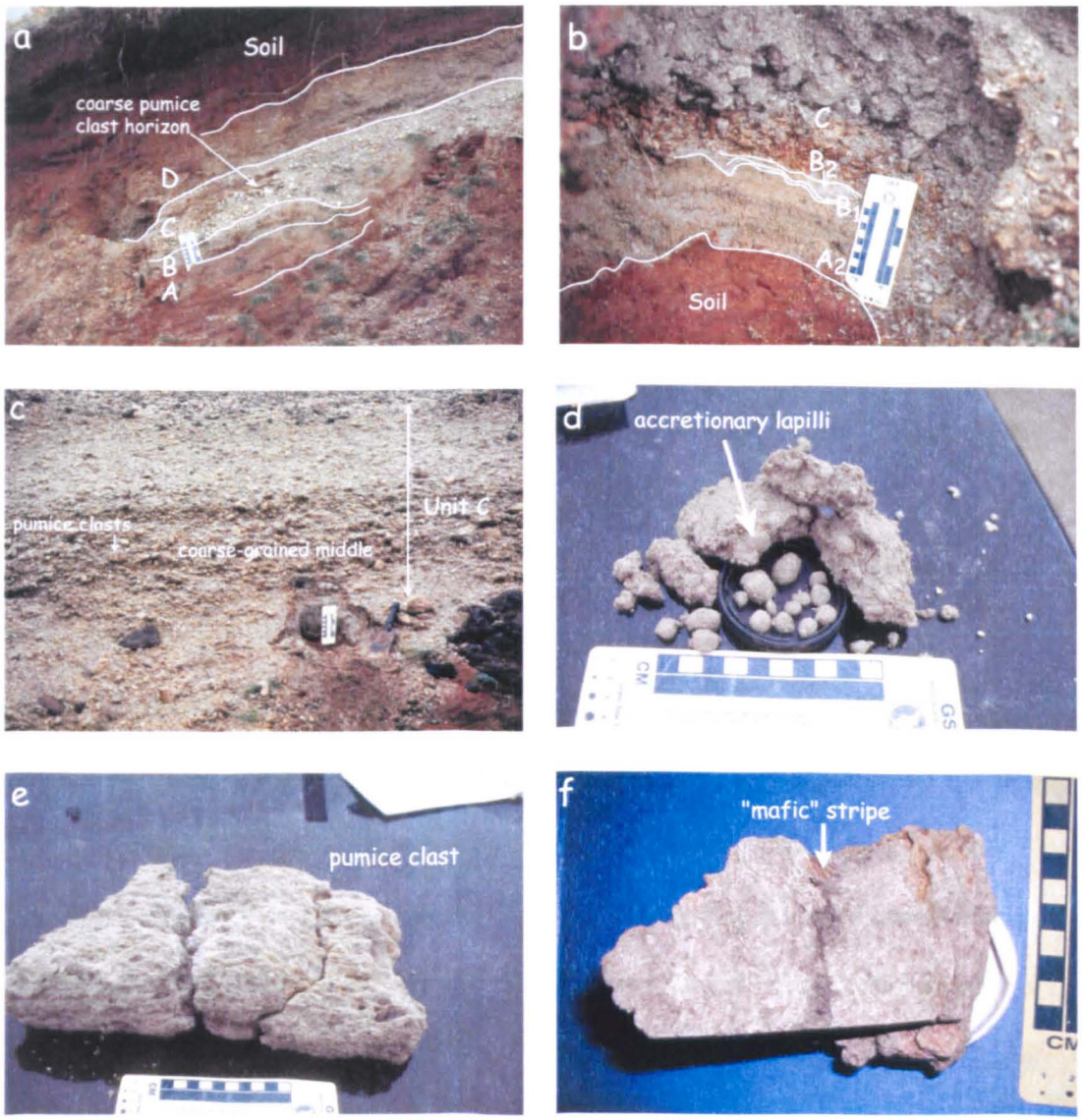

Figure 3.3 Photographs showing Öræfajökull 1362 deposits and detailed clast/unit features. (a) Proximal 1362 stratigraphic sequence, ~ 55 cm thick, shows different deposits of main eruption phases stages. Sequence is from location 9, 12 km to NW and upwind from vent (see also log of deposit sequence at location 9, Fig. 3.2). Soil above section contains thin horizons of fine grained basaltic ash. (b) Detail of base at location 9; sub-unit A_2 forms base of sequence; A_1 missing at this location; B_1 also missing. Stratification, resulting from changes in grain size in unit A can be seen in the base of this section. Above A, unit B forms thin bands of fine ash fallout. (c) Unit C (arrowed) at location 4, totalling 70 cm thick; note horizon enriched in coarse pumice and lithic clasts towards middle. (d) Sample of delicate, accretionary lapilli-bearing ash sub-unit B_3 from location 10. (e) Typical large, platy, fractured pumice clast > 20 cm long from middle of unit C at location 4. (f) Cut section through pumice clast with a dark band from unit C, collected from middle of deposit at location 10. Scale on all photographs is 10 cm with 1 cm bars.

In the proximal region we also identify additional local layers that are present at very few localities and cannot be correlated with the other sub-units. These layers (B_3 and B_4) are grouped as part of the unit *B* sequence, and are most likely the result of minor pyroclastic flow activity occurring prior to or during the activity that produced unit *C*.

3.2.3 Layer B_3

Layer B_3 consists of accretionary-lapilli-bearing fine- to medium-grained ash, and is found only at locations 10, 11 and 13. At location 13, the most proximal exposure studied, B_3 is a very fine grained dark grey ash, ~30 cm thick, containing accretionary lapilli "ghosts" and ash aggregates. At location 10, ~20 km away from the vent, this ash layer is thinner (~ 15 cm) and contains abundant accretionary lapilli with a maximum diameter of 1-1.5 cm; they are extremely fragile and fall apart when touched (Figure 3.3d). At the base of this layer, a sandy, crystal-rich, 2 to 3 cm-thick sub-layer is often found.

3.2.4 Layer B_4

Layer B_4 is preserved only at the most proximal location (13). It is a 30-cm-thick, medium-to-coarse-grained ash deposit with some small (~0.1 to 0.5 cm) pumice lapilli. The poorly sorted nature of this bed and the ash-dominated matrix suggest that this deposit is a proximal, local pyroclastic-flow-deposited layer, possibly derived from small column collapses before the climactic stage of the eruption (*cf.* June 13-14 pre-climactic events during the 1991 Pinatubo eruption, Hoblitt et al. (1996)).

3.2.5 Unit C

Unit *C* represents the deposit of the main eruptive pulse and consists of a well-preserved, mostly unstructured pumice lapilli- to bomb-size fall deposit. The pumice fall deposit forms a thinning sheet, extending ~ 20-25 km out to the south coast, but at the most distal exposure found (location 11) the thickness is truncated by erosion. Based on its fines-poor,

well-sorted nature, this unit is interpreted to be a medium-to coarse-grained, clast-supported fall deposit dominated by coarse pumice lapilli with minor lithic clasts. Where fully preserved, the unit varies in thickness from 60 to 180 cm in the sections examined and shows both normal and reverse grading. In most sections, the middle of the deposit is very coarse-grained (Figure 3.3c); above this, however, coarse pumice lapilli beds alternate with beds of finer pumice lapilli. The pumice clasts are rounded to sub-angular (Figure 3.3e), although in some sections clasts are elongate, parallel to vesicle shapes. Large pumice clasts are extremely fragile and have an exceptionally low density, ~280 kg/m^3, calculated by measuring the volume and weight of a cube of typical pumice. Individual clasts commonly range in diameter from 1 to 30 cm, with some clasts up to 60 cm in maximum diameter. Breakage upon impact must partly control the observed clast size. The pumice is light grey to white in colour with a platy texture, extremely vesicular and phenocryst-poor in hand specimen. At location 10 larger pumice clasts are sometimes coated with fine ash, signifying that clasts fell through a wet, fines-rich eruption cloud.

At locations 2 and 10, pumice clasts containing a dark mafic band occur (Figure 3.3f), and at location 4 small, scattered dark grey pumice clasts are found within the deposit together with the white rhyolite clasts. The mafic band and mafic pumice clasts are both phenocryst-poor. The grey pumices are small in maximum diameter (up to 6 cm) and denser than the accompanying rhyolite clasts. The mafic streaks form 2 to 3-cm-thick bands thorough white rhyolite pumice clasts.

There are very few lithic clasts in unit *C*. Where present they are typically small (maximum diameter ~1-3 cm) weathered fragments of basaltic and rhyolitic eruptives, most likely derived from older sub-glacially erupted material that forms the volcano core. Lithic clasts often display a red-brown staining, indicative of hydrothermal alteration. Occasionally, in the upper parts of unit *C*, 1-cm-thick lithic-rich horizons are found

consisting of 1-2-cm diameter rhyolite obsidian clasts (e.g., locations 10 & 13, Figure 3.2). In some proximal locations (e.g., locations 2, 4 & 10) a thin, localised, discontinuous medium-grained grey ash layer (layer C_1), with scarce small pumice fragments is found on top of the main pumice fall unit and below unit *D*.

3.2.6 Unit D (sub-units D_1, D_2)

Overlying unit *C* at most locations is a poorly preserved flow unit, ~ 70-110 cm thick in total that probably has a pyroclastic flow origin. We give primary deposit thickness values, and do not include re-worked material e.g., as present at locations 5, 7 and 9. In the proximal sections this deposit can be divided into two distinct sub-units (D_1 and D_2). D_1 is a poorly-sorted, sometimes stratified, matrix-rich, thin bed, with medium to coarse-sized pumice and lithic lapilli, supported in a vesicular ash matrix. Above D_1, unit D_2 is a very poorly sorted bed, consisting of a fine, vesicular ash matrix and small (2-3 cm diameter) dense pumice clasts (Figure 3.3a). Occasionally accretionary lapilli "ghosts" and fragile ash aggregates are present towards the top of the deposit. Crude normal grading can sometimes be recognised, along with a fine ashy top. In sections where the pyroclastic flow deposit is better-preserved (e.g., location 5), a fine-grained ash fall layer sits on top of unit D_2; it is usually mixed into the soil above. Thin horizons of fine grained dark basaltic ash are also found intercalated within the soil; these layers consist of fine fallout originating from later explosive activity in the Eastern Volcanic Zone (EVZ), including Öræfajökull 1727 and Laki 1783.

3.3 Deposit dispersal characteristics

Owing to the different dispersal and thinning characteristics of each fall unit in the 1362 sequence, separate isopach maps were constructed to assess the dispersal characteristics of each fall unit in the proximal-medial areas around the volcano (Figure 3.4). Isopach maps

are presented on the basis of control provided by the ten locations logged and occasional other observations.

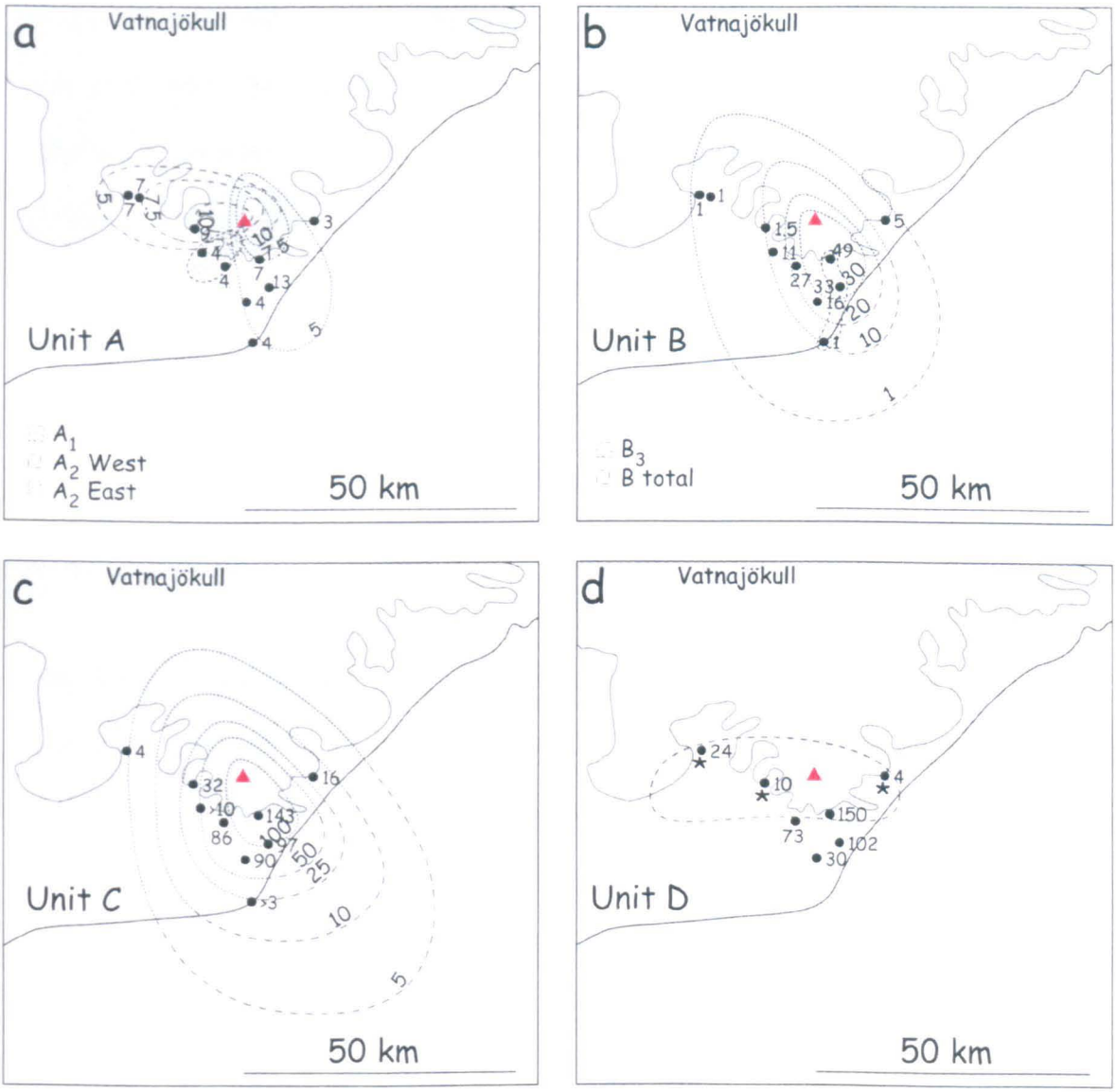

Figure 3.4 Thickness distribution maps for Öræfajökull 1362 proximal fall and flow units (isopach and individual location data in cm). Only locations where primary unit thickness was preserved are shown. Isopachs on unit *A* map are based on unit A_2 thicknesses; isopachs on unit *B* map are based on unit B_1+B_2 thickness. Stippled areas on maps a and b define distribution area of proximal fall sub-units A_1 and B_3 respectively. Map d shows locations where primary pyroclastic flow material was logged; total pyroclastic flow thickness (unit D_1 + D_2); dotted line on map d shows approximation of unit *D* distribution at base of volcano. Locations where possible pyroclastic flow bed is largely reworked are marked with an asterisk.

The Öræfajökull fall units form sheet-like deposits, dispersed by the wind into elliptical fans. Deposits of the opening phase of the eruption have a complex internal stratigraphy and different-appearing units occur at the different locations logged. These are here grouped as unit *A*. Sub-unit A_1 can be seen only in two locations, is small, and distributed to the south-west. The isopach map for fall unit A_2 (Figure 3.4a) suggests a bi-lobate dispersal, with one lobe extending directly to the west, and a second lobe dispersed SSE of the vent. These two separate lobes may reflect changing wind conditions; however, the exact relationship between these two lobes is uncertain and difficult to define based on the available data. Thus, for the whole of unit *A*, multiple lobes suggest at least three explosive events, each with a different dispersal axis (and, thus wind field). There may have been more sub-units dispersed in northerly directions, onto the ice cap; however, these cannot be mapped now.

Isopachs for the total fall unit *B* define a narrow south-easterly dispersal (Figure 3.4b), similar to the distribution of the main fall unit (*C*). The 1-cm isopach is the smallest mapped isopach, and is predicted (based on contouring of the isopachs and isopach extrapolation) to extend ~15-20 km off the south coast. Insufficient data exists to produce separate maps for sub-units B_1-B_3, but layer B_3 has a very narrow distribution, extending directly south from the vent for ~ 20 km (Figure 3.4b).

The main fall deposit – unit *C* – is widely dispersed with an axis to the SSE of the vent area (Figure 3.4c). Isopachs are regularly spaced and indicate thinning occurs at exponential rates. The 5-cm isopach is the smallest mapped and is predicted to extend to ~25 km offshore to the south but does not extend as far to the NW (i.e. the deposit thins upwind to the NW).

Larsen et al. (1999) also produced a distribution map for the 1362 fall deposit; the dispersal area on this map extends out to the south-east, consistent with the dispersal direction of the proximal units determined in this study.

Owing to the poor preservation of the pyroclastic flow deposits (unit *D*) it is impossible to accurately constrain the original extent and distribution of the deposits and calculate a volume. Figure 3.4d shows the proximal locations where primary flow sequences were measured. A contemporary description of offshore pumice rafts from Öræfajökull (as described from contemporary reports by Thorarinsson, 1958) suggests that pyroclastic flows must have travelled at least 30 to 35 km from the vent, and that they were sufficiently powerful to continue flowing out into the ocean. However, the location and configuration of the coastline in 1362 may have been different from that of today.

3.4 Clast size

Maximum clast sizes in unit *C* (maximum pumice, MP; maximum lithic, ML) were determined in the field by measuring and averaging the long axes of the five largest clasts found in the deposit. Care was taken to select clasts that were *in situ* and, in the case of the maximum pumice measurements, had not undergone any breakage. The dense nature of lithic clasts means that they are unlikely to break during transport, therefore their distribution is often a better indicator of eruption column dynamics. However, in the case of Öræfajökull, maximum lithic data were difficult to obtain as the fall deposit is lithic-poor and in the proximal sections lithic clasts are small and few in number. Although the pumice clasts are more fragile in nature, they at least present a complete size range in the proximal area. Pumice clasts 25-30 cm in length can be found ~ 10 km from the vent, along the dispersal axis; Clasts up to 3 cm long can be found 15-20 km away from the vent area, indicating energetic eruption conditions. This is confirmed by the maximum lithic

data: lithic clasts up to 1 cm in length can be found 20-25 km from source. Isopleth maps for average maximum pumice and maximum lithic data (values are based on measurements of the long axis of 5 clasts) are plotted in Figure 3.5. Both maximum lithic and pumice isopleths are ellipsoidal in shape and follow the same distribution as the isopachs for unit *C*.

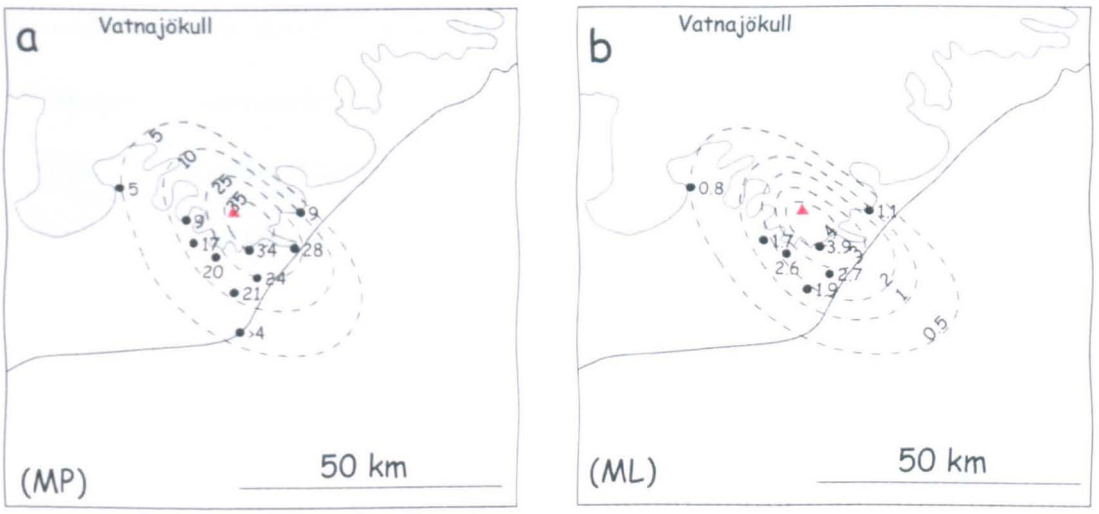

Figure 3.5 Isopleth maps for Öræfajökull 1362 unit *C*. (a) Isopleth map based on average maximum pumice (MP) data. (b) Average maximum lithic data (ML) isopleth map. Maximum clast sizes and isopleths are shown in cm. Both maximum clast size isopleths are dispersed to the SE.

3.5 Grain size characteristics

Owing to the fragile nature of the pumice clasts that make up the bulk of the 1362 deposit, granulometric analyses were completed on only a few samples from the main eruptive units. It was noted that many of the large pumice clasts in the deposit had breakage fractures. Samples were dry sieved by hand, to prevent further clast breakage, at half-phi (ϕ) intervals in the -4.5 (25 mm) to <4ϕ (<0.063 mm) size range. Grain size distributions of the selected samples from the different units are shown in Figure 3.6 (complete grain size dataset is listed in Appendix B2). Coarse tails of the grain size distributions are almost certainly under-represented in those units with abundant coarse clasts (*C* and *D*), due to breakage of the fragile clasts.

We have size-analyzed six samples to characterize the units. Grain size distributions are described by the statistical measures of Inman (1952): mean (M_z), standard deviation (sorting, σ_ϕ), median diameter (Md_ϕ) and skewness (Sk_G) (see Appendix B2 for equations). Histograms showing grain size distributions for the 1362 eruptive units reveal broad unimodal distributions except for unit A_2. Sub-unit A_2 sample has a sorting value (σ_ϕ) of 3.03, is polymodal and it is the most poorly sorted bed. The median diameter (Md_ϕ) of this poorly sorted unit is 0.75 and mean grain size is 0.75ϕ for unit A_2. The sub-unit B_3 sample is better sorted shows a σ_ϕ of 1.59 (with a negative skew); median diameter and average grain size values for this sub-unit are 2.65 and 2.35ϕ respectively.

Unit *C* pumice fall deposit samples (Figure 3.6c-d) show a relatively poorly sorted grain size distribution for this type of deposit, with a fine tail reflected as a positive skew. Sorting (σ_ϕ) ranges from 1.79 to 2.23; this can be attributed to two causes – the unit *C* samples are proximal and proximal Plinian deposits tend to show poor sorting; and

breakage of clasts. Md_ϕ for the fall deposit (unit *C*) ranges from -1.32 to -3.15; and mean grain size is -2.54ϕ, decreasing to -1.33ϕ further away from the vent.

The unit *D* sample (Figure 3.6e) has a sorting parameter of 1.73, a negative skew (i.e. coarse tail), and a bimodal grain size distribution reflecting the ash-rich nature for the unit is matrix. This sample shows a similar grain size distribution to the B_3 sample, (i.e. with a negative skew and bimodal distribution); median diameter is 2.19 and mean grain size is 1.82ϕ for unit *D*.

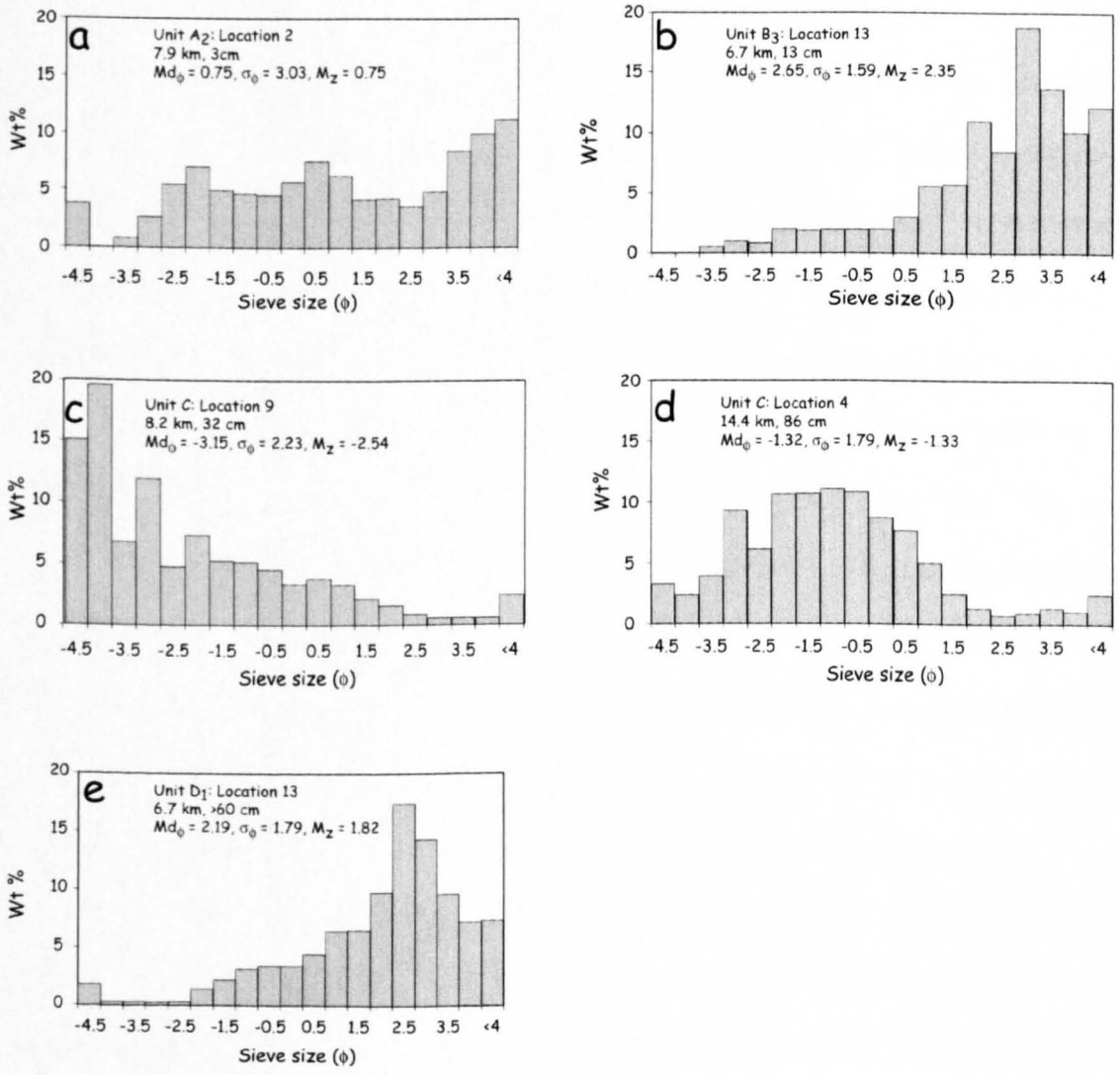

Figure 3.6 Histograms illustrating grain size distributions for selected samples from sub-units A_2 (a), B_3 (b), *C* (c, d) and D_1 (e), from five proximal locations. Distance from the vent, unit thickness, and the Inman parameters mean (M_z), sorting (σ_ϕ), and median diameter (Md_ϕ) are shown for each sample. Grain size is measured using the phi (ϕ) scale; each grain size class is denoted by the sieve mesh size that retains it.

3.6 Deposit Interpretation

Based on our descriptions of the proximal 1362 deposits, together with grain size data and information on the distribution of these eruptive units, we conclude that three main units were produced as a result of changing styles of explosive activity – the start of the eruption was characterised by phreatomagmatic activity; this was followed by a climactic Plinian phase, and, finally, column collapse and pyroclastic flow activity ensued.

The lower part of the 1362 sequence (i.e. sub-units A_1, A_2, B_1, B_2), formed as a result of the initial phreatomagmatic activity that characterised the start of the eruption. The presence of fragmented juvenile lithic clasts in sub-unit A_2 suggests a high degree of magma-water interaction at the vent, with dense obsidian shards indicating fragmentation by either steam or water (Kokelaar 1986). The low degree of sorting (i.e. $\sigma_\phi \geq 2$) may also indicate that this opening phreatomagmatic phase of the eruption involved abundant external water (Houghton et al., 2000) with fine wet ash deposited along with coarser clasts. Stratified beds within unit A_2, imply that this early activity was pulsating (e.g., Luhr 2000). The presence of both ash and pumice lapilli in sub-unit A_2 and hence its bi-modal grain size distribution, indicates that water may have been entrained into the eruption column near the vent, enhancing fragmentation to produce ash and resulting in the premature deposition of ash aggregates (which were held together by the surface tension of water in the eruption column) alongside coarser ash lapilli. Falling lapilli can also flush out finer, wet (cohesive) ash if it is in the column, and rain seeded from the eruption cloud can possibly do the same (Sparks et al. 1997; Houghton et al. 2004). The unit A deposits can be classed as locally dispersed, water-dominated, phreatomagmatic ash beds – not surprising as the vent must have opened up under ice.

The unit *B* deposit shows features that are more typical than unit *A* of phreatoplinian deposits, e.g., a fine grain-size near source, poor sorting and a widespread dispersal, most likely caused by magma fragmentation resulting from magma-water interaction and higher magma flux rates during the transition to a dryer Plinian phase of activity (Sparks et al. 1981). The origin of layer B_3 may be attributable to co-ignimbrite ash clouds associated with early, localized pyroclastic flows, emplaced prior to the main explosive activity that produced unit *C*. Alternatively, layer B_3 may simply represent localized accretionary lapilli-bearing phreatoplinian ash fall, although this is considered more unlikely. Despite the distinct nature of this unit, Thorarinsson (1958) makes no mention of an accretionary-lapilli-rich ash bed in his 1362 deposit stratigraphy, leading us to conclude that this unit is locally distributed within the proximal region only. Thus, unit *B* is the result of a higher intensity magma flux with water (from ice) still having free access to the vent.

Unit *C* (massive pumice fall deposit) is interpreted to have formed via a steady, sustained, high Plinian eruption column linked to a stable, established vent. This deposit represents the climactic phase of explosive activity. "Lithic-rich" intervals (although only up to 2-6 wt%) within this deposit may perhaps reflect episodes of increased vent erosion and possible vent-wall collapse (*cf.* Wilson et al. 1980; Adams et al. 2001). Grading patterns within the deposit, together with the absence of well-defined fall units suggests constant-rate activity that perhaps occasionally exhibited fluctuations in eruption vigour – e.g., the presence of upper layer C_1, which sometimes shows fine-grained discontinuous horizons, most likely indicates a reduction in the eruptive power during the Plinian event (*cf.* 1991 Hudson eruption, Chile, Scasso et al. 1994). The highly vesicular nature of the pumice lapilli in unit *C* suggests that they formed via magmatic fragmentation. Lack of ash in this proximal unit indicates that water no longer had free access to the vent, thus there was less water in the eruption column to promote fine particle aggregation. At this time there were

sufficient deposits around the vent and most of the ice had been removed, therefore making the vent more or less dry at this stage.

As stated earlier, the pyroclastic flow deposits (unit *D*) are especially poorly preserved. In proximal sections they often show evidence of fluvial reworking, including what is interpreted as secondary cross-bedding at the top. It is therefore impossible to accurately constrain the original extent of the deposits and thus calculate their precise volume. It is possible that the ash bed on top of the thin pyroclastic flow deposit seen at location 5 is fine co-ignimbrite fallout relating to pyroclastic flows "taking off" over the very steep glacially-eroded slopes of the volcano and generating fine ash clouds. However, as exposures of the uppermost 1362 layers are often truncated, reworked, and much reduced by wind erosion, it was not possible to identify flow-related fallout with certainty.

If preserved 1362 deposits and exposures were more numerous and closely-spaced it might have been possible to sub-divide the stratigraphy into thinner sub-units, as most of the identified units show quite a large degree of change in thickness and detailed character between the widely spaced exposures. This indicates that there may have been more variability in the units than can be presently resolved; certainly there was some syn-eruptive, intra-fall unit erosion occurring in this dynamic environment. Units *A-B* were most likely produced in a series of short-lived, early explosive episodes, with a hiatus between each one permitting erosion, building up to the climactic episodes and the deposition of units *C* and *D* (*cf.* the opening phases of the Pinatubo 1991 eruption; Hoblitt et al. 1996).

3.7 Distal ashfall

Thorarinsson's (1958) map of the 1362 deposit in distal areas of Eastern Iceland indicates that a widespread fine ash fall deposit exists. He first recognised this distal ash in many soil profiles and described it as a medium to coarse grained ash, containing silt size pumice clasts. The ash layer is usually 0.1 to 1.5-cm-thick (Figure 3.7a). In the few places where it is ~2-3 cm thick, clasts are described as larger and more porous (pumice-like). In some sections the ash is described as having primary stratification, resulting from changes in the intensity of volcanic paroxysms (Thorarinsson 1958). However, these layers were not described in sufficient detail to permit correlation with the proximal units described here. At present the precise relationship of the mapped distal ash fall layer to those units preserved in the proximal stratigraphy is uncertain. Thorarinsson (1958) did not divide the 1362 deposit into individual fall units; however, he does comment on various layers in some proximal exposures. His map is of total deposit thickness and measurements may include some reworked material at the top of the primary 1362 deposit. This may account for the small differences in thickness between his map and where we have logged the deposit in the same near-source areas. We observed and sampled the distal ash fall (which shows no discernable layering) to the west of the volcano (location 12, ~ 70 km from the volcano where it is a few millimetres thick) and our distal ash fall thickness map presented here is supplemented by additional deposit thickness data from this area (Th. Thordarson, pers. comm. 2005). We also received a deposit sample from 65 km N of the volcano (G. Larsen, pers. comm. 2001) for comparison with the proximal samples.

The isopach map produced by Thorarinsson (1958), however, shows a different isopach distribution pattern to the general trend of the proximal fall units (Figure 3.7a). Isopachs are regularly spaced, ellipsoidal in shape and extend offshore out to the east, defining an east-south-east dispersal axis; the smallest mapped isopach is 0.1 cm. On this map, the 0.1

cm isopach lies ~100 km to the west and ~180 km north of the volcano. The deposit, at trace thicknesses, probably does continue to exist west and north of the areas where it is shown by Thorarinsson (Figure 3.7a) to be absent (G. Larsen pers. comm. 2006). As described earlier, the isopach maps based on the proximal locations described in this study (Figure 3.4) show a differing dispersal. On these maps, isopachs extend offshore with a dominant south east dispersal axis. Individual fall units (e.g., units *B* and *C*) can be tracked across a south-easterly dispersal axis in both thickness and grain size going from thinner and finer on the SW side of Öræfajökull to thicker and coarser south of the summit crater and thinner and finer on the SE side (Figure 3.4). By comparison, the proximal isopach shape on Thorarinsson's map seems to be largely controlled by his interpretation of the distal ashfall dispersal across Eastern Iceland.

Due to the differing isopach maps (Figures 3.4a-c and 3.7a), to assess the total deposit distribution and estimate the fall deposit volume we constructed a total fall deposit isopach map (Figure 3.7b-c), on which we plot our proximal data and selected distal thickness data from Thorarinsson's map, together with new thickness data from exposures west of the volcano. Thorarinson's deposit thicknesses were mainly used to supplement our lack of data in the distal areas east of the volcano. For the purpose of this study the Thorarinsson (1958) thickness data are taken to represent primary fallout thicknesses, i.e. not reworked or thinned by secondary processes. Figure 3.7b shows the land-based distribution only and Figure 3.7c shows the extrapolated isopachs.

On this total deposit map (Figure 3.7b-c), isopachs extend out to the north east, defining a NNE dispersal axis. The deposit thins towards the south west. The 0.1-cm isopach is the thinnest isopach that can be reasonably completed and can be extrapolated to fall ~ 100 km offshore from the easternmost point of Iceland and 125 km offshore from the south coast; its extrapolated area covers ~ 195,000 km^2, defining an ellipse that extends across eastern

Iceland and out to the Atlantic Ocean in a roughly NE direction (Figure 3.7c). The isopachs are drawn to show a slight bulge towards the south; this reflects the distribution of the proximal fall units (*A*, *B*, and *C*), which are all largely dispersed to the SE of the vent. The isopach shape and distribution for this total deposit isopach map appears to be largely controlled by the widespread fine-grained distal ash fallout across Eastern Iceland (mapped by Thorarinsson).

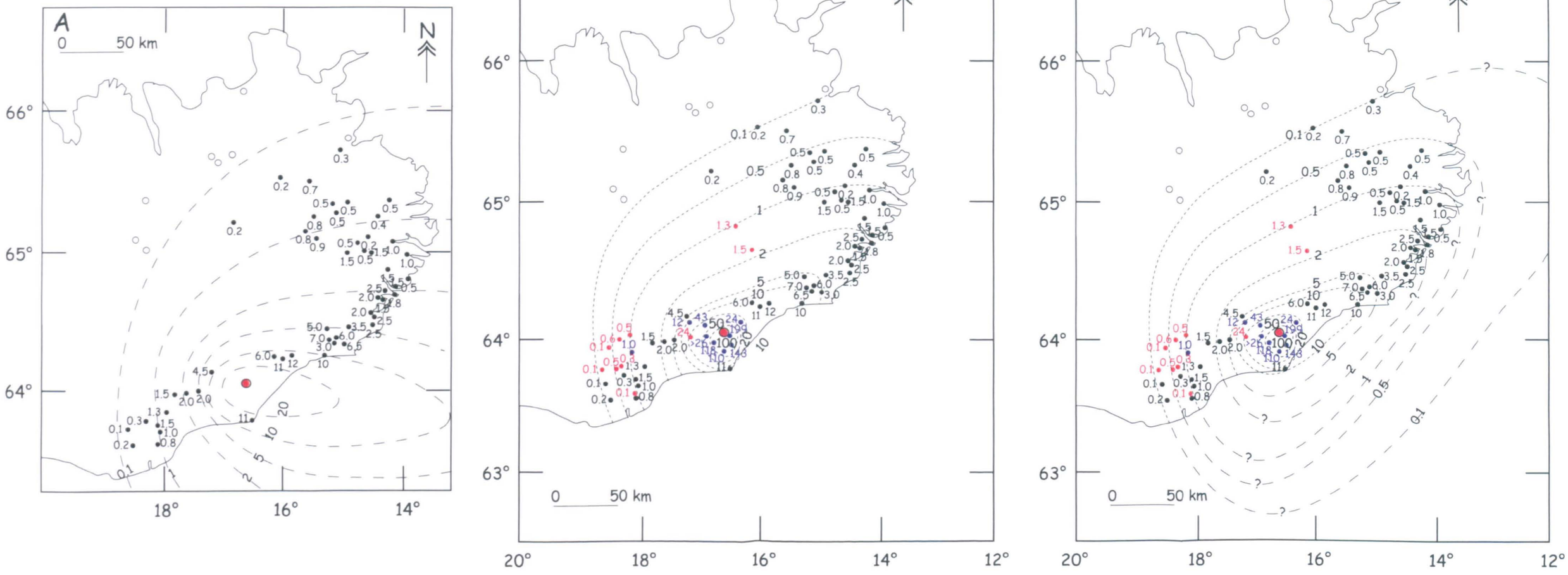

Figure 3.7 Isopach maps for the whole Öræfajökull 1362 (Ö1362) fall deposits. Map A is Thorarinsons 1958 original isopach map. Black circles mark locations where primary deposit thickness was measured, open circles mark locations where the 1362 deposit was not found. Map B is a total fall deposit map showing land-based deposit distribution only as interpreted by this study. Map is based on our proximal data (blue circles), selected data points from Thorarinsons map (black circles) and new data from the west of the volcano (data provided by G. Larsen, Th. Thordarson) (red circles). Proximal thicknesses (data from this study) are cumulative fall unit thicknesses (i.e. Unit *A* + Unit *B* + Unit *C*). This map also reflects the more southerly dispersal of fall units *B* and *C*. Map C is an extrapolated version of Map B, isopachs were extrapolated to calculate isopach areas and deposit volume. On all maps isopach thickness is shown in cm.

3.8 Interpretation of deposit dispersal

There is an apparent misfit between the dispersal for the whole deposit and the dispersal of the individual proximal fall units (*A–C*); in this section we attempt to explain the possible reasons for this.

The shape of the total deposit isopach map (Figure 3.7c), i.e., the whole fallout dispersal across eastern Iceland, strongly suggests deposition from an umbrella cloud during the main *C* (and possibly *D*) phase, including the 75-100 km up-wind dispersal to the WSW. Based on the isopach maps for units *A* and *B* (Figure 3.4) which show that these units have a limited widespread distribution, it seems likely that these eruptive episodes contributed very little to the distal ash fall to the east of Öræfajökull This scenario is similar to that of the 1991 Pinatubo eruption; during the Pinatubo eruption most of the fine ash rose in one convective eruption column and was dispersed as a single umbrella cloud, with fine ash fallout occurring up to 200 km up-wind (Koyaguchi 1996) (Figure 3.8).

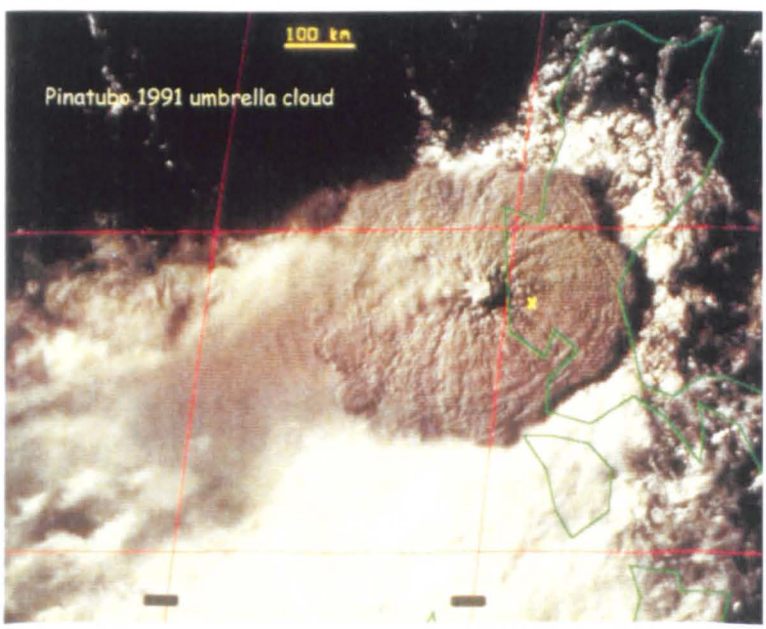

Figure 3.8 Satellite image of the 1991 Pinatubo umbrella cloud (Japanese Meteorological Satellite, visible wavelength data). Yellow cross marks vent location. Note scale (1 cm ≈ 100 km).

The 1815 eruption of Tambora also involved a major Plinian phase that produced several fall units, with a subordinate amount of pyroclastic flow deposits (Self et al. 2004). However, approximately 90% of the erupted volume at Tambora appears to have been distal fallout. Thus, in the Tambora eruption we have a precedent for this type of situation where the proximal equivalent of the distal ash is not a specific bed. At Tambora the distal fallout is believed to be the distal equivalent of the proximal Plinian unit F4 and fall units intercalated within the pyroclastic flow deposits plus some co-ignimbrite ash (Self et al. 2004). It is possible that a similar situation occurred during the 1362 Öræfajökull eruption, with a large proportion of the dominantly fine-grained fallout being deposited in distal regions.

The isopach shapes and resulting easterly dispersal on Thorarinsson's (1958) isopach map may have resulted from the following: Realizing that he only had part of the deposit on land, he may have assumed a uniform dispersal and based his isopach shape on a mirror image exercise – i.e. based on folding the on-land thickness data over to the S on an E-W axis. Thus he would have had the same thickness at the same distance from the volcano directly to the south of the on-land point. This would most likely produce deposit isopachs with an almost easterly dispersal axis.

When isopachs on the total deposit map (Figure 3.7b) are drawn from on-land data alone, without consideration of the expected shape of the dispersal pattern, the deposit as a whole appears to have a NE dispersal axis (Figure 3.7b). At Öræfajökull this is consistent with the prevailing direction of strong stratospheric winds during the early summer months in Iceland. At elevations of 30-35 km, early summer stratospheric winds will blow from an approximate west to south-west direction (Lacasse 2001), therefore dispersing fine ash from high Plinian eruption columns in a general E-NE direction. This is also consistent

with the dispersal direction of fine ash from other large Plinian eruptions in this area (e.g., Askja 1875, R. Carey pers. comm. (2006)). In this case, we consider that the proximal deposits distributed to the SSE probably represent fallout from a lower part of the eruption column and dispersal by strong, lower level winds, and thus, the distal ash represents fallout from the upper part of the eruption plume and dispersal by prevailing stratospheric winds.

Based on these considerations, we propose three possibilities to explain the dispersal of the distal fallout material:

1. Dispersal of fine ash from an umbrella cloud

The three straight line segments on the Öræfajökull 1362 thickness versus $A^{1/2}$ plot (Figure 3.9b) are similar to those seen on similar plots for other Plinian deposits, e.g., Quizapu, 1932 (Hildreth and Drake, 1992) and Huaynaputina 1600 AD (Adams et al., 2001). Fierstein and Nathenson (1992) and Hildreth and Drake (1992) recognised that these inflection points between the straight line segments represent changing regimes in the depositing eruption column. As a result of modelling work relating particle Reynolds number to column sedimentation models, Bonadonna et al. (1998) concluded that the proximal segment is related to fallout and dispersal of high Reynolds number particles, derived from the eruption column margins and possibly the lower parts of an umbrella cloud and transported mainly via a low-altitude wind field. However, the more distal segments are related to dispersal and fallout of low Reynolds number particles, by upper-level winds from the uppermost parts of an umbrella cloud. At Öræfajökull, the first inflection point at $A^{1/2}$ ~25-28 km possibly represents the maximum spread of the convecting column and the decrease in ballistic contributions, thus signalling a change to umbrella cloud deposition, as seen during the 1932 eruption of Volcan Quizapu (Hildreth and Drake, 1992). Note that thickness data for unit *C*, when plotted on the $A^{1/2}$-thickness

diagram for the total deposit (Figure 3.9b), has a similar slope and segment length to segment 1 for the total deposit, consistent with the fact that segment 1 for the total deposit represents coarse, clast dominated fallout in the proximal region. The second inflection point, at $A^{1/2}$ ~75 km, reflects the transition from coarse grained fallout, dominated by pumice clasts, to fine grained, slower-settling fallout, rich in glass shards. Thus, the second, distal inflection point at Öræfajökull on Figure 3.9b is representative of changes in the particle settling behaviour of the co-Plinian ash, similar to that described at Huaynaputina 1600 AD (Adams et al. 2001) and Novarupta 1912 (Fierstein and Hildreth, 1992). In these case, fine grained Plinian ash, decoupled from the more coarse grained fallout, is held aloft by turbulence in the upper atmosphere for a longer period of time before fallout from the umbrella cloud. Based on the up-wind dispersal (~75-100 km) much of phase *C* was also accompanied by an umbrella cloud. Units *A* and *B* probably contributed very little to the distal ash fall to the ENE.

2. Wind-shift during the main Plinian phase

The proximal, coarse pumice fall unit *C*, possibly represents a few hours of deposition, and forms the mapped dispersal pattern, which has an axis to the SSE. This dispersal pattern is also supported by the maximum clast size (maximum pumice and lithic) data. However, perhaps as phase *C* continued a wind shift occurred that resulted in the dispersal of fall deposits on a more north-easterly dispersal axis. It is possible that the early unit *C* distal fallout was out at sea and therefore not recorded, whereas the later unit *C* ash fell out over the eastern part of the island and formed the distal deposit mapped by Thorarinsson. If this did occur, much of the proximal fallout of this later unit *C* probably fell onto the ice-cap.

3. Co-ignimbrite ash

Studies have also shown that the distal segment inflection on the thickness versus $A^{1/2}$ plot (Figure 3.9b) can be attributed to the input of large amounts of co-ignimbrite ash to distal fallout (e.g., Hildreth and Drake 1992). Thus, this could possibly be a third explanation for the large amounts of distal ash observed at Öræfajökull. The pyroclastic flow volume appears too small now to have generated significant amounts of co-ignimbrite fallout in the distal region, but there may have been much more deposition of pyroclastic flows, which have been eroded away or buried. This scenario also probably requires the pyroclastic flow activity to have continued after the climactic fallout phase of the eruption. Based on crystal concentration studies approximately 2-3 km^3 of pyroclastic flow deposit is required to generate ~1 km^3 (bulk volume) of associated co-ignimbrite ash (Walker 1972). The bulk deposit volume calculated from the extrapolation of the isopach areas on Thorarinssons map (using the Pyle method) (Figure 3.7a) is ~ 5 km^3. If we assume that the majority of this volume makes up the widely distributed distal ash deposit, then ~ 8-12 km^3 of pyroclastic flow deposit is required to generate ~4 km^3 of co-ignimbrite ash. Based on this study, our data suggests that it is highly unlikely that such large volumes of pyroclastic flow deposit existed, and this is therefore the least likely option for the origin of the distal ash cloud.

Although all of the above scenarios could reasonably be invoked to explain the dispersal of the 1362 fallout, with the data in hand I consider that option 1 best explains the distribution and dispersal of the 1362 deposits. The 1362 eruption column probably involved a powerful umbrella cloud system; fallout from the lower part of the column produced the proximal deposits dispersed to the SSE by strong non-stratospheric winds, whereas the distal deposit was derived from fallout from the upper reaches of the umbrella cloud and dispersed via stratospheric winds to the ENE-NE.

3.9 Volume Estimates and Dispersal Characteristics

3.9.1 Volume

The volume of explosive eruption deposits that occur in ocean island settings, such as Öræfajökull 1362, is particularly difficult to estimate because a large proportion of pyroclastic material is dispersed offshore (Walker 1981). This fact, coupled with the poor preservation and lack of complete exposures of the 1362 deposit in the harsh proximal environment, means that any calculated volume will have a large associated uncertainty. Also, due to the small number of localities in which the deposit is well-preserved, isopach maps are necessarily based on few data points. However obtaining a realistic estimate of the volume of the 1362 deposits is critical to assessing the eruption volatile release and any related atmospheric impact. We use the total extrapolated deposit isopach map (Figure 3.7c) to estimate a bulk fall deposit volume.

As the 1362 pyroclastic flow deposits are poorly preserved, an estimate of the original volume is difficult to obtain. Based upon the proximal sections where primary flow sequences were measured, we crudely estimate that the 1362 pyroclastic flows have an areal distribution of ~80 km^2 (Figure 3.4d). Using a minimum thickness of 1 m, a minimum volume of approximately < 0.1 km^3 is indicated.

Using the approach of Pyle (1989, 1995), the square root of the area ($A^{1/2}$) enclosed by each isopach is plotted against thickness on a log scale (Figure 3.9). On such a plot, thickness data of pyroclastic fall units tend to follow a general exponential decrease, producing one or more straight line segments. Many Plinian fall deposits also show a third segment which represents the distal portion of the fall deposit (Pyle, 1995) and which may fall under a different fluid dynamical regime (Bonadonna et al. 1998). The area beneath each segment can be integrated to yield a minimum bulk deposit volume (including the volume

outside the smallest mapped isopach). On the $A^{1/2}$ versus thickness diagram for the proximal fall units (*A-C*), data for fall units *A* (both lobes plotted separately) and *B* are represented by single line segments, and unit *C* is defined by two segments (Figure 3.9a). Integrating the area under these line segments gives fall unit deposit volumes of 0.11 km^3, 0.12 km^3, and 0.58 km^3 for units *A*, *B*, and *C* respectively.

Figure 3.9b shows the $A^{1/2}$ versus thickness plot for the whole Öræfajökull 1362 tephra fall deposit, including the distal ash fall (based on Figure 3.7c). Three discrete line segments can be recognised. Following the method of Fierstein and Nathanson (1992), the area under each of these three line segments was integrated to obtain the deposit volume, (including the volume beyond the smallest mapped isopach (0.1 cm) to infinity (Pyle, 1989)). Using this approach we completed several versions of the volume calculation, each time changing the points used to create the three segments. We also ran the model by fitting only one or two line segments to the data. Each variation produced similar values for the total volume (Table 3.2). Averaging these results yields a bulk fall deposit volume of 2.2 ± 0.05 km^3 which, when we include the small pyroclastic flow volume, yields a total volume of 2.3 km^3. This is equivalent to about 1.2 km^3 (~ 3.0×10^{12} kg) dense-rock equivalent (DRE) based on a magma density of 2470 kg/m^3 and a bulk deposit density of 1250 kg/m^3 (Carey and Sigurdsson 1989), significantly smaller than the 6 km^3 calculated by Thorarinsson[2] based on his isopach map (Figure 3.7a). The thickness-$A^{1/2}$ plot was also used to obtain a theoretical maximum thickness (T_0) of ~350 cm for the total deposit; this approximately agrees with the total deposit thicknesses (unit *A* + unit *B* + unit *C*) measured in the field at the most proximal locality (290 cm at location 13, Figure 3.2).

[2] Note the 10 km^3 deposit volume quoted in Thorarinsson (1958) is the freshly fallen, uncompacted ash volume. The actual bulk deposit volume is ~ 6 km^3.

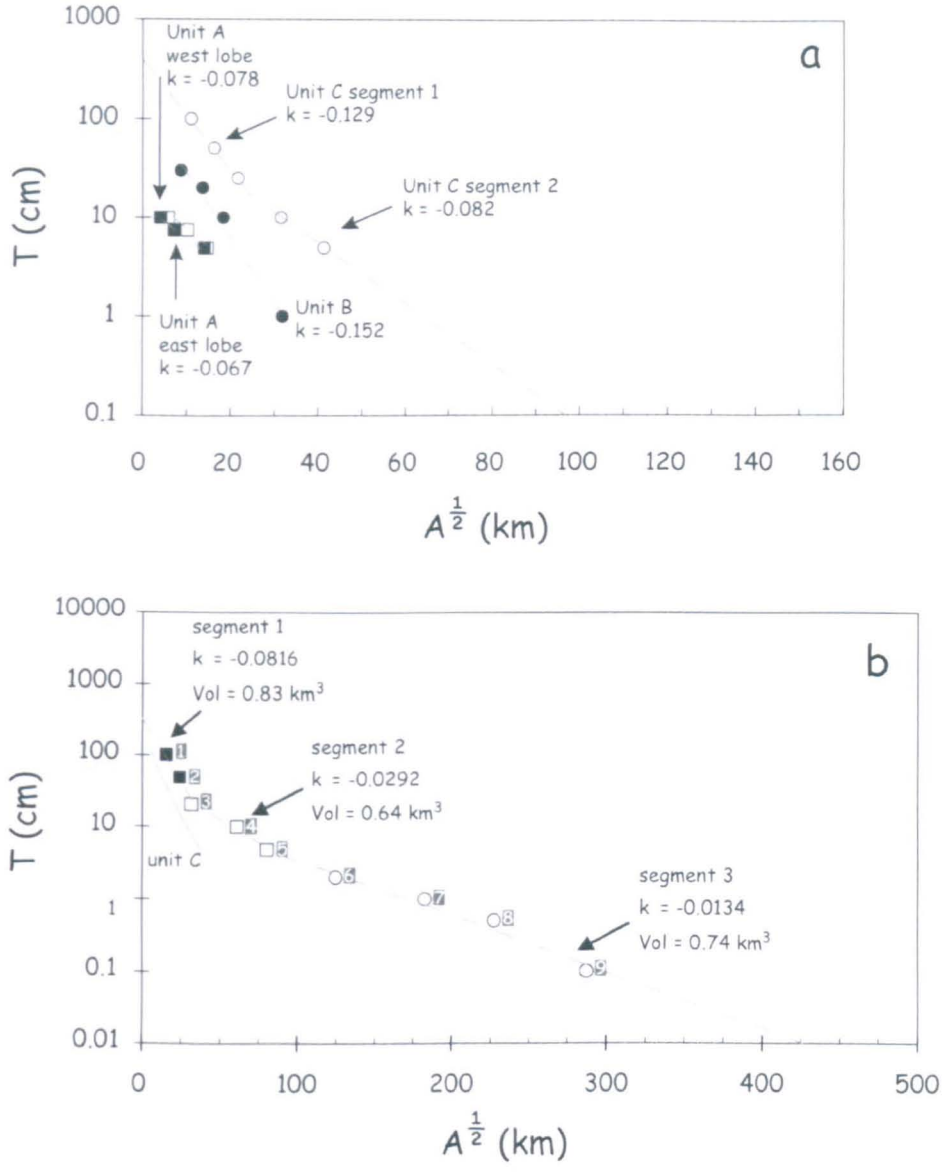

Figure 3.9 Log thickness versus $A^{\frac{1}{2}}$ plots for Ö1362 fall units. (a) Shows data for individual fall units, *A* to *C*, based upon proximal thickness data (shown on isopach maps, Figure 3.5a-c). Fall units *A* and *B* are represented by a single line segment; unit *C* by two line segments with different slopes (see text for discussion). West (black squares) and east (white squares) lobes for fall unit *A* are plotted separately. Volumes are calculated by integration of area under each of these line segments; data is extrapolated to infinity from the smallest mapped isopach. (b) Represents total fall deposit thickness (based upon extrapolated isopach map in Figure 3.7c). Ö1362 total fall deposit data can be divided into three distinct line segments. Number labels on each point correspond to numbers used in defining the three segments in Table 3.2; *k* is slope of line segments. Calculating the area under the three segments gives a bulk fall deposit volume of ~ 2.2 km^3. The two inflection points (at 25 km and 75 km) may represent changes in nature of the depositing column (refer to text for more information). For comparison the unit *C* proximal segment is also plotted on (b) as a solid line.

Table 3.1 Summary of Öræfajökull 1362 associated volume data for fall units *A-C*. Note all volumes calculated to ∝. Dense rock equivalent (DRE) volume is shown in brackets. Volume of Unit *D*, the pyroclastic flow deposit is crudely estimated to be ~ 0.1 km^3, refer to text for further information.

Unit	Bulk volume (km^3) [DRE]	T_0 (cm)	k	b_t (km) (proximal)	b_t (km) (medial)	b_t (km) (distal)	b_c (km) (MP)	b_c (km) (ML)
A (left lobe)	0.053 [0.03]	16.03	0.078	5.03	-	-	-	
A (right lobe)	0.056 [0.03]	12.66	0.067	5.81	-	-	-	
B	0.12 [0.06]	137.55	0.152	2.58	-	-	-	
C	0.58 [0.29]	252.60	0.098	3.97	-	-	3.86	4.74
C – segment 1		411.82	0.129					
C – segment 2		144.29	0.082	-				

Table 3.2 Summary of thickness versus $A^{1/2}$ dataset for Öræfajökull 1362 total fall deposit.

Data for combined total deposit isopach map (Figure 3.7c)					
Single Segment					
Points	Segment Number	Volume (km^3)	Volume inside last mapped isopach (km^3)	Volume outside last mapped isopach (km^3)	Last mapped isopach (cm)
1-9	-	2.22	2.06	0.15	0.1
1-8	-	2.24	2.08	0.16	0.5
Two Segments					
Points	Segment Number	Volume (km^3)	Volume inside last mapped isopach (km^3)	Volume outside last mapped isopach (km^3)	Last mapped isopach (cm)
1-2 3-8	1 2	2.23	2.04	0.20	0.5
1-3 4-8	1 2	2.15	1.94	0.21	0.5
1-3 3-8	1 2	2.24	2.04	0.20	0.5
Three segments					
Points	Segment number	Volume (km^3)	Volume inside last mapped isopach (km^3)	Volume outside last mapped isopach (km^3)	Last mapped isopach (cm)
1-3 4-5 6.8	1 2 3	2.10	1.81	0.30	0.5
1-3 3-6 3-8	1 2 3	2.28	2.02	0.26	0.5
1-3 3-4 5-8	1 2 3	2.22	1.90	0.33	0.5
1-2 3-5 6-9	1 2 3	2.20	1.83	0.38	0.5

3.9.2 Dispersal characteristics

Isopach and isopleth areas for the Öræfajökull 1362 eruption were also compared with data from other Plinian eruptions using the method outlined in Hildreth and Drake (1992). The dispersive power of different historical explosive eruptions can be interpreted from each panel shown in Figure 3.10. Plotting the data in this way illustrates the vigour of the Öræfajökull 1362 eruption in relation to other Plinian events, as dispersive power and intensity are closely related. The intensity of an eruption is a key factor in determining the behaviour of an eruption column – in particular the height to which material is injected into the atmosphere and the sequential development of eruptive phases (Carey and Sigurdsson 1989). Furthermore, the prominent inflections seen in the thickness versus $A^{1/2}$ plot are also present when thickness is plotted against isopach area (A), suggesting a need to distinguish between the dispersal characteristics of proximal pumice falls and those of downwind, distal ash (Hildreth and Drake 1992).

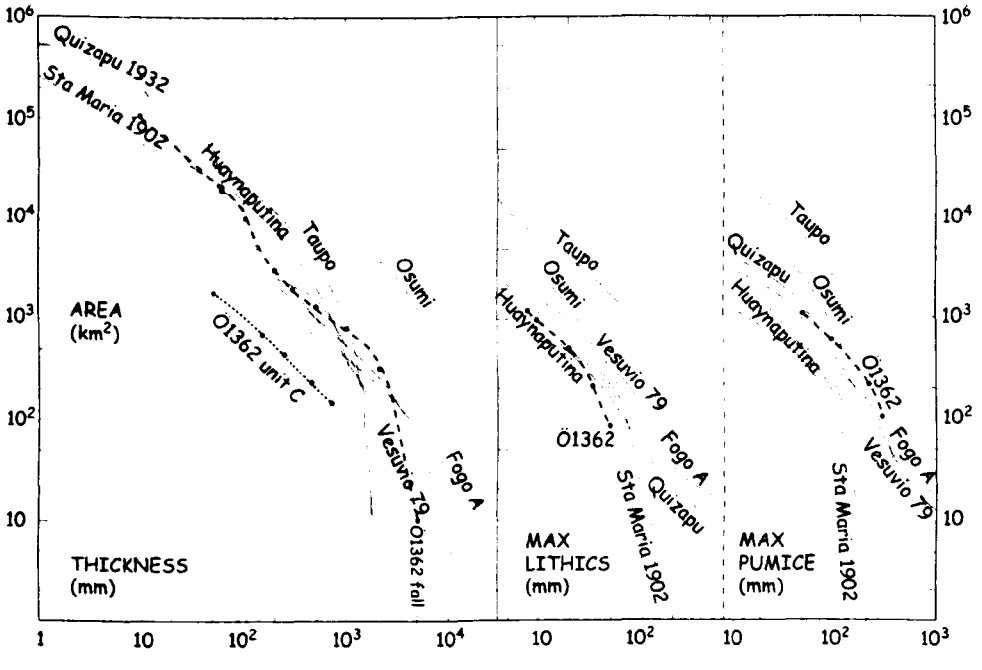

Figure 3.10 Dispersive power comparisons for several major Plinian eruptions after Hildreth & Drake (1992); Adams et al. (2001). Each panel provides different criterion to evaluate the dispersive power of explosive volcanic eruptions. Thickness (mm), maximum lithic clast size (mm) and maximum pumice clast size (mm) are plotted against isopach/isopleth area (km^2). Dashed line represents Öræfajökull 1362 total deposit thickness (based on Figure 3.7c-total deposit isopach map), thickness-area curve of unit *C* is also shown in thickness panel (dotted line). Maximum lithic and maximum pumice data is based on unit *C* isopleths areas (Figure 3.8).

3.10 Eruption Parameters

To help quantify and compare Plinian fall deposits, Pyle (1989; 1995) proposed several parameters to describe thinning rates for fall deposits and changes in clast size with distance from the vent. The thickness half distance parameter, b_t, defines the $A^{1/2}$ distance over which the deposit thickness halves and tephra deposit plots often have more than one segment with different b_t values. Typically, b_t ranges between 1 and 10 km for the proximal portion, and can range from 20 to ≥100 km over the distal portion (Houghton et al. 2000). Using isopach area and thickness data, b_t for the Öræfajökull 1362 Plinian pumice fall unit (*C*) was estimated to be 3.0 km in the proximal region and 4.8 km in the medial portion. The maximum clast half distance, b_c, defines the average distance across which the maximum clast-size halves. Using maximum lithic (ML) and maximum pumice (MP) data, b_c for MP is ~3.9 km and for ML ~4.7 km (Figure 3.11).

Pyle (1989) also used the slope of the best fit line on an area$^{1/2}$-maximum clast size plot (Figure 3.11) to determine H_B (neutral buoyancy height of an eruption column). The neutral buoyancy height (H_B) can be related to the total column height (H_T) by the approximation $H_B/H_T \cong 0.7$. Using these relationships, H_B for the Öræfajökull 1362 climactic Plinian phase (i.e. unit *C*) is 21 km (MP) and 24 km (ML); therefore H_T is 30 km (MP) to 34 km (ML). Thus the data supports a high eruption column for the main phase *C* activity.

The total eruption column height (H_T) can be used in conjunction with the temperature of the erupting mixture to estimate dense-rock mass discharge rate (MDR) and volumetric discharge rate (VDR), following the method outlined in Figure 6 of Sparks (1986). For Öræfajökull the magmatic temperature (obtained from Fe-Ti oxide geothermometry) is 828 °C, which I use as a reasonable proxy for the temperature of the erupting mixture.

Combining this temperature with a column height (H_T) estimate of ~ 30 km, and assuming temperate atmospheric conditions, yields a MDR of 1.2×10^8 kg/s and a VDR of 6×10^4 m^3/s. Mass discharge rates provide a measure of eruptive intensity (Carey and Sigurdsson 1989); the Öræfajökull 1362 fall units were emplaced in conditions similar in intensity to major Plinian events such as the eruptions of Santa Maria (1902), Fogo A, and El Chichón (1982) unit A.

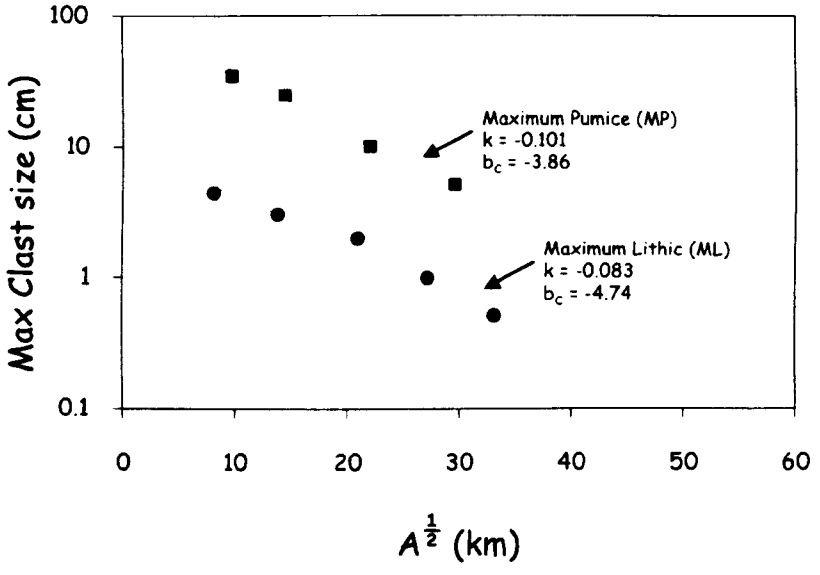

Figure 3.11 Log maximum clast size versus $A^{\frac{1}{2}}$ plot for maximum pumice (MP) and maximum lithic (ML) data from unit *C*, shown in Figure 3.5. The slope of the best fit line, *k* can be used to estimate b_c (clast half-distance), which can then be used to calculate H_B (neutral buoyancy height), see text for further discussion.

Pyle (2000, (after Walker (1981)) also proposes the use of an eruption magnitude and eruption intensity scale to help characterize the size and power of a volcanic eruption. The eruption magnitude (*M*) is defined as $\log_{10}$ [erupted mass (kg)] – 7; and the eruption intensity (*I*) is defined as $\log_{10}$ [mass eruption rate (kg/s)] + 3. Based on the total mass of fall and pyroclastic flow units (~ 3.0×10^{12} kg), the magnitude index for Öræfajökull 1362 is *M*5.3. The eruption intensity index is *I*11.1, calculated using a mass discharge rate of 1.2×10^8 kg/s. Using these parameters the 1362 eruption of Öræfajökull was almost identical in magnitude and intensity to the 1956 Bezimianny eruption, and similar in

intensity to the Pinatubo (1991) and Novarupta (1912) events. The magnitude (*M*5.3) is considerably smaller than Pinatubo (*M*6.1) or Novarupta (*M*6.3).

As the timing and total duration of the 1362 eruption is unclear from historical accounts, we attempt to constrain the duration of the main phase using known accumulation rates of Plinian fall deposits. Wilson and Hildreth (1997) present a compilation of known accumulation rates based upon eruption column height for several Plinian fall deposits. Using our estimate of 30 km for H_T, the Wilson and Hildreth data suggest an accumulation rate of 0.023 to 0.030 mm/s at location 10 (~ 16 km along the dispersal axis; Unit *C* thickness ~ 97 cm) and location 13 (~ 9 km along the dispersal axis; Unit *C* thickness ~ 143 cm), respectively. Based on these rates and the unit *C* thicknesses at these locations, the duration for the main Plinian phase is estimated to be 1.1-1.6 hours. This figure compares well with the eruption duration determined semi-independently using volumetric discharge rates (6×10^4 m^3/s) and unit *C* eruption volume (0.6 km^3), which is on the order of 2.7 hours. As the measured thicknesses are minimum values, the calculated duration must also be considered a minimum. Nevertheless, our approximation broadly agrees with that of Thorarinsson (1958), who also suggested that the main phase of the eruption was relatively short in duration (probably not much more than about a day), based upon "the regular distribution of the land-based tephra".

To describe the dispersal and fragmentation of Plinian fall deposits Hildreth and Drake (1992) suggest using the ratio of the areas enclosed by the 20-cm and 100-cm isopachs as a dispersal index. Using this method the dispersal index at Öræfajökull is ~4.4, similar to the value for the Quizapu 1932 deposit described by Hildreth and Drake (1992), and higher than the values for Mount St Helens 1980 (3.3) (Carey and Sigurdsson 1985) and El Chichón 1982 unit A1 (2.5) (Carey and Sigurdsson 1986). By comparison, Hildreth and Drake (1992) report dispersal indices of ~7.5 for Vesuvius AD 79 and ~11.5 for the very

high intensity Taupo Plinian eruption. The high dispersive power for the 1362 event is also reflected in the clast half-distance parameters (b_c) and half-distance ratio (b_c/b_t). The 1362 Plinian phase has a large b_c value (~3.9 to 4.7 km) but a relatively small b_c/b_t ratio (1.27 km). These eruption parameters rank the 1362 Öræfajökull eruption alongside other intense Plinian events such as Quizapu (1932), Fogo A and El Chichón A (1982) (Carey and Sigurdsson, 1989). The relatively high dispersive power shown by the 1362 Plinian event partly reflects the high eruption plume (~30 km), that, due to the location of the volcano and the position of the tropopause (~10 km) during the summer months, was able to easily reach stratospheric levels where strong stratospheric winds are more likely to carry aloft fine ash and lapilli particles for greater distances. We noted earlier that during early June, stratospheric winds above Iceland blow from an approximate SSW direction (Lacasse 2001), thus dispersing fine tephra fall in a general NNE to NE direction, consistent with our interpretation of the 1362 fallout.

Pyle (1989) suggests using the ratio b_c/b_t as a magma fragmentation index, as this parameter normalises data by removing the effects of the absolute magnitude of the eruption and considers only dispersal features. The b_c/b_t ratio also does not require total deposit grain size data if the maximum clast size is used and both b_c and b_t can be calculated from a minimum of two isopachs and isopleths (Pyle 1989). The b_c/b_t ratio is principally controlled by the grain size characteristics of the erupting mixture at the vent. Thus there is a wide variation in b_c/b_t values, with lower ratios expected in deposits that are dominated by finer-grained clasts. Most deposits, however, exhibit b_c/b_t ratios between 0.5 and 1.5 (Houghton et al. 2000); therefore the dispersal, (D) must vary for eruptions with similar column heights (Pyle 1989). A small b_c/b_t ratio thus implies greater dispersal, as the deposit thins more slowly.

Figure 3.12 shows Pyle's revised classification scheme for fall deposits. As in the original classification of Walker (1973), fragmentation increases towards the top of the diagram and dispersal increases from left to right. In this diagram, contours of the clast half-distance, b_c, which reflect model eruption column heights, are used to subdivide deposits according to the height of the depositing column. On Figure 3.12, the 1362 Plinian phase that produced unit *C* has a half-distance ratio of 1.27, indicating efficient fragmentation of magma, possibly resulting in a large volume of fine ash being produced during the Plinian phase – which possibly contributed to the considerable amount of distal fallout. Thus, only a small amount of the magma erupted during phase *C* forms the coarse proximal pumice fall layer. The rest of the magma was well fragmented and went into the high umbrella cloud region of the eruption plume.

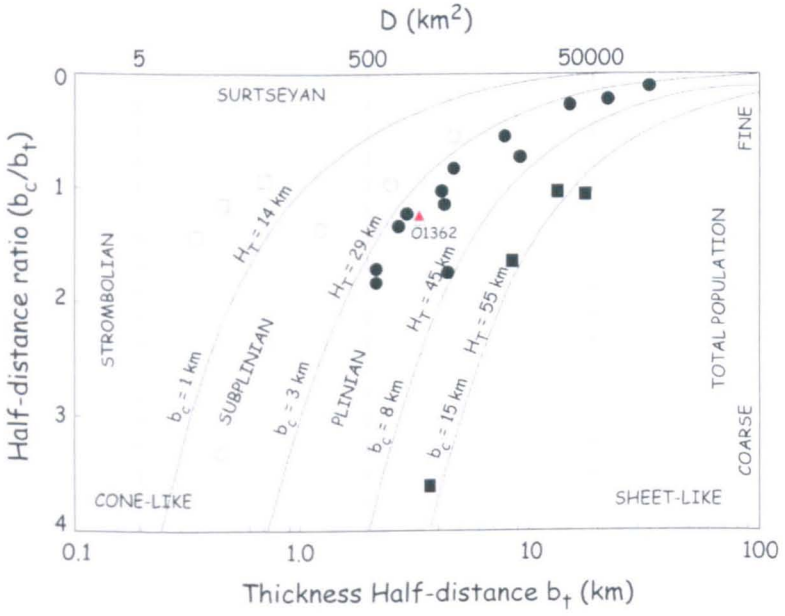

Figure 3.12 Classification scheme for tephra fall deposits (after Pyle 1989). The half distance ratio (b_c/b_t) represents the total grain size population and the thickness half-distance (b_t) represents the dispersal. The diagram is contoured for clast half-distance (b_c) and total column height, H_T (km). Öræfajökull 1362, together with most Plinian deposits, plots between the b_c = 3 km and b_c = 8 km contours.

Table 3.3 Summary of physical parameters for the Öræfajökull 1362 eruption and its deposits

(a) Total deposit	
Total deposit bulk volume	2.3 km^3 ± 0.05
DRE[a] volume	0.85 km^3
h_t (proximal) total deposit	4.79 km
h_t (medial) total deposit	13.41 km
h_t (distal) total deposit	29.21 km
(b) Unit *C*	
Unit C bulk volume	0.58 km^3 (DRE
Minimum eruption duration[b]	1.2-1.3 hours
Eruption column height (H_T)[c]	30-33 km
MDR[d]	1.2×10^8 kg/s
VDR[e]	6.0×10^4 m^3/s
h_t (MP)[f]	3.9 km
h_t (ML)	4.7 km
h_t (proximal) unit C[g]	3.0 km
h_t/h_t (unit C)[h]	1.3
Dispersal index[i]	4.4

[a] Based on a rhyolite magma density of 2470 g/cm^3 and a bulk deposit density of 1250 g/cm^3

[b] Minimum eruption duration of Plinian phase, estimated using accumulation rates by column height, (Wilson and Hildreth 1997)

[c] Calculated using maximum clast size data, MP (maximum pumice), ML (maximum lithic)

[d] Mass discharge rate (MDR) estimated from Figure 6, Sparks (1986)

[e] Volumetric discharge rate (VDR) estimated from Figure 6, Sparks (1986)

[f] Clast half distance (Pyle 1989)

[g] Thickness half distance (Pyle 1989)

[h] Half distance ratio, used to classify deposit dispersal and fragmentation (Pyle 1989)

[i] Following method of Hildreth and Drake (1992)

3.11 Petrology and major element geochemistry

Samples of the 1362 pumice from the major eruptive units were collected for analysis. In this section we outline the petrology, major and trace element whole-rock geochemistry, and glass geochemistry. We also present compositional information pertaining to the mafic pumice samples.

Pumice samples were crushed by hand and sieved into smaller size fractions from which matrix glass shards and crystals were hand-picked for electron microprobe analysis. To analyse the mafic material from the banded pumice, the band was trimmed and crushed separately and small glass fragments were picked for analysis. Major element and S, Cl and F analyses of glasses were conducted at The Open University on a Cameca SX-100 electron microprobe, using a 20 kV accelerating voltage, 20 nA beam current and a 10-20 μm diameter beam. These operating conditions were selected to minimize Na and K loss during analysis of pumice glass fragments. The full analytical setup is described in Chapter 2. 1σ analytical precision based upon replicate analyses of the glass standard VG-568 (Yellowstone obsidian, USNM 72854) is <1% for major elements and <5% for minor elements (e.g., Mn, K, P). All reported analyses are the average of 3-10 spots. For S, Cl, and F precision, replicate analyses of the glass standard VG-2 (Juan de Fuca Ridge glass, USNM 111240/52) gave 1480 ± 50 (2σ) ppm S (n = 80), and replicate analyses of the glass standard VG-568 gave 2000 ± 70 (2σ) ppm Cl (n = 100) and 1200 ± 100 (2σ) ppm F (n = 100), all in good agreement with values reported in previous studies (Appendix A7).

H_2O and CO_2 contents of the 1362 rhyolite magma were determined from doubly polished wafers of glass inclusions and matrix glasses using Fourier Transform Infrared (FTIR) spectroscopy. Spectra were collected with a Thermo Nicolet Nexus FTIR spectrometer

coupled with a Thermo Continuµm IR microscope. For all spectra, standard EverGlo mid-infra-red source optics, a Ge-on-KBr beamsplitter, and MCT-A* detector (11,700-750 cm^{-1}) were used. The full quantitative procedure used in this thesis is described in Ohlhorst et al. (2001).

Weight percent H_2O and CO_2 concentrations were ascertained using Beer's law:

$$c = \left[\frac{MA}{(\rho d \varepsilon)}\right] \times 100 \qquad [1]$$

where c is the species concentration, M is the molecular weight (18.02 for total H_2O and 44 for CO_3); A is the absorbance, ρ is the room temperature density of the glass (g/l), d is the sample thickness (cm) and ε is the molar absorption coefficient ($l\ mol^{-1}cm^{-1}$). Sample thickness was measured using a Mitutoyo Digimatic Indicator, to a precision of 3 microns. Glass density, based on major element glass composition, was calculated using the MELTS© software and extrapolated to obtain density at room temperature. Molar absorption coefficients for H_2O and CO_2 were 78 $l\ mol^{-1}cm^{-1}$ and 1066 $l\ mol^{-1}cm^{-1}$ respectively (Tamic et al. 2001). In rhyolite melt, dissolved H_2O occurs as two different species: molecular H_2O and OH^- (Wallace and Anderson 2000). H_2O concentration was obtained by measuring the height of the total water peak (i.e. molecular H_2O + OH^-) at 3550 cm^{-1}, and CO_2 concentration was acquired by measuring peak height of CO_2 at 2346 cm^{-1}.

Trace element chemistry for the banded pumice sample (Ö2-03) was obtained using ICP-MS analysis as the sample of dark material that we derived by picking and cutting was too small for standard XRF analysis. A pumice sample from unit C (Ö4-06) was also analysed

Table 3.4 (a) Major and trace element whole-rock geochemistry for selected Öræfajökull 1362 samples, (b) Average glass analyses for whole-rock geochemistry for selected Öræfajökull 1362 samples, (b) Average glass analyses for Öræfajökull 1362 eruptive units, (c) mafic pumice glass geochemistry. Each glass analyses represents an 'average' composition. Full glass dataset is listed in appendix B3. n.a. = not analysed.

(a) Major and trace element whole-rock geochemistry

Sample	Ö4-05	Ö2-03	Ö13-03	Ö9-06	Ö4-06	Ö10-2A	Ö1-01	Ö13-01
Unit	C^*	C^*	D_1	C	C	C	C	A_2
Location	4	2	13	9	4	10	1	13
SiO_2	63.33	66.54	70.21	69.93	70.58	70.46	70.67	70.91
TiO_2	0.73	0.69	0.27	0.33	0.28	0.27	0.29	0.28
Al_2O_3	13.25	13.99	13.24	13.18	13.26	13.17	13.30	13.31
Fe_2O_3	10.24	5.66	3.74	4.00	3.89	3.79	3.83	3.86
MnO	0.32	0.13	0.10	0.11	0.11	0.10	0.10	0.10
MgO	0.16	0.67	0.05	0.12	0.05	0.03	0.07	0.04
CaO	3.44	1.66	1.07	1.21	1.13	1.12	1.16	1.09
Na_2O	5.91	4.83	5.67	5.55	5.64	5.64	5.62	5.74
K_2O	2.11	2.95	3.37	3.31	3.34	3.35	3.34	3.38
P_2O_5	0.11	0.08	0.02	0.03	0.02	0.02	0.02	0.02
Total	100.15	99.78	99.40	99.35	99.60	99.06	99.76	100.21
LOI	0.54	2.58	1.65	1.60	1.31	1.11	1.36	1.41

* "mafic" pumice samples found within unit C. Ö2-03 is the banded pumice sample (i.e. analysis of bands of darker material) from location 2 and Ö4-05 is a sample of the grey pumice from location 4
'indicates samples analysed by ICP-MS

(a) Major and trace element whole-rock geochemistry

Sample	Ö4-05	Ö2-03	Ö13-03	Ö9-06	Ö4-06	Ö10-2A	Ö1-01	Ö13-01
Rb	4	2	13	4	4	10	1	13
Sr	45	73	77	78	78	81	78	78
Y	231	110	63	72	66	67	70	65
Zr	98	104	113	111	116	119	116	115
Nb	1019	694	765	701	772	794	766	785
Ba	68	70	75	75	74	76	75	75
Pb	619	643	644	646	648	645	654	658
Th	5	8	6	8	11	10	9	7
U	6	10	9	10	9	10	12	9
Sc	2	3	3	3	3	4	5	3
V	n.a.	7	1	n.a.	2	3	1	1
Cr	1	43	0	1	3	5	6	0
Co	1	6	4	0	6	5	7	4
Ni	1	5	1	0	3	1	3	0
Cu	1	6	4	0	3	4	5	5
Zn	8	15	7	7	7	6	8	8
Ga	209	160	163	158	152	152	149	164
Mo	n.a.	27	27	n.a.	27	27	27	27
As	4	3	4	5	4	5	4	3
S	n.a.	0	2	n.a.	2	3	0	4

(b) Glass geochemistry								
Sample	Ö2-06	Ö11-02	Ö2-05	Ö9-02	Ö4-06	Ö13-01	Ö9-02	Ö4-06
Unit	A_2	B_2	B_1	C	B_3	D_1	C	B_3
SiO_2	73.57	72.36	73.79	72.52	71.96	72.84	72.52	71.96
TiO_2	0.25	0.23	0.22	0.23	0.25	0.25	0.23	0.25
Al_2O_3	13.21	13.24	13.78	13.08	13.12	13.00	13.08	13.12
FeO	3.33	3.32	3.35	3.36	3.39	3.28	3.36	3.39
MnO	0.12	0.10	0.08	0.12	0.09	0.12	0.12	0.09
MgO	0.01	0.02	0.01	0.01	0.03	0.01	0.01	0.03
CaO	1.04	0.97	0.98	0.98	0.98	1.01	0.98	0.98
Na_2O	5.06	4.58	3.87	5.29	5.03	4.83	5.29	5.03
K_2O	3.49	3.56	3.53	3.39	3.76	3.37	3.39	3.76
P_2O_5	0.01	0.008	0.016	0.02	0.01	0.02	0.02	0.01
S	0.002	0.000	0.002	0.008	0.002	0.006	0.008	0.002
Cl	0.128	0.196	0.186	0.207	0.187	0.213	0.207	0.187
F	0.062	0.022	0.061	0.151	0.145	0.074	0.151	0.145
Total	100.28	98.61	99.88	99.36	99.06	99.02	99.36	99.06

(c) Mafic pumice glass geochemistry						
Sample	Ö10-04	Ö10-04	Ö2-03	Ö4-05	Ö4-05	Ö4-05
Unit	*banded*	*banded*	*banded*	*grey*	*grey*	*grey*
SiO_2	61.09	59.83	71.97	55.66	55.74	50.23
TiO_2	0.94	0.26	0.25	1.29	1.85	1.84
Al_2O_3	11.74	13.29	13.64	16.34	13.63	13.63
FeO	12.97	12.52	3.49	10.34	12.14	12.83
MnO	0.52	0.61	0.10	0.33	0.34	0.22
MgO	0.21	0.28	0.04	2.44	2.84	6.58
CaO	6.06	7.34	0.99	10.21	10.14	10.81
Na_2O	5.18	6.71	4.61	5.77	4.79	2.42
K_2O	2.17	0.83	3.39	0.38	0.80	0.23
P_2O_5	0.05	0.02	0.00	0.41	0.78	0.17
S	n/a	n/a	0.00	0.03	0.13	n/a
Cl	n/a	n/a	0.19	0.01	0.04	n/a
F	n/a	n/a	0.11	0.02	0.06	n/a
Total	100.92	101.67	98.8	101.3	101.4	99.0

in this way to test and compare the results of both techniques. Both XRF and ICP-MS analyses are shown in Table 3.4.

3.11.1 Whole-rock geochemistry

Major and trace element bulk compositions of the Öræfajökull 1362 ejecta were determined by analysing selected crushed and powdered pumice clasts using X-ray Fluorescence Spectroscopy (XRF), the results of which are shown in Table 3.4a. As indicated by whole-rock chemistry, the 1362 white pumices are all low silica high-K rhyolites, with approximately 70 wt% SiO_2 and ~ 9 wt% $Na_2O + K_2O$ (Figure 3.13). For a rhyolite magma, the 1362 melt also has a high concentration of iron (mean Fe_2O_3 ~3.8 wt%) in agreement with previous studies (e.g., Prestvik 1982, Larsen et al. 1999). There is no discernible difference in the whole-rock composition between the various eruptive units *A-D*, (Table 3.4). The Öræfajökull 1362 rhyolite can be distinguished from other Icelandic silicic eruption deposits by its low MgO and CaO content (<0.1 wt% and <1.2 wt% respectively) and higher Na_2O (~5 wt%) values (Larsen et al. 1999), this is useful when 'fingerprinting' distal 1362 samples.

3.11.2 Glass geochemistry

Glass from the Öræfajökull 1362 pumices is rhyolitic in composition, as demonstrated on the total alkalis ($Na_2O + K_2O$)-silica diagram (Figure 3.13). Matrix glass compositions from each of the eruptive units (*A-D*) and glass inclusion compositions show some minor overlap both with each other and with the whole-rock composition (Figure 3.13). SiO_2 contents vary in a non-systematic fashion, ranging 69.9 to 74.2 wt% in all eruptive units (Figure 3.14). The similarity of glass inclusion compositions to matrix glass compositions suggests that the inclusion composition was not significantly modified following entrapment (Figure 3.14).

Analysis of a small number of picked glass shards from sub-unit B_1 showed that some of these were basaltic in composition (Figure 3.13). These shards have ~48 wt% SiO_2, ~13.1-14.2 wt% FeO and 5.2-5.8 wt% MgO. Currently the relationship between these basaltic glass shards and the 1362 rhyolite pumice is unclear. Determining the origin and relevance of this basaltic material will require more detailed sampling and analysis. It is possible that these shards are completely un-related to the 1362 eruption; G. Larsen (pers. comm. 2004) suggests that they may originate from a slightly later basaltic eruption of Grimsvötn and are simply contaminants within the 1362 deposit. Glass shards from the mafic pumice and from the mafic component of the banded pumice were also analysed, the mafic pumice geochemistry is discussed in more detail in section 3.9.4.

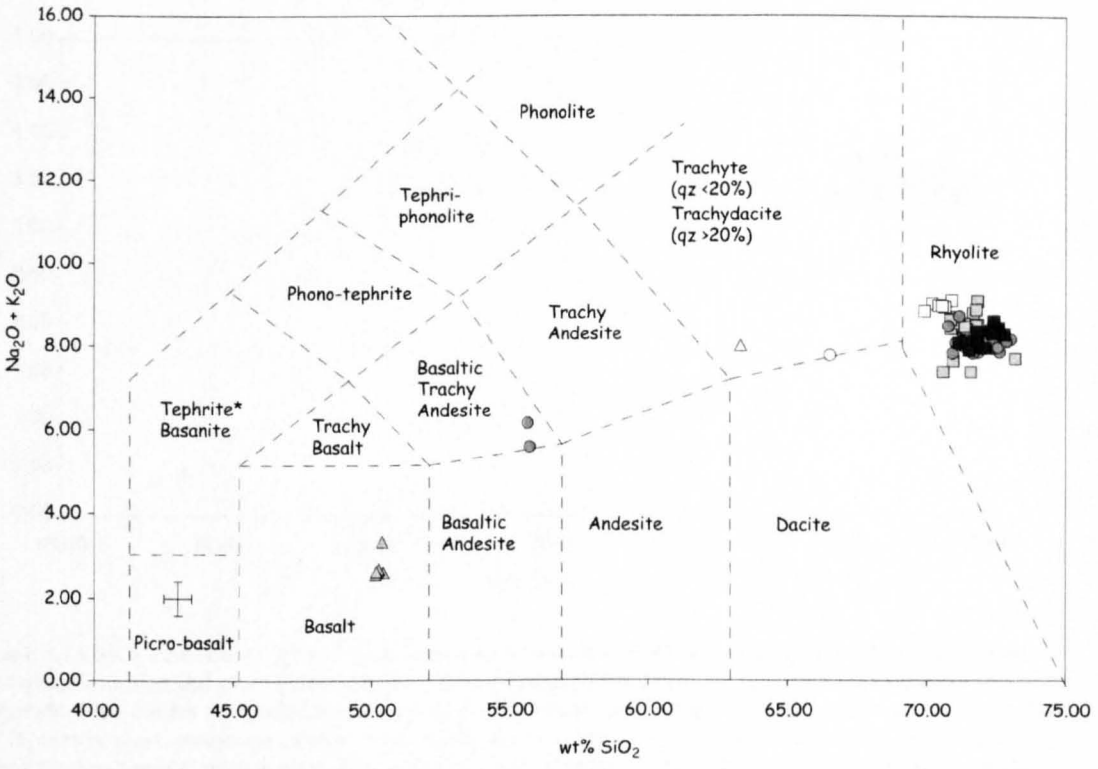

Figure 3.13 Total alkalis ($Na_2O + K_2O$) versus SiO_2 diagram for all 1362 whole-rock and glass data. Field boundaries based on the classification of Le Bas et al. (1986). Grey squares = rhyolite pumice glass inclusions, black squares = rhyolite pumice matrix glass, white squares = rhyolite pumice whole-rock analyses, grey triangles = grey pumice matrix glass, white triangles = grey pumice whole-rock, grey circles = banded pumice matrix glass, white circles = banded pumice whole-rock. 2σ error bar shown for reference.

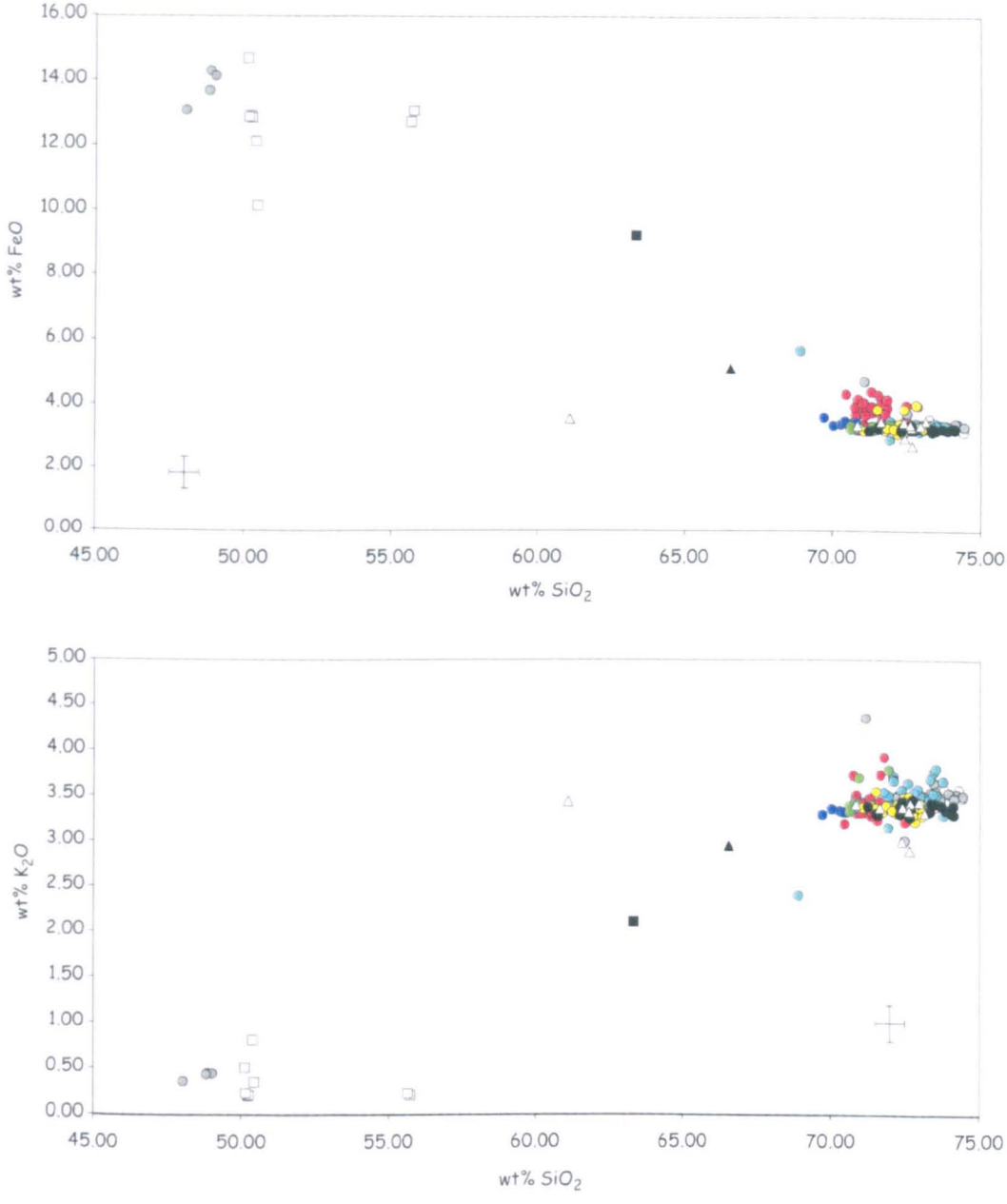

Figure 3.14 SiO_2 versus FeO (a) and SiO_2 versus K_2O (b) whole-rock and glass composition data for all Öræfajökull pumice and glass shard samples. In both diagrams red circles = rhyolite pumice glass inclusions, blue circles = rhyolite pumice whole-rocks, white circles = unit *A* matrix glass, grey circles = sub unit B_1 matrix glass, turquoise circles = sub unit B_2 matrix glass, green circles = sub unit B_3 matrix glass, yellow circles = unit *C* matrix glass, black circles = unit *D* matrix glass, black triangles = banded pumice whole rock, white triangles = banded pumice matrix glass, black squares = grey pumice whole rock, white squares = grey pumice matrix glass. 2σ error bar shown for reference. Note that the unit B_1 points (grey circles) that show low SiO_2 values (~48 wt% SiO_2) represent analyses of a few random basaltic glass shards found within sub unit B_1 (see text for further details).

3.11.3 Petrography and mineral chemistry

White pumice clasts from the 1362 deposits are relatively crystal poor. They contain ~ 1-3% (determined via point counting of thin sections and back-scatter electron images) phenocrysts (defined here as ≥ 0.3 mm) set in a glassy, microlite-poor matrix. The mineral assemblage consists of clinopyroxene, olivine, and feldspar with minor amounts of Fe-Ti oxides and very occasional apatite crystals.

Olivine crystals are typically 0.2 to 0.7 mm in size and show a subhedral to euhedral morphology. Olivine is present as fayalite, with the majority of crystals showing forsterite values of $Fo_{1.8}$ and showing little variation in forsterite content between crystals. Most crystals contain both glass inclusions and small (< 0.02 mm) magnetite inclusions. Olivine crystals are unzoned and show little compositional difference between core and rim.

Feldspar occurs as euhedral to anhedral plagioclase phenocrysts, 0.3 to 0.6 mm in size; and also as occasional needle-like microlite crystals (~ 0.03-0.05 mm in length) within the glassy matrix. Plagioclase crystals lack crystal zonation; anorthite contents range between An_{12-22} with an average composition $Ab_{79.8}An_{15.2}Or_{5.0}$.

The third major mineral phase, pyroxene, exists as thin, black, acicular (0.5 to 1 mm in length) clinopyroxene phenocrysts. Pyroxene compositions are constant, show little change between rim and core, and are typically hedenbergite ($En_{4.3}Fs_{51.5}Wo_{44.2}$).

The composition of these main mineral phases is similar in the different eruptive units, consistent with both the constant bulk whole-rock and glass chemistry (Table 3.4, appendix B3-B4). Fe-Ti oxide crystals occur both as mineral inclusions and as small groundmass crystals. Both ilmenite and magnetite crystals are present and Mg/Mn ratios for ilmenite

and magnetite (Bacon and Hirschmann 1988) range from 0.04-0.07 and 0.01-0.12 respectively.

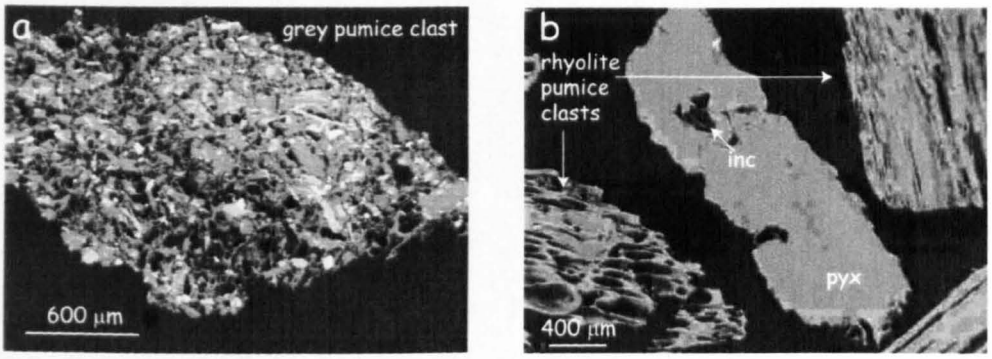

Figure 3.15 Back-scatter electron (BSE) images showing textural features of 1362 grey pumice clasts. (a) – grey pumice clast, note dense microlite content, in particular high amounts of Fe-Ti oxide minerals (bright white areas = crystal phases). (b) – pyroxene crystal with glass inclusion from rhyolite pumice, together with rhyolite pumice clasts, note rhyolite clasts are microlite-poor.

3.11.4 Geochemistry of grey and banded pumice

As mentioned earlier, Unit *C* contains sparse grey pumice clasts together with a few rhyolite pumice clasts that contain bands of dark grey to black material (Figure 3.3f). These are too small and rare to do much with, all of the material was used to make XRF pellets and beads, and probe mounts. Both the grey pumice and the bands of darker material are less finely vesicular; where present vesicles are sub-rounded to angular in shape and are often elongated or coalesced (Figure 3.15). Phenocryst contents of these samples are small, <0.5 % (measured via point counting of thin sections). However, the main difference between the grey and banded pumice and the rhyolite pumice is in the groundmass crystallinity, with both types of mafic samples containing a large amount of feldspar and pyroxene microlites (Figure 3.15).

Whole-rock major and trace element analyses (XRF) of the grey pumice (Table 3.4) show that it is dacitic in composition (~63 wt% SiO_2). The grey pumice shows slightly different trace element concentrations when compared with the rhyolite pumice, with marked

differences in the Rb, Sr and Zr contents and to a lesser extent in Cu, Zn and V concentrations (Table 3.4). The grey pumice glass compositions range from basaltic to basaltic-andesite (Figure 3.13). Phenocrysts, microphenocrysts and microlites of feldspar and clinopyroxene are the main mineral phases present in the grey pumice, although minor amounts of Fe-Ti oxides and apatite are also present. Apatite occurs both as small microlite-size crystals and also as small inclusions within clinopyroxene crystals. Pyroxene crystals exhibit a narrow range in composition, with all analysed crystals having a mean composition of approximately $En_{30.8}Fs_{28.9}Wo_{40.3}$. Feldspar crystals show a wide range in composition, with anorthite contents varying from $An_{21.5}$-$An_{91.7}$.

The data above indicate that the bulk whole-rock composition of the grey pumice is more evolved than the glass composition. This discrepancy between the bulk (dacite) and glass (basalt-basaltic andesite) compositions could possibly occur if the glass represents a hybrid (co-mingled) melt – e.g., rhyolite glass with streaks of mafic glass. This would give a dacitic bulk composition but as only dark spots of glass were analysed all glass analyses represent the basaltic component.

Although similar in many respects to the grey pumice, the band of mafic material (banded pumice) does show slight differences in its whole-rock and glass composition. The dark band shows slightly higher SiO_2 and slightly lower Fe_2O_3 contents (~66% and 6% respectively). Analyses of the glassy material from the mafic band show that the glass composition is dominantly rhyolite, although a few picked shards show basaltic-andesite compositions (Table 3.4). The mineral assemblage in the banded pumice is identical to that observed in the grey pumice, with pyroxene the dominant phase, and feldspar, apatite and Fe-Ti oxides present as accessory phases. Occasional crystals of olivine are also present. Clinopyroxene compositions vary from $En_{16.0}Fs_{41.0}Wo_{43.0}$ to $En_{29.5}Fs_{30.9}Wo_{39.6}$. Feldspar crystals are rare in the mafic band; the few crystals present are similar in

composition to those in the rhyolite pumice ($Ab_{72.2}An_{25.1}Or_{2.7}$). Occasional feldspar crystals differ from this mean composition, showing high anorthite and low orthoclase contents ($Ab_{26.7}An_{73.1}Or_{0.2}$), implying that these crystals possibly formed in a more mafic melt. Olivine is uncommon in the banded pumice; a single crystal was analysed and shown to have higher forsterite content ($Fo_{11.9}$) than that of the olivine analysed in the rhyolite pumice (Appendix B5).

The geochemical data presented here indicate that the 1362 magma was a homogenous rhyolite melt; the bulk magma composition did not apparently change as the eruption progressed, indicating tapping of a simple, dominantly homogenous magma system, a trend which is also reflected in the glass and mineral chemistry.

Although the presence of the grey pumice and the dark banded material (banded pumice) provides some tantalising evidence for possible magma mixing, our limited sample suite of this material means that we cannot make concrete conclusions regarding the origin of this mixing or its significance during the 1362 eruption.

Isotope geochemistry studies (e.g., Prestvik et al. 2001) suggest that the silicic rocks of Öræfajökull formed by fractional crystallization from mafic melts rather than by partial melting of older crust. Anomalously high Sr isotope ratios are common to the basic, intermediate and silicic rocks of Öræfajökull, suggesting that all rocks formed from a common enriched source, and that the rhyolites formed via varying degrees of fractional crystallization of basic melts (Prestvik et al. 2001). It is therefore not impossible that a more mafic component may have been involved in the 1362 eruption.

3.12 Magmatic intensive parameters

In order to quantify the eruptive sulphur release, information on the pre-eruptive magma storage conditions (e.g., temperature, oxygen fugacity, and melt H_2O content) is required (see Chapter 2 of this thesis). In this section we use co-existing Fe-Ti oxide compositions (i.e. ilmenite and magnetite), in equilibrium with one another and the melt, to ascertain the temperature and oxygen fugacity conditions for the 1362 magma. H_2O and CO_2 contents are estimated via FTIR spectroscopy.

3.12.1 Temperature and oxygen fugacity

Magmatic temperature and oxygen fugacity for the Öræfajökull 1362 rhyolite magma were determined using co-existing magnetite and ilmenite compositions (Appendix B4), following the method of Anderson et al. (1993). As Fe-Ti oxides re-equilibrate faster than silicates following changes in P-T-X conditions (Gardner et al. 1995), they are the crystal phases most likely to record pre-eruptive P-T conditions. Equilibrium pairs of Fe-Ti oxide crystals were identified by the Mg/Mn partitioning criterion of Bacon and Hirschmann (1988). Oxide mineral compositions were then used in the QUILF 4.1 software (Anderson et al., 1993) to obtain magmatic temperature estimates. For Öræfajökull 1362 rhyolite a magmatic temperature of ~ 828 °C is calculated, and a $\log fO_2$ of -15.6, ΔNNO = -2.0 (approximately two log units below the Ni-NiO buffer). The ΔNNO value is calculated as the deviation in $\log fO_2$ from the Ni-NiO buffer at the same temperature. Our value for the oxygen fugacity of the 1362 magma is in excellent agreement with the $\log fO_2$ determined by Carmichael (1967), who estimated a value of -15.2 at a temperature of 820 °C. These values indicate that the 1362 Öræfajökull magma was comparatively reduced.

3.12.2 Magma H_2O and CO_2 content

Four glass inclusions together with two matrix glass shards (bubble wall fragments) from unit *C* pumice clasts were analysed using FTIR spectroscopy following the analytical method described above. Average values show that the Öræfajökull pre-eruptive magma (measured in glass inclusions) contained 1.87 wt% H_2O, with degassed matrix glasses recording H_2O contents of 0.2-0.3 wt%. CO_2 in both glass inclusions and matrix glasses is negligible in concentration (below detection limit).

Using the microprobe analytical total as an indicator of unanalysed volatiles (e.g., Devine et al. 1995), the inclusion H_2O values determined via FTIR are in broad agreement with the average of ~30 electron microprobe analyses of rhyolitic glass inclusions (Table 3.4, Appendix B3 (g)). The matrix glass FTIR determinations of are however smaller than those obtained by electron microprobe totals (Table 3.4, Appendix B3 (e)). This difference probably occurs as a result of variable, post-deposition glass hydration which apparently did not affect the inclusions inside the crystals.

3.13 Estimates of volatile release from the 1362 eruption

3.13.1 Melt sulphur content

Sulphur concentrations in both matrix glasses and glass inclusions were determined for all eruptive episodes via electron microprobe analysis (Appendix B3). As expected for rhyolites, sulphur contents are much lower in the Öræfajökull magmas than in other Icelandic melts (Figure 3.16). Matrix glass (from unit C) sulphur concentrations range from 0.008 to 0.011 wt% S. In contrast, compositionally similar glass inclusions show a range of pre-eruptive sulphur concentrations, ranging from ~0.006 to ~0.024 wt% S (Figure 3.16). As a large proportion of the matrix glass sulphur contents are close to the microprobe detection limit for sulphur (3σ detection limit [D.I.] ~78 ppm), a value of 80

ppm was assumed for C_{matrix} in analyses where the sulphur value falls below the detection limit; this value is in good agreement with ion chromatography analyses of the bulk sulphur content: this technique estimates a bulk S value of 72 ppm (A. DiMuro pers. comm. 2004). These values are slightly higher than those calculated by Palais and Sigurdsson (1989) (Figure 3.16); however, this may simply be due to improved microprobe analytical techniques.

3.13.2 Petrologic determination of sulphur degassing

The mass of sulphur released to the atmosphere by volcanic eruptions can be accurately estimated using a petrological approach as described in chapter 2 of this thesis. The petrologic method uses the difference between pre-eruptive and degassed sulphur contents multiplied by the mass of magma erupted and the magma glass (liquid) mass fraction to yield the mass of sulphur.

In this study we follow the petrologic method as described in Chapter 2, and use the following equation to calculate the mass of SO_2 ($SO_2 = 2M_S$) emitted to the atmosphere.

$$M_S = \frac{M_1 \cdot (1 - W_{xtls})[C_{inc} - C_{matrix}]}{100} \qquad [2]$$

Glasses and inclusions were selected and analysed from unit *C* pumice clasts as this represents the suspected largest volume and most intense part of the eruption. Only glass inclusions with the same major element composition as the matrix glass were considered for use in this calculation, thus making sure that the inclusions used represent non-degassed equivalents of the degassed matrix liquid. Glass inclusions were selected on a statistical basis (as outlined in chapter 2). A result of this selection process very few inclusions statistically matched the mean matrix glass composition (n = 6). The sulphur

content of the statistically similar glass inclusions ranges from 0.012 to 0.024 wt% S. As one of the statistically similar inclusions contains the highest recorded S concentration (0.024 wt% S), we choose to use this value for the pre-eruptive S concentration to calculate a possible S degassing maximum, in addition to using an average value for C_{inc} (0.02 wt% S), as per the conventional petrologic calculation (see data in Appendix B3).

Based on this technique, we estimate that between 1.3 and 1.7 ± 0.45 Mt SO_2 was injected via a 30 km high Plinian eruption column into the upper atmosphere during the 1362 eruption. This figure is based upon a total magma mass of 2.27×10^9 kg, and a crystal mass fraction of 0.02 (liquid fraction 0.98).

There are two possibilities for why the petrologic estimate of SO_2 release for the1362 eruption yields only a small mass. One reason for this may be that the Öræfajökull 1362 magma contained little or no sulphur to begin with. As sulphur concentrations are strongly correlated with magmatic iron content, the behaviour of iron during magma chamber crystallization and melting processes can influence the melt sulphur content. At Öræfajökull isotope geochemistry implies that the silicic melts form via fractional crystallization of more mafic magmas – typical ocean island basalts, rich in iron and sulphur, (Prestvik et al. 2001). During initial stages in this fractional crystallization process, the fractionating melt shows a classic iron enrichment trend. Once the fractionating melt becomes saturated with respect to iron, iron rapidly starts to partition into Fe-Ti oxide minerals (magnetite), thus removing iron from the magma. This reaction usually occurs as the melt fraction reaches andesitic bulk compositions. Crystallization of magnetite causes further removal of iron from the melt. The removal of iron from the melt can cause a rapid reduction in the melt sulphur capacity (this occurs once the melt is almost sulphide-saturated). In a reducing magma this leads to removal of sulphur from the melt by crystallization of sulphide mineral phases (e.g., pyrrhotite). Therefore, as the

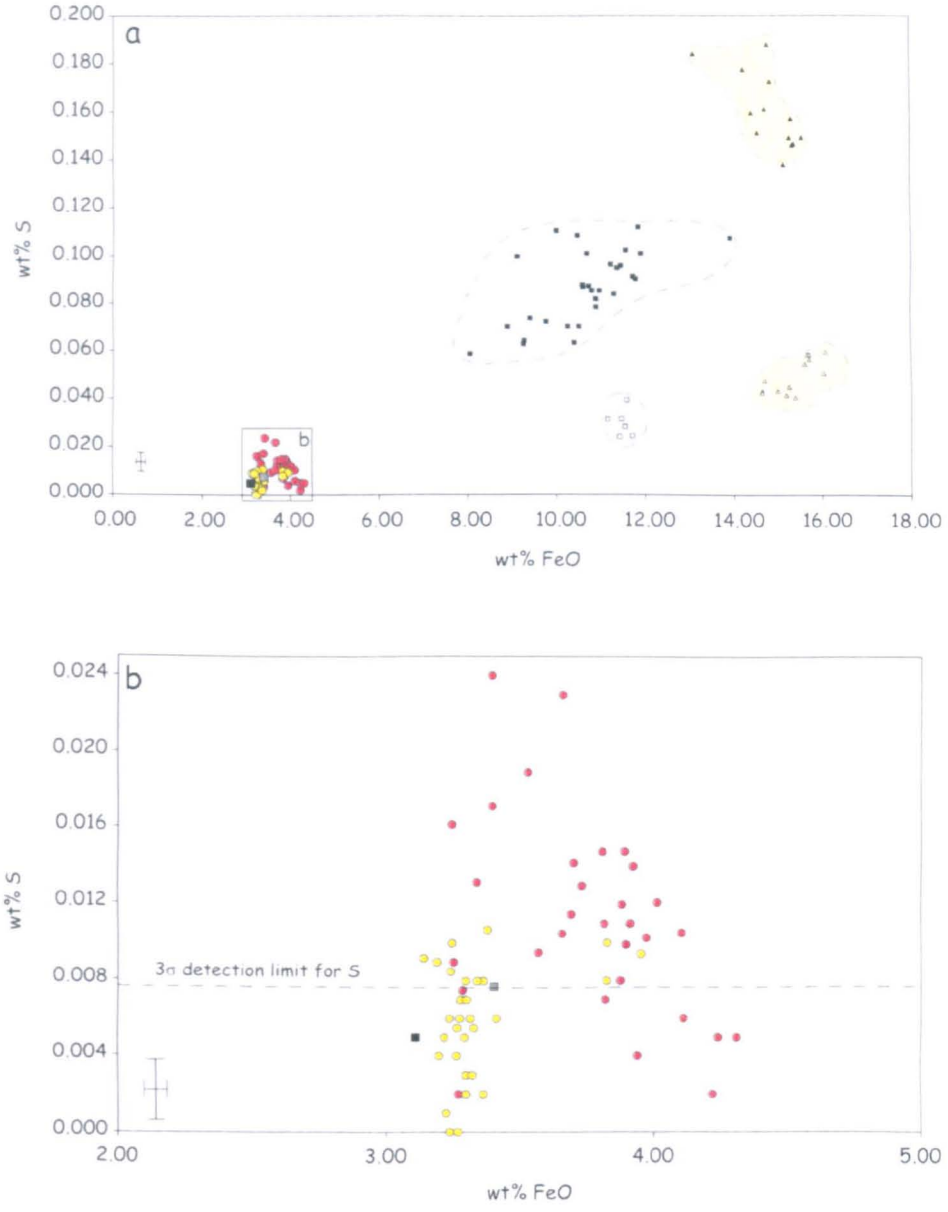

Figure 3.16 (a) S versus FeO for all unit *C* matrix glasses and glass inclusions, red circles = glass inclusions, yellow circles = matrix glass. Also shown are data from Palais and Sigurdsson (1989), grey square = glass inclusion, black square = matrix glass. S data from Icelandic basalts is also shown for comparison (data from Chapter 2), blue fields = Hekla 2000 (black squares = glass inclusions, white squares = matrix glasses), yellow fields = Krafla 1984 (black triangles = glass inclusions, white triangles = matrix glasses). (b) Expanded S versus FeO diagram for all Öræfajökull data. On this diagram dashed line indicates 3σ microprobe detection limit for S; analyses that lie below this line cannot be considered reliable and are therefore excluded from the petrologic method calculation (see text for further information). Note that the Palais and Sigurdsson (1989) data fall below this line. 1σ error bar shown for reference.

fractionating melt reaches rhyolite compositions in the fractional crystallization process, there is little sulphur remaining in the melt; the stable sulphide minerals remain within the magma chamber cumulate material. Consequently only a small amount of magmatic sulphur is available to degas.

Alternatively, the low mass of S may be caused by the presence of a sulphur-rich volatile phase present in the magma system prior to eruption. Several recent studies (e.g., Wallace 2001; 2004) have noted a discrepancy between petrologic estimates of SO_2 release and satellite measurements of volcanic SO_2 in arc eruptions (e.g., Pinatubo 1991). This discrepancy has been attributed to the presence of a sulphur-rich gas phase: in arc magmas sulphur is sequestered from the melt into a separate S-bearing fluid phase, thus depleting the magma with respect to sulphur. Sharma et al. (2004) report that excess sulphur does not seem to be a significant factor in non-arc basaltic volcanic systems and that if any excess fluid phase was to form in these systems, then it is likely to be sulphur poor (see chapter 2). In the case of Öræfajökull, independent estimates of the SO_2 release (ice core acidity peak data – see next section) also imply a small SO_2 mass, suggesting that the 1362 magma did not develop an excess sulphur rich fluid phase. Studies on the dependence of sulphur solubility on oxygen fugacity in rhyolite melts (e.g., Scaillet et al. 1998) also attest to this, together with the fact that low sulphur solubility in rhyolites is attributed to a combination of low melt FeO content and low temperatures of silicic magma. The comparatively low $\log fO_2$ (ΔNNO -2.0) for the 1362 magma means that the development of a separate, pre-eruption S-rich fluid phase is extremely unlikely. At these low ΔNNO values, the magma is reduced and thus stabilises formation of an immiscible sulphide phase rather than sequestering sulphur into a SO_4^{2-} sulphate-bearing phase. Experimental work by Scaillet et al. (1998) also shows that in more reduced silicic magmas (i.e. those co-existing with pyrrhotite), fluid/melt partition coefficients are drastically reduced (values

around 1 compared with 50-2612 for oxidised magmas), as pyrrhotite locks up nearly all the sulphur in the magma. Thus explosive eruptions involving reduced, cool silicic magmas tend to release negligible amounts of SO_2 into the atmosphere.

3.13.3 Melt chlorine and fluorine content

Pre-eruptive chlorine and fluorine concentrations were measured by electron microprobe analysis of crystal-hosted glass inclusions in unit *C* pumices (Appendix B3). Similarly matrix glasses were analysed to obtain degassed halogen contents. Pre-eruptive chlorine contents have a narrow range varying from 0.191-0.219 wt%. Chlorine values in matrix glasses show almost identical concentrations, ranging between 0.195-0.215 wt%. In contrast, fluorine contents in both inclusions and matrix glasses show significant variations. Pre-eruptive fluorine values range between 0.043 and 0.190 wt%; however the majority of inclusions exhibit values between 0.071 and 0.090 wt%. Fluorine in the matrix glasses shows ranges from 0.096 to 0.164 wt%. These figures suggest that neither halogen species did not efficiently de-gas from the melt during eruption.

3.14 Aerosol mass loading and atmospheric impact of the 1362 eruption

Small glass shards (~30 μm in diameter) attributed to the 1362 eruption have been identified in the GISP-2 Greenland ice core (Palais et al. 1991). Associated with this shard "horizon" is a minor sulphate peak (SO_4^{2-}). Following the method outlined by Zielinski (1996), acidity peaks in ice cores can be used to infer the mass of syn-eruptive SO_2 (a more complete discussion regarding ice core acidity peak data can be found in Chapter 4). For the 1362 eruption, the SO_2 mass derived this way is very small, on the order of 0.4 to 0.9 Mt. Taking into account the relative proximity of the volcano to the Greenland ice sheet, this low figure is even more unusual.

Based on this work, we estimate that the 1362 Plinian eruption column had a column height of 30-33 km; this, coupled with the fact that during the summer months the tropopause height in Iceland is at an altitude of ~9-10 km, suggests that most of the SO_2 released was injected into the stratosphere. The amount of SO_2 released during the 1362 eruption is theoretically sufficient to have generated between 2.0-2.7 Mt of sulphate aerosol into the upper atmosphere. This calculation assumes a gas (SO_2) to particle ($H_2SO_4 + H_2O$) conversion efficiency of 86%. This conversion factor is based on the satellite-observed stratospheric aerosol conversion efficiency during the 1991 Pinatubo eruption (McCormick et al. 1995). A small stratospheric aerosol mass such as this would have an almost negligible long-term atmospheric impact. Halogen degassing was also unimportant during this event and certainly not large enough to cause any major atmospheric perturbations.

Based on pre-eruptive and degassed sulphur concentrations obtained for the 1362 eruption, an eruption of Öræfajökull would need to discharge at least 70 km^3 (32 km^3, DRE) of magma in order to generate the same amount of stratospheric aerosols as the 1991 eruption of Mount Pinatubo. The 1991 eruption of Pinatubo released ~20 Mt SO_2 to the upper atmosphere, with the resultant sulphate aerosol cloud causing a 0.5 °C reduction in the mean northern hemisphere surface temperatures (Self et al. 1996).

In light of this, taking into account the low tropopause position above Iceland during June (~10 km), and the high eruption columns (~30 km) generated during the Plinian phase together with the wide dispersal area of the fine distal ash, perhaps the greatest atmospheric or environmental impact from the 1362 Öræfajökull eruption resulted from the injection of large amounts of volcanic ash and fine dust particles into the stratosphere.

3.15 Volcanic hazards from future activity at Öræfajökull

Due to the location of Öræfajökull with respect to Europe, it is vital that any study of the 1362 eruption addresses the possible hazards that may result from similar eruptive activity in the future. Recent work (e.g., Lacasse 2001) has shown that even if tephra fall off Iceland is dispersed away from the UK (i.e. not south-eastwards), volcanic ash and aerosols can still reach the UK via upper tropospheric and stratospheric transport. Also, Iceland is directly under major flight paths for transatlantic flights between Europe and North America. Several studies have examined the impact of volcanic ash clouds on air travel (e.g., Casadevall and Krohn 1995), and have concluded that injection of large amounts of volcanic ash and gas can have extremely detrimental effects on aircraft jet engines, and also to passenger health and safety (i.e. from inhaling gases brought into the fuselage). As the tropopause height is low above Iceland (~10 km in summer, ~7 km in winter), a Plinian eruption column, such as the one produced in 1362, could inject large amounts of volcanic ash and aerosols into the stratosphere, causing serious problems for aviation traffic flying close to Iceland at cruising altitudes of ~30,000-36,000 feet (~9-12 km).

Öræfajökull is only one of Iceland's volcanoes capable of producing Plinian type eruptions. The proximity to the Atlantic Ocean means that hazards to shipping traffic from such activity must also be seriously considered. Fine distal ashfall can seep into engine room cooling systems and drive-shafts causing significant amounts of erosion. Pyroclastic fall accumulating at rates greater than 2 cm/hr would also cause problems with on board radar and GPS navigation equipment (L.P. Cragg, pers. comm. 2005). Finally, the formation of pumice rafts during Plinian and pyroclastic flow activity can also present a severe oceanic hazard (Bryan et al. 2004).

3.16 Conclusions

The 1362 eruption of Öræfajökull produced three main fall units during phreatomagmatic and intense Plinian activity. The climactic phase of the eruption was an intense 10-13 hour long Plinian eruption that generated a 30 km high eruption plume and produced a pumice-dominated, coarse fall deposit, dispersed to the south, in proximal areas, and a widespread fine, distal ash that covered much of north east Iceland. The differing dispersals possibly resulted from decoupling of fines material from the coarser pumice-dominated material, with the fines held at higher levels in a dynamic umbrella cloud system and the coarse proximal pumice fallout dispersed via lower level winds, before fallout from higher levels with differing atmospheric wind conditions occurred. This is consistent with recent work suggesting decoupled fallout paths and independent dispersal of coarse and fine particles in Plinian eruption clouds (e.g., Hildreth and Drake 1992; Fierstein and Hildreth 1992; Adams et al. 2001).

Although still a significant eruptive event, the 1362 eruption is volumetrically smaller than previously thought. A total of 2.3 km^3 (~ 1.2 km^3 DRE) was erupted during the energetic Plinian eruption, accompanied by pyroclastic flow activity of a much smaller volume (~ 0.1km^3).

Low SiO_2, high alkali pumice dominates the deposit; however a small amount of mafic clasts is also found intermingled within the unit *C* deposit. The mafic clasts consist of two distinct types – grey pumices and white rhyolite pumices that have a distinct mafic band (banded pumice). Both types are dacitic in bulk composition. Our sample suite limits further conclusions regarding the origin of these mafic components; however, we can conclude that a mafic component was involved in the 1362 eruption. Future studies will

need to consider the origin of the mixed melts and assess their possible role in triggering rhyolite volcanism at Öræfajökull.

Only a small amount of SO_2 (1.7 Mt) was released into the stratosphere during the 1362 event; thus a significant amount of stratospheric sulphate aerosol was not produced. Halogen chemistry also indicates that fluorine and chlorine did not degas. Thus, despite the violent nature and relatively large magnitude of the eruption, the environmental and atmospheric impact of the 1362 activity is limited to the injection of significant volumes of fine ash and volcanic dust to upper atmospheric levels.

Chapter 4: Physical volcanology, SO_2 release and atmospheric impact of the 1730-36 eruption of Lanzarote, Canary Islands

Abstract

The AD 1730-36 eruption of Lanzarote (Canary Islands) is the third largest basaltic fissure eruption known to have occurred in the last 1000 years, after the Icelandic events of Laki (AD 1783-84) and Eldgja (AD 934). Our new volume estimates suggest that the Lanzarote eruption produced ~5 km^3 of alkali basalt to tholeiite magma along a 15-km long, E-W trending fissure. Eruptive activity occurred in five distinct phases. Each phase began with Strombolian fire fountain activity, building large spatter and scoria cones. This was accompanied and followed by effusive aa and pahoehoe lava flow emplacement. As studies in Iceland have shown, this type of sustained fissure eruption can release large amounts of SO_2 to the upper atmosphere, generating sulphate aerosols, causing widespread environmental damage and human suffering.

Matrix glasses in scoria and surface lava samples have 80-300 ppm S (EMPA) and 300-600 ppm H_2O (FTIR), whereas glass inclusions in olivine have 300-2650 ppm S and 1000-5000 ppm H_2O. Low sulphur inclusions are believed to be partially degassed, representing melt that was trapped during degassing-induced crystallization that occurred as a result of shallow decompression. The inclusions with the highest sulphur contents trap the original un-degassed melt, as indicated by their consistent S/K_2O ratio (0.22). The high sulphur contents are also consistent with our finding, from olivine-spinel equilibria, that the magma was relatively oxidized ($\log fO_2$ -7.9) therefore favouring the formation of sulphate species and preventing sulphide saturation. Our glass analyses indicate that 45 Mt of SO_2 was injected into the upper troposphere – lower stratosphere via 12-16-km-high eruption plumes and that over half this amount was released during the first year of activity. This figure correlates with published Greenland ice-core (GISP-2) data that shows an acidity spike in 1731, suggesting stratospheric transport of sulphate aerosol north during the first year of eruption. Historical records note the presence of a dry fog over much of Europe during 1733. This, together with proxy climate indicators such as a marked tree ring anomaly in 1732 and a known decrease in the Northern hemisphere surface temperatures, suggests that the Lanzarote eruption had an impact on Northern Hemisphere climate in the years following the activity.

Keywords: *Lanzarote, fire-fountain, lava flow, sulphur degassing, atmospheric impact*

4.1 Introduction

Lanzarote is one of the north-easternmost of the Canary Islands, which are situated in the Atlantic Ocean (29°N 13.6°W), approximately 100 km from the north coast of Morocco, Africa (Figure 4.1). The Canary archipelago consists of seven major islands forming a volcanic chain that extends for ~500 km across the eastern Atlantic (Thomas et al. 1999). The origin of oceanic intraplate volcanism on these islands has been attributed to either the presence of a hotspot or mantle plume, or magmatism linked to a propagating fracture (e.g., Carracedo et al. 1998). There have been two major eruptive events on Lanzarote in historic times, the1730-36 basaltic fissure eruption (occasionally referred to as the Timanfaya event), and a much smaller basaltic eruption known as Volcan Nuevo in 1824 (Carracedo et al. 1992).

Studies on the Icelandic basaltic fissure eruptions of Laki (1783 AD) and Eldgja (934 AD) have demonstrated that these types of eruptions can release significant amounts of sulphur into the atmosphere, thus causing major atmospheric and climatic perturbations (e.g., Thordarson et al. 1996; Thordarson and Self 2003; Thordarson et al. 2001). As the Lanzarote 1730-36 eruption has previously been reported to be of quite a high magnitude (e.g., Carracedo et al. 1992) it may also have had some impact on northern hemisphere climate. This study attempts to reassess the magma volumes produced, study eruption mechanisms, and quantify the amount of sulphur released during this event. Combining these three aspects will allow us to assess the atmospheric and environmental impact of this major fissure eruption.

In this chapter we present new descriptions and interpretations of the volcanic features on the 1730-36 eruptive fissure and volcanic deposits and correlate this information with

contemporary accounts of the activity. Using this information we calculate the eruption parameters required to assess the magnitude of the sulphur release, e.g., volumes, mass eruption rates and plume heights. To calculate the syn-eruptive volatile release we use a petrological approach which has been validated for basaltic magma compositions (see chapter 2 of this thesis) (e.g., Devine et al. 1984; Sharma et al. 2004). The petrologic method combines estimates of erupted magma volume with measurements of sulphur concentrations in the eruptive products. Major element glass and mineral compositional data is also required. Finally information regarding eruption style, plume dispersal and local atmospheric conditions is needed to evaluate both the atmospheric mass loading of sulphur into the atmosphere, and the possible environmental and climatic consequences resulting from this.

Fieldwork for this study was carried out in December 2003, when possible fallout and lava samples were collected from each of the major eruptive episodes. Sixteen locations were studied in detail (Figure 4.2; appendix C1); at each of these localities we described the main characteristics of the fallout deposit and lava flows, and assessed their stratigraphic relationships.

Figure 4.1 Landsat ETM© image of Lanzarote, Canary Islands and location map. Inset map shows location of Lanzarote in the Canary Islands archipelago (shaded red). Landsat image shows island of Lanzarote; major towns are marked with black circles. The 1730-36 fissure can clearly be seen extending from the centre of the island out to the W coast. Note older eruptive fissures south of the 1730-36 fissure.

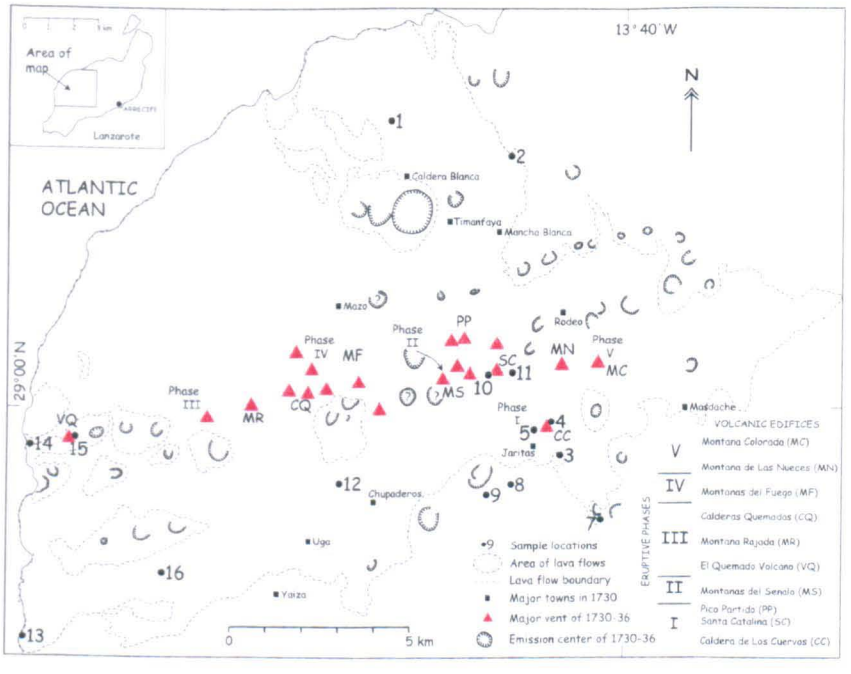

Figure 4.2 Detailed map of the central part of Lanzarote showing area covered by lava flows (grey shaded areas). Red triangles mark the major 1730-36 eruptive vents (letters signify volcanic edifice names – see key for details). Major towns are also marked. Numbered black circles indicate sample locations.

4.2 Chronology of the 1730-36 Lanzarote eruption

Contemporary historical accounts (summarized in Table 1; and in Carracedo et al. 1992 and based on Hernandez-Pacheco (1960) and Ruiz (1997)) report that the eruption began on September 1st 1730 and continued for approximately six years until 16th April 1736. Eruptive activity produced ~5 km^3 of lava and pyroclastic fallout material. Activity was concentrated along a 15-km-long E-W trending fissure system, composed of ~30 different volcanic vents arranged in an *en echelon* pattern. The fissure system extends from the central part of the island out to the west coast, and probably offshore as there are contemporary accounts of near-shore submarine activity (Carracedo et al. 1992). Activity started on the eastern side of the rift but shifted up and down the fissure system in a random fashion during the course of the eruption.

Each phase of the eruption appears to have followed roughly the same pattern (see also descriptions of the 1783-84 Laki eruption – e.g., Thordarson and Self 1993). Each phase began with the formation of a new vent along the fissure segment, followed by an early sustained explosive stage involving Strombolian fire fountain activity generating ash-rich plumes that reached heights of ~3-12 km above the vent, resulting in widespread ash fall deposits. Next, effusive activity tended to dominate producing a variety of lava flows. Eventually, the lava covered approximately one-quarter of the island and entered the ocean on the north and west coasts. The eruption of lavas and tephra caused widespread destruction, destroying villages and key areas of farmland in populated regions of the island; the subsequent famine that ensued led to eventual abandonment of the island around 1732 (Carracedo et al. 1992).

Using contemporary eyewitness reports of the eruption together with field mapping Carracedo et al. (1991; 1992) established an eruptive stratigraphy for the 1730-36 volcanic activity. Based on changes in eruptive activity and eruptive centres, magma composition and emplacement area in the main structural fracture zone on Lanzarote, Carracedo et al. (1991) divided the eruption into five major phases, with each phase containing one to three distinct episodes (Table 4.1; Figure 4.3). Information on the timing, duration and nature of the major eruptive events in phases I and II is especially well described and constrained by these accounts. However, during the latter episodes of phase III and phase IV historical information was sparse as most islanders had fled Lanzarote in 1732.

Below we present a description of the main eruptive episodes mainly based on these contemporary accounts. We adopt the same stratigraphic nomenclature as Carracedo et al. (1990, 1992). Some of the information presented below is summarized in Carracedo et al. (1992); however, we supplement this with additional information obtained via translation of additional contemporary accounts (summarized in Ruiz (1997) and Hernandez-Pacheco (1960)).

Table 4.1 Summary of eruption episodes, activity, and historical evidence of the Lanzarote 1730-36 event

Phase	Episode	Date[+]	Main Vent Area	Activity	Historical Information
I	1	1 Sept - 19 Sept 1730	Caldera de Los Cuervos	Cinder/spatter cone tephra fall lava flows	Between 9 and 10 pm, earth opened 2 miles (3 km) from Yaiza. Flames from mountain continued to burn for 19 days. Lava was cast over Timanfaya, Rodeo and parts of Mancha Blanca and flowed north. On 17 Sept lava flow direction changed to NW-WNW, instantly destroying Maceto and Santa Catalina. On 11 September for 6 days lava began to flow with greater force, covering and destroying Mazo and continuing to the coast where it formed lava cascades as it entered the ocean.
I	2	10 Oct 1730 – Feb 1731? [10 Oct – 31 Oct 1730][1]	Pico Partido, Caldera de Santa Catalina	Scoria cones, cinder/spatter ramparts tephra fallout lava flows	Intense scoriaceous sand and ash fall covers the island, powerful explosions plunging the island into total darkness. Game and cattle drop dead as a result of pestilent vapours and acid rain, strong sulphur smell coming from the soil - wiping out crop yields and damaging fertile farmland. Lavas spread north and west, covering earlier phase I flows. By the 16th December lava began to flow to the SW reaching Chupadero and the fertile Uga meadow. Ash, rocks, and dense smoke made life impossible. From February 3rd to 28th the final activity of this episode occurred from a new cone above the hamlet of Rodeo, which subsequently devastated Rodeo. Continuous, high fire fountains reported to have been seen from neighbouring Canary Islands to the west.
II		7th March – June 1731	Montañas del Señalo	Strong seismicity Scoria tephra fallout lava flows	New cones arose close to the Pico Partido volcanic edifice on 7th March; ensuing lava flows travelled N devastating Tingafa. New cones arose in this area on March 20th, on April 6th these vents experienced extremely violent activity, spewing a lava flow that extended almost to Yaiza. On April 13th these vents collapsed, however by May 2nd a new hill arose, again sending lava flows that threatened the parish of Yaiza. On June 4th more openings appeared, accompanied by violent seismic activity, large flames, and never before seen thick white smoke (steam) these openings quickly merged into one high elevated cone, (Montañas del Señalo)
III	1	June – July 1731?	Volcán del Quemado	Submarine volcanism Cinder cones Scoria fallout Small lava flow Phreatomagmatic explosions Littoral cone/lava delta	Activity moves to the west coast, with initial submarine eruptions reported. Deep submarine eruptions brought deep water fish species to the shore, some of the fish species had never previously been seen before. NW of Yaiza a great mass of smoke & flames seen rising - new vent on land consisting of cones; phreatomagmatic explosions also common.
III	2	July – December 1731	Montaña Rajadas	Strong seismicity Cinder/scoria cones Tephra fallout Lava flows	Eruptive activity migrated eastwards, islands agitated by earthquakes – the most violent which had occurred in these two disastrous years. Huge fires observed on the western side of Rubicon, islanders note that the position of eruptive cones from this episode cannot be precisely placed.

Table 4.1 (cont'd)

Phase	Episode	Date[†]	Main Vent Area	Activity	Historical Information
III	3	December 1731 – January 1732?	Calderas Quemadas	Cinder cones Hornitos Lava flows	On December 28th lava flows spewed from a cone that had arisen towards Jaretas - burning the village and destroying the chapel of St John the Baptist, near Yaiza. Lava flows demolished Yaiza farmlands at this time, almost reaching the town. Most inhabitants of Yaiza and other nearby parishes left the island at this time.
IV[2]		Early 1732-1736?	Montañas del Fuego	Strong seismicity Hornitos Scoria/cinder cones Lava flows	Activity concentrated around Timanfaya volcano, voluminous lava flows travelled NW of vent, filling a wide, fertile valley before flowing into the sea on the north side.
V	1	March – April 1736	Moñtana de Las Nueces	Strong seismicity Tephra fall Lava flows	During mid-March, lavas flowed south, entering the sea at Arrecife, at the same time a separate lava flow travelled north towards the town of Tinajo.
V	2	1 April – 16 April 1736	Montaña Colorado	Tephra fall Lava flows	Final episode of eruption, all volcanic activity ceased on 16th April 1736. Lavas flowed towards the north.

[†]Dates for each eruptive phase have been deduced from historical eyewitness accounts (diary of the parish priest of Yaiza (1730-1732) and official crisis reports to the Royal Court of Justice of the Canary Islands (1730-early 1731)), summarized in Hernandez-Pacheco (1960) and Carracedo et al. (1992); ? indicates estimated dates.
[1] Note that at the start of phase I, episode 2; Pico Partido and Santa Catalina vents were erupting simultaneously, but by 31 Oct 1730, Santa Catalina was no longer active. Bracketed dates denote approximate date and duration of Santa Catalina eruptive activity.
[2]Note there are no contemporary eyewitness accounts during 1732-1736 (eruption phase IV).

4.2.1 Phase I episode 1

The initial episode of the eruption started on September 1st 1730 and continued until the 19th of September. A new vent opened up in the centre of the island on the eastern side of the main fissure that developed as the eruption progressed (Carracedo et al. 1992). Activity started with intense explosive activity, involving fire fountains that played for 19 days and covered "local" areas (up to 5-10 km from the vent) with a 3 to 4-m-thick scoria lapilli and ash fall blanket. Around the vent a spatter cone, Caldera de Los Cuervos, was built up, ~1 km long and 60-80 m high above the surrounding surface. This vigorous explosive activity was accompanied and followed by lava effusion; lava flowed to the N and NW destroying several towns and villages (see Table 1). Lava cascaded into the ocean, possibly creating a sustained ocean entry at the north coast. Lava flows from

Caldera de Los Cuervos are not especially well exposed, having been covered by lava flows and fallout from the later eruptive phases.

4.2.2 Phase I Episode 2

Episode 2 of Phase I involved at least two vents around which the spatter/scoria cone groups of Santa Catalina and Pico Partido grew. These are located ~3.5 km NNW from Caldera de Los Cuervos (Figure 4.3). Between October 1st and 31st 1730 Santa Catalina and Pico Partido erupted simultaneously (Carracedo et al. 1992). After this time activity became concentrated in Pico Partido and several smaller surrounding vents, building a complex volcanic edifice (~500 m long and 150 m high at its highest point) dominated by spatter. Powerful fountaining activity on the fissure at this time resulted in pyroclastic fall deposits covering the bulk of the island, with the continuous high fire fountains visible from neighbouring Canary Islands (Hernandez-Pacheco 1909). The accompanying degassing caused a strong sulphurous odour and haze (described by eyewitness accounts as pestilent vapours) and acid rain which destroyed many fertile farmlands and killed game and farm animals. Lavas again travelled north and west, covering the earlier episode 1 flows and extending beyond them, and also reaching the ocean. On the 16th December 1730, lava started to flow to the south-west of the island destroying the fertile "Uga meadow" area and threatening the parish of Yaiza (Figure 4.2, 4.3) (Carracedo et al. 1992). Towards the end of this episode eyewitness accounts mention a new spatter cone forming over the hamlet of Rodeo; this was the final activity of episode 2, and it devastated Rodeo (Hernandez-Pacheco 1909; Ruiz 1997).

4.2.3 Phase II

Following a slight hiatus in eruptive activity, on March 7th 1731 strong seismic activity marked the onset of Phase II. A new vent that opened up close to Pico Partido - Montanas del Senalo was the sole focus for eruptive activity during phase II. Initial lava flows in this phase flowed to the north destroying the village of Tingafa. By April of 1731 the eruption involved extremely violent explosive activity interspersed with lava flow effusion that again threatened Yaiza. A few days later, reports surfaced stating that the vents had collapsed and new cones arose – indicating that perhaps periodic small collapses of unstable spatter ramparts and small cones occurred; these collapsed portions were then rafted along on top of the lava flow (Figure 4.5e). At the end of this phase the small cones and fractures merged into a single cone.

4.2.4 Phase III Episode 1

Following phase II, activity shifted to the extreme west of the fissure system. Activity during episode 1 of phase III was concentrated within the low-lying spatter rampart of Volcan do el Quemado (~40 m high) on the west coast of Lanzarote close to El Golfo. Fallout and lavas produced during this short episode (June to July 1731) are volumetrically minor; only one single lava flow 1.5 km long, was produced. Possible submarine activity was associated with episode 1 – previously never-before-seen deep-ocean fish species were discovered floating near the shore (Carracedo et al. 1992). The presence of these new fish species could result from either submarine activity or simply violent phreatomagmatic activity that churned up the lower reaches of the ocean bringing deep water fish onshore. Eyewitness accounts of activity (e.g., Hernandez-Pacheco 1909) indicate that phreatomagmatic activity was occurring at this time, producing small littoral cones and lava deltas as lavas entered the ocean.

4.2.5 Phase III Episode 2

The second episode of Phase III began in July 1731 and continued until December of that year. The onset of this episode was marked by violent earthquakes – the strongest seismic activity to have occurred since the start of the eruption. Activity migrated back towards the east of the fissure with vents opening up approximately 5 km from the episode 1 vent although eyewitness accounts report that the position of the episode 2 eruptive vents cannot be placed accurately. Explosive activity from Montana Rajadas consisted of large fire fountaining events which could be seen from the western side of Rubicon (Hernandez-Pacheco 1960). Lava flows extended towards the west coast, forming a broad lava fan ~20 m across.

4.2.6 Phase III Episode 3

The final episode of activity during phase III was centred in Calderas Quemadas, a close linear alignment of 4 cinder cones, 1.5 km east from Montana Rajada. Lavas continued to flow westwards covering a large proportion of the earlier phase III flows, although these lava flows did reach the west coast. By December 28th 1731 lavas erupted from a cone near the village of Jaretas – destroying the village. This lava flow again threatened Yaiza. At this time the Yaiza farmlands were completely ruined as was the chapel of St John the Baptist on the outskirts of Yaiza. This renewed activity close to Yaiza resulted in the inhabitants of Yaiza and nearby parishes leaving the island permanently sometime in early 1732 (Hernandez-Pacheco 1960).

4.2.7 Phase IV

By 1732, as a large majority of islanders had left the island, contemporary eyewitness accounts detailing phase IV of the eruption are no longer available. In the early part of 1732 the island was once more shaken by strong seismic activity. Volcanic activity moved

a little further east along the 1730 eruptive fissure (~ 1-1.5 km from Calderas Quemadas) and was concentrated around Timanfaya volcano. After initial explosive activity, Montanas del Fuego – a complex volcanic edifice consisting of overlapping cinder cones – formed. Lavas from phase IV flowed to the north-west of the vent area covering wide, fertile valleys before entering the ocean on the north side (Ruiz 1997). During Phase IV the eruptive style changed towards long lived lava effusion, with the lavas mostly emitted from clusters of hornitos situated NW and SE of Montanas del Fuego (Carracedo et al. 1992), (Figure 3).

4.2.8 Phase V Episode 1

In March 1736, contemporary historical accounts are once more available documenting the eruption. Episode 1 of phase V began in March 1736 with intense seismicity and opening of vents at the extreme eastern end of the fissure system (~ 2 km east from Santa Catalina and ~2 km NNE from Caldera de Los Cuervos). The Montana de Las Nueces was the single vent that fed the eruption at this time. Initial explosive activity that built up the cone generated near-vent tephra. However this eruption was largely effusive. Episode 1 lasted approximately 1 month and produced the longest, most voluminous lava flows of the entire eruption. Lavas flowed towards the east of the vent forming a broad lava flow field with two distinct branches. One branch turned towards the south coast and entered the ocean at Arrecife, ~25 km from source. A second branch of the Nueces lava travelled north towards the town of Tinajo, with a third branch (Puerto del Carmen lava flow) emplaced directly south of Montana de Las Nueces extending towards the coast at Puerto del Carmen (Carracedo et al. 1992). Note that both the geological maps of Fuster (1969) and Carracedo et al. (1991) show this Puerto del Carmen branch terminating ~10 km from the coast; however we believe that this lava flow in fact continues to the coast at Puerto del Carmen where small lobes entered the ocean.

4.2.9 Phase V Episode 2

The final episode of the 1730-36 eruption was centred in Montana Colorado, ~1 km further east of Montana de Las Nueces (Carracedo et al. 1992) and started with explosive fire fountain activity. A thin lava flow that travelled towards the north coast was produced during the latter stage of the eruption. Activity lasted ~16 days. By April 16th 1736, after almost 6 years of near-continuous volcanism, eruptive activity ceased on the island (Hernandez-Pacheco 1960).

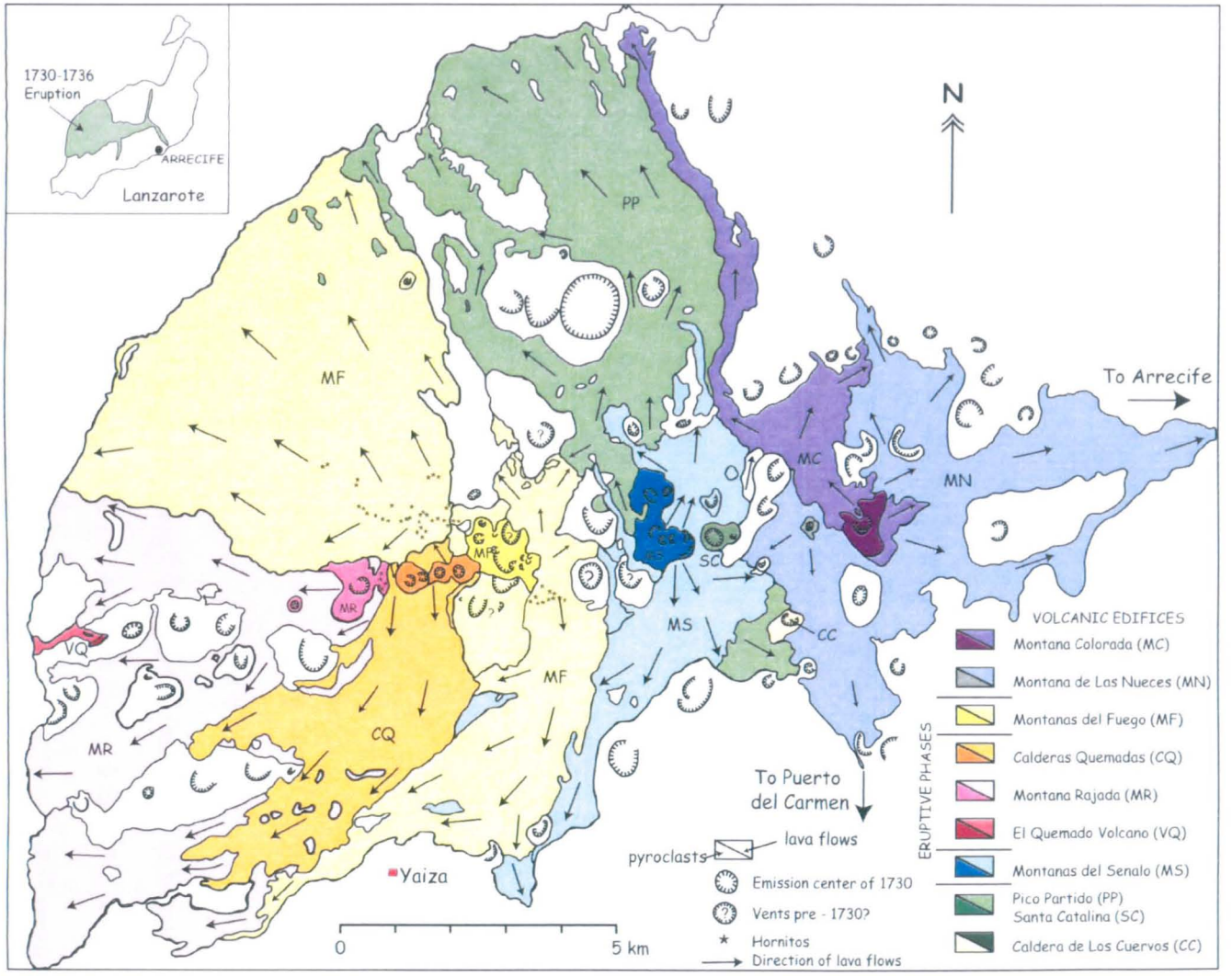

Figure 4.3 Simplified geological map of lava flows, pyroclasts and main eruptive vents of the five phases of the 1730-1736 Lanzarote eruption. Note the west-to-east trend of the activity. Actual extent of phase V episode 1 lava flows is shown in inset map, (adapted from Carracedo and Badiola 1991; Carracedo et al. 1992).

4.3 Field observations, deposit description, and interpretation

On Lanzarote, the high aridity has ensured that the 1730-36 lavas are reasonably well preserved. However fallout deposits have a poor preservation, especially in densely populated regions of the island. Due to the fertile nature of volcanic soils, most of the fallout has been reworked and ploughed over for agricultural purposes. Nevertheless there are proximal, near-vent locations where primary fallout sequences can be described and sampled. As stated, where possible, samples of both lava and fallout from all the major eruptive episodes were collected for analytical work during December 2003. We were unable to sample fallout from the later episodes (2 and 3) of phase III as the vents (and thus the majority of the proximal fallout) for these eruption episodes are located within the Timanfaya National Park; access within the park is restricted in order to preserve the park's natural state. In this section, I briefly describe the main eruptive features that formed during the 1730-36 eruption, with the descriptions and interpretations presented here based on new field observations.

4.3.1 Vent structures

The Lanzarote eruption has been classified as a typical basaltic fissure eruption (Carracedo et al. 1992). Walker (1999) described the 1730-36 fissure as a rift zone marked by parallel rows of elongate cinder cones or scattered vents lacking cone elongations or alignments. Volcanic activity was fed by dyke swarms, with the eruptive vents for all phases opening up along the E-W trending fracture system. Although the vent location is dominantly controlled by the main E-W volcano-tectonic fracture (Carracedo et al. 1992), emission centres within each phase are predominantly aligned in a NW-SE direction, reflecting the direction of vent propagation as the eruptive phase progressed (figure 4.6). The only

exceptions to this are phases III and V (vent propagation W-E). Vents are typically welded spatter cones, non-welded scoria cones, cinder cones or spatter ramparts (figure 4.4).

The volcanic features on the fissure vary in height. Spatter and scoria cones are typically the highest features ranging in height from 60 to 215 m, with the highest cones forming early on in the eruption sequence (during phases I and II), where the greatest magma discharge occurred (figure 4.4). Spatter cones and ramparts are the most common vent-type occurring on the fissure – spatter cones are smaller in height than the scoria cones – ranging in height from 40 to 150 m. Often spatter cones and ramparts can be found superimposed on scoria cones, producing larger spatter structures (e.g., Santa Catalina, Caldera de Los Cuervos).

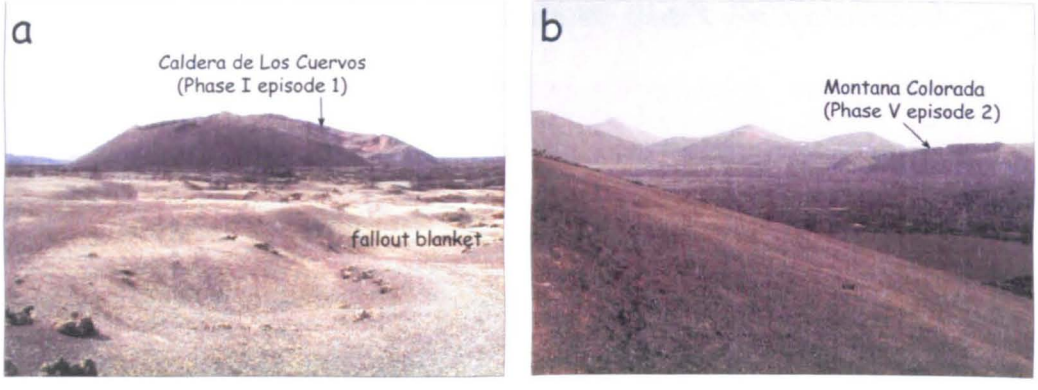

Figure 4.4 Photographs showing typical 1730-36 eruptive cones, photograph a is of the phase I episode 1 vent Caldera de Los Cuervos – a typical high scoria and spatter cone. Fallout blanket consists of fine scoria clasts and ash fallout. Photograph b shows Montana Colorada, eruptive vent for phase V episode 2 – one of the low-level cinder cones.

Each scoria cone is usually built up of a series of scoria fall layers, often capped by a thin layer of spatter (figure 4.5b). Cone walls are usually highest on the SW side, reflecting the prevailing wind direction (N to NE) during eruptive activity. The cinder cones in Lanzarote usually form smaller features on the fissure (20-60 m high) (e.g., Montana Colorada – Figure 4.4b); these cones are usually low-lying and composed of non-welded,

loose cinders and ash. Ash and cinder blankets are usually deposited asymmetrically around the vent (reflecting dominant wind conditions) and extend only for a few hundred metres from the base of the cones.

The spatter cones (e.g., Caldera de Los Cuervos) usually contain one or more vents, are generally circular and are constructed of partly welded, agglutinated reddish-brown spatter. Very little fines material is present within the immediate cone interior; however, the outer flanks of some spatter cones (e.g., Caldera de Los Cuervos) are blanketed with fine ash fallout. There is also a lack of vesicular or 'frothy' spatter material; however, dense spatter bombs litter the cone area – with some of these spatter rags and bombs up to 1 m in length. More typically, clast sizes range from 5 to 55 cm in length (clast long axis). Spatter clasts are crystal-poor (although in clasts from Caldera de Los Cuervos, Santa Catalina and Montana Senalo peridotite nodules are commonly found), dense, and reddish-brown in colour, signifying that these clasts were hot when they landed. Vent walls are covered with either layers of dense agglutinated spatter clasts (clast outlines difficult to see) (Figure 4.5d), or plastered with medium to coarse grained scoria clasts. Some spatter cones are breached, with the breached cone wall corresponding to the fissure propagation direction (e.g., SE wall at Montana del Senalo (figure 4.5e), N wall at Caldera de Los Cuervos). Around these breached cone sites, spatter-fed, coalesced lava flows are common, often containing large pieces of cone material rafted along with the lava; e.g., near-vent lava directly in front of Montana Senalo contains lots of intermingled welded air fall material – these are most likely rafts of collapsed cone material (Figure 4.5e). Cone walls are highly unstable and prone to slumping, generating concentric cracks and faults within the cone walls (Carracedo et al. 1992). Most spatter cones are steep walled, e.g., the Santa Catalina circular spatter cone (phase I episode 2), ~100-m high; on the western wall three rims are visible – these are annular spatter rings (Figure 4.7d), indicative of fluctuating fountain

heights, i.e. with high fire fountaining occurring followed by episodes of successively lower fountaining. Many of the spatter (and scoria) cone craters are floored with solidified lava ponds (e.g., Santa Catalina), and often show evidence of lava drainback – e.g., collapse pits and chaotic piles of lava crusts and sheet flows draped along the vent mouth (e.g., at Caldera de Los Cuervos). Lava drainback occurs as degassed magma returns to the sub-surface by flowing into open cracks, fissures or into the vent conduit. Drainback is especially common during late stages of eruptive episodes (e.g., on Kilauea, Mauna Loa, Hawaii), (Wolfe et al. 1987).

Spatter ramparts (e.g., Pico Partido) are usually composed of a complex series of nested spatter and cinder cones: e.g., the western end of Pico Partido consists of a cinder cone; however, elongate spatter ramparts extend out to the eastern side of this complex (Figure 4.5b). The immediate near-vent Pico Partido deposits are covered by the phase II proximal lavas; however, examination of the cone shows that it is dominantly composed of coarse spatter and cinders with little fines material – possibly indicating that fine ash and lapilli was transported to medial and distal areas and coarser material fell near-vent.

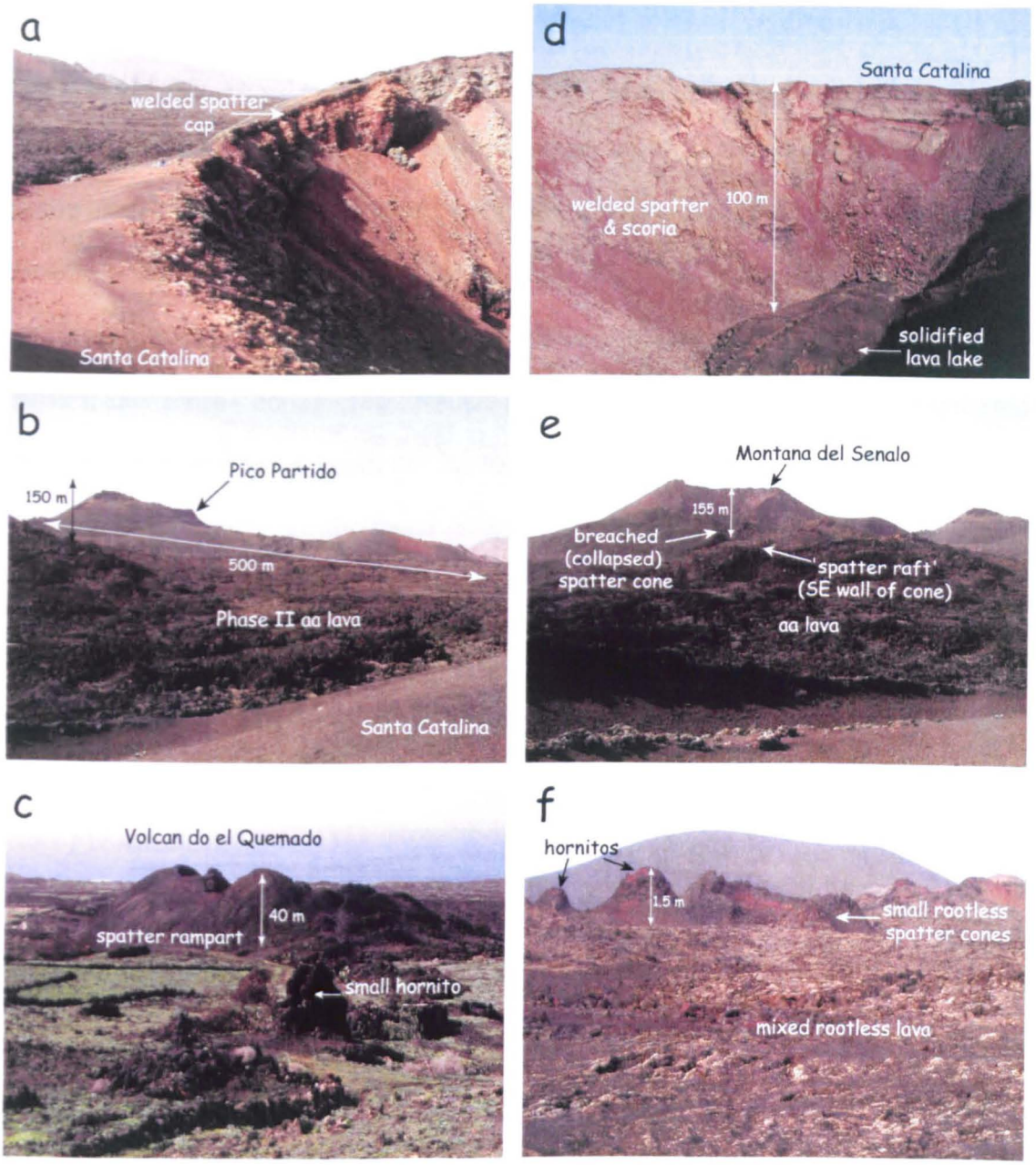

Figure 4.5 Photographs showing 1730-36 eruptive vent features (a) phase I episode 2 spatter cone – Santa Catalina showing typical steep walls and welded spatter cap, note small spatter bombs and blocks on crater rim, (b) Pico Partido (phase I episode 2) – elongate spatter and cinder cone, base of Santa Catalina cone can be seen in foreground, lava flow is phase II aa lava, (c) Volcan do el Quemado (phase III episode 1) – small spatter rampart, note hornito in foreground, (d) Interior of Santa Catalina – showing solidified lava pond, (e) Montana del Senalo (phase II) – breached spatter cone, (f) Phase IV rootless vents, hornitos and spatter cones – lava in foreground is a mix of aa and pahoehoe.

In addition to the main vent structures (spatter and scoria cones) lavas were also erupted from smaller rootless vents (figure 4.5f). During phase IV, following an initial explosive phase the style of activity changed – lavas emitted from a cluster of rootless shields and

hornitos (Carracedo et al. 1992). The hornitos or rootless spatter cones are small (~1-5 m high) and usually show a rounded shape, often with jagged rims. Hornitos commonly form over lava tubes; high lava flux rates through the tube can lead to breakouts of lava from points along the tube. If the lava has partially degassed then rootless shields – mounds of lava flows that build up forming elongate ridges tend to form. However, if the lava is relatively gas-rich then tube breakouts will be more explosive, leading to the formation of small spatter cones – hornitos (e.g., Heliker et al. 2004). The occurrence of hornitos during phase IV of the eruption suggests that the lava was volatile-rich at this time. Smaller hornitos (1-1.5 m high) are also found close to the phase I episode 2 and phase III episode 1 vents. The main phase V episode 2 cone (Montana Colorada) is also composed of rootless flows in addition to spatter, scoria and ash, and can be described as a low-level rootless lava shield.

4.3.2 Pyroclastic deposits

Based on the grain size and deposit characteristics, the initial explosive phases that characterized the start of each eruptive episode can be classified into two main types of fire-fountain-derived pyroclastic deposit. Fallout from phases I and II is typically medium to coarse grained Strombolian tephra, although certain episodes may also have exhibited Hawaiian style fountaining events. Fallout from phase III episode 1 is a classic Hawaiian style fall deposit, and material from phase V is Strombolian to Hawaiian tephra. It is difficult to assess in detail the character of the fallout from latter episodes of phase III and also from phase IV, as the main vents for these episodes are located within the national park; however, one would assume that they are either one or both of these fire-fountain style fallout deposits. Within deposits from phases I, III and V, minor layers of phreatomagmatic fallout can also be found.

The Strombolian tephra is a typical scoria fall deposit, dark brown to black in colour, clast supported and containing medium to coarse grained scoria lapilli with minor fines material. Scoria clasts range in size from 0.5 to 8 cm and are angular, glassy and moderately vesicular or 'frothy' in texture. The Strombolian fall deposits also contain abundant (~20-30 % of the clast population) *Pele's hair* and *Pele's tears*. Pele's hair is formed when molten droplets of magma are flung from the vent and 'spun' into long golden threads of glass. Particles can be carried tens of kilometres from the vent. Pele's tears are formed when small droplets of magma are quenched rapidly during flight forming dense, droplets or beads of shiny black glass. Pele's tears are typically spherical in shape and range from 0.3 to 1-cm in size. Occasional tears up to 3-4 cm in size have also been found. Large bundles of fine Pele's hair are also found near-vent in Lanzarote and also in more distal regions; here the strands are thicker and contain stretched vesicles parallel to the strand long axis. Fallout material from the initial episodes also contains abundant large disaggregated peridotite nodules. These nodules are fragments of mantle olivine xenoliths. Scoria clasts are often covered with a thin glassy coating (~1-2 mm thick) suggesting that these clasts fractured either within the column or upon impact with the ground (e.g., Thordarson and Self 1993).

Hawaiian fallout material is black in colour, coarse grained and consists mainly of small black cinders, small amounts of reddish-brown small spatter clasts, Pele's hair and tears, and brownish vesicular reticulite clasts with a small amount of medium to coarse grained fines material. The deposit is clast supported, shows normal grading and contains a moderate amount of lithic clasts. Lithics are usually angular in shape and consist mainly of fragmented peridotite nodules, and altered basaltic hyaloclastite material.

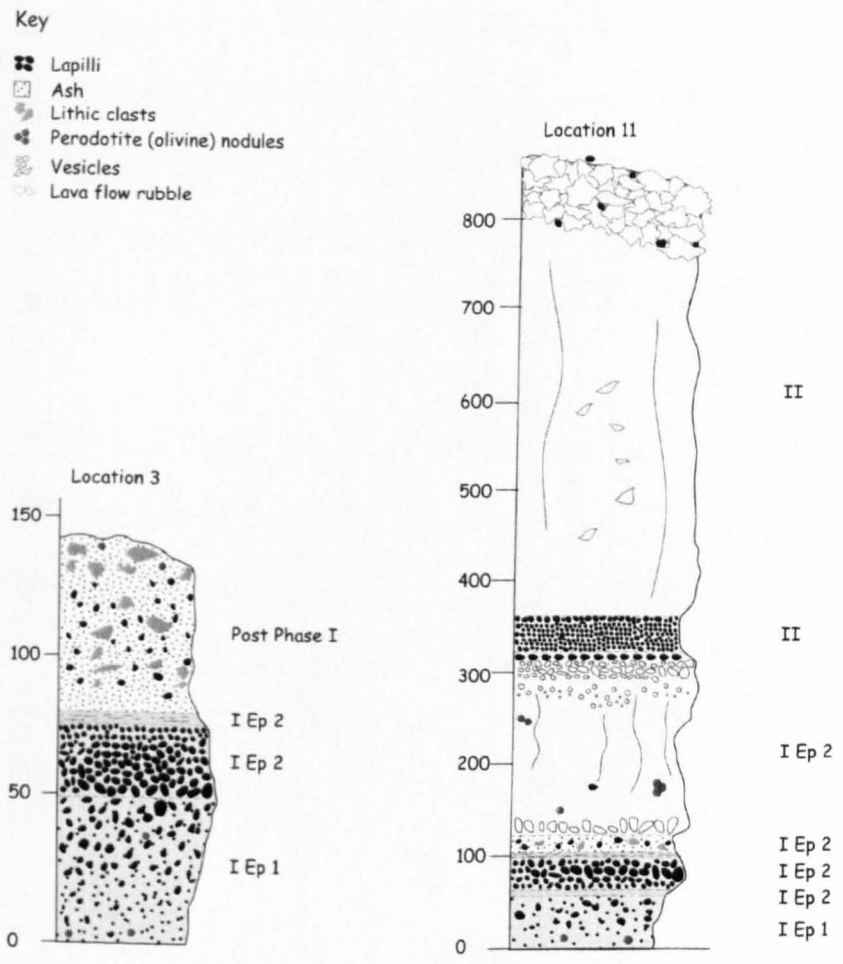

Figure 4.6 Stratigraphic sections through initial phases (I & II) of the Lanzarote eruption deposits. Section locations are marked on Figure 4.2. Height of section is measured on a centimetre scale. Location 3 section represents a primary fallout sequence for Phase I, location 11 section is a complete section representing fallout and lava flows from Phase I & II.

Associated with the phase I and phase III episode 1 fallout units is a thin ash layer. At locations 4, 11 and 15 this layer occurs beneath the main lapilli fall deposit. The contact between this ash layer and the overlying deposit is sharp. The ash is brown in colour, fine to medium grained and predominantly composed of small glassy shards. At locations 4 and 11 this ash layer is stratified and contains a small number of altered scoria lapilli fragments.

Spatter clasts tend to be agglutinated and welded in the early eruption episodes (II, 1; II) (e.g., Figure 4.7c); a higher degree of welding is also observed closer to the vent site. Welded clasts show a variety of clast shapes – occurring as *ribbon bombs*, *spatter rags*, *spindle bombs* and *cow pat* shape clasts. Large scoriaceous clasts are common in the later stages of eruptive activity - e.g., dense *breadcrust bombs* (non-vesicular bombs with a fractured surface) are found scattered around Montana Colorada (phase V episode 2).

All fall units vary in thickness from ~1 cm to 450 cm. Thick fallout blankets from the initial eruption episodes are observed near-vent (e.g., Figure 4.7e). The north and south sides of many of the older cones, together with occasional cone tops near the phase I and II vent areas, are covered with smooth blankets of unconsolidated tephra (Figure 4.7f). Smaller more localized fallout blankets covering older cones are also associated with the phase III eruptive cones.

4.3.3 Lava flows

Following the initial explosive activity that characterized the start of each eruption episode during the 1730-36 eruption, the eruptive activity became more effusive producing both 'a'ā and pahoehoe lava flows, together with some minor rubbly-topped pahoehoe lavas (Figure 4.8) (e.g., Guilbaud et al. 2005). During initial phases lava was dominantly 'a'ā, common during periods of high magma effusion with aa flows fed via fallback from high fire fountains, thus resulting in more viscous lava with a high yield strength owing to loss of heat and gas during fountaining (e.g., Sparks and Pinkerton 1978). However as the eruption progressed pahoehoe lavas began to dominate (late phase IV, phase V) forming via overspill of lava ponds at the base of smaller Hawaiian style fountains – emplacing long lava flows, >25 km in length (Solana et al. 2004), perhaps reflecting the change to more steady-state effusive activity as the eruption began to wane.

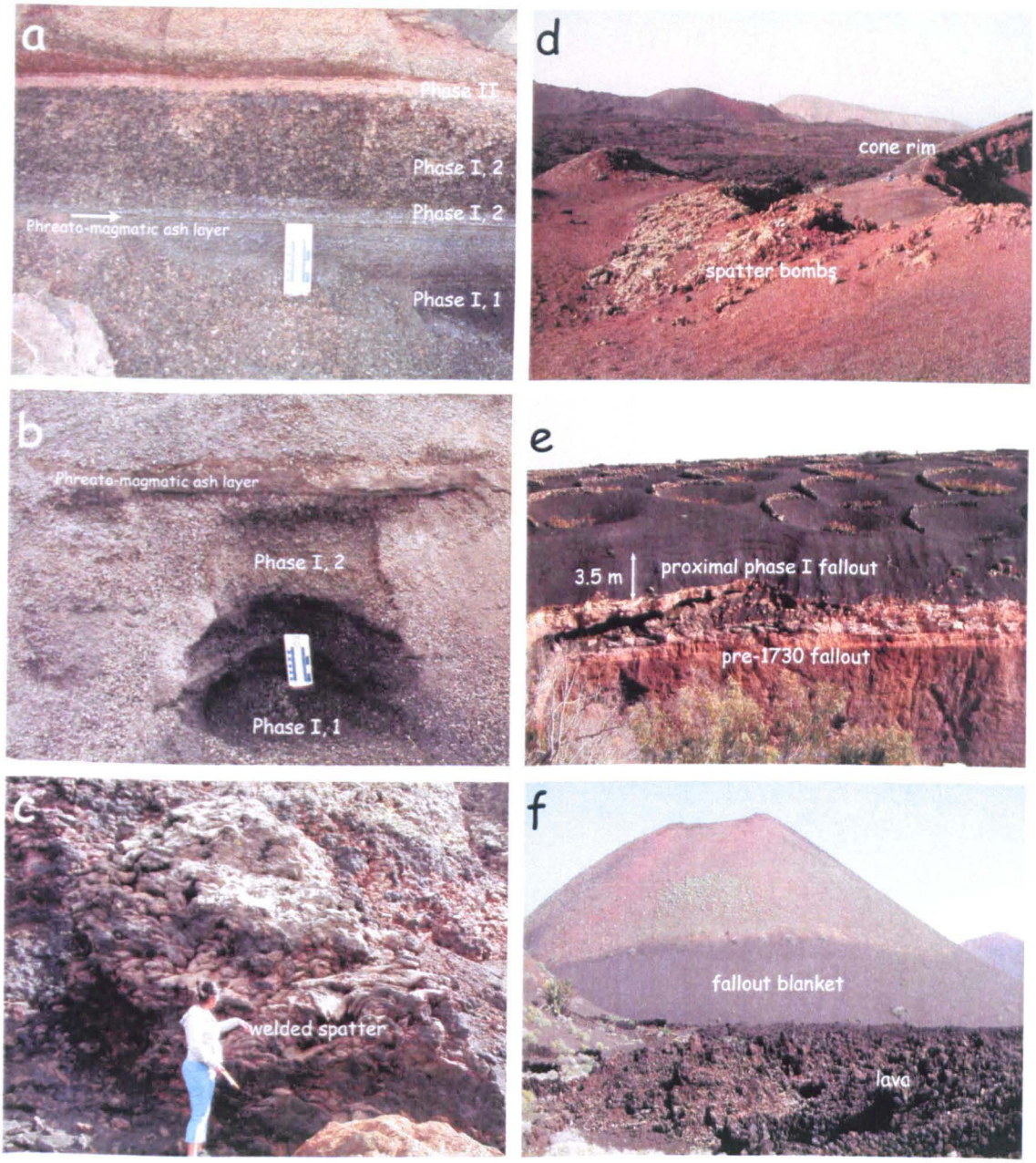

Figure 4.7 Photographs showing fallout deposits (a) section through proximal fallout units at location 11, (b) proximal fallout section at location 4, (c) interior of Caldera de los Cuervos (phase I episode 1) inside wall composed dominantly of large welded spatter clasts and rags, very little fines material present, (d) Spatter bombs on rim of Santa Catalina (phase I episode 2), note annular spatter ring (i.e. cone rim) just above spatter bomb text label, (e) phase I proximal fallout section 3.5-4 m thick ~3-8 km from vent, (f) older volcanic cone covered with 1730-36 fallout blanket (mostly fine ash and lapilli).

'A'ā lava flows are typical channelized flows with a spiny or rubbly surface and dense, poorly vesicular core; vesicles present are usually irregular in shape and often stretched. Often a layer of rubble can be found at the base of these flows, suggesting steep flow fronts: cooler clinker fragments roll down these steep fronts and are subsequently buried by the advancing flow, resulting in a rubbly basal layer. These lavas range in thickness from 3-4 m near-vent to 15-30 m in distal segments (e.g., Phase I episode 2 lavas are ~12-15 m thick at Tenasar on the north coast). Occasionally lavas are 30-55 m thick in coastal sections (e.g., Montana Rajada lava – phase III episode 2) and two to three units can be seen stacked on top of one another (Figure 4.8). The small phase III episode 1 'a'ā lava is, however, much thinner (maximum thickness 2-3 m at coast). The larger 'a'ā flows also contain large rafts of pahoehoe lava– these disrupted ropy pahoehoe crusts are likely to have formed from localized pahoehoe breakouts from either the flow front or from within the lava core. Accretionary lava balls (ALBs) are also commonly found within these channelized lavas – ALBs are roughly spherical masses that form on the surface of an 'a'ā flow – they range in diameter from a few tens of centimetres to several metres and grow when a small fragment of solidified lava rolls along the surface of an active flow and lava sticks or accretes to its surface; the balls continue to grow as more lava adheres to the surface. ALBs range in size from 0.5-8 m in Lanzarote, and are common in 'a'ā lavas from all of the eruption episodes (Figure 4.8f).

The 1730-36 pahoehoe lava flows in Lanzarote form typical inflated pahoehoe flow fields, very similar to the ones observed on Hawaiian volcanoes (e.g., Kilauea, Mauna Loa) (e.g., Self et al. 1998). Pahoehoe flows dominated the latter eruption stages (particularly phase V) although minor amounts of pahoehoe lavas were emplaced during the earlier phases – e.g., 12-15 m thick S-type pahoehoe lobes with basal pipe vesicles are common during phase I episode 2. Smaller pahoehoe lavas tend to show surface ropes and hummocky

surfaces. *Entrail* pahoehoe is common within the phase IV lava flow fields, associated with both the rootless cones and near the coast where lava has flowed down steep scarps prior to entering the ocean.

The main pahoehoe flows emplaced during phase V episode 1 (Montana de las Nueces) form typical pahoehoe sheet lavas. The Nueces lava flow field is the largest flow field that formed from a single source during the Lanzarote eruption (Solana et al. 2004). Three main branches or lava flows have been identified – Puerto del Carmen, Famara and Arrecife. The Arrecife branch is the largest of the three flows and extends for ~20-25 km from the vent; the Famara branch was not examined during this study (Carracedo et al. 1992). Carracedo et al. (1992) and Solana et al. (2004) (among others) state that the Puerto del Carmen branch extends for only a short distance from the vent area towards the south coast. However, more recent observations indicate that the Puerto del Carmen lava continues to the shoreline at Puerto del Carmen on the south coast (L. McArdell pers. comm. 2004); in agreement with the geological map of the island (Fuster 1969). Pahoehoe flows near-vent are characterized by spatter-fed lavas and small slabby pahoehoe flows. Shelly pahoehoe is also common; near-vent shelly pahoehoe is characterized by a fragile crust (1-2 cm thick) which breaks easily underfoot often revealing a hollow interior. Shelly pahoehoe tends to form from gas-rich lava. Note that there seems to be a complete absence of shelly pahoehoe in earlier eruption episodes. Medial to distal pahoehoe flows are classic tube-fed pahoehoe sheet flows, initially emplaced as small (20-70 cm thick) lobate flows that grow via an endogenous inflation process (e.g., Hon et al. 1994; Self et al. 1998). Inflation occurs as the initial lobe of the actively fed pahoehoe flow begins to crust over; beneath this viscous crust continued injection of new fresh lava into the still molten interior of the flow causes the upper crust to be lifted, crack and grow downwards as the flow thickens in situ (Hon et al. 1994). The

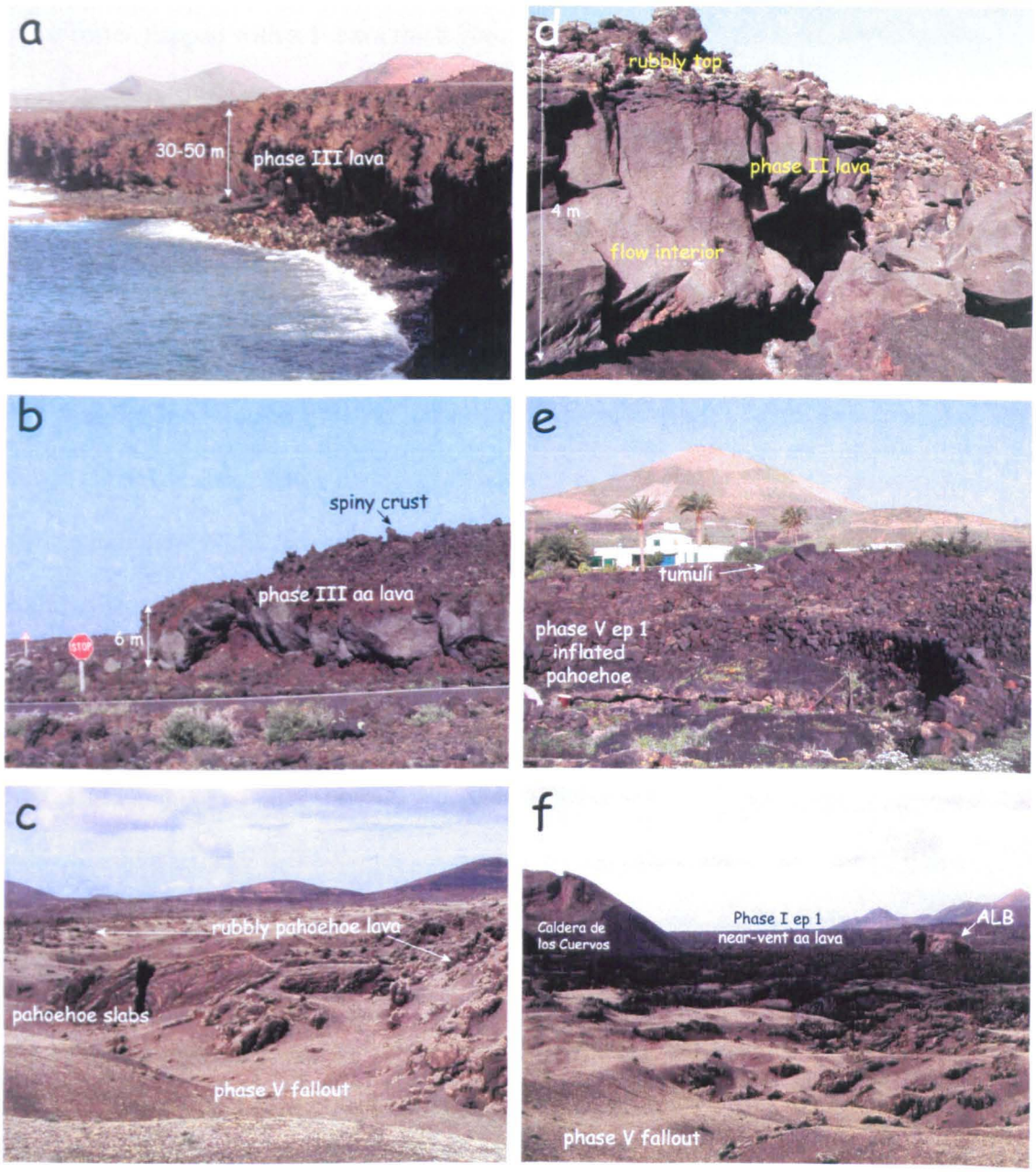

Figure 4.8 Photographs showing 1730-36 lava flows (a) coastal section through distal phase III 'a'ā lavas, (b) section through phase III distal 'a'ā lava showing classic 'a'ā features – spiny, rubbly top and dense, poorly vesicular core, (c) rubbly pahoehoe lava from phase I of the eruption, note large pahoehoe slabs with ropy surfaces in lava, also phase V proximal fallout on top of lava, (d) section through phase II 'a'ā lava, (e) inflated pahoehoe flow from phase V episode 1, lava is from Puerto del Carmen flow, note tumuli (pahoehoe inflation feature) in background, (f) phase I episode 1 near-vent lava, note large accretionary lava ball (ALB) in middle of 'a'ā lava.

Nueces lava shows many features indicative of emplacement via inflation – e.g., tumuli, lava rise pits. In cross section the lava flows show a typical 25-50 m thick vesicular upper crust (often capped with a 1-2 cm thick glassy selvage), a 60-90 cm thick dense, poorly vesicular core and a thin lower basal crust (10-15 cm thick). *Mega vesicles* or *bell vesicles* are also common within the core of the flow (e.g., Self et al. 1998). Overall pahoehoe flow thicknesses range between 20 and 80 cm for the smaller pahoehoe lobes to 2-12 m thick for the larger sheet flows and inflated lobes.

The thin finger of Nueces lava that extends to the coast at Puerto del Carmen is a tube-fed single pahoehoe sheet flow containing tumuli and smooth glassy surfaces (Figure 4.8e), although in parts of the flow rubbly pahoehoe is also found. Along parts of this flow tube-collapse features are common (e.g., skylights). Small channels of rubbly pahoehoe lava are also present within this flow signifying that the lava most likely filled small valleys: the transition to rubbly lava may occur as a result of lava flowing downslope into a valley (e.g., Guilbaud et al. 2005). Rubbly pahoehoe is a transitional lava type that contains a pahoehoe-like internal structure but a rubbly or clinkery flow top (Figure 4.8d-e); this lava type commonly occurs on the Laki 1783-84 lava field (Guilbaud et al. 2005).

4.3.4 Deposit interpretation

Based on the examination of the 1730-36 vent structures, pyroclastic deposits and lava flows, we conclude that this eruption was indeed a typical fissure style eruption characterized by Hawaiian and Strombolian explosive activity followed by more effusive activity that generated both 'a'ā and pahoehoe lava flows and some rubbly pahoehoe lavas. The presence of a fine-to medium-grained phreatomagmatic ash bed at the base of some of the explosive fountain deposit beds (e.g., phreatomagmatic basal layer beneath the phase I episode 2 lapilli fall deposit – Figure 4.7a) indicates that initial explosive activity at the

start of these episodes may have involved magma-groundwater interaction, possibly generating brief, intense sub-phreatoplinian explosive activity. The sharp contact between the ash layer and the overlying Strombolian lapilli fall deposit (Figure 4.7a) reflects a rapid change in the eruptive style as the influence of water decreased. The thin ash bed found beneath the phase III episode 1 Hawaiian fallout deposit may also have a similar origin, although due to the location of the phase III episode 1 vent it is possible that this bed may have formed as a result of either lava-seawater interaction or shallow submarine activity – detailed grain size studies are required to confirm this.

The main Strombolian and Hawaiian fallout deposits are exceptionally thick near source (3-4 m thick, at ~3-7 km from the vent) and thinner in medial to distal regions, although patchy preservation of some of the earlier units makes unit thicknesses difficult to confirm in these areas.

Changes in the thickness and distribution of fallout units with distance from the vent reflect differing transport and deposition modes. Near-vent (proximal) ejecta dominantly consists of coarse particles that have a limited distribution area (up to 2-3 km from source), dispersed via low altitude wind-influenced transport. The distal fallout is dominated by fine pyroclastic material with a wider dispersal area (>3-4 km from source), resulting from buoyancy-driven rise within the eruption column; this fine particle fraction is dispersed via high altitude winds (Thordarson et al. 1993). Fallout from the early, highly explosive phases of the Lanzarote eruption reflects these transport and dispersal patterns suggesting a powerful eruption – e.g., at Pico Partido (phase I episode 2) near-vent fallout consists of large blocks, spatter bombs and coarse lapilli, with fine ash and lapilli particles transported out to downwind distal areas (~5-8 km from Pico Partido). There is little fallout deposition upwind from the vent during these episodes.

In the latter eruption phases (IV, V) fallout is only locally distributed suggesting a decline in the intensity of explosive activity at this time. During phase V there was no fallout in medial and distal areas and fallout blankets were restricted to proximal areas (phase V episode 2 ash blanket extends for only 800 m from the base of the cone).

4.4 Volume estimates

The total magma volume erupted during the 1730-36 eruption is estimated using area-thickness data for the lava flows from each of the eruptive episodes. As initial activity produced a large fallout blanket we also calculate the tephra volume for phase I. Combining the above with published volume datasets for episode 1 of Phase V allows us to obtain a minimum erupted volume.

The areal extent of lava flows from each eruptive unit was reconstructed based on geological mapping (Carracedo et al. 1992), eyewitness accounts and my own field-based information. Lava flow volumes were calculated using this area data together with field measurements of primary flow thickness. Phase I fallout volumes were estimated by constructing crude isopach maps (figure 4.9) based on limited fallout thicknesses measured in the field and using the approximate distribution of pyroclasts at different stages of the eruption (deduced from eye-witness accounts) as shown in Carracedo et al. (1992) (dashed lines on figure 4.9). We suggest that these dashed lines representing the extent of lapilli fallout can be used to infer a maximum distribution area of the phase I fall units at different times during the activity. Fallout from phase I episode 1 is ~1-3.5-m-thick near-vent, is of limited distribution (extending out for ~1 km from the base of the cone), and is generally dispersed south west of the vent area, consistent with the NE prevailing trade wind

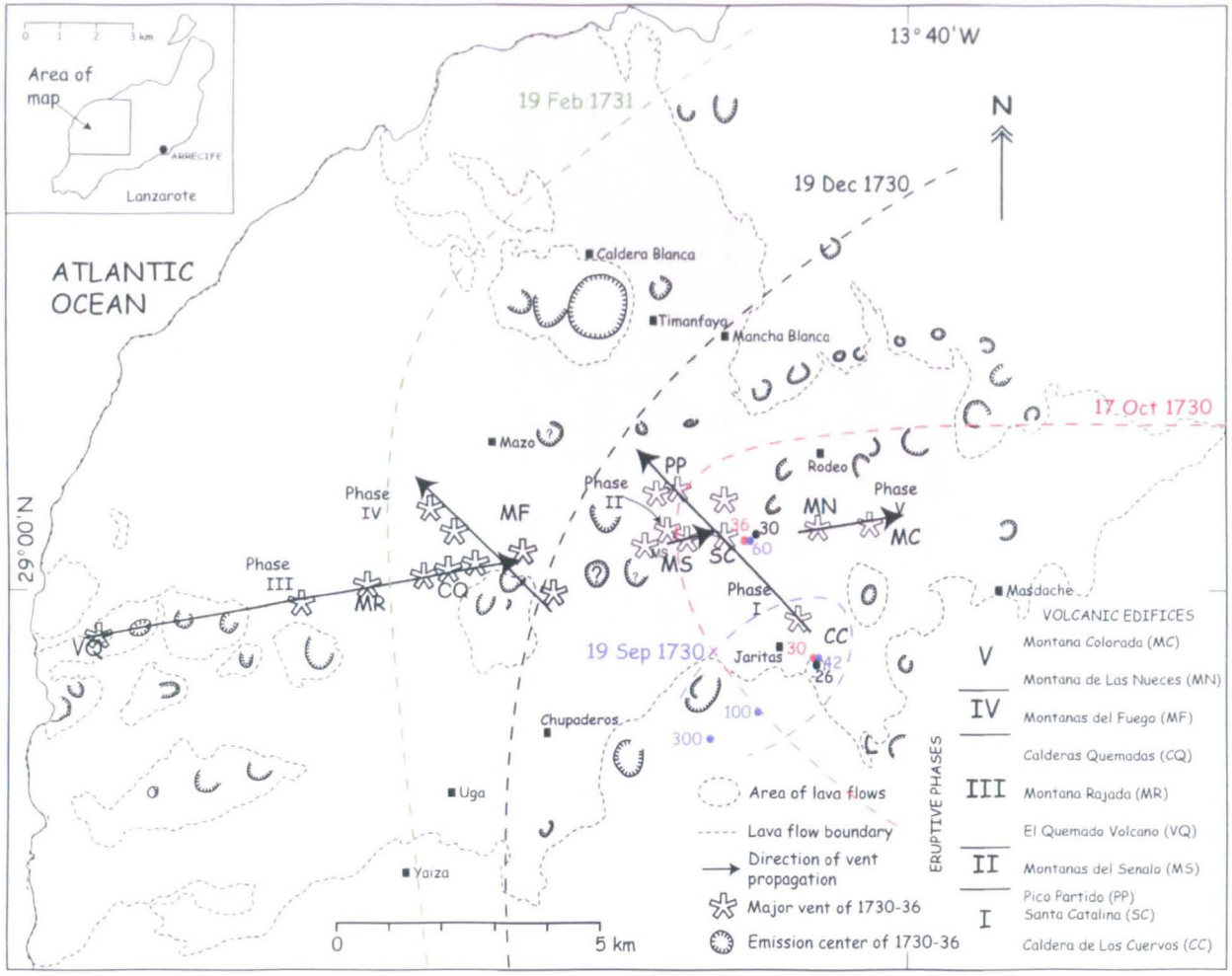

Figure 4.9 Simplified geological map showing the main eruptive centres of the Lanzarote eruption together with fallout thickness data measured in the field. Dashed lines represent maximum extent of lapilli fallout (deduced from eyewitness accounts) (after Carracedo et al. 1992). Thickness data is colour coded to correspond with these maximum distribution areas. Blue represents phase I episode 1, red phase I episode 2 (Santa Catalina phase), black and green represent phase I episode 2 (Pico Partido phase). Areas/towns affected by the 1730-36 eruption are also marked here for reference.

direction. Pyroclastic material from the second episode of phase I has a larger distribution area (figure 4.9) and is mainly dispersed to the E-ESE of the island.

Using the method of Pyle (1989), thickness versus area$^{1/2}$ plots were constructed (Figure 4.10). On such a plot, fallout unit thickness tends to follow a simple exponential thinning law with distance from the vent, producing one or more straight line segments on the diagram. The area under each of these segments can be integrated to yield a minimum bulk deposit volume (Pyle 1989, Fierstein and Nathanson 1992) – see Chapter 3 for further discussion on this technique. On $A^{1/2}$ versus thickness plots for both episodes of phase I (Figure 4.10), a single line segment can be recognised, the area under which is integrated to infinity to estimate a pyroclastic fall volume of ~ 0.06 km^3 (0.03 km^3 DRE, assuming a magma density of 2600 kg/m^3 and a bulk deposit density of 1100 kg/m^3) for episode 1 of phase I and 0.90 km^3 (0.40 km^3 DRE) for episode 2. Lava volumes range from 0.005 km^3 (for the smallest lava flows) to 1.68 km^3 (for the more voluminous early effusions of lava) (table 4.2). The volume of the eruptive cones is ~0.1 km^3, estimated using simple geometry (assuming cone volume is equal to $\frac{1}{3} \pi r^2 h$, where h = cone height, r = cone radius); most cones are ~50-200 m high and have diameters in the range 0.5 to 1.5 km. It is more difficult to estimate the volume of the spatter ramparts and smaller eruptive centres and their associated near-vent deposits; however we assume that their volume, like the total cone volume is trivial; therefore we choose not to consider it when calculating the volatile release budgets. The total volume erupted during the 1730-36 Lanzarote eruption is 5.32 ± 1.35 km^3 (Table 4.2). This estimate is in good agreement with the maximum eruption volume estimate (3-5 km^3) calculated by Carracedo et al. (1992). Based on these figures, more than 60% of the volume was erupted in the first 2 phases of activity (I & II) with most of the eruptive volume (>90%) produced before 1736 (Phase V).

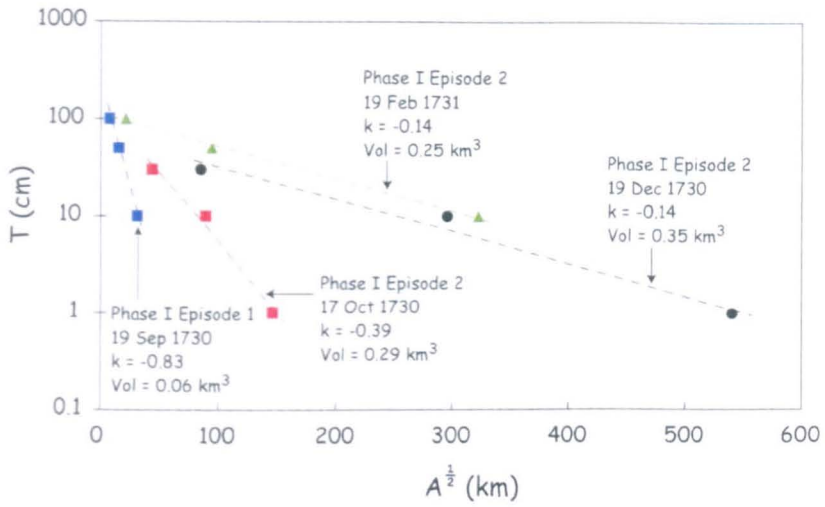

Figure 4.10 Thickness versus $A^{1/2}$ (following Pyle 1989: 1995). See Figure 4.9 caption for colour/symbol explanation. k = line slope.

The total bulk volume of the Lanzarote eruption (~5.23 km^3) must be considered a minimum estimate. As the majority of the lava flows entered the ocean one cannot estimate the offshore volume of lava. Although the fall deposits are well preserved close to the vent area, in the medial and distal regions the deposits have been extensively re-worked, and eroded, making it difficult to obtain accurate primary fallout thicknesses. To refine the fallout volume, more extensive field mapping is required.

Table 4.2 Summary of Lanzarote 1730-36 volume and area covered data for all eruptive episodes. Volume of all eruptive vents/cones is ~0.1 km^3 (see text for further explanation).

Phase [Episode]	Area covered (km^2)*	Volume (km^3) [Fallout volume (km^3)]†
I [1]	75.12	0.75 [0.06]
I [2]	88.28	1.68 [0.90]
II	26.33	0.20
III [1]	0.19	5.8×10^{-4}
III [2]	37.95	0.61
III [3]	26.33	0.29
IV	40.26	0.56
V [1]	~32[a]	0.14[a]
V [2]	6.35	0.03
Total volume		5.32

Fallout volumes

Phase	Date‡	Volume
I [1]	19 Sep 1730	0.06
I [2]	17 Oct 1730	0.29
I [2]	19 Dec 1730	0.35
I [2]	19 Feb 1731	0.25

Individual phase volumes

Phase	Volume	% Volume
I	3.39	63.7
II	0.20	3.8
III	0.90	16.9
IV	0.56	10.5
V	0.17	3.2
Cone volume	0.1	1.8

*Indicates area covered by lava flows (based on geological map of Carracedo and Badiola (1991))

†Fallout volumes calculated following the method of Pyle (1995) see text for explanation.

[a]Phase V episode 1 volume from Solana et al. (2004).

‡Date refers to dashed fallout distribution lines on figure 4.6

4.5 Lanzarote 1730-36 eruption dynamics

To fully quantify the sulphur release from the 1730-36 Lanzarote and make reasonable conclusions regarding the atmospheric impact of this event, we need to estimate the eruption intensive parameters (e.g., eruption rates, plume heights).

Volumetric discharge rates (VDR) (or eruption rates) were calculated by dividing the total volume of lava erupted during each episode by the total duration of each episode (e.g., Wadge 1981). Note that this method is dependent on accurate estimates of both the eruption duration and the volume of magma erupted. As explained in the previous section, all volume estimates for the Lanzarote eruption are considered to be minimum values, as it is difficult to constrain the true extent of the lava and tephra erupted. Historical accounts provide us with reasonably well-constrained eruption durations for phase I, part of phase II and episode 2 of phase V. The duration of phases III and IV are not so well known. Therefore caution must be applied when assessing the eruption dynamics of these phases: eruption rates and any subsequent parameters calculated based on this are crude estimates only.

Table 4.3 shows volumetric discharge rates calculated as described above. Rates vary considerably throughout the Lanzarote eruption, with peak rates reached in the early phases of activity. Volumetric discharge rates for episodes 1 and 2 of phase I are ~ 600 m^3/s (approximate mass eruption rate of 1.4×10^6 kg/s) and 250 m^3/s, respectively. During phase II, the average discharge rate decreases to ~ 50 m^3/s. In phases III and IV the rate is even lower with average VDR values ranging between 47 and 112 m^3/s (phase III) and ~10 m^3/s (phase IV). Volume eruption rates for phase V are on the order of 22 (episode 2) to 116 m^3/s (episode 1). Volumetric discharge rates calculated after the event represent an average rate that does not take into account potential variations in the lava flux; therefore

the above results probably underestimate the actual discharge rates. Nevertheless the volumetric discharge rate for phase I is approximately sixty times greater than the rates calculated for the current Pu'u 'O'o eruption in Hawaii (Heliker et al. 2003); however, these rates are still smaller than the peak effusion rate during the 1783 Laki eruption (Thordarson and Self 1993). Generally discharge rates derived for the less explosive eruption phases of the Lanzarote eruption are in good agreement with volumetric discharge rates measured at Kilauea – discharge rates of 30-490 m^3/s were measured during episodes 1 to 48 of the current Kilauea eruption (Rowland and Walker 1987) and rates between 45 and 139 m^3/s were estimated for the 1969-1971 Mauna Ulu eruption (Swanson 1973). Both these eruptions are typified by high fountaining activity, generating fountain-fed 'a'ā flows – probably very similar to the phases II to V of the Lanzarote eruption. Rowland and Walker (1987) also note that the formation of Hawaiian (Kilauea, Mauna Loa) pahoehoe lava flows is linked to low effusion rates (< 20 m^3/s), whereas higher effusion rates (> 20 m^3/s) are associated with 'a'ā lavas; however, long-duration lava flows tend to have lower effusion rates. This last point could well explain the low volume eruption rate (~10 m^3/s) calculated for phase IV (phase IV possibly continued for two years). Overall, the volumetric discharge rates estimated for the Lanzarote event reflect changing eruptive styles, with the explosive fire-fountaining activity sustained by high discharge rates; as the eruption progresses and more effusive lava flow activity begins to dominate VDR tends to decrease.

To refine the discharge rate estimates for the initial eruption phases where eruption duration is reasonably well constrained by the historical documentation, we calculate probable maximum volumetric discharge rates (VDR_{max}), based on the assumption that most of the magma may be erupted in a shorter period of time than that specified by historical reports. During the phase I episode 1 activity, it is conceivable that all of the

magma volume could have been extruded in the first 5-10 days of activity; if this were the case, then maximum volume eruption rates could be as high as 1560 m^3/s, closer to the peak eruption rate during the 1783 Laki eruption. During episode 2 of phase I, if one were to assume that the tephra volume was largely generated during the activity at Santa Catalina (a duration of 21 days), then values of VDR_{max} as high as 500 m^3/s are feasible. Assuming flow durations were shorter (~10 days) for phase II and episode 2 of phase V gives VDR_{max} values 2-3 times greater than the earlier estimated rates (Table 4.3).

Table 4.3 Summary of volume estimates, mass eruption rates and plume heights for all Lanzarote eruptive episodes.

Phase [Episode]	Volume (km^3) [Fallout volume (km^3)][1]	Volumetric discharge rate (m^3/s)[2]	Plume height (km)[3]
I [1]	0.75 [0.06]	586 [1560]	12-16
I [2]*	1.68 [0.90]	248 [496]	9-14
II	0.20	50 [170]	3
III [1]	5.8×10^{-4}	0.22	~0.3
III [2]	0.61	47	2.5
III [3]	0.29	112	4.5
IV	0.56	8.9	≤ 2
V [1]	0.14[a]	58-116	3-4.5
V [2]	0.03	23 [55]	≤ 3

[1]Bracketed values refer to fallout volumes.
[2]Volume eruption rate (VDR) calculated using eruption durations listed in Table 4.1. Bracketed values indicate VDR_{max} - see text for further discussion.
[3]Plume heights calculated using the Stothers et al. (1987) model.

Historical accounts (summarized in Table 4.1) report that the fire fountains from phase I of the eruption were seen from other Canary Islands, located ~90 km to the west of Lanzarote, suggesting that these early eruption fountains had to be at least 600-800 m high to be seen from the neighbouring islands. Wilson and Head (1981) suggest using eruption rates and initial volatile contents to estimate fountain heights in basaltic eruptions. The initial volatile contents of the phase I magmas are ~0.86 wt% for episode 1 and 0.6 for episode 2

(section 4.8.1). Using these figures together with the peak eruption rates shown in table 4.3, the estimated peak fountain heights range between 1100 m and 1500 m for episode 1, and between 600 m and 1000 m for episode 2. Both estimates are consistent with historical observations and with field observations of the cone heights (cone heights up to 200 m high).

The height of the convecting column above the fire fountains is calculated using the model of Stothers et al. (1986). Observational estimates of the convective plume height above fire fountains in the 1984 Mauna Loa eruption and the 1961 Askja eruption are in good agreement with theoretical predictions of column height using the Stothers model (Stothers et al. 1986; Thordarson and Self 1993). Using the magma discharge rates calculated here (peak VDR in table 4.3), and assuming a fines (i.e. particles < 1 mm in size) content of 20% and ΔT_f of 50 °C (temperature decrease of clasts while in the fountain), convective plume heights for the initial phases of the eruption range from 9-13 km (dry atmosphere) or 12-16 km (moist atmosphere). At the latitude of Lanzarote (~29°N) these eruption plumes reached upper tropospheric to lower stratospheric levels. Applying the same technique to phase II and the latter phases of the eruption (phases III to V), column heights range from 3-6 km in phase II, and between ~0.3 to 4.5 km in phases III, IV and V (table 4.3), and were thus largely confined to the mid-upper troposphere. Note that the height estimates for the latter phases of the eruption (especially phases III and IV) can only be used as a very rough guide, due to the uncertainties associated with the discharge rate calculation. The fire fountain heights and plume heights generated during the high-intensity phase I explosive activity are very similar in magnitude to the fire fountains exhibited during the main explosive phase of the Izu-Oshima eruption in Japan. During this eruption fire fountains ~1500 to 1600 m in height were observed, and eruption plumes above the fountains were ~16 km high (Sumner 1998). High, intense fountaining activity

coupled with the generation of upper tropospheric-lower stratospheric eruption columns (e.g., as in phase I of the eruption) allow for the efficient transport of large quantities of volcanic ash and gas to upper atmospheric levels.

The eruption rate and magma mass can also be used to characterize the magnitude and eruptive power of a volcanic event (Pyle 2000) as described in chapter 3. Based on the total volume erupted, the overall magnitude index for the 1730-36 Lanzarote eruption is ~6.1. The eruption intensity index is ~9.5, calculated using the maximum peak mass eruption rates (0.3×10^7 kg/s). Based on these parameters, the Lanzarote eruption is similar in magnitude to the 1783-84 Laki eruption (Laki magnitude index ~6.5). The peak intensity index of the Lanzarote eruption is however smaller than the intensity calculated for Laki (~10.4), but has a similar value to the Mauna Loa 1950 (~9.8) and the Sakurajima 1914 (~9.7) peak intensities.

Pyle (2000) also defines a destructiveness index to assess the destructive power of a volcanic event. The destructiveness index can be defined as the logarithm of the total area affected by lava, lahars, pyroclastic flows and surges and tephra fall accumulations of more than 100 kg/m^2. Although this index does not take into account eruption style and duration, magma volume, or volcano location, it can be used to compare the destructiveness of different types of volcanic eruption (Pyle 2000). Based on the total area covered by lava during the 1730-36 Lanzarote event (~333 km^2), the destructiveness index for this event is ~2.5. For comparison the 1783-84 Laki eruption has a destructiveness index of ~2.8.

4.6 Petrology and Major Element Chemistry

With the aim of analysing glass inclusions in phenocrysts and matrix glasses so as to measure the pre-eruptive and degassed sulphur content and thus estimate the syn-eruptive sulphur loss, we collected samples representing all of the main eruptive episodes of the 1730-36 Lanzarote eruption from various locations across the island. Where possible, lava flows were sampled in both proximal and distal parts of the flow field, and fallout material was collected from proximal vent regions. Sample locations are summarized in Appendix C1 and Figure 4.2. In this section we outline the petrology and major element chemistry of glass inclusions, matrix glasses, and minerals.

Published whole-rock chemical analyses of the 1730-36 Lanzarote lavas (Thomas et al. 1999; Lundstrom et al. 2003) reveal that the bulk composition changed during the course of the eruption, with alkali basalts erupting at the start of the eruption and olivine tholeiites extruded during the latter stages of activity. The lavas have high Mg-numbers (Mg# = Mg/Mg + Fe_t, with Fe_t = total Fe) >50 and contain xenoliths of mantle-derived spinel peridotites (Carracedo et al. 1994). Thomas et al. (1999) argue that the range of magma compositions reflect different degrees of partial melting, with the later tholeiitic magmas being the product of the highest degrees of partial melting. As this study is aimed at estimating the sulphur budgets of the Lanzarote magmas, further petrogenetic modelling and discussion is beyond the scope of this thesis. Whole-rock XRF data from Thomas et al. (1999) and from Lundstrom et al. (2003) are used here to compare with new glass chemistry data; however, it is often difficult to match some of the published whole-rock data to a particular eruption episode.

Major element and volatile (S, Cl, F) glass composition data were obtained using a Cameca SX-100 wavelength dispersive electron microprobe; the full analytical setup is described in chapters 2 and 3. Samples were sieved and picked to obtain crystal separates and glass chips which were then mounted into epoxy resin blocks and polished to expose clean surfaces. We show data here with a 1σ error – based on replicate analyses of two glass standards (VG-2 - MORB glass from Juan de Fuca Ridge and KBT-1G – alkali basalt glass from Knippa, Texas - appendix A7).

Where possible, clean, crystal-free areas of matrix glass were selected for analysis; however, in the distal lava samples where the groundmass is dominantly semi-crystalline care was taken to select interstitial matrix glass. For glass inclusion analyses, clean, vesicle-free inclusions with no cracks or small fractures were selected. Glass inclusions occur in the rims and cores of olivine crystals, and range in size from 20 μm to 100 μm. Occasional inclusions ~140-160 μm in size were also found. Inclusions are typically near-spherical, oval, or sub-rectangular in shape; however, a few more irregular shaped inclusions are also present. Inclusions are mostly located in the centre of the crystal, however some inclusions can also be found close to the crystal rims. Daughter crystals are absent in all inclusions. Host olivine crystals were also analysed to check mineral and melt equilibrium and also to ensure that analysed olivine crystals were not xenocrystic.

4.6.1 Glass chemistry

The Lanzarote lavas and tephras exhibit variable glass compositions, as demonstrated on the total alkalis ($Na_2O + K_2O$)-silica diagram (Figure 4.11). Glass inclusion and matrix glass compositions show a bimodal distribution – basanites and alkali olivine basalts (SiO_2 ~ 43-45 wt%) form one group with the second group exhibiting more tholeiitic basalt compositions (SiO_2 ~ 47-50 wt%), (Figure 4.11); magnesium numbers (Mg#) range from

30 to 39. SiO_2 contents increase as the eruption progresses, with the earlier eruptive episodes (Phase I) showing the lowest SiO_2 contents. However the last episode in Phase V shows a return to low SiO_2 basalt compositions. Matrix glass and glass inclusion compositions are shown in Appendix C and Figures 4.11, 4.12. Matrix glasses and glass inclusions for all phases overlap in major element composition (Figure 4.11, 4.12), suggesting that the inclusion composition was not significantly modified following entrapment. This is consistent with back-scatter images (Figure 4.15) of olivine crystals which show clear, un-altered rims around the inclusions suggesting that no modification has occurred.

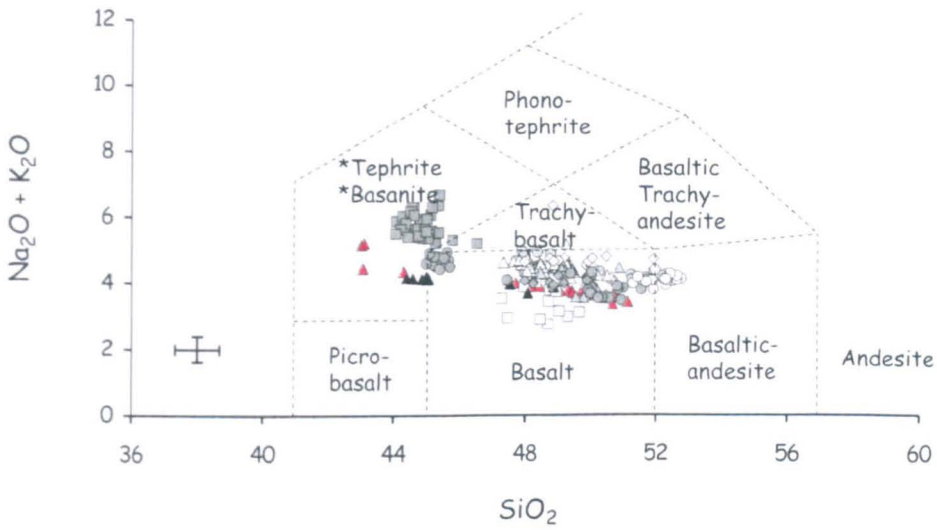

Figure 4.11 Total alkalis ($Na_2O + K_2O$) versus SiO_2 diagram for all glass analyses from Lanzarote eruption episodes. Classification fields defined by Le Bas et al. (1986), *tephrite = modal olivine <10%, *basanite = modal olivine >10%. Grey squares = Phase I Episode 1, white squares = Phase I Episode 2, grey circles = Phase II, white triangles = Phase III Episode 1, black triangles = Phase III Episode 1, grey triangles = Phase III Episode 3, white diamonds = Phase IV, grey diamonds = Phase IV lava, white circles = Phase V Episode 1, grey circles = Phase V Episode 2. Red triangles denote whole-rock XRF data. 2σ error bar shown for reference.

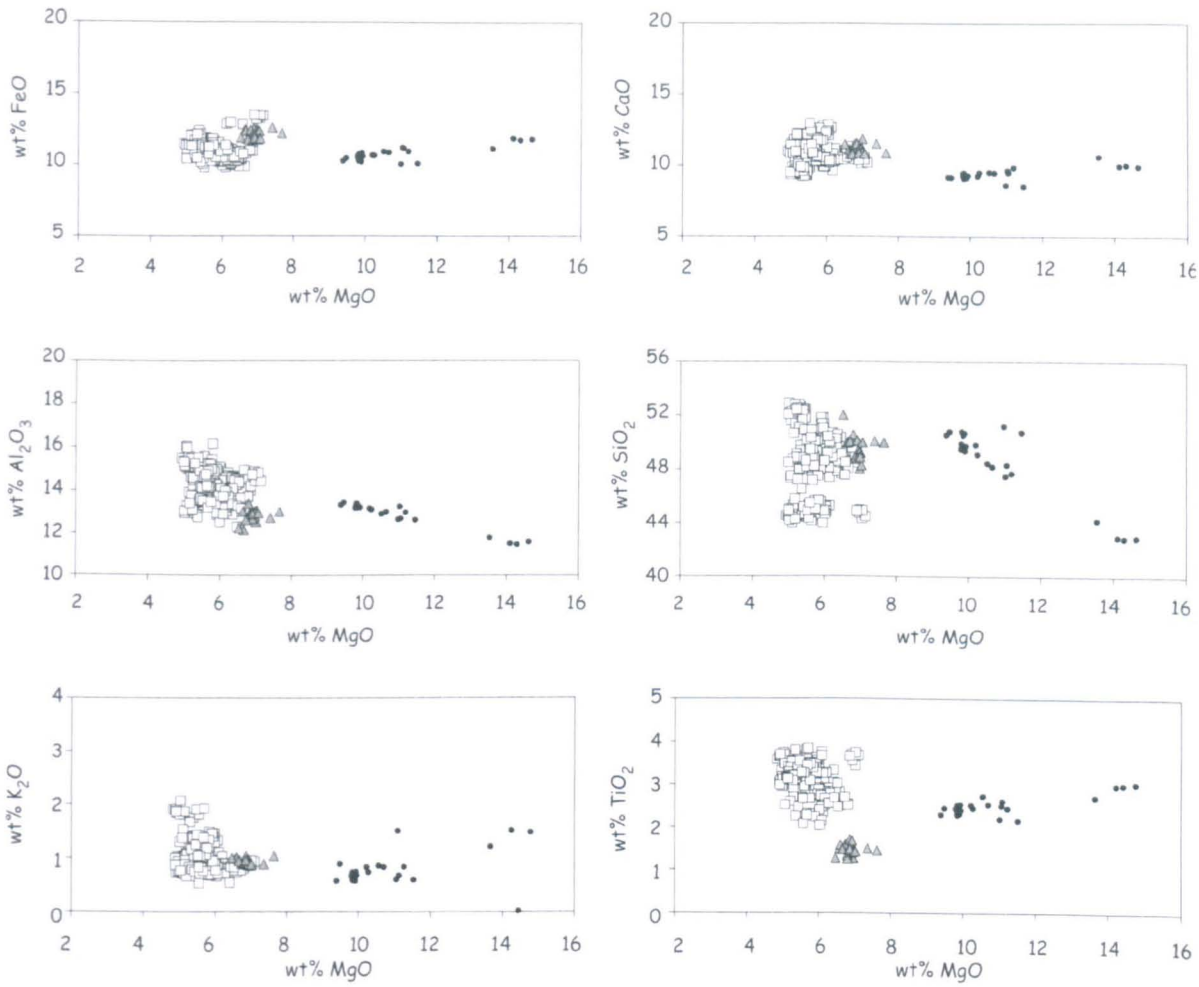

Figure 4.12 MgO variation diagrams showing matrix glass and glass inclusion compositions for all Lanzarote 1730-36 eruption episodes. Black circles represent whole-rocks (data from Thomas et al. 1999 and Lundstrom et al. 2003). Grey triangles denote glasses from the phase IV lava sample, on all diagrams this sample plots outside of the main Lanzarote glass compositional range.

Glass from the Phase IV eruptive episode exhibits compositional differences when compared with the other eruptive phases and also when compared with a Phase IV fallout sample (Figure 4.12, 4.13). The lava sample shows the highest MgO and has significantly lower TiO_2 (<2 wt%) and higher FeO contents when compared with the rest of the eruptive units. These compositional differences may possibly reflect the steady state eruptive activity that was occurring during Phase IV. Carracedo et al. (1992) suggest that Phase IV possibly lasted up to two years, with more effusive lava flow activity dominating. It is conceivable, that during this continuous eruption episode, source magma compositions

changed slightly, with these subtle differences large enough to alter the lava glass composition.

The glass composition varies considerably when compared with the whole-rock bulk composition, with glasses showing lower MgO contents (4.8 to 7.2 wt%), and slightly higher TiO_2 and Al_2O_3 contents (> 3wt% and > 13.5 wt%, respectively). This striking difference may be attributed to the fact that the bulk whole-rock composition represents a mixture of glass and main mineral phases (in this case olivine and spinel) (Figure 4.14).

The difference between the primitive melt composition (whole-rock data) and the erupted melt composition (glass data) needs to be considered as it may also have some bearing on the sulphur evolution of the melt. The difference between these compositions could result from fractionation of the melt, e.g., the difference between primitive melt MgO (~ 14 wt%) and the matrix glass (~ 5 wt% MgO) could equate to ~ 30-40 % melt fractionation. This degree of fractionation will concentrate incompatible elements such as S in the melt (e.g., if the original pre-eruptive S content is 1000 ppm; 20 to 40% fractionation would increase the S content to ~ 1250 to 1600 ppm). Therefore, in the Lanzarote magmas it may be possible to increase the pre-eruptive melt sulphur content in this way. This process has obvious implications for the amount of SO_2 released upon eruption: a S-enriched melt has a high SO_2 release potential.

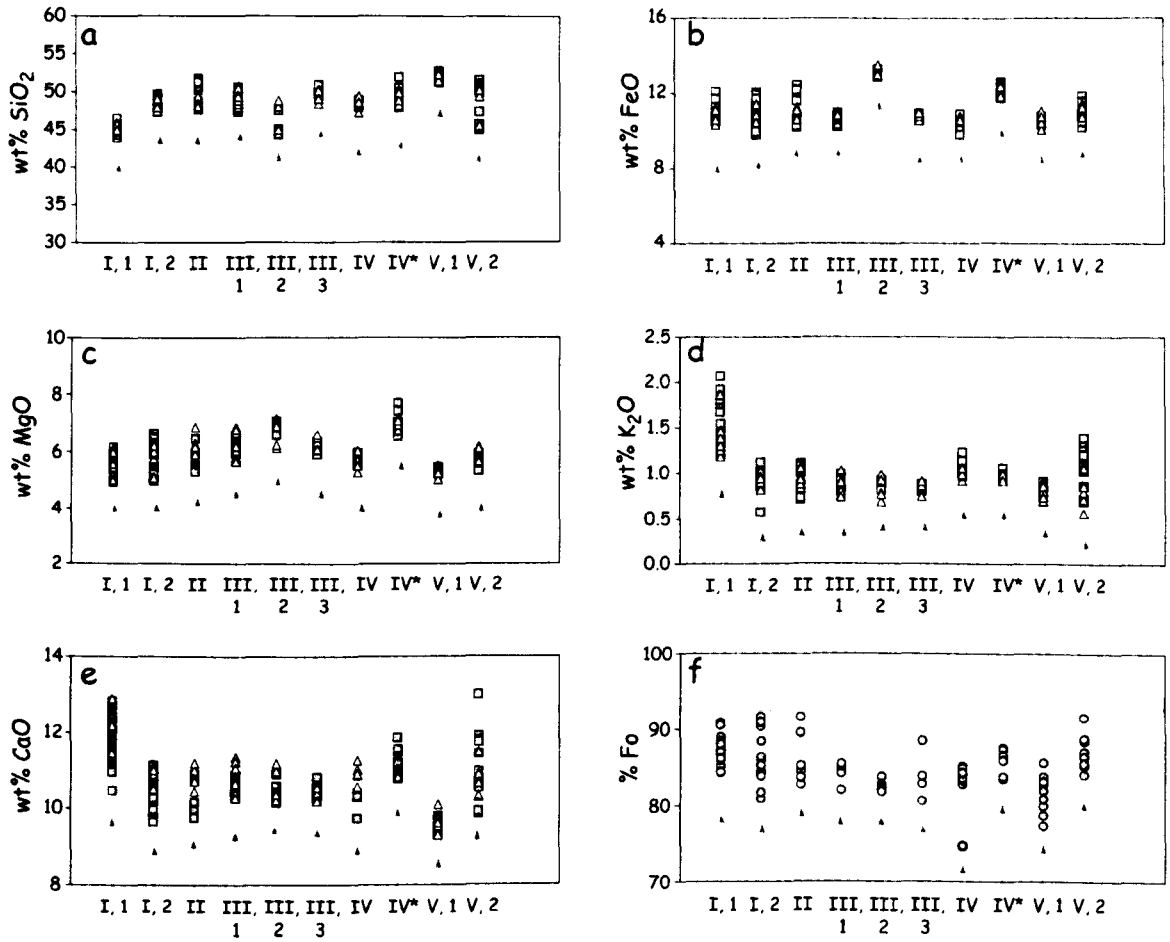

Figure 4.13 Selected major element glass chemistry (SiO_2, FeO, MgO, K_2O, CaO) versus Lanzarote 1730-36 eruption episodes. In figures (a) to (e) grey squares represent matrix glasses and white triangles denote glass inclusions. Figure (f) shows olivine forsterite content for each episode, grey band in (f) marks xenolith (mantle) olivine composition. IV* indicates phase IV lava sample. Analytical error is approximately symbol size.

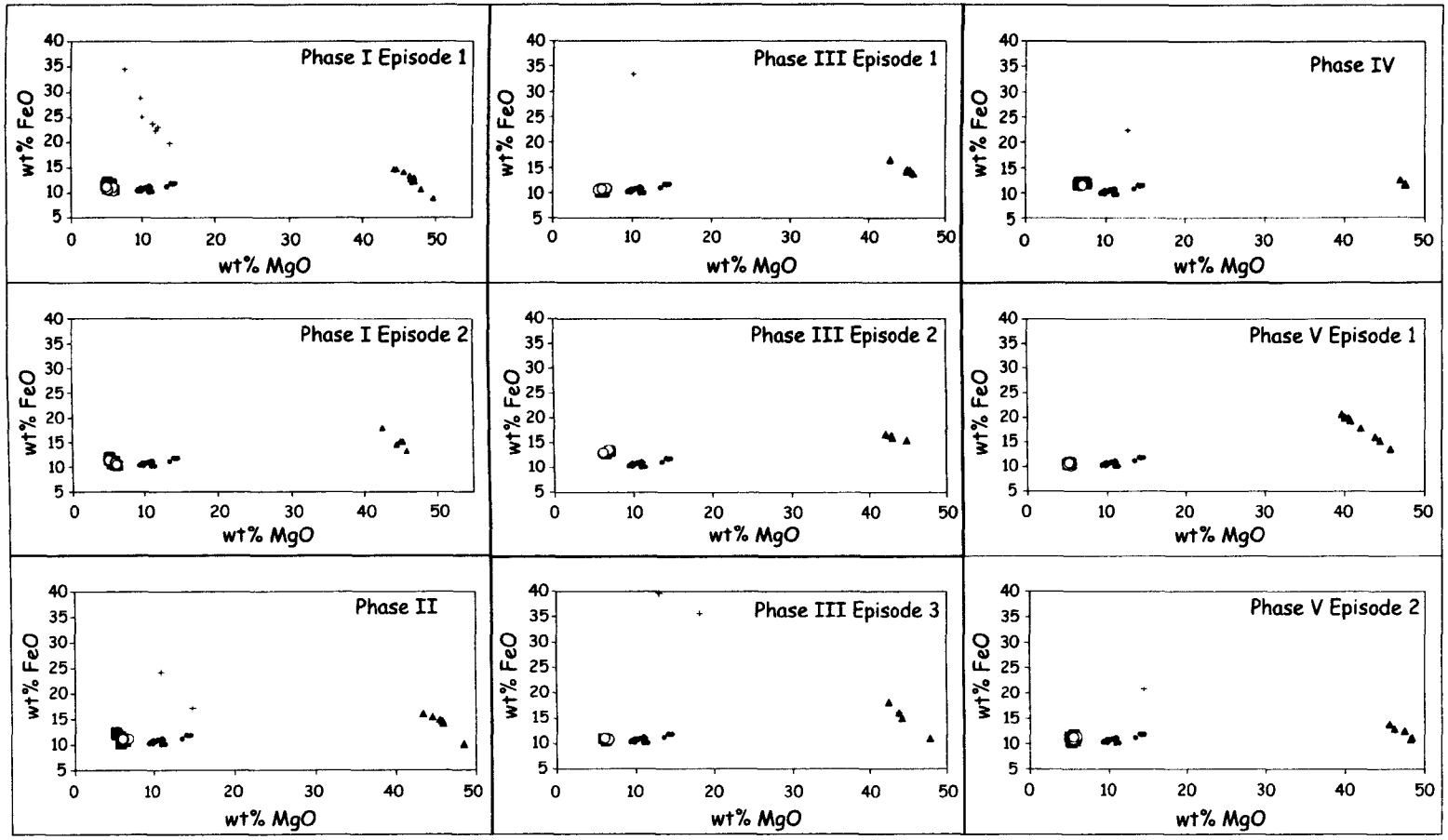

Figure 4.14 MgO versus FeO variation diagrams for each eruptive episode. On each diagram matrix glasses and inclusions (white circles and black squares), olivines (black triangles), cr-spinels (crosses), and whole-rock data (back circles) are shown. Diagrams show that the whole-rock data represents a mixture between glass, olivine and cr-spinel, thus accounting for the differences between the bulk whole-rock composition and the glass composition.

4.6.2 Petrography and Mineral Chemistry

The Lanzarote tephra samples contain ~2-5 % phenocrysts set in a glassy (hypo-hyaline) matrix, whereas the lava samples have slightly higher phenocryst contents (~3-7 %) set in a glassy to semi-crystalline (hypo-crystalline) matrix. Occasional samples from the early eruption phases are also sparsely porphyritic (<2 % crystals). The mineral assemblage consists of olivine and clinopyroxene with minor amounts of plagioclase feldspar and Fe-Ti oxides. Olivine is the most abundant phenocryst phase in the 1730-36 magma; crystals are typically 0.1 to 0.6 mm in size and show a subhedral to euhedral morphology (Figure 4.15). Most crystals contain glass and chromium spinel (Cr-spinel) inclusions. Most glass inclusions are located in the centre of the olivine crystals. Olivine compositions vary from Fo_{80} to Fo_{90} with the majority of crystals showing forsterite values of Fo_{82-86}; however, a small amount of olivine crystals from phase V episode 1 have forsterite values as low as Fo_{77-79}. Olivine crystals from all eruptive episodes are commonly unzoned and show little difference between core and rim compositions. Spinel occurs mainly as small (<0.05 mm) inclusions in olivine crystals. The inclusions are mainly located in the centre of the crystals however some are also found in crystal rims (Figure 4.15c). Spinel compositions typically have Mg# ($Mg/(Mg + Fe^{2+})$) values between 0.35 and 0.8 and Cr# ($Cr/(Cr+Al)$) values in the range 0.35-0.77 (Figure 4.16). Plagioclase feldspar occurs as small (<0.05 mm) lath-like microlite crystals in samples from all eruptive units; average feldspar composition is $Ab_{41.3}An_{55.9}Or_{2.8}$. Clinopyroxene (average composition $En_{40.9}Fs_{10.8}Wo_{48.3}$) exists mainly as a groundmass phase. Minor amounts of Fe-Ti oxides are also present in samples from all phases except phase V; oxides are mainly microlite size crystals of magnetite.

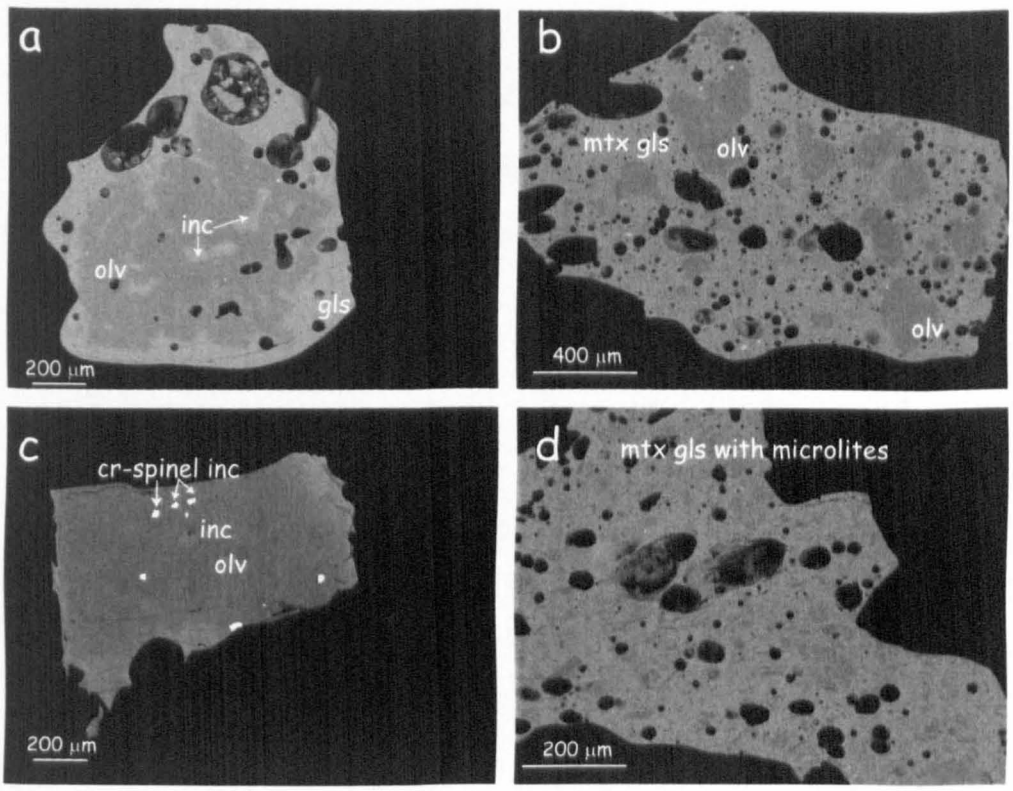

Figure 4.15 Back-scatter electron (BSE) images of Lanzarote matrix glasses and crystals. Figures (a) and (c) show olivine crystals with both glass and cr-spinel inclusions. Pictures (b) and (d) show matrix glass shards from both glassy scoria (b) and glassy lava rinds (d). Note that in picture (d) matrix glass from the lava selvage (rind) has a larger microlite crystallinity when compared to the scoria glass.

4.6.3 Xenolith Chemistry

Xenoliths found within the 1730-36 ejecta consist mainly of olivine with some minor orthopyroxene and spinel. Xenolith crystals exhibit euhedral morphologies and often occur as glomerocrystic aggregates – where olivine and pyroxene are intergrown with one another. Spinel is found as both inclusions and as scattered, fine grained crystals. Occasional olivine crystals also contain small bubbles and melt inclusions. Based on mineralogy xenoliths have been sub-divided into two groups - spinel harzburgites and spinel dunites (Thomas et al. 1999; Neumann et al. 2004). To discriminate magmatic olivine from xenolith (mantle) olivine we use the classification of Burton et al. (2002). In that study, which includes xenolith olivine from Gran Canaria, mantle olivines are distinguished on the basis of high forsterite contents (Fo_{91} – Fo_{96}) and low Ca contents

(<0.01 wt% CaO). We analysed selected olivine xenocrysts from the mantle xenolith sample (sample L1-2P-2) of Thomas et al. (1999). These crystals show extremely high forsterite (Fo_{91} – Fo_{95}) and low Ca contents (<0.02 wt %) when compared with corresponding magmatic olivines (Figure 4.16).

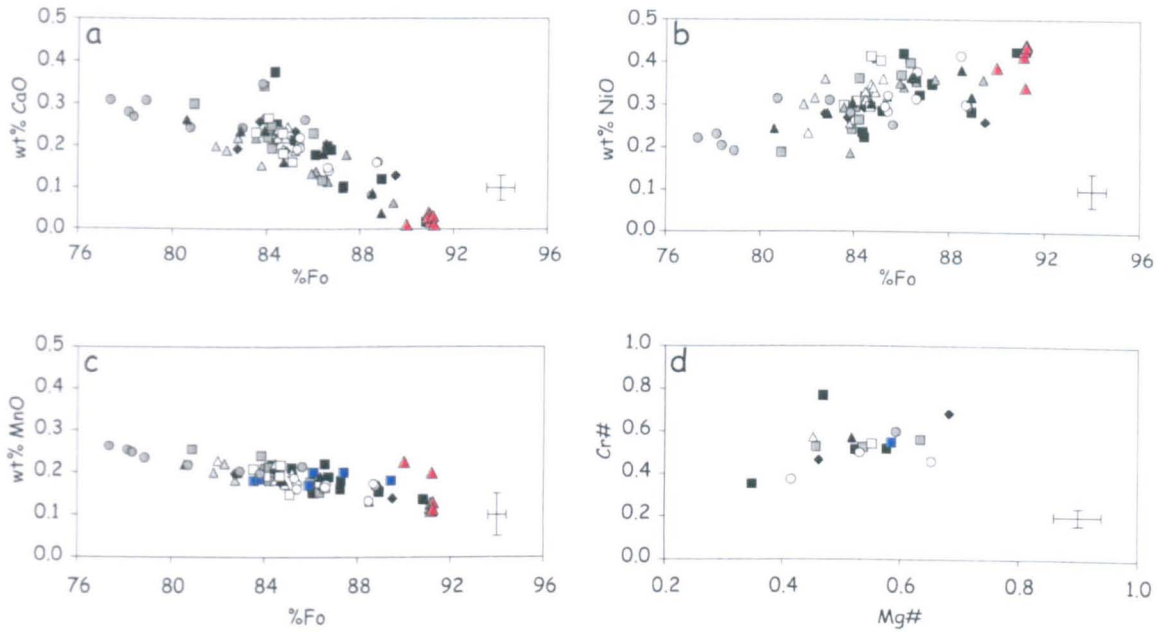

Figure 4.16 Olivine forsterite composition (%Fo) versus corresponding CaO (a), NiO (b) and MnO (c) content. Red triangles in figures (a) to (c) denote compositionally distinct olivine mantle xenolith analyses for comparison. Figure (d) shows olivine-hosted spinel inclusions, in this diagram Mg# = ($Mg^{2+}/Mg^{2+} + Fe^{2+}$) and Cr# = ($Cr^{3+}/Cr^{3+} + Al^{3+}$). In all plots colours and symbols represent each of the eruptive episodes, with black squares = phase I episode 1, grey squares = phase I episode 2, black diamonds = phase II, white triangles = phase III episode 1, grey triangles = phase III episode 2, black triangles = phase III episode 3, white squares = phase IV, blue squares = phase IV lava, grey circles = phase V episode 1, white circles = phase V episode 2. 1σ error bar shown for reference (errors based on electron microprobe mineral standard reproducibility error).

4.7 Magmatic Intensive Parameters

As the solubility of sulphur species in a magma varies with temperature and oxygen fugacity, and to some extent pressure (see Chapter 2 of this thesis) (Carroll and Rutherford 1988), in order to quantify the sulphur emissions we therefore need to have some understanding of the pre-eruptive magma storage conditions, e.g., temperature, oxygen

fugacity. We use olivine-liquid composition to determine temperatures and olivine-spinel mineral equilibria to calculate oxygen fugacity.

Geothermometry requires olivine crystals to be in equilibrium with the liquid composition used in the calculation (in the case of the Lanzarote magmas we refer to the glass inclusion and host olivine crystal composition). Based on the similarity of glass inclusion and matrix glass compositions (Figure 4.13, 4.17) there was little modification of the glass inclusion major element composition following inclusion entrapment; thus we assume the glass inclusion-host olivine pairs used in the temperature calculations are in equilibrium with one another.

4.7.1 Temperature

Magmatic temperatures were calculated using olivine-liquid geothermometry. We use two different thermometers – both calibrated using glass MgO contents. The geothermometer of Helz and Thornber (1987) utilizes the variation of MgO with temperature for glass coexisting with olivine. The geothermometer is calibrated for temperatures between 1260 to 1060 °C for experimental runs on Kilauea Iki tholeiite, with the following relationship used to calculate the liquidus temperature of quenched, glassy eruption products:

$$T_{Mg}\,^{\circ}C = 20.1 \times \text{wt\% MgO} + 1014 \qquad [1]$$

In their investigation of olivine-liquid partitioning in mid ocean ridge petrogenesis, Langmuir et al. (1992) define the following relationship which can be used to calculate magmatic temperatures:

$$\text{Ln}K_D\text{Mg} = 6921/T + 0.034\text{Na} + 0.063\text{K} + 0.01154P - 3.27 \qquad [2]$$

where K_DMg is the olivine-liquid partition coefficient, P = pressure in kbars, and T = temperature (°C). Temperatures calculated using this equation have mean errors of ± 5.3%.

Both these methods yield temperatures in the range 1120 to 1180 °C (at pressures of 1-2 kbar) for the Lanzarote glass compositions (Appendix C), with a reasonable correlation existing between the two techniques ($R^2 = 0.50$) (Figure 4.18). However, temperatures calculated using the technique of Langmuir et al. (1992) yield slightly higher values than those estimated via the Helz and Thornber (1987) geothermometer. This may partly be due to the compositional differences between the Lanzarote magma and the Kilauea Iki magma (used for the Helz and Thornber geothermometer calibration), which is more tholeiitic than any of the Lanzarote compositions. In this study we therefore use the temperatures calculated from equation [2].

4.7.2 Oxygen fugacity

We use the composition of co-existing olivine and chromium spinel to calculate oxygen fugacity for the Lanzarote magma. Care was taken to ensure equilibrium pairs were used in this calibration (i.e. if the spinel inclusion is located in the centre of the crystal then an olivine core composition was used, if the spinel inclusion is on the edge of the crystal then an olivine rim composition was used). $\Delta\log (fO_2)^{FMQ}$ is calculated using the experimental calibration of Balhaus et al. (1991).

$$\Delta\log (fO_2)^{FMQ} = 0.27 + 2505/T - 400P/T - 6\log(X^{olv}_{Fe}) - 3200(1-X^{olv}_{Fe})^2/T + 2\log(X^{sp}_{Fe^{2+}}) + 4\log(X^{sp}_{Fe^{3+}}) + 2630\,(X^{sp}_{Al})^2/T \quad [3]$$

where P (pressure) is in GPa, T (temperature) in K, $X^{sp}_{Fe^{3+}} = Fe^{3+}/\sum R^{3+}$, $X^{sp}_{Al} = Al/\sum R^{3+}$, X^{olv}_{Fe} and $X^{sp}_{Fe^{2+}} = Fe^{2+}/(Fe^{2+} + Mg)$ ratio in spinel and olivine. Equation [3] gives results relative to the FMQ buffer; thus to obtain $\log fO_2$ the value of the FMQ buffer was calculated following the method of O'Neill (1987a) ($FMQ = 82.75 + 0.00484T - 30681/T - 24.45 \log T + 940\ P/T - 0.02P$) and added to the $\Delta\log (fO_2)^{FMQ}$ value to obtain $\log fO_2$.

This technique is applicable to the entire spectrum of spinel compositions in mantle-derived melts, and gives reasonable results to temperatures as low as 800 °C. The technique cannot be applied to assemblages significantly more iron-rich than $X^{olv}_{Fe} = 0.15$ (i.e. with Fo < 81) (Balhaus et al. 1991); however, the Lanzarote olivine compositions used to calculate oxygen fugacities satisfy this condition (Fo > 82). We report oxygen fugacity relative to the NNO (Ni-NiO) oxygen buffer; this is calculated using equation [4], after O'Neill (1987b):

$$NNO = 12.78 - 25073/T - 1.1\log T + 450P/T + 0.025P \qquad [4]$$

ΔNNO is defined as the deviation in $\log fO_2$ from the Ni-NiO buffer at a given temperature, ($\Delta NNO = \log fO_2 - NNO$). At pressures of 0.0001-0.0003 GPa, oxygen fugacities ($\log fO_2$) for the Lanzarote magma compositions, at temperatures ranging from 1120-1180 °C, are between -5.9 and -8.7 (mean value, -7.9), (~0.1 to 1.1 units above the NNO buffer (ΔNNO = 2.0)) (Table 4.4 Figure 4.18). All $\log fO_2$ values derived here suggest that the Lanzarote 1730-36 magma is oxidised.

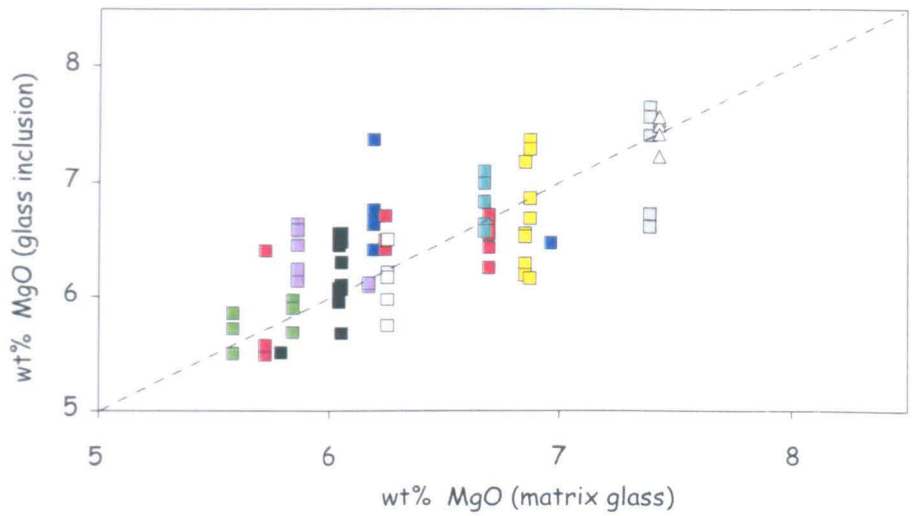

Figure 4.17 MgO content (wt%) of glass inclusions versus mean matrix glass MgO. Colours represent each of the different eruptive episodes, with black = phase I episode 1, red = phase I episode 2, blue = phase II, yellow = phase III episode 1, grey = phase III episode 2, turquoise = phase III episode 3, white = phase IV, green = phase V episode 1, lilac = phase V episode 2. White triangles denote glass inclusions from the phase IV lava sample. Dashed line represents a 1:1 line of perfect correlation, distance away from this line is a measure of compositional variation.

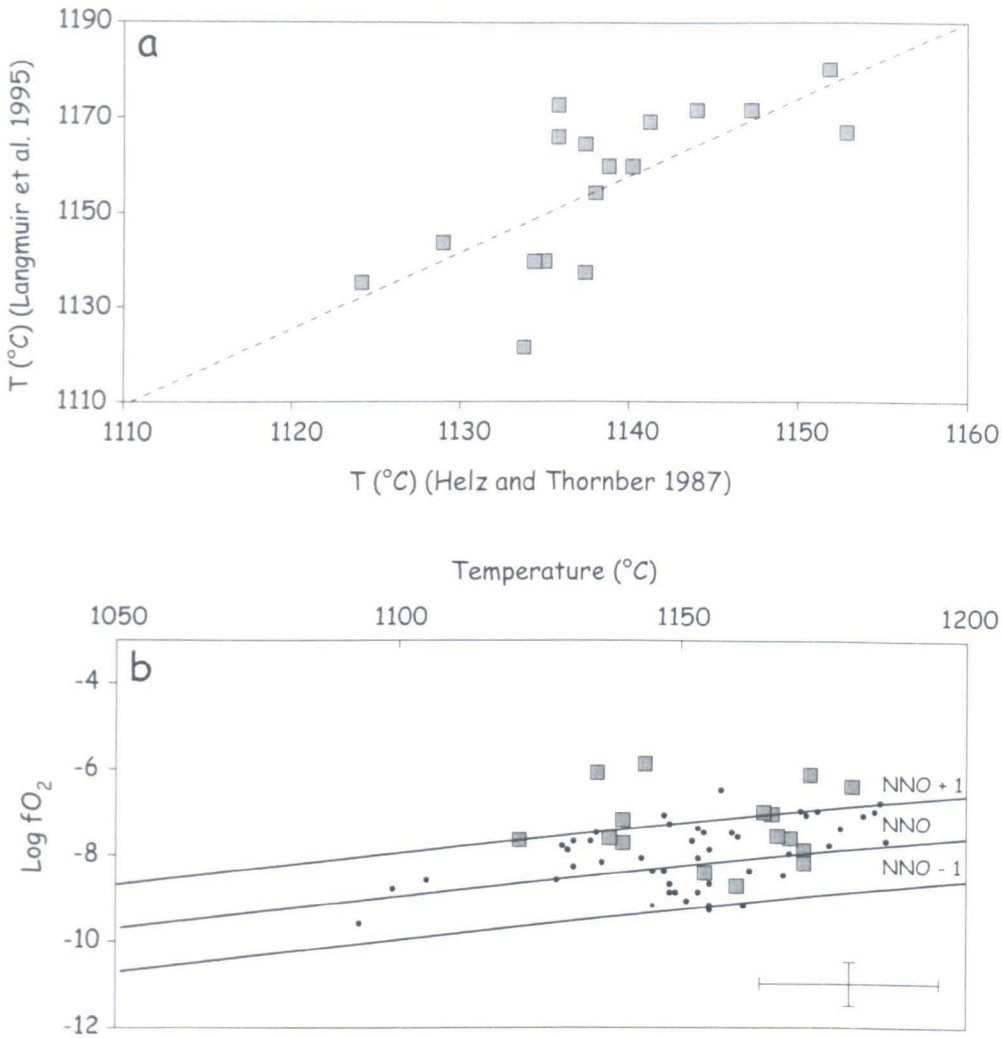

Figure 4.18 Temperature and oxygen fugacity data for selected Lanzarote eruption episodes. Figure (a) shows temperatures calculated via two different geothermometers (see text for details). Dashed line represents 1:1 line of perfect correlation. Figure (b) shows temperature versus log fO_2 for Lanzarote 1730-36 magmas (squares). Log fO_2 is calculated using olivine-spinel geothermometry (see text for details). For comparison small circles represent oxidised Gran Canaria Miocene basalts, (data from Gurenko and Schmincke 2000). Solid lines mark position of the Ni-NiO buffer (NNO). 1σ error bar is shown for reference.

4.7.3 Olivine-melt equilibrium

The Fe-Mg olivine liquid partition coefficient ($K_D = [Fe^{2+}/Mg]_{olv}/[Fe^{2+}/Mg]_{liq} = 0.30 \pm 0.03$), following the method of Roeder and Emslie (1970), provides an assessment of the degree of equilibrium between the magmatic olivine phenocryst cores and co-existing melt inclusions. Based on the method of Kress and Carmichael (1991), we calculate the ferric-ferrous iron (Fe^{3+}/Fe^{2+}) ratio of the glass inclusions using temperature and oxygen fugacity (estimated earlier in section 4.7.2) data together with glass inclusion compositions; a

pressure of 1×10^5 Pa is used. With this technique, the ferric-ferrous iron (Fe^{3+}/Fe^{2+}) ratio of the glass inclusions is estimated as ~0.2-0.45. Re-calculating the glass inclusion composition to account for the Fe^{3+} gives Fe^{2+}/Mg ratios between 0.45 and 0.9 and K_D for Fe-Mg olivine-liquid between 0.22 and 0.36, however, most K_D values now fall closer to the equilibrium value of 0.3 (K_D = 0.27 to 0.33) (Figure 4.19, Appendix C3).

Taking into account the recalculated K_D values (corrected for the presence of Fe^{3+}), which indicate olivine-liquid equilibrium conditions, and the compositional similarity between glass inclusions and corresponding matrix glasses, it is unlikely that post-entrapment crystallization of glass inclusions occurred. Instead, these inclusions most likely represent samples of un-degassed (or partially degassed) magmatic liquids.

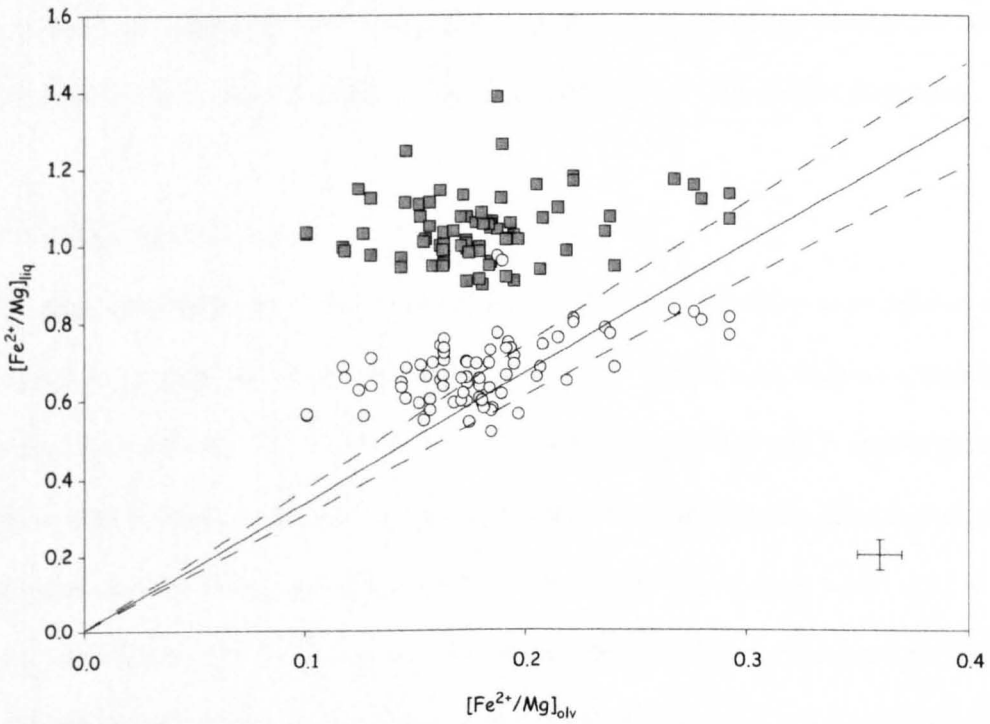

Figure 4.19 Fe^{2+}/Mg ratio in glass inclusions versus Fe^{2+}/Mg ratio in host olivine crystals. Solid line marks partition coefficient, $K_D = 0.3 = [Fe^{2+}/Mg]_{olv}/[Fe^{2+}/Mg]_{liq}$ (after Roeder and Emslie 1974), dashed lines mark upper (0.33) and lower (0.27) limits of K_D. Grey squares represent inclusion-olivine pairs from all Lanzarote eruptive episodes with Fe^{2+} = Fe total. The majority of these points lie outside the calculated K_D upper limit. Circles represent the same inclusion-olivine pairs; however, this group has been corrected to take account of the presence of Fe^{3+} in the liquid composition. Once corrected the majority of these points sit closer to the equilibrium value of K_D (0.30 ± 0.03); see text for more information.

4.8 Estimates of Volatile Release from the 1730-36 eruption

4.8.1 Melt water content

Melt water content was determined using Fourier Transform Infrared Spectroscopy (FTIR) on doubly polished wafers of glass inclusions and matrix glass shards. We use the same technique as outlined in Chapter 3. The molar absorption coefficient (ε) for H_2O was 63 l mol^{-1} cm^{-1} (Dixon et al. 1995) In total, six glass inclusions were analysed from the initial eruptive phase and five fragments of crystal-free matrix glass from phases I and II were also analysed; H_2O data is in appendix C). Pre-eruptive water contents range from ~0.05 to 0.5 for episode 1 of phase I, whereas episode 2 water contents are significantly lower, ranging from 0.1 to 0.12 wt% H_2O. Degassed water concentrations are ~0.03 wt% for phase I episode 1 matrix glasses, rising to ~0.05 wt% H_2O and ~0.06 wt% H_2O for phase I episode 2 and phase II respectively (Figure 4.20). The lack of any correlation between H_2O and K_2O (highly incompatible) indicates that H_2O is affected by degassing.

4.8.2 Melt sulphur content

Sulphur concentrations of both matrix glasses and glass inclusions were determined for all eruptive episodes via electron microprobe analysis. Matrix glass sulphur concentrations range from 0.009 to 0.029 wt% S, with the higher values observed in matrix glass shards from the pyroclastic material. In contrast, compositionally similar glass inclusions show a considerable range of pre-eruptive sulphur concentrations, ranging from ~0.03 to ~0.26 wt% S (Figure 4.21). This range seems to indicate that glass inclusions were trapped at different points during the evolution of the magma and that the low S inclusions represent partially degassed melt. This is feasible if degassing induces crystallization at shallow depths in the magmatic system – decompression leads to melt degassing which in turn causes crystallization; any inclusions trapped during crystal growth here and while the melt

is degassing will show reduced volatile contents reflecting the partially degassed melt composition.

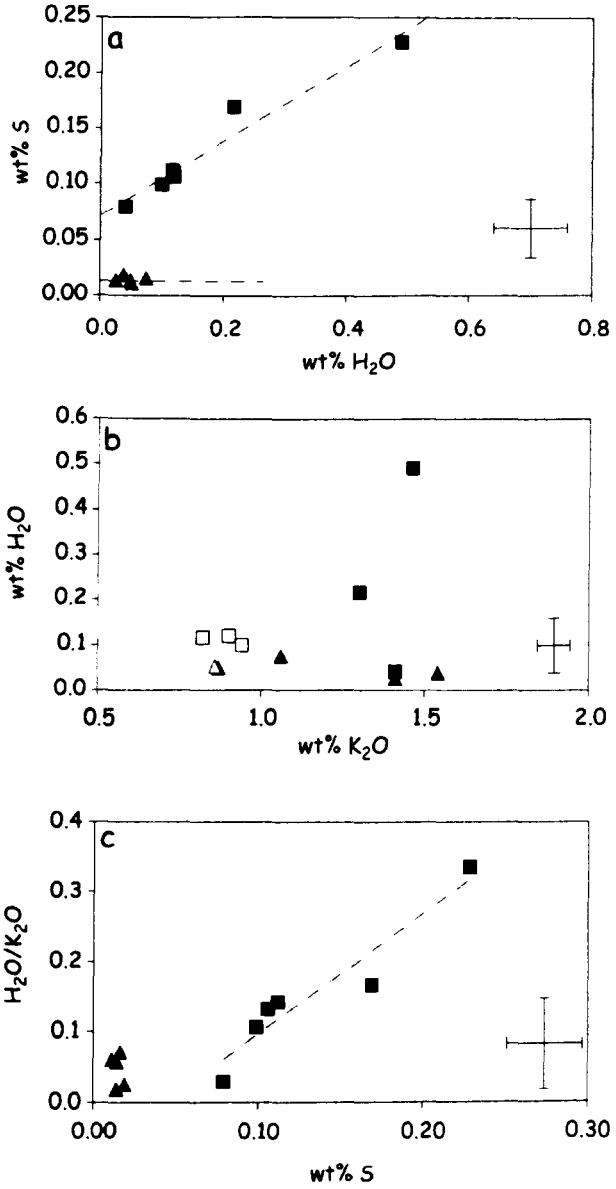

Figure 4.20 H_2O versus S (a), H_2O versus K_2O (b), H_2O/K_2O versus S (c). In figures (a) and (c) glass inclusions are shown with grey squares, grey triangles denote matrix glasses, dashed lines are regression lines of best fit. S shows an excellent correlation with H_2O ($R^2 = 0.95$) and with H_2O/K_2O ($R^2 = 0.90$); however, H_2O does not correlate with K_2O indicating that H_2O is affected by degassing - see text for further explanation. In figure (b) squares represent glass inclusions, with grey squares = Phase I Episode 1, white squares = Phase I Episode 2; triangles denote matrix glasses, with grey triangles = Phase I Episode 1, white triangles = Phase I Episode 2, black triangles = Phase II. 1σ error bars shown for reference.

This decompression – degassing – crystallization sequence is a common occurrence in mafic magmas, e.g., Mauna Loa 1984. Figure 4.21 (a) shows that a large burst of crystallization occurs when melt sulphur concentrations have been reduced (via low-pressure degassing) to ~0.05-0.1 wt% S. H_2O concentrations in the glass inclusions show an excellent correlation with sulphur contents (Figure 4.20c), with inclusions containing the highest S values characterized by the highest H_2O and H_2O/K_2O ratios (Figure 4.20). This range in pre-eruptive water contents (0.05 – 0.5 wt% H_2O) also supports the notion of low-pressure degassing resulting in crystallization of slightly volatile-reduced melts. The positive correlations between S and H_2O and H_2O/K_2O indicates that H_2O and S are coupled in the degassing process (e.g., Davis et al. 2003), with the highest concentrations of both volatiles representing the least degassed melt. The similarity of the melt inclusion and matrix glass compositions (Figure 4.17), together with the high CaO contents of Lanzarote host olivine crystals (0.17 to 0.22 wt% CaO), suggests that these olivine crystals grew in a low-pressure environment (Burton et al. 2002), e.g., at a shallow level in the magmatic plumbing system – where melt compositions are volatile-poor due to degassing.

Figure 4.21 shows a plot of inclusion and matrix glass sulphur concentrations against total FeO. On this plot, the high sulphur inclusions (> 0.16 wt% S) lie above the sulphur solubility (or sulphide saturation) limit determined for un-degassed MORB glasses (Mathez 1976). A smaller number of inclusions exhibit much lower sulphur contents (0.025 to 0.07 wt% S) and plot below the experimentally derived sulphur solubility curve for basaltic magmas (Haughton et al. 1974). As many Lanzarote inclusion compositions plot above both solubility lines, this indicates that the Lanzarote magmas are seemingly able to dissolve much larger amounts of sulphur than we currently see in the majority of the Lanzarote glass inclusions. This is consistent with the majority of the inclusions being partially degassed and the oxidised fO_2 values (determined via olivine-spinel equilibria) indicating that sulphur is present as the sulphate species and that these melts are sulphide-

undersaturated. To dissolve in excess of 2600 ppm sulphur the original melt must originate under relatively oxidized fO_2 conditions. Gurenko and Schmincke (2000) also report high sulphur concentrations in other Canary Island (Miocene basalts from Gran Canaria) basaltic melts (~1740-5810 ppm S, ΔNNO = -1.1 to +1.8). Based on the presence of anhydrite-bearing peridotite xenoliths from recent Gran Canarian lavas, Amundsen (1987) and Gurenko and Schmincke (2000) suggest that oxidised fO_2 conditions at upper mantle or lower crustal depths might be common beneath Gran Canaria, and this may possibly be the case beneath Lanzarote. This data is also in agreement with more recent studies on sulphur solubility (e.g., Jugo et al. 2005). Jugo et al. (1995) indicate that reasonably oxidized melts (QFM +1) can dissolve up to 10,000 ppm S without precipitating sulphide.

4.8.3 Petrologic Determination of sulphur degassing

The quantity of sulphur released into the atmosphere during the Lanzarote eruption is estimated here using a petrological approach (e.g., Devine et al. 1984; Sharma et al. 2004). Assuming that glass inclusions in magmatic crystals represent volatile-bearing liquid trapped during crystal growth at depth, then the mass of sulphur released via melt degassing can be calculated using the difference in sulphur concentration between glass inclusions (C_{inc}) in magmatic crystals and the degassed matrix glass (C_{matrix}) of the volcanic rock, scaled to the mass of erupted magma and corrected for the crystal content. A full assessment of this technique is provided in chapter 2. Using partially degassed inclusion values to represent pre-eruptive volatile concentrations in the petrologic method calculation will result in an underestimation of the sulphur degassing from this eruption; thus in this section we devise a method to allow us to back-calculate original sulphur concentrations for a given melt composition and thus obtain a more reasonable value of the pre-eruptive sulphur concentration (C_o).

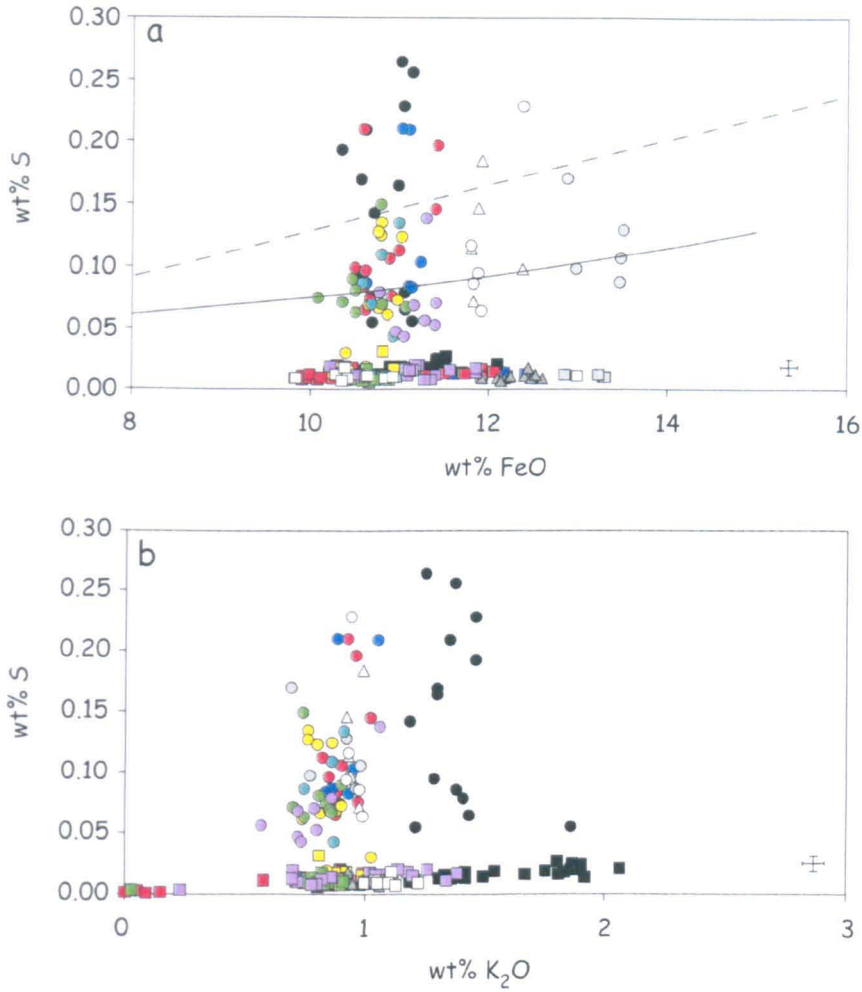

Figure 4.21 S versus FeO (a) and K_2O (b). In figure (a) dashed line represents limit of S solubility as defined by Mathez (1976) and solid line is the experimentally derived S-solubility curve for basaltic magmas (Haughton et al. 1974) – see text for further explanation. In both figures circles denote glass inclusions and square symbols matrix glasses with colours representing each of the different eruption episodes; black = phase I episode 1, red = phase II episode 2, blue = phase II, yellow = phase III episode 1, grey = phase III episode 2, turquoise = phase III episode 3, white = phase IV, green = phase V episode 1, lilac = phase V episode 2. In both figures grey triangles denote matrix glasses and white triangles glass inclusions from the phase IV lava sample. 1σ error bar shown for reference.

The original sulphur concentration of the magma (C_o) is determined by several factors – including original source composition, degree of partial melting at source, and any subsequent fractional crystallization. In a sulphide-undersaturated magma, fractional crystallization will not remove sulphur from the melt (as is the case in a sulphide-saturated melt where sulphur is removed into sulphide mineral phases, e.g., as in the Mathez (1976) MORB data – Figure 4.21). Therefore, as sulphur behaves as an incompatible element during fractional crystallization of a highly oxidised basalt, the S/*I* ratio (where *I* is a highly incompatible element, e.g., Ti, K, P) should remain constant until degassing starts. The inclusions that have undergone the least amount of degassing will have the highest S/*I* ratios and un-degassed magmas from the same liquid line of descent will have the same S/*I* ratio. Knowing that ratio, the original S content of a degassed liquid (matrix glass) can then be calculated from its concentration of *I*.

As the Lanzarote eruption has magmas that are from different source regions and/or are the products of varying degrees of partial melting (e.g., Thomas et al. 1999; Lundstrom et al. 2003), the original S/*I* ratio may not have been the same for all magma compositions. Thus, looking at the variation of the S/*I* ratio as a function of other incompatible element ratios ensures that any correlations do not reflect source trends of fractional crystallization or partial melting. Such a process would result in constant concentrations of trace elements, and decreasing La/Yb ratios with time. As the P_2O_5/TiO_2, P_2O_5/K_2O and K_2O/TiO_2 ratios correlate well with La/Yb ratios, these ratios can be used as indices of the degree of source partial melting (Figure 4.22) (Thomas et al. 1999). As variation of La/Yb with each of these ratios (P_2O_5/TiO_2, P_2O_5/K_2O and K_2O/TiO_2) is not systematic through the eruption we can assume that the compositional variations seen on the diagrams using these ratios cannot be attributed to progressive extraction of mantle partial melt.

Figure 4.23 shows S/*I* ratio as a function of the highly incompatible element ratios – K_2O/TiO_2, P_2O_5/K_2O and P_2O_5/TiO_2. Vertical variations on this diagram are an indicator of melt degassing while the horizontal variation can be attributed to different degrees of partial melting (as reflected in the La/Yb trace element data). On each of these three diagrams the S/*I* ratio is extremely variable, ranging from 0.05 to 0.25 (S/K_2O), 0.025 to 0.25 (S/P_2O_5) and 0.02 to 0.08 (S/TiO_2). This range in values can be attributed to different degrees of melt degassing, with the highest S/*I* values representing un-degassed glass inclusions. The S/*I* ratio shows very little vertical variation for matrix glasses from all of the eruptive phases, and is much lower (<0.05) – reflecting the degassed nature of these samples. There is no correlation between eruption episode and the S/*I* ratio: samples from all phases show considerable overlap with one another. However, the anomalous Phase IV lava sample, described in section 4.6, does stand out on these ratio diagrams (white triangles on Figure 4.23), thus we choose not to include these points when defining the regressions based on these ratios.

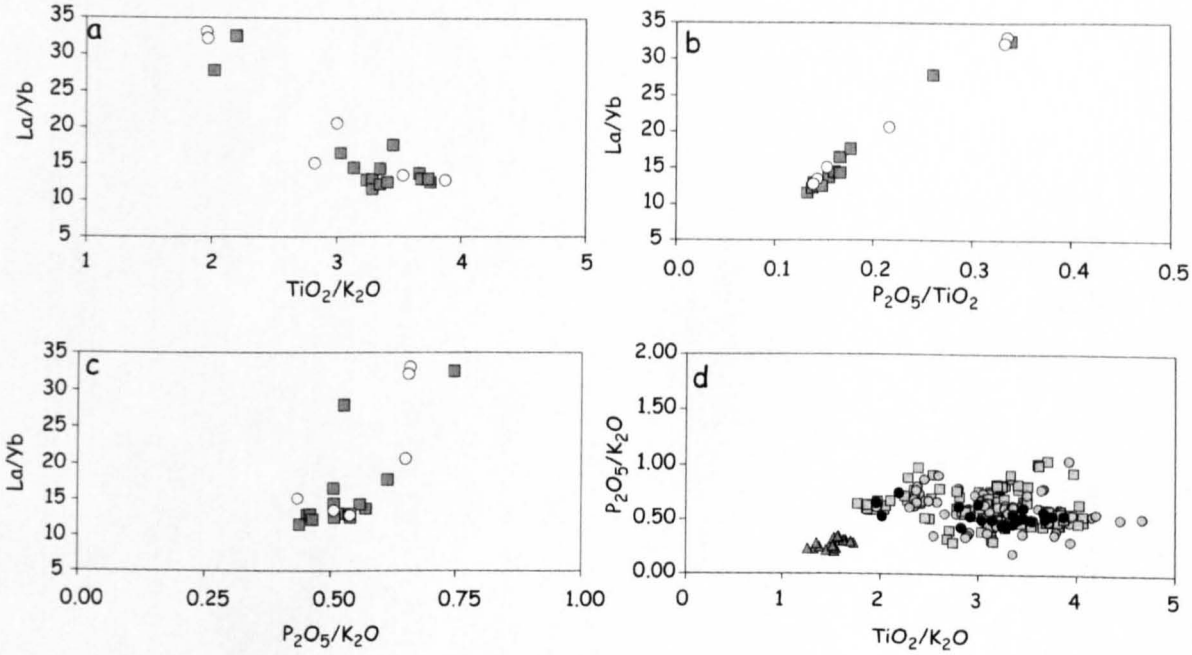

Figure 4.22 Whole-rock major and trace element data for Lanzarote magmas. Figures (a) to (c) show La/Yb trace element ratios against incompatible element ratios TiO_2/K_2O, P_2O_5/TiO_2 and P_2O_5/K_2O. La/Yb can be used as an index of degrees of source partial melting with La/Yb decreasing with increasing partial melting. In figures (a) to (c) grey squares represent whole-rock data from Thomas et al. (1999) and white circles denote whole-rock data from Lundstrom et al. (2003). Figure (d) shows TiO_2/K_2O versus P_2O_5/K_2O data for all analysed matrix glasses and glass inclusions, on this plot grey squares = matrix glasses, grey circles = glass inclusions, black circles represent whole-rock data from Thomas et al. (1999) and Lundstrom et al. (2003). Grey triangles denote matrix glass and glass compositions from a Phase IV lava sample, which is compositionally distinct from the remainder of the Lanzarote glass chemistry (see text for details). 1σ error bar is shown for reference.

Table 4.4 S/*I* ratio and incompatible element data for the nine glass inclusions used to calibrate the empirical method for estimating original magmatic sulphur concentrations (C_o). IV* indicates Phase IV lava sample (shaded) which is not included in this calibration, but is used to estimate C_o from matrix glass analyses (see text for further explanation). Log fO_2 and ΔNNO (calculated via olivine-spinel mineral equilibria) values are also included here for reference. Oxide data are shown in weight percent.

Phase	I, 1	I, 1	I, 2	I, 2	II	II	III, 2	IV	IV*
P_2O_5	0.99	0.98	0.51	0.71	0.69	0.69	0.21	0.56	0.26
TiO_2	3.23	3.5	2.81	2.93	3.24	3.22	2.72	3.31	1.5
K_2O	1.37	1.25	0.92	0.96	1.05	0.88	0.69	0.92	0.99
S	0.256	0.265	0.210	0.196	0.209	0.210	0.170	0.228	0.184
S/K_2O	0.186	0.212	0.227	0.204	0.199	0.239	0.246	0.249	0.186
S/P_2O_5	0.259	0.270	0.412	0.276	0.303	0.304	0.810	0.407	0.708
S/TiO_2	0.079	0.076	0.075	0.067	0.065	0.065	0.063	0.069	0.123
P_2O_5/K_2O	0.72	0.79	0.56	0.74	0.66	0.78	0.30	0.61	0.26
TiO_2/K_2O	2.36	2.80	3.05	3.05	3.09	3.66	3.94	3.60	1.52
P_2O_5/TiO_2	0.31	0.28	0.18	0.24	0.21	0.21	0.08	0.17	0.17
log fO_2	-7.4	-7.6	-8.3	-8.7	-8.8	-7.8	-6.8	-8.2	-7.9
ΔNNO	0.9	0.7	-0.2	-0.5	-0.5	0.3	1.2	0.2	0.2

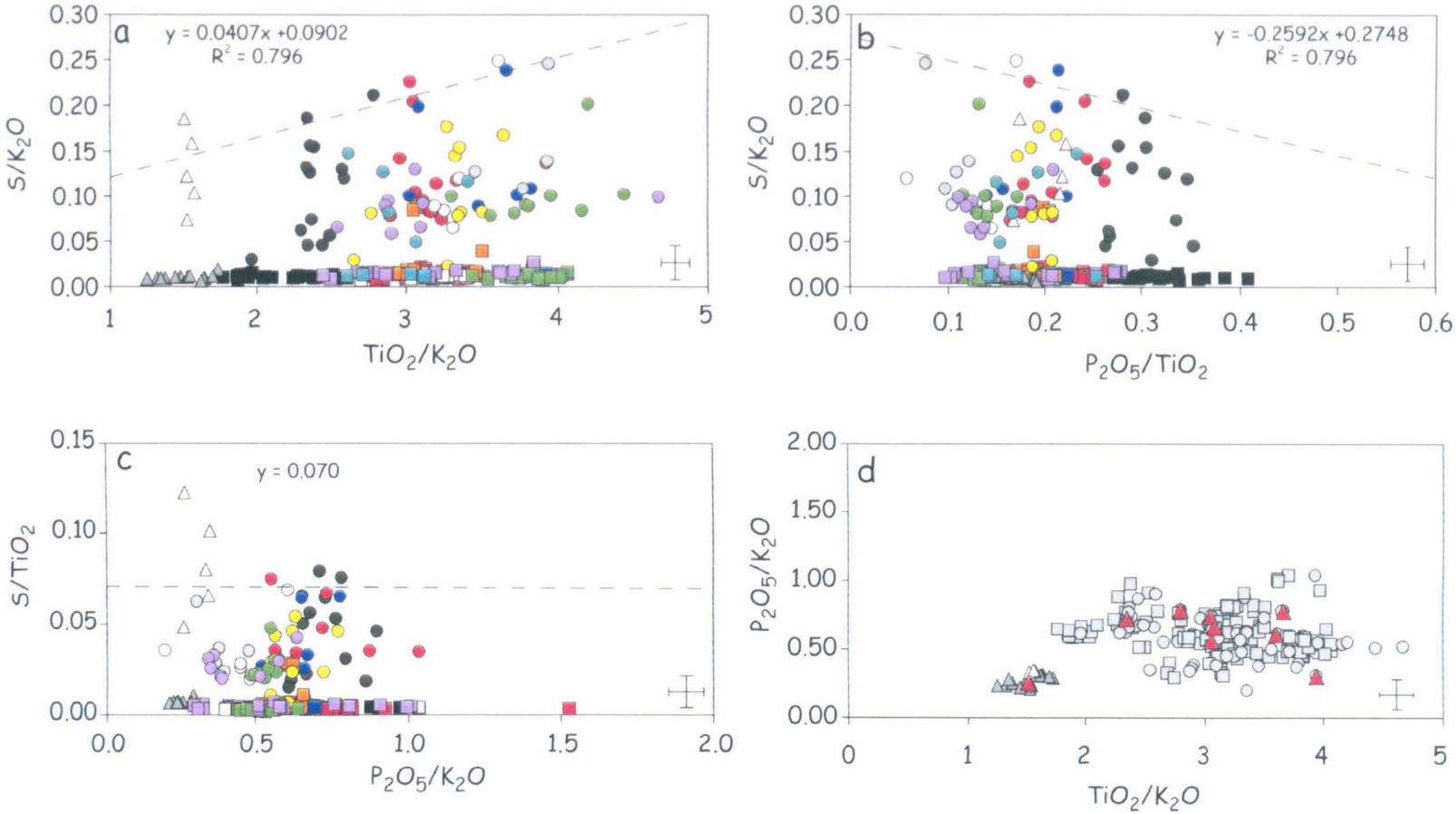

Figure 4.23 Incompatible element ratio diagrams for all Lanzarote matrix glasses and glass inclusions. Matrix glasses are shown with square symbols, glass inclusions as circles. In figures a-c colours represent each of the different eruptive episodes, with black = Phase I Episode 1, red = Phase I Episode 2, blue = Phase II, orange = Phase III Episode 1, grey = Phase III Episode 2, turquoise = Phase III Episode 3, white = Phase IV, green = Phase V Episode 1, lilac = Phase V Episode 2. In all figures, grey triangles denote matrix glasses and white triangles glass inclusions from the Phase IV lava sample. Dashed lines are regression lines of best fit through the high S/I (where I is an incompatible trace element) inclusion data. On Figure d red triangles represent glass inclusion points with high S/I ratios used to calibrate empirical relationships shown in figures a-c. 1σ error bar is shown for reference. See text for further explanation and discussion.

These diagrams demonstrate that glass inclusions with the highest S/*I* ratios exhibit a positive correlation when plotted against highly incompatible element ratios. Eight glass inclusions (data listed in Table 4.4) ($S/K_2O > 0.2$, $S/TiO_2 > 0.06$) define distinct, consistent trends (dashed lines on Figure 4.23) all three ratio plots, can be used to calibrate the S/*I* relationship. On a plot of K_2O/TiO_2 versus P_2O_5/K_2O all eight inclusions used in this calibration also fall within the general trend observed for all glass data, suggesting that they are not anomalous and are indeed representative analyses, therefore can be used to calibrate the regressions. Based on this, we derive an empirical method for estimating the original pre-eruptive sulphur concentration (C_o), and thus removing the effect of partially degassed inclusions when applying the petrologic method. The following expressions represent a best fit linear regression line through the glass inclusions that show the highest S/K_2O values on Figure 4.23 (a) and (b).

$$C_o = 0.090\ K_2O + 0.041\ TiO_2 \qquad [5]$$

$$C_o = (-0.259\ P_2O_5/TiO_2)\ K_2O + 0.275\ K_2O \qquad [6]$$

$$C_o = 0.070\ TiO_2 \qquad [7]$$

Major element concentrations are expressed in weight percent.

Using the major element composition of matrix glasses the above regressions are used to calculate C_o (original pre-eruptive S content), i.e. assuming the matrix glass composition represents degassed melt, then, these regressions allow us to calculate the original, un-degassed S content.

The S/K_2O ratio provides the best correlation ($R^2 = 0.8$) when plotted against K_2O/TiO_2 and P_2O_5/TiO_2 , whereas the S/TiO_2 ratio remains constant. All three formulae values of C_o are in good agreement with one another. We use all three equations to calculate a representative mean value of C_o for all eruption phases. However this method cannot be used to calculate C_o for melt compositions from the Phase IV lava sample, as this sample sits outside the calibration field for the above relationships (white triangles on Figure 4.23). For this reason, we assume a constant S/I ratio value ($S/K_2O = 0.186$; S/P_2O_5; = 0.708, $S/TiO_2 = 0.123$) for the single inclusion with the highest S content from this sample, and use this to determine C_o. Therefore to calculate the volcanic SO_2 release we use the formula:

$$M_S = \frac{M_V (1 - W_{xtls})[C_{inc} - C_{matrix}]}{100} \qquad [8]$$

where M_v is the mass of material erupted, W_{xtls} is the crystal content of the undegassed magma, C_{matrix} is the matrix glass (degassed) sulphur concentration and C_o is the corresponding original pre-eruptive sulphur concentration (calculated using equations [5] to [7] from the major element composition of the matrix glass). To account for the molecular weights of S and SO_2, the amount of sulphur released to the atmosphere (estimated using equation [8]) is $2M_S$.

Petrologic method calculation data is summarized in Table 4.5. Based on this technique, we estimate that 45 Mt of SO_2 was released into the atmosphere during the Lanzarote eruption, with 65% of this (~28 Mt) released during the initial two eruption phases (Phases I & II). Subsequent phases of activity collectively released ~19 Mt SO_2.

Based on this work, it is likely that this eruption did not possess an excess sulphur phase. Although the melt is oxidising, the correlation between S and FeO indicates that the melt was able to dissolve large amounts of sulphur – these high S concentrations are reflected in the calculations used to calculate pre-eruptive S concentration. It is unlikely that S was sequestered out from the melt into a separate gas phase (Chapter 2). The similarity of the SO_2 release estimate deduced from the ice core data (see next section) to the SO_2 release estimate calculated petrologically for phase I suggests that all of the dissolved S was released via melt degassing on eruption.

Table 4.5 Summary of the main components used in the petrologic method calculation for estimating volcanic SO_2 release, together with the petrologic estimate. Density values used to convert erupted volume (km^3) to erupted magma mass are also shown. Errors associated with C_o and C_{matrix} measurements are 1σ and errors associated with petrologic estimates are 2σ. [n] = number of analyses. ΔNNO values are shown for reference (n.a. = oxygen fugacity not available for eruption episode).

Phase [Episode]	C_o^* [n]	C_{matrix} [n]	Mass (kg)† [Density kg/m³]	W_{xtls}	Petrologic SO_2 (Mt)	ΔNNO
I [1]	0.280 ± 0.008 [24]	0.012 ± 0.008 [24]	1.73×10^{12} (L) 6.60×10^{10} (F) [1100[a], 2300[b]]	0.04	9.23 ± 1.3	0.3-0.9
I [2]	0.215 ± 0.008 [30]	0.013 ± 0.005 [30]	3.95×10^{12} (L) 9.90×10^{11} (F) [1100[a], 2350[b]]	0.05	19.13 ± 2.8	-0.2, -0.9
II	0.210 ± 0.008 [12]	0.012 ± 0.005 [12]	4.80×10^{11} [2400]	0.05	1.81 ± 0.3	-0.5-0.8
III [1]	0.195 ± 0.006 [25]	0.019 ± 0.006 [25]	1.39×10^{8} [2400]	0.04	0.005 ± 0.002	1.2
III [2]	0.221 ± 0.017 [4]	0.011 ± 0.005 [4]	1.46×10^{12} [2400]	0.05	5.83 ± 1.1	n.a.
III [3]	0.179 ± 0.007 [4]	0.010 ± 0.005 [4]	6.96×10^{11} [2400]	0.06	2.21 ± 0.3	0.1
IV	0.242 ± 0.008 [12]	0.012 ± 0.004 [12]	1.34×10^{12} [2400]	0.06	5.82 ± 1.1	2.1
V [1]	0.206 ± 0.004 [16]	0.008 ± 0.002 [16]	3.44×10^{11} [2460]	0.06	1.27 ± 0.2	2.0
V [2]	0.218 ± 0.004 [16]	0.009 ± 0.002 [16]	7.38×10^{10} [2460]	0.05	0.29 ± 0.04	0.5-0.6

*Pre-eruptive S content (C_o) calculated using S/*I* ratio (*I* = incompatible trace element), see text for details.
†(L) = mass of lava erupted, (F) = fallout mass
[a]tephra scoria bulk density
[b]lava density

4.8.4 Melt chlorine content

Chlorine was analysed in all matrix glasses and glass inclusions. Degassed chlorine concentrations (measured in matrix glasses) are all less than 0.027 wt%. However, a few matrix glass samples have chlorine concentrations in excess of 0.05 wt%. There is considerable scatter in the glass inclusion chlorine data – with inclusion chlorine contents ranging from 0.04 wt% to 0.20 wt%. Figure 4.24a shows evidence of a positive correlation between sulphur and chlorine in the glass inclusions – the wide range in chlorine values may also be attributed to inclusions trapping partially degassed melt. The positive correlation between these two elements and the absence of any correlation between Cl and K_2O indicates that chlorine is behaving in a similar fashion to sulphur in these magmas and is affected by degassing.

We attempted to analyse fluorine concentrations in the Lanzarote glasses; however, due to the analytical uncertainty in analysing fluorine accurately we were unable to obtain accurate fluorine data. Where analysed, fluorine for both glass inclusions and matrix glasses show a non-systematic scatter and therefore cannot usefully be interpreted.

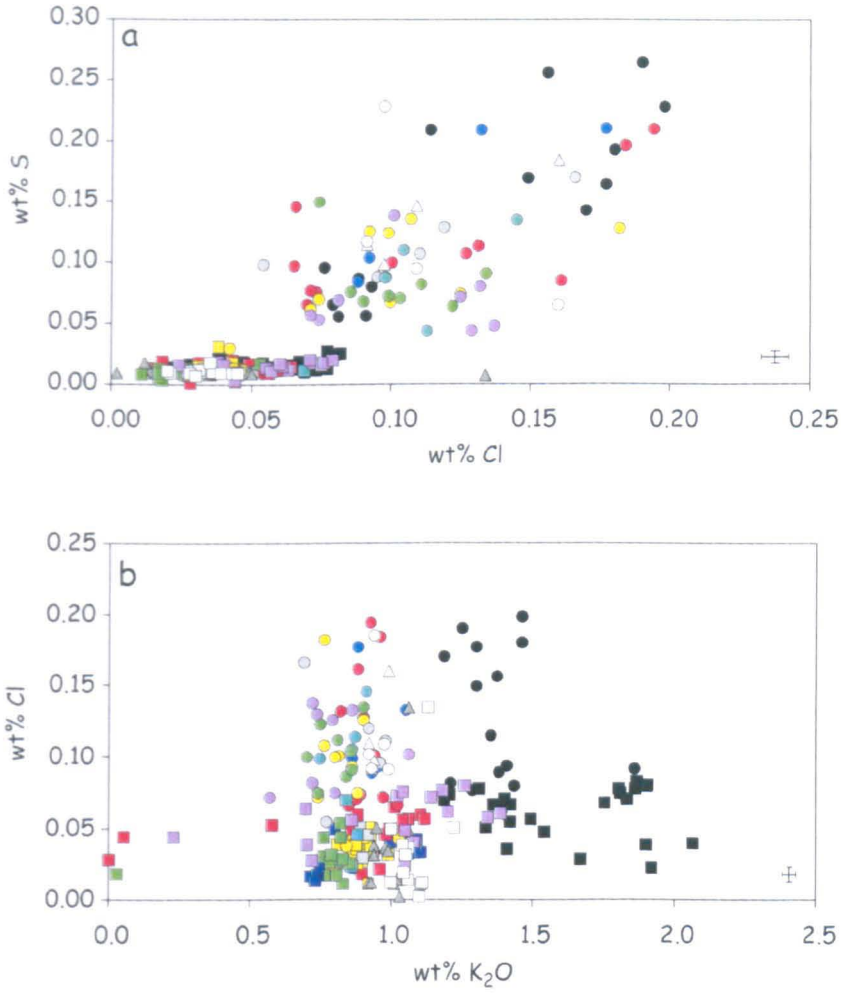

Figure 4.24 Cl versus S (a), K_2O (b). In both figures colours represent each of the different eruptive episodes, with black = Phase I Episode 1, red = Phase I Episode 2, blue = Phase II, yellow = Phase III Episode 1, grey = Phase III Episode 2, turquoise = Phase III Episode 3, white = Phase IV, green = Phase V Episode 1, lilac = Phase V Episode 2. In all figures, grey triangles denote matrix glasses and white triangles glass inclusions from the Phase IV lava sample. 1σ error bar shown for reference.

4.9 Aerosol mass loading from the 1730-36 Lanzarote eruption

As shown in section 4.8 (Table 4.6), approximately 44 Mt (1Mt = 1 × 10^9 kg) of SO_2 was released during the six-year-long Lanzarote eruption, with 64% of this total (~28 Mt) emitted during the first eight to nine months of eruptive activity (during Phases I and II). This high rate of magma degassing coincides with the peak magma discharge; ~68% of the total erupted volume (~3.4 km^3) was erupted during this time. Historical accounts of the eruption (summarized in Table 4.1), in conjunction with dispersal data obtained by studying the fall deposit, suggest that these initial two phases were characterized by high magma discharge rates and intense explosive activity that generated 12-16 km high eruption columns. The height of the tropopause above Lanzarote is approximately 14 km (Crutcher 1969); it therefore seems reasonable to assume that the first eight to nine months of activity had the greatest potential to inject large amounts of SO_2 into the upper atmosphere and cause widespread atmospheric and environmental perturbations. Therefore when assessing the probable aerosol mass loading from this event we consider the vent-derived volatile degassing contributions from phases I and II (largely injected to upper atmospheric levels) separately from the volatiles contributed by the latter phases (III to V) of the eruption (largely confined to the troposphere, eruption columns 6-12 km in height).

In basaltic fissure eruptions such as this, the release of sulphur (and other volatiles) during eruptive activity occurs in two stages. Initially, magmatic sulphur is degassed during the explosive fire fountaining stage (stage 1) to upper atmospheric levels, followed by degassing during transport, emplacement, and cooling of lava flows (stage 2), mainly into the troposphere (Figure 4.25). Applying this model to the initial Lanzarote phases (I & II), we calculate that approximately 94% of the sulphur was released during the explosive

vent-based activity (stage 1), with 6% degassed during lava flow emplacement (stage 2) (Table 4.7). As the eruption progressed this ratio changes slightly; during the latter phases of the eruption (IV & V) this ratio is ~86% (stage one – vent degassing) and ~14% (stage two – degassing during lava flow transport) (Table 4.7).

Table 4.6 Summary of the SO_2 (in megatons (Mt)) release from each of the Lanzarote eruptive episodes (Phase I to V. Episode durations, shown in months (unless otherwise stated) are given for reference.

Phase	I	I	II	III	III	III	IV	IV*	V	V
Episode	1	2	-	1	2	3	-	-	1	2
SO_2	9.23	19.13	1.81	0.005	5.83	2.21	5.82	4.41	1.27	0.29
Duration	19 days	4	4	1	5	1	2 years	2 years	1	16 days

Phase	I	II	III	IV	V
Total SO_2	26.4	1.8	8.0	5.8	1.6
% SO_2	60.5	4.1	18.3	13.3	3.7

*Indicates SO_2 release calculated using sulphur data from the Phase IV lava sample (see text for details). This value is shown for reference purpose only & is not used in calculation of eruptive SO_2.

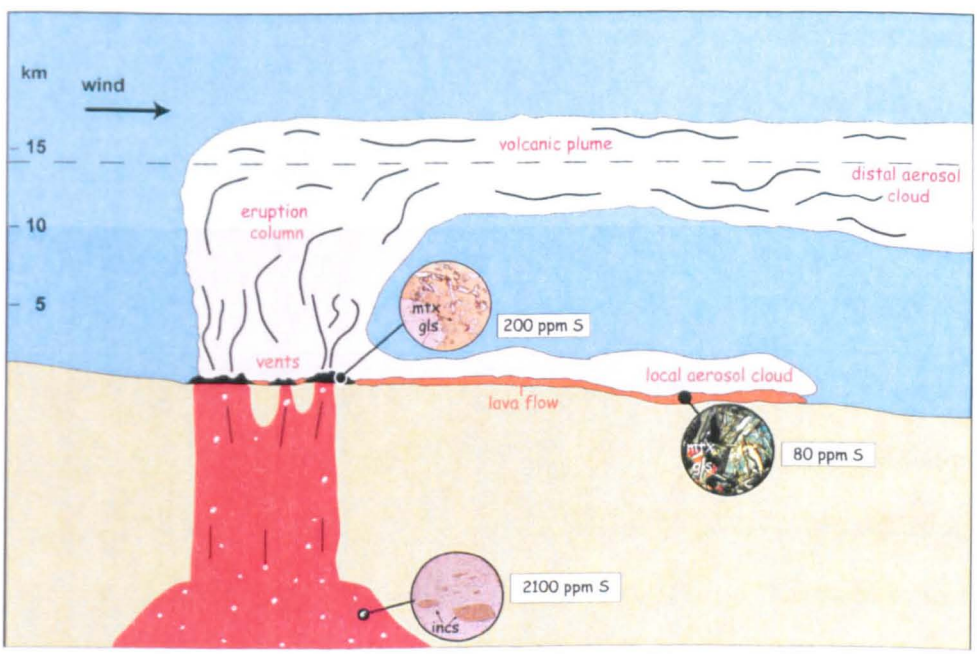

Figure 4.25 Schematic diagram of sulphur release from fissure style eruptions, such as the Lanzarote 1730-36 event. S release occurs in two stages - initially via degassing at the vent (stage 1), and then during emplacement of lava flows (stage 2). S values are mean values of pre-eruptive S (glass inclusions), vent degassed S (tephra matrix glass) and lava degassed S (lava matrix glass), from phase I episode 2 samples used to calculate vent/lava flow degassing ratios, (see Table 4.7). Dashed line marks tropopause position above Lanzarote. Modified from Thordarson and Self (2003).

Table 4.7 Summary of mean phase I episode 2 and phase V episode 1 inclusion, tephra matrix glass and lava matrix glass sulphur contents, used to calculate ratio of sulphur degassing at vents (difference between inclusion S content and tephra matrix glass S content) versus sulphur degassing during lava flow generation and transport (difference between tephra matrix glass and lava matrix glass S content). S contents shown in ppm, 2σ error on S data is ~40 ppm.

	Phase I Episode 2		
	Inclusions	Matrix glass tephra	Matrix glass lava
Measured S content (ppm)	2100	200	80
Degassing ratio (vent:lava) (%)		94:6	
	Phase V Episode 2		
	Inclusions	Matrix glass tephra	Matrix glass lava
Measured S content (ppm)	1480	272	90
Degassing ratio (vent:lava) (%)		86:14	

Thordarson et al. (1996) calculated that during the 1783 Laki eruption, approximately 75% of the volatile degassing occurred during stage 1 with ~25% occurring during stage 2. This two-stage degassing ratio for the Lanzarote eruption is however slightly different. It is not surprising that a greater proportion of sulphur was degassed at the vent during the early eruption phases; these magma compositions are lower in SiO_2 and hotter than the Laki magmas, thus generating more fluid, low viscosity lavas. During the latter stages of the Lanzarote eruption, as magmas evolved to more tholeiitic compositions, this ratio is closer to the ratio calculated for the Laki eruption.

Based on the above ratios, we estimate that approximately 27 Mt of SO_2 was released at the vents and injected into the lower stratosphere (~14 km) during the initial phases of intense explosive activity (I and II), with Phases III to V collectively releasing ~13 Mt of SO_2 into the atmosphere during vigorous vent degassing. As discussed in section 4.4, the main phase III, IV and V eruptive vents consist of either low-lying cinder/spatter cones or elongate spatter ramparts. The explosive activity that built these smaller cones was

typically much less intense Hawaiian-style fire fountaining, generating eruption columns no more than 2-10 km high (section 4.4).

The total amount of SO_2 released during the entire eruption, via explosive activity at the vents (~40 Mt), is theoretically sufficient to generate 81 Mt of sulphate aerosol. This calculation is based on the assumption that each aerosol particle consists of 75% H_2SO_4 and 25% H_2O by weight (Thomason and Osborne 1992), and assuming a conversion efficiency of 100%. The 1991 Pinatubo eruption released ~17 Mt of stratospheric SO_2, generating ~30 Mt of H_2SO_4 aerosol – a gas to particle conversion efficiency of 86% (McCormick et al. 1995). If we assume this same conversion factor for Lanzarote, then a theoretical maximum aerosol loading is ~74 Mt. However, this aerosol yield assumes that all of the SO_2 generated during vent degassing was injected into the stratosphere and converted to stratospheric aerosol. As stated earlier, it is unlikely that the explosive activity during phases III to V supplied SO_2 to the stratosphere. Therefore, to obtain a more realistic estimate of the stratospheric mass aerosol loading, we consider only the vent sulphur output from phases I and II when estimating the stratospheric aerosol yield from the 1730-36 Lanzarote eruption. As stated above, SO_2 emissions from phases III to V were injected into the troposphere. On this basis, Phases I and II released ~27 Mt SO_2 into the stratosphere, producing a maximum sulphate aerosol loading of ~55 Mt. Correcting this value by adopting the Pinatubo gas-particle conversion efficiency we calculate that ~47 Mt of H_2SO_4 aerosols were generated during the explosive, stratosphere-reaching phases of the Lanzarote eruption (Table 4.8).

Table 4.8 Estimates of sulphate aerosol mass loading from the Lanzarote eruption. To assess the atmospheric impact of this eruption we divide the activity into two main stages, stage 1 (phases I & II) and stage 2 (phases III to V) (refer to text for further information). Cumulative estimates of stage duration and volume are shown for reference. SO_2 release and aerosol loading shown in megatons (Mt).

Summary of eruption episode duration, volume, SO_2 release and aerosol mass loading							
Stage [Phases]	**Duration**	**Magma volume (km^3)**	**Total SO_2 released**	**SO_2 released at vent[1]**	**SO_2 released during lava degassing[1]**	**H_2SO_4 aerosol yield (vent)[2]**	**H_2SO_4 aerosol yield (lava)[3]**
1 [I, II]	1 Sept 1730 – June 1731	3.44	29	27	2	47	4
2 [III, IV, V]	June 1731 – 16 Apr 1736	1.63	19.1	13	2	23	4

[1]Based on degassing ratios shown in table 4.9 (refer to text for further details)
[2]Maximum upper atmospheric (stratosphere) H_2SO_4 aerosol yield, calculated assuming a conversion efficiency of 86% assuming aerosol particles are 75% H_2SO_4, 25% H_2O
[3]Maximum H_2SO_4 aerosols derived via degassing during lava flow transport

This aerosol loading is equivalent in mass to the stratospheric aerosol cloud generated during the initial 8-10 days of the 1783 Laki eruption (*cf.* Thordarson and Self 2003) and is one and a half times greater than the aerosol mass produced during the 1991 Pinatubo eruption. Although the Lanzarote aerosol mass loading was spread out over a period of months, it still represents a significant aerosol injection with the potential to cause grave atmospheric and environmental perturbations. Adopting the same conversion factor, we estimate that phases III, IV and V of the eruption generated a maximum of ~23 Mt H_2SO_4 aerosols, all of which were most likely injected into the upper troposphere (Table 4.8). Note that this figure is obtained by assuming that all of the SO_2 gas released into the troposphere is converted into sulphate aerosol; however, the gas-aerosol conversion efficiency may be much less at lower atmospheric levels, thus this figure should be considered as the maximum tropospheric aerosol loading.

4.9.1 Estimating volcanic aerosol loading using ice core acidity peak data

An estimate of the Lanzarote stratospheric aerosol mass can also be obtained by analysis of acidity peaks in the Greenland ice cores. The Greenland ice sheet provides a semi-continuous, partial proxy record, from which volcanic aerosol emissions can be reconstructed (e.g., Clausen and Hammer 1980; Zielinski 1995), with high sulphate signals (SO_4^{2-}) a measure of volcanically derived stratospheric sulphate. Observations of the 1991 Mount Pinatubo stratospheric aerosol cloud revealed that the cloud rapidly spread zonally before dispersing towards the polar regions (Trepte et al. 1993), where aerosols are deposited as particles on the ice-cap, leading to elevated acidity signals.

Stratospheric aerosol loading associated with each volcanic event recorded in the Greenland ice core is estimated following the technique outlined in Hammer et al. (1980), Clausen and Hammer (1988) and Zielinski (1995). This technique is based on the mid-stratospheric (> 15 km) transport and dispersal of radioactive nuclides generated during nuclear bomb testing, and their eventual deposition onto the Greenland ice sheet. It accounts for differences in the amount of fallout from low-latitude bomb tests versus high-latitude bomb tests, and applies a multiplier to convert concentration of deposited material on the ice sheet to an estimate of global stratospheric loading (Zielinski 1995). Although this technique can be used to obtain a rough estimate of the volcanic aerosol loading, one must use caution when interpreting the results. The nuclear bomb fallout models assume that the generated aerosol cloud is dispersed globally and equally into both hemispheres – this is probably not the case with all volcanic eruptions. The model developed for the transport of bomb fallout is based on bomb tests from only two northern hemisphere locations. The latitudes of source volcanoes differ from these locations, thus one would expect that the transport and dispersal of volcanic aerosols to Greenland is also different. Recent studies (Gao et al. 2004) show that the conversion factors derived from bomb

testing models result in stratospheric loading estimates that are 2 to 5 times greater than those calculated from stratospheric observations of recent eruptions (e.g., Sato et al. 1993). Another complication affecting the reliability of ice core data is the signal variability due to the large spatial variation of volcanic aerosol deposition on the ice sheet (e.g., Zielinski 1994; Free and Robock 1999; C. Gao pers. comm. 2004).

However, despite the above flaws, ice core data can still provide semi-quantitative information regarding the mass loading and transport of stratospheric aerosols from a volcanic eruption. In the case of the 1730-36 Lanzarote eruption, there is a clear acidity signal dated at 1731 in two Greenland ice cores (Figure 4.26) – the Crete (Hammer et al. 1980), and the GISP-2 core (Zielinski 1995). Although there was other volcanic activity during 1729 and 1730 that could potentially have contributed to the 1731 acidity peak, most of this volcanic activity originated from either short-lived eruptions, with VEI (volcanic explosivity index, Newhall and Self 1982) values < 2 (e.g., Asama, Japan; Vesuvius, Italy); or from small explosive volcanoes (Taal, Philippines; Villarica, Chile) located in the Southern Hemisphere, (Simkin and Siebert 1994). These eruptions were too small and/or to far south to produce a large aerosol mass that could have been transported north. Therefore, we conclude that only phases I and II of the Lanzarote eruption were capable of generating the 1731 acidity spike. Hammer et al. calculated a global aerosol fallout of ~60 Mt (Crete) for the Lanzarote peak, and Zielinski estimated an aerosol mass of ~29 Mt (GISP-2). These figures suggest that approximately 14 to 29 Mt SO_2 is required to generate this amount of volcanic aerosols. These estimates of the eruption's sulphur yield, derived from the ice core data, are comparable to the calculated petrological estimate of SO_2 release for phases I and II of the eruption. The large range in the aerosol mass loading estimates can be attributed to the variability in aerosol deposition on the ice sheet.

However, the ice-core peak represents only a fraction of the Lanzarote aerosol cloud – i.e. the stratospheric component transported north to Greenland.

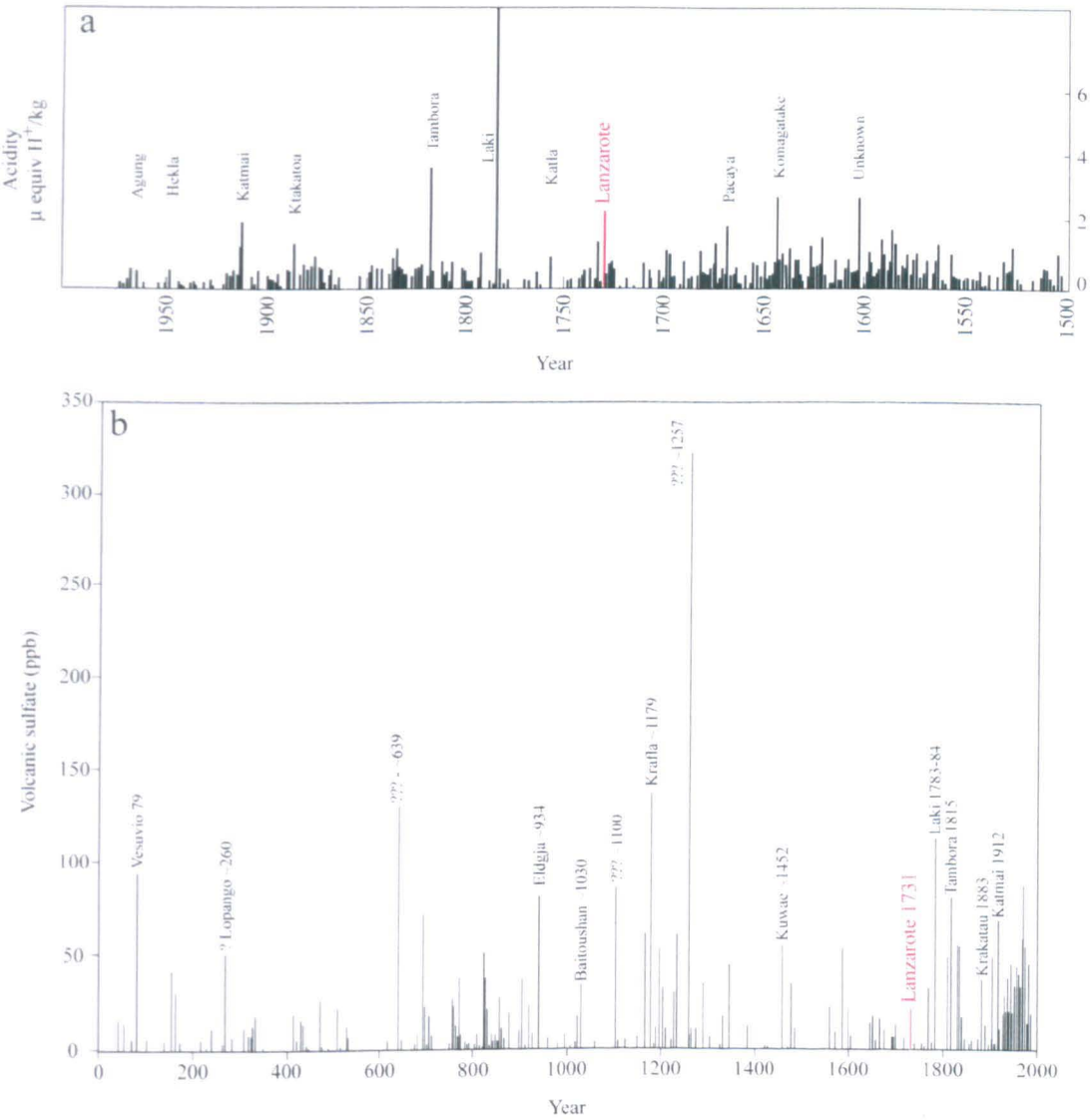

Figure 4.26 Greenland ice core time-series. (a) mean acidity of annual layers from AD 1500 to 1972 in the Crete ice core, central Greenland (after Hammer et al. 1980). (b) volcanic sulphate peaks from the bi-annual GISP-2 core (after Zielinski 1994; 1995). In both figures, the peaks attributed to the initial phases (I and II) of the Lanzarote eruption is highlighted in red. Note that there is an absence of any significant acidity peaks in the years following 1732.

The strong sulphate signal in 1731 appears to be the only major acidity spike in the Greenland ice cores attributed to the Lanzarote eruption (Figure 4.26). The lack of a strong ice core signal in the mid 1730s provides additional evidence indicating that the

later phases of the eruption either did not generate a large mass of stratospheric aerosols, or alternatively the aerosol cloud produced did not penetrate the stratosphere but instead was restricted to the troposphere, and thus was not transported as far north as Greenland.

4.9.2 Atmospheric optical depth

Acidity peaks in the ice core can be used to calculate atmospheric optical depth (τ_D) (e.g., Zielinski 1995). Optical depth is a measure of the degree of opacity of the stratosphere to sunlight transmission. The injection of volcanic sulphate aerosols into the stratosphere will increase atmospheric optical depth (and hence atmospheric turbidity). An increase in optical depth can result in surface temperature changes, thus it is necessary to determine the optical depth of individual events in order to evaluate the atmospheric impact caused by volcanic eruptions (Zielinski 1995). As described above, the ice core time series can be used to calculate the stratospheric loading of H_2SO_4 aerosols from any given volcanic eruption. The aerosol mass loading can then be used to estimate global stratospheric optical depth, using the relationship defined by Stothers (1984):

$$M_D = 1.5 \times 10^{14} \tau_D \qquad [1]$$

where M_D = total stratospheric mass loading (kg) (estimated from the ice core sulphate signal), τ_D = maximum stratospheric optical depth. For several recent eruptions, maximum optical depth values estimated in this way are considered reasonably reliable ($R^2 = 0.73$) (Zielinski et al. 1995). Based on this method, the maximum atmospheric optical depth for the Lanzarote event implied by the ice core is 0.19 (Zielinski 1995). However, a more reliable optical depth estimate for the Lanzarote eruption can be made by substituting the value of M_D calculated in this study (47 Mt of H_2SO_4 aerosol – based on the petrologic estimate of SO_2 injected into the stratosphere) into the above formula; then the atmospheric

optical depth for the Lanzarote eruption is 0.31. This value is comparable to the measured optical depth (τ_D = 0.3-0.4) for the mid-stratospheric aerosol cloud generated during the 1991 Pinatubo eruption (Self et al. 1996), and is approximately half the optical depth value estimated for the 1783 Laki eruption ($\tau_D \cong 0.8$) (Thordarson and Self 2003).

4.9.3 Estimates of tropospheric aerosol loading

The eruption of Lanzarote also released SO_2 into the lower atmosphere. The release of volcanic sulphur gases into the troposphere via low-level degassing (e.g., degassing during lava flow emplacement, effusive vent degassing) can also have detrimental effects on local and regional atmospheric conditions (refer to Chapter 1). SO_2 derived from vent degassing during phases III, IV, and V was probably injected into the troposphere. In total, these latter phase vent-derived emissions injected ~23 Mt of sulphate aerosol into the troposphere. It is also conceivable that some tropospheric aerosols were generated during the less explosive vent activity during phases I and II. Degassing during lava flow transport and emplacement in phases I and II released 2 Mt of SO_2 (degassing ratio ~94%:6%), with an identical amount of SO_2 emitted during lava flow degassing during phases III to V (degassing ratio ~86%:14%). SO_2 emissions resulting from lava flow activity account for only 9% of the total sulphur released. These gas emissions were released into the boundary layer, thus any resulting atmospheric impact was probably only locally confined, as species residence time is extremely short, due to high deposition rates and rainout (Stevenson et al. 2001). In the troposphere, the residence time of sulphate aerosols is shorter and is dependent on the volcano latitude and elevation, with modelled lifetimes (of sulphate aerosol) ranging from 2-5 days at low altitudes (< 2 km) to > 10 days near the tropics (4 km) (Stevenson et al. 2003). These figures imply that the tropospheric aerosol cloud from the latter stages of the Lanzarote eruption may have remained in the troposphere for only a few days; however, continuous eruptive activity can still maintain

high tropospheric aerosol concentrations creating a persistent lower atmospheric aerosol cloud.

The presence of a persistent lower atmospheric gas and aerosol cloud (commonly referred to as a "dry fog" (e.g., Stothers 1999, Thordarson et al. 1996) can result in atmospheric and environmental perturbations on both a local and regional scale. Dry fogs, consisting mainly of SO_2 gas and H_2SO_4 aerosols, tend to remain in the atmospheric boundary layer creating a thick fog, often with an acrid sulphurous odour. High concentrations of sulphate aerosols in these persistent plumes can lead to a multitude of problems – respiratory difficulties, damage to vegetation and crop yields and obscuration of the Sun's rays leading to reduced visibility (e.g., Grattan and Pyatt 1999; Rampino and Self 2000). Rainout from these low-level dry fogs can cause additional concerns – the generation of acidic rain can kill plants, trees and livestock, leading to loss of livelihood and possible famine. Acid rain fallout can burn humans and animals, producing skin lesions and internal organ damage (inhalation of fine acid particles can burn lungs and other organs) (e.g., Rampino and Self 2000). Fallout of aerosol particles from these dry fog veils can occur at large distances from source due to wide dispersal resulting from strong tropospheric winds (Stothers 1999), leading to unusual atmospheric conditions and acidic precipitation further afield.

4.9.4 Transport of volcanic aerosols to Northern Europe

The ice core acidity peak attributed to the Lanzarote eruption indicates that volcanic aerosol was transported extensive distances from source. The explosive phases of the Lanzarote eruption generated eruption plumes ranging from 12-16 km high (section 4.4). At the latitude of Lanzarote (~28°N), plumes of this height would reach upper tropospheric – lower stratospheric levels. Based on mean zonal wind profiles (e.g., Holten 1975), at this height and latitude, ~30 m s^{-1} westerly blowing winds prevail. Westerly stratospheric

winds would result in explosive eruption plumes being dispersed eastwards, towards northern Europe; thus transport of volcanic ash and aerosol particles from Lanzarote to Greenland is a realistic scenario. It is also possible that material injected into the upper troposphere was transported and dispersed to central and northern Europe. Transport by surface winds during winter months will move air masses from Lanzarote along west and then north trajectories to northern Europe, resulting in the transfer of volcanic particles north.

Recent studies of the phenomenon of Saharan dust storms (e.g., Goudie and Middleton 2001; Middleton et al. 2001) show that seasonally variable tropospheric winds can move air masses from these regions towards northern Europe. Saharan dust, derived from source regions ~100 km east of the Canary Islands but at the same latitude as Lanzarote, is regularly transported northward across the Mediterranean to Southern and Western Europe, and often as far north as the United Kingdom and Scandinavia. The majority of dust particles, collected from fallout events in the UK are < 20 μm in diameter, although sand-sized particles (> 62.5 μm in diameter) have also been reported, demonstrating that small particles can be effectively transported in the troposphere to distances in excess of 3000 km from latitudes of the Canaries. Thus, there exists a possibility for both extensive stratospheric and tropospheric transport of ash and volcanic aerosols across to northern Europe and the UK that cannot be ignored

4.10 Proxy climate records: evidence for the atmospheric impact of the Lanzarote eruption

Evidence for possible atmospheric and climatic impact of the Lanzarote eruption can be obtained by integrating information from proxy climate records (e.g., dendrochronological data), descriptions of anomalous weather patterns and optical effects, and contemporary historical accounts of unusual phenomena. Using a multidisciplinary approach such as this will allow us to clarify the climatic and environmental impact of this eruption. In this section, we start by examining the datasets used as indicators of past climate.

4.10.1 Dust Veil Index (DVI)

The dust veil index (DVI) developed by Lamb (1970) was one of the first attempts to categorize and compare the atmospheric and climatic impact of past volcanic eruptions. Lamb defined the term DVI/E_{max} as a numerical indicator of the relationship between climatic impact and eruption magnitude, with each eruption assigned a single DVI value. E_{max} indicates the magnitudes of the eruptions as dust producers without regard to the area over which the dust veil may have been spread by the general circulation of the atmosphere. Although this index allows one to compare the possible climatic forcing resulting from a single volcanic event, there are inherent assumptions associated with the calibration of this index that need to be considered. Firstly Lamb uses temperature data as one of the criteria in the DVI calculation; however, as temperature may be influenced by other climate forcing factors, this circular reasoning leads to some questionable DVI values (Robock 1981). Secondly, this index overemphasizes dust output from volcanic eruptions; however, recent studies have shown that volcanic aerosols, generated during activity, form the major climate-forcing component. These factors make it difficult to obtain quantitative data from the dust veil index.

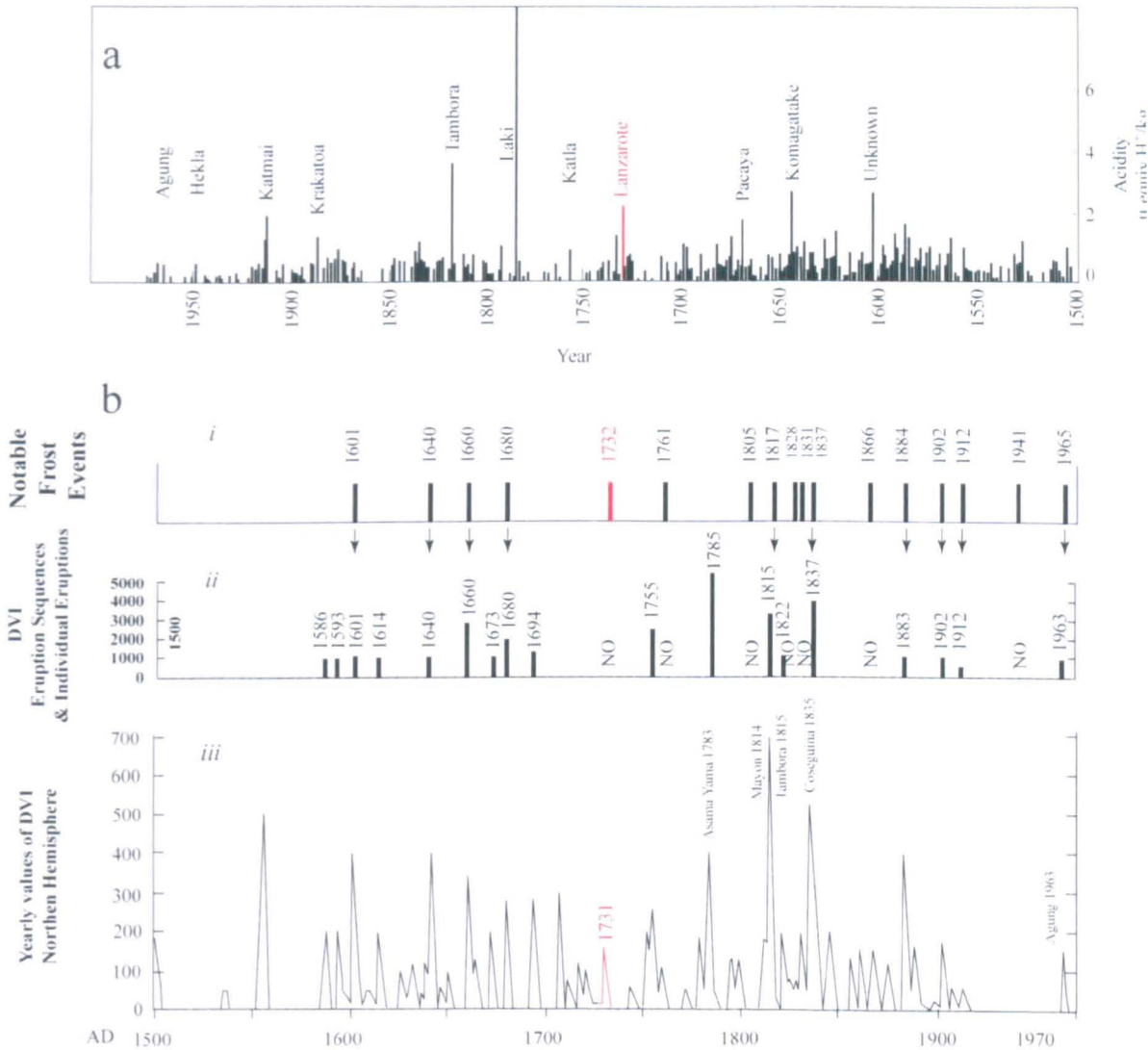

Figure 4.27 (a) shows acidity layers in the Crete ice core, central Greenland (after Hammer et al. 1980). The 1731 acidity peak attributed to the initial phases of the Lanzarote eruption is highlighted. See figure 4.26 caption for further information. (b) shows timing of frost ring events in bristlecone pine of the western United States (plate i), together with the DVI (dust veil index) volcanic eruption record of Lamb (plate ii) and yearly Northern Hemisphere (NH) DVI record (plate iii) (after LaMarche and Hirschboeck 1984). In figure (b) although no volcanic eruption is assigned to the 1732 notable frost event, we infer that this 1732 frost ring corresponds to phase I of the Lanzarote eruption, as indicated by the 1731 peak in the annual NH DVI record.

Nevertheless, the dust veil index does reflect direct evidence of sulphate aerosols in the atmosphere and therefore may still be of some qualitative use when considering the climatic influence of past eruptive activity (Figure 4.27).

Lamb (1970) describes the 1730-36 Lanzarote eruption as a "great" event – defined as an event for which a dust veil index (DVI) of ≥ 250 is probable. The eruption was assigned a DVI/E_{max} value of 400 (spread over 1730-33). In the notes accompanying the tabulated DVI information for the Lanzarote eruption, Lamb quotes two sources (Sapper 1917, 1927; Shaw 1936) that state that an extensive dry fog was reported in Europe in 1733, providing additional evidence of the climatic impact of this eruption.

4.10.2 Northern hemisphere mean surface temperature records

Volcanic aerosols injected into the upper atmosphere can cause significant climate forcing (e.g., Sato et al. 1993), with several statistical studies (e.g., Hammer et al. 1980; Grove 1988) suggesting that global climate trends observed over the past 1000 years can be explained by variations in volcanic aerosol forcing. However, these statistical studies rely on correlations between databases, which may be inadequate to evaluate volcanic signals (e.g., ice-core record) (Bertrand et al. 1999). Despite this, other studies (e.g., Robock and Mao 1995) indicate that the correlation between volcanic eruptions and surface temperature reductions can be observed in the northern hemisphere instrumental temperature record.

Based on this, we examined the mean, northern hemisphere temperature record, compiled by Mann et al. (1998). This index combines a large number of proxy datasets to produce a reconstruction of annual northern hemisphere, land surface temperatures. There is a marked decrease of ~0.3°C in this temperature series in both 1732 and 1734. The 1732

temperature anomaly can be attributed to the generation of a stratospheric aerosol cloud following intense explosive activity during eruption phases I and II. However, the lack of a significant volcanic sulphate signal in the Greenland ice core record after 1732 implies that the tropospheric aerosol burden from phases III and IV of the Lanzarote eruption may be responsible for the 1734 surface temperature anomaly. Based on theoretical modelling, Hansen et al. (1980) show that fine ash and small tropospheric aerosols in continuous production, with extensive horizontal dispersion, may be able to initiate a cooling of this size. These observed temperature perturbations agree with theoretical predictions of surface temperatures in the region 30°N to 30°S, with theoretical results suggesting a surface temperature decrease of a few tenths of a degree over a period of ~1 year (e.g., Hansen et al. 1978). More detailed two-dimensional climate models, used to evaluate the effects of volcanic aerosols on climate, also support evidence for hemispheric cooling of a few tenths of a degree Celsius following large historic eruptions (e.g., Robock 1981).

Several studies (e.g., Pollack et al. 1976) also identify a correlation between atmospheric optical depth and global temperature perturbations. Pollack et al. (1976) give a modelled relationship between stratospheric optical depth and global average temperature perturbations of:

$$\Delta T = 0.35 - 6.8\tau \qquad [2]$$

Based on the atmospheric optical depth calculated in section 4.9.2, this method gives ΔT = -1.8. Miles et al. (2003), however, present an alternative relationship between surface temperature perturbations following volcanic eruptions and optical depth [3], and also between maximum temperature response and total SO_2 loading (in grams):

$$\Delta T = (-4.5 \pm 7.5)\tau \qquad [3]$$

$$\Delta T = -3.2 \pm 0.9 \times 10^{-14}[SO_2] \qquad [4]$$

Using these relationships, equation 3 yields a ΔT range of -3.7 to 0.9, and equation 4 gives ΔT = -5.7 to -0.7. All of these figures provide additional constraints on the temperature changes following the Lanzarote eruption.

4.10.3 Dendrochronological data

An annual record of past climatic conditions is available via the study of tree ring sequences. The presence of narrow ring widths and low densities suggests cold summers were prevalent leading to years of poor growth. The correlation between low densities and known volcanic eruptions suggests volcanism is the most probable cause of the cool summers that produce these characteristics in the tree ring record (Briffa et al. 1998; Zielinski 2000); hence, tree ring datasets offer a useful means to evaluate temperature changes following a volcanic eruption.

One of the first attempts to use tree rings to derive a record of explosive volcanism was proposed by LaMarche and Hirschboeck (1984). This study suggests that the occurrence of frost-damage zones in accurately dated tree-ring sequences from sub-alpine bristlecone pines in the western USA can be linked to the climatic cooling associated with volcanic eruptions, thus frost rings represent independent proxy records of climatically effective volcanism (LaMarche and Hirschboeck 1984). A decrease in stratospheric zonal wind intensity coupled with a decrease in mean hemispheric temperature will contribute to the occurrence of frost rings. Examination of this index shows that there is a notable latewood frost event (i.e., an event occurring at two or more localities or in ≥ 50% of sampled trees

in any one locality) in 1732 (Figure 4.27b), which may correlate with the generation of stratospheric aerosols during the early stages of the Lanzarote eruption.

Jones et al. (1995) present a compilation of average maximum latewood density (MXD) and tree-ring widths (TRW) from sites in north America and western Europe to examine evidence for large-scale volcanic forcing of northern hemisphere temperature. In this index, 1732 is the 18th most extreme negative value (North America MXD index value -0.73), implying a moderate reduction in summer temperatures, particularly in the western United States. Briffa et al. (1998) present data from two alternative proxy climate records – NHD1 and NHD2. In the calibrated northern hemisphere (NHD1) record, there is a small cooling signal in 1732; this signature defines a summertime temperature anomaly of ~0.25 °C. Note that the degree of surface cooling estimated using the tree-ring record closely matches the surface temperature decrease derived from other proxy sources (Mann et al. 1998).

4.10.4 Atmospheric and climatic impact of the Lanzarote eruption: evidence from contemporary accounts

To evaluate the atmospheric and environmental impact of a volcanic eruption, such as the 1730-36 Lanzarote event, we present here a review of available historical records in conjunction with the volcanological and proxy climate data in order to evaluate the magnitude and impact of any climatic perturbations. A detailed search of historical sources to unearth accounts of this eruption and its possible effects is beyond the scope of this thesis. Nevertheless, here we present a brief review of some of the available historical material pertaining to the environmental impact of the eruption (mostly summarized in Carracedo et al. (1992))

Contemporary chronicles (e.g., diary of the parish priest of Yaiza – summarized in Table 4.1) describe phenomena caused by syn-eruptive volcanic gas release. Historical accounts of the eruption talk about "*...enormous clouds of smoke escaping, accompanied by volcanic ashes, sand and debris. The clouds condensed and dropped boiling rain on the land for ten whole days, with cattle dropping dead, asphyxiated by the vapours...*" Other accounts mention a thick haze hanging in the atmosphere with an acrid sulphurous odour causing breathing difficulties in humans, pestilent vapours causing cattle and game to drop dead, and a strong sulphur smell coming from the soil – wiping out crop yields and destroying fertile farmland. These accounts probably relate to the low-level tropospheric haze generated both during effusive vent activity and during lava flow transport during phases I and II of the eruption, indicating that there were especially high concentrations of SO_2 in the lower atmosphere from the latter part of 1730 to mid 1731. These observations agree with our estimates of high atmospheric venting of sulphur during the first two phases of activity. This localized haze is similar to the lower atmospheric haze produced during the 1783 Laki eruption, that had a damaging effect on vegetation, animals and people in 1783-84 (Thordarson and Self 2003). The mention of boiling rains and acidic waters suggests that the haze was accompanied by acidic rainfall (rainout from the acidic haze) over parts of Lanzarote. During the Laki eruption the acidity of the rainfall was such that drops burned holes in dock leaves and caused skin wounds and eye irritations in both animals and humans (Thordarson and Self 2003). We can presume that acid rain would have had similar detrimental effects on crop harvests, fertile rural lands, livestock and people in Lanzarote, and possibly on other local Canary Islands.

Evidence for the more widespread occurrence of the Lanzarote haze (or dry fog) across northern Europe can also be found in contemporary chronicles. Icelandic historical records report anomalously cold conditions and the presence of a low-level haze (*cf.* Laki 1783) in

the years following the Lanzarote eruption (T. Thordarson pers. comm.). Shaw (1936) reports the presence of an extensive dry fog over much of Europe in 1733. Camuffo and Enzi (1995) describe the appearance of a dry fog in southern Europe in 1734 and 1735. The widespread dry fog of 1734 persisted for approximately three weeks in the northeastern district of Ravenna. The dry fog of 1735 caused significant damage to crop yields – Italian historical records describe how a foul-smelling, acidic fog dried out and destroyed grain harvests, scorching corn ears yellow. This same fog enveloped the regions of Lombardy and Emilia (northern Italy) with strong, dry westerly winds carrying a caustic element that was responsible for drying out vegetation. The latter phases of the Lanzarote eruption were probably responsible for the Italian acid fogs (Camuffo and Enzi 1995).

4.10.5 Summary

As our results in this section show, the 1730-36 eruption of Lanzarote released ~44 Mt of SO_2 into the atmosphere, with ~27 Mt of this amount injected via explosive vent activity directly into the stratosphere, and ~13 Mt injected into the troposphere. Degassing during lava flow transport and emplacement released ~4 Mt of SO_2 into the atmospheric boundary layer. A prominent acidity peak in the Greenland ice core in 1731 indicates that the stratospheric injection of SO_2 was restricted to the initial 10 months of eruptive activity (during phases I and II); after this time, eruptive SO_2 emissions were dominantly tropospheric. Meteorological data suggest that a tropospheric gas and aerosol cloud can be efficiently transported large distances; therefore, climate perturbations across Northern Europe are plausible.

Although there is probably more documentary evidence supporting the widespread climatic effects from the Lanzarote eruption, the sources quoted above demonstrate that both tropospheric and stratospheric aerosol loading from the Lanzarote eruption did indeed

influence atmospheric and climatic systems on both a local and hemispheric scale. Dendrochronology confirms the existence of at least one freezing event in 1732 (evident from the frost ring data of LaMarche and Hirschboeck (1984)). The tree ring datasets, in conjunction with the northern hemisphere surface temperature record, also provide evidence for two relatively cold summers (1732 and 1734; cooling signal of ~0.3 °C). Contemporary chronicles describe phenomena that form in response to a large atmospheric injection of volcanic SO_2, e.g., tropospheric haze, stratospheric aerosol cloud, acid rain. The widespread occurrence of these phenomena is the most likely cause of the related cooling anomalies in the proxy climate records.

It is likely that an eruption of this magnitude and type will occur in the Canary Islands again. If such an eruption were to occur today, the resultant aerosol injection could have drastic effects on the environment, population, and infrastructure. The information presented in this section will enable atmospheric models (using the above data as inputs) to investigate the atmospheric and climatic perturbations that result from an injection of SO_2 into the upper troposphere/lower stratosphere, and the subsequent generation of volcanic aerosols from a persistent (1-6 years) eruptive source.

4.11 Conclusions

This study of the 1730-36 Lanzarote eruption has revealed several new insights and interpretations regarding the nature and magnitude of the eruption and its effects on northern hemisphere climate. We show that in addition to the 1783-84 Laki eruption, there was an earlier 18th century volcanic event that generated a significant amount of sulphate aerosols causing marked atmospheric and climatic perturbations. Volume estimates suggest approximately 5.3 km^3 magma was erupted as lava and tephra along a 15-km long,

E-W trending fissure, covering up to half of the island. Eruptive activity occurred in five distinct phases, with each phase containing 1-3 distinct episodes. Approximately 68% of the total volume was erupted during the first ten months of activity (during phases I and II). Each eruption episode began with sustained explosive Hawaiian to Strombolian, fire fountain activity, building large spatter and scoria cones and depositing a 3-4-m-thick scoriaceous ash blanket in proximal areas. This vent activity was accompanied and followed by effusive lava flow emplacement, producing voluminous 'a'ā and pahoehoe flows. Volumetric eruption rates range from 600 m^3/s (phases I, II) to 300 m^3/s (phases III to V), an order of magnitude smaller than volume eruption rates calculated for the Laki 1783 eruption. However, calculation of the magnitude and peak intensity parameters (after Pyle 2000) yields almost identical values to those calculated for the Laki eruption.

Glass geochemistry reveals changing magma compositions during the course of the eruption, with alkali olivine basalts common during the initial eruption phases, evolving to olivine tholeiites towards the later eruption phases. The presence of abundant peridotite xenoliths in the lavas indicate that the magma was mantle-derived. Fe^{3+}/Fe^{2+} ratios in glass inclusions calculated using fO_2, T and inclusion composition show equilibrium glass olivine Fe^{2+}/Mg partitioning. Studies on the redox conditions of magma storage indicate that the Lanzarote magmas are oxidised (fO_2 = -7.4) and sulphide-undersaturated.

Magmatic volatile studies show that both S and H_2O are coupled in the degassing process with the highest concentrations of both volatiles representing the least degassed melt. Both water and sulphur show a large range in pre-eruptive concentrations (0.03-0.26 wt% S; 0.05-0.5 wt% H_2O), indicating that inclusions are trapped at different points during magma evolution. Low S inclusions form in response to significant degassing in the conduit or shallow magma reservoirs open for volatile exsolution. Range in H_2O concentrations also

supports this notion of low-pressure degassing resulting in crystallization of volatile-reduced melts. Chlorine also shows variable pre-eruptive concentrations (0.04-0.20 wt%). Matrix glass volatile contents are generally lower for all three volatile elements, ranging from 0.01-0.03 wt% S, 0.03-0.06 wt% H_2O and <0.027 wt% Cl.

Based on this work, we show that use of the conventional petrologic method (which relies on an average pre-eruptive S content) will significantly underestimate the sulphur release from this event, therefore we devise a method to back-calculate original sulphur concentrations using the S/*I* ratio (where *I* is a highly incompatible element, e.g., K, P, Ti). This ratio remains constant until the onset of degassing, glass inclusions with the highest S/*I* ratios undergo the least amount of degassing and undegassed magmas from the same liquid line of descent will have the same S/*I* ratio. Thus knowing this ratio, original S contents of degassed liquids can be calculated using their *I* concentrations. This original S content (C_o) can then be used in the petrologic method to obtain a more reasonable estimate of the sulphur release.

Using this refined petrological approach we estimate that ~45 Mt of SO_2 was released during this eruption. Approximately 65% of this SO_2 (~29 Mt) was injected to upper tropospheric and lower stratospheric levels over a 6-8 month period (i.e. during phases I and II). Later phases of the eruption although not as explosive still contributed ~15 Mt in total to the overall sulphur budget. Although the total amount of SO_2 is half the amount produced during the 1783-84 Laki eruption, it still represents a significant sulphur release – the amount released here is double the amount released during the 1991 Pinatubo eruption. Assuming a gas-particle conversion efficiency of 86%, we estimate that ~47 Mt of stratospheric sulphate aerosol was generated during the initial explosive activity of phases I

and II. Phases III to V injected ~23 Mt of H_2SO_4 aerosols mainly to upper tropospheric levels.

There is a prominent ice core acidity peak in the Greenland ice core in 1731, indicating that at least 20 Mt of SO_2 was required to generate the aerosol loading recorded by this sulphate peak. It also provides evidence that eruption plumes containing sulphur species, injected to upper tropospheric/lower stratospheric heights, can be transported via regional weather systems to Northern Europe. The lack of strong peaks after 1731 suggests that stratospheric injection of SO_2 was perhaps restricted to the initial ten months of eruptive activity; after this time volatile emissions were dominantly tropospheric. For latitudes of the Canaries, initial investigations show that seasonally variable tropospheric winds may move air masses from those regions towards Britain (e.g., Saharan dust transport to the UK). When coupled with initial high altitude ash cloud transport by westerly stratospheric winds for explosive eruption columns (such as Fogo AD 1563) (Walker and Croasdale, 1971) the potential for efficient long-distance transport of ash and aerosols from eruptions in the Canaries across to the UK cannot be ignored.

An examination of available proxy climate records and historical reports suggests that the 1730-36 Lanzarote eruption had a marked environmental and atmospheric impact in the northern hemisphere. The injection of sulphate aerosols directly into the upper atmosphere was responsible for reported atmospheric turbidity (e.g., reports of dry fogs over southern Europe) and a decrease in Northern Hemisphere summer temperatures of 0.3 °C. A further measure of the climatic impact can be found by studying the environmental response of trees to volcanic forcing of climate. The record of stress in the dendrochronological record (two cool summers – 1732 and 1734 and a frost ring event in 1732) together with the acid peaks in the ice-core record indicate that these climate perturbations are plausibly related

to the amount of SO_2 released during the eruption of Lanzarote. Future studies need to concentrate on the development of atmospheric models to help constrain and predict the generation, transport and fate of both stratospheric and tropospheric aerosol clouds from persistent, long-lasting volcanic activity such as the 1730 Lanzarote eruption.

Chapter 5: Conclusions

This chapter provides a brief summary of the main conclusions arising from this study. Volcanic eruptions can have a profound influence on the Earth's atmosphere and biosphere (Chapter 1). In particular the release of volcanic SO_2 can result in detrimental climatic, atmospheric and environmental effects.

We conclude that the mass of gas released during activity (related to magma composition, initial volatile content, magma volume) together with the atmospheric level that receives the gas emissions (related to eruption style, intensity, duration and explosivity) are two of the most important factors in determining the environmental impact. Volcano location and local atmospheric conditions also play a part (albeit to a lesser extent). It is therefore vital to conduct a complete volcanological study of the eruptive event prior to assessing the volatile release and resultant atmospheric impact (e.g., chapters 3 and 4).

Accurately estimating how much sulphur is released by volcanic activity can be achieved via a variety of methods – we show here that the classic petrological approach provides realistic estimates of volcanic SO_2 emissions for tholeiitic to transitional basaltic magmas from ocean island basaltic eruptions. This situation is in contrast to that in many arc eruptions where the petrologic method underestimates the sulphur release, due to the development of excess sulphur (Chapter 2). However this work also shows that adaptations of the petrologic method (Chapter 2 – section 2.8) may produce viable SO_2 estimates from a variety of volcanic settings of variable magma compositions.

Studies on the 1362 Öræfajökull eruption (Iceland) indicate that, although this eruption was a highly explosive Plinian eruption that generated a 30 km high stratospheric eruption

column, the sulphur release from this event was minor. Less than 2 Mt of SO_2 was released via melt degassing. The injection of large volumes of ash into the upper atmosphere seems to be the major environmental hazard resulting from this event. Future studies need to concentrate on building up a more complete picture of the eruptive history of Öræfajökull – this will allow us to ascertain the frequency of large explosive eruptions from this volcano and assess whether or not future eruptions have the potential to release larger volumes of magma and thus emit a greater amount of volatiles into the upper atmosphere.

In contrast, the 1730-36 eruption of Lanzarote released ~45 Mt of SO_2 (chapter 4) – double the amount released during the 1991 Pinatubo eruption. This study has shown that these magmas are relatively oxidised therefore are able to dissolve large amounts of S (> 2600 ppm S) without sulphide precipitation. Thus, as the melt retains large amounts of S, the S-release potential of the magma is high; thus even small volume eruptions on Lanzarote have the ability to release large amounts of SO_2 into the atmosphere.

This event was a major supplier of SO_2 to the atmosphere and thus caused significant atmospheric perturbations, e.g., mean northern hemisphere surface temperatures decreased by ~0.5 °C in the years following the eruption. Contemporary accounts also report the presence of dry fogs and cooler conditions across Europe. This event was similar in style to the 1783-84 Laki eruption in Iceland. Many studies have documented the SO_2 release from the Laki event and modelled its atmospheric and climate impact. Although these studies can be applied to the Lanzarote eruption, future work needs to concentrate on the development of atmospheric models to help constrain and predict the generation, transport and fate of both stratospheric and tropospheric aerosol clouds from these types of fissure eruptions. It is possible that tropospheric injection of sulphate aerosols and the subsequent

transport of these aerosols can generate atmospheric and environmental responses of a similar magnitude to that of a large stratospheric sulphur injection.

References

Adams NK, de Silva SL, Self S, Salas G, Schubring S, Permenter JL, Arbesman K (2001) The physical volcanology of the 1600 eruption of Huaynaputina, southern Peru. Bull Volcanol 62: 493-518

Amundsen HEF (1987) Peridotite xenoliths from Gran Canaria, Canary Islands: Evidence for metasomatic processes and partial melting in the lower oceanic crust. N Jb Miner Abh 156: 121-140

Anderson AT (1974) Chlorine, sulfur, and water in magmas and oceans. Geol Soc Am Bull, 85: 1485-1492

Anderson DJ, Lindsley DH, Davidson PM (1993) QUILF: a Pascal program to assess equilibria among Fe-Mg-Mn-Ti oxides, pyroxenes, olivine and quartz. Comp Geosci, 19: 1333-1350

Bacon CR, Hirschmann MM (1988) Mg/Mn partitioning as a test for equilibrium between co-existing Fe-Ti oxides. Am Mineral 73: 57-61

Balhaus C, Berry RF, Green DH (1991) High pressure experimental calibration of the olivine-orthopyroxene-spinel oxygen geobarometer: implications for the oxidation state of the upper mantle. Contrib Min Petrol 107: 27-40

Bay RC, Bramall N, Buford Price P (2004) Bipolar correlation of volcanism with millennial climate change. Proc Natl Acad Sci 101 (17): 6341-6345

Blake S (2003) Correlations between eruption magnitude, SO_2 yield, and surface cooling. In Volcanic Degassing, C. Oppenheimer et al. (eds). Geol Soc of London Spec Pubs 213 pp 371-381

Bluth GJS., Schnetzler CC, Krueger AJ, and Walter LS (1993) The contribution of explosive volcanism to global atmospheric sulfur dioxide concentrations. Nature 366: 327-329

Bluth GJS, Casadevall, TJ, Schnetzler, CC, Doiron SD, Walter LS, Krueger AJ, Badruddin M (1994) Evaluation of sulfur dioxide emissions from explosive volcanism: the 1982-83 eruptions of Galunggung, Java, Indonesia. J Volc Geotherm Res 63: 243-256

Bonadonna C, Ernst GGJ, Sparks RSJ (1998) Thickness variations and volume estimates of tephra fall deposits: the importance of particle Reynolds number. Journal of Volc and Geotherm Res, 81: 173-187

Briffa KR, Jones PD, Schweingruber FH, Osborn TJ (1998) Influence of volcanic eruptions on Northern Hemisphere summer temperature over the past 600 years. Nature 393: 450-454

Briffa KR, Osborn TJ, Schweingruber FH (2004) Large-scale temperature inferences from tree rings: a review. Global and Planetary Change 40: 11-26

Bryan SE, Cook A, Evans JP, Colls PW, Wells MG, Lawrence MG, Jell JS, Greig A, Leslie R (2004) Pumice rafting and faunal dispersion during 2001-2002 in the Southwest Pacific: record of a dacitic submarine explosive eruption from Tonga. Earth and Planetary Sci Lett 227 (1-2): 135-154

Burton KW, Gannoun A, Birck JL, Allegre CJ, Schiano P, Clocchiatti R, Alard O (2002) The compatibility of rhenium and osmium in natural olivine and their behaviour during mantle melting and basalt genesis. Earth Planet Sci Lett 198: 63-76

Camuffo D, Enzi S (1995) Impact of the clouds of volcanic aerosols in Italy during the last 7 centuries. Nat Hazards 11: 135-161

Carey S, Sparks RSJ (1986) Quantitative models of the fallout and dispersal of tephra from volcanic eruption columns. Bull Volcanol, 48: 109-125

Carey S, Sigurdsson H (1989) The intensity of Plinian eruptions. Bull Volcanol 51: 28-40

Carey S, Gardner J, Sigurdsson H (1995) The intensity and magnitude of Holocene Plinian eruptions from Mount St Helens volcano. Journal of Volc and Geotherm Res, 66: 185-202

Carmichael ISE (1967) The iron-titanium oxides of salic volcanic rocks and their associated ferromagnesian silicates. Contrib Min and Petrol, 14: 36-64

Carmichael ISE, Ghiorso MS (1990) The effect of oxygen fugacity on the redox state of natural liquids and their crystallizing phases. Reviews in Mineralogy 24: 191-212

Carn SA, Krueger AJ, Bluth GJS, Schaefer SJ, Krotkov NA, Watson IM, Datta S (2003) Volcanic eruption detection by the Total Ozone Mapping Spectrometer (TOMS) instruments: a 22-year record of sulphur dioxide and ash emissions. In Volcanic Degassing, Oppenheimer C, Pyle DM, Barclay J (eds), Geol Soc of London Spec Pub 213: pp 177-20

Carracedo JC, Badiola ER (1991) Mapa geologico de la erupcion de Lanzarote de 1730-36. 1;25 000 Estacion Volcanologica de Canarias. In Carracedo JC and Badiola ER (eds) Lanzarote, La erupcion volcanica de 1730, Cabildo Insular de Lanzarote

Carracedo JC, Badiola ER, Soler V (1992) The 1730-36 eruption of Lanzarote, Canary Islands: a long high magnitude basaltic fissure eruption. J Volc Geotherm Res 53: 239-250

Carracedo JC, Day S, Guillou H, Rodriguez Badiola E, Canas JA, Perez Torrado FJ (1998) Hotspot volcanism close to a passive continental margin: the Canary Islands. Geol Mag 135: 591-604

Carroll MR, Rutherford MJ (1988) Sulfur speciation in hydrous experimental glasses of varying oxidation state: Results from measured wavelength shifts of sulphur x-rays. Am Mineral 73: 845-849

Casadevall TJ, Krohn MD (1995) Effects of the 1992 Crater Peak eruptions on airports and aviation operations in the United States and Canada. US Geol Surv Bull, 2139: 205-220

Cervantes P, Wallace P (2003) Magma degassing and basaltic eruption styles: a case study of ~2000 year BP Xitle volcano in central Mexico. J Volc Geotherm Res 120: 249-270

Cioni R, Marianelli P, Santacroce R, Sbrana A (2000) Plinian and subPlinian eruptions. In Encyclopedia of Volcanoes, H Sigurdsson, BF Houghton et al. (eds), academic press, San Diego, pp 477-494

Clausen HB, Hammer CU (1988) The Laki and Tambora eruptions as revealed in the Greenland ice cores from 11 locations. Annals of Glacialogy 10: 16-22

Clemente B, Scaillet B, Pichavant, M (2004) The solubility of sulphur in hydrous rhyolitic melts. Journal of Petrol, 45: 2171-2196

Coffey MT (1996) Observations of the impact of volcanic activity on stratospheric chemistry. J Geophys Res 101 (D3): 6767-6780

Crutcher HL (1969) Temperature and humidity in the troposphere. In Climate of the free atmosphere, Rex DF (ed), World Surv of Climat 4: 45-84

Davis MG, Garcia MO, Wallace PJ (2003) Volatiles in glasses from Mauna Loa Volcano, Hawaii: Implications for magma degassing and contamination and growth of Hawaiian volcanoes. Contrib Mineral Petrol 144: 570-591

De Hoog JCM Koetsier GW, Bronto S, Sriwana T, van Bergen MJ (2001) Sulfur and chlorine degassing from primitive arc magmas: temporal changes during the 1982-1983 eruptions of Galunggung (West Java, Indonesia). J Volc Geotherm Res 108: 55-83

De Silva S, Zielinski GA (1998) Global influence of the AD 1600 Huaynaputina eruption, Peru. Nature 393: 455-458

Devine JD, Sigurdsson H, Davis AN, Self S (1984) Estimates of sulfur and chlorine yield to the atmosphere from volcanic eruptions and potential climatic effects. J Geophys Res 89: 6309-6325

Devine JD, Gardner JE, Brack HP, Layne GD, Rutherford MJ (1995) Comparison of microanalytical methods for estimating H_2O contents of silicic volcanic glasses. Amer Mineral 80: 319-328

Dixon JE, Clague DA, Stolper EM (1991) Degassing history of water, sulfur and carbon in submarine lavas from Kilauea Volcano, Hawaii. Journal of Geol 99: 371-394

Dunbar NW, Zielinski GA, Voisins DT (2003) Tephra layers in the Siple Dome and Taylor Dome ice cores, Antarctica: sources and correlations. J Geophys Res 108: 6-11

Durand M, Grattan J (1999) Extensive respiratory health effects of volcanogenic dry fog in 1783 inferred from European documentary sources. Environmental Geochem and Health 21: 371-376

Free M, Robock A (1999) Global warming in the context of the Little Ice Age. J Geophys Res 104: 19057-19070

Fierstein J, Hildreth W (1992) The Plinian eruptions of 1912 at Novarupta, Katmai National Park, Alaska. Bull Volcanol, 54: 646-684

Fierstein J, Nathenson M (1992) Another look at the calculation of fallout tephra volumes. Bull Volcanol, 54: 156-167

Francis P, Horrocks L, Oppenheimer C (2000) Monitoring gases from andesite volcanoes. Phil Trans R Soc London 358: 1567-1584

Fuster JM, Fernandez Santin S, Sagredo J (1968) Geologia y volcanologia de las Islas Canarias, Lanzarote. Inst Lucas Mallada, CSIC, Madrid

Gardner JE, Rutherford M, Carey S, Sigurdsson H (1995) Experimental constraints on pre-eruptive water contents and changing magma storage prior to explosive eruptions of Mount St Helens volcano. Bull Volcanol 57: 1-17

Gardner JE, Thomas RME, Jaupart C, Tait S (1996) Fragmentation of magma during Plinian volcanic eruptions. Bull Volcanol 58: 144-162

Gardner JE, Tait S (2000) The caldera-forming eruption of Volcan Ceboruco, Mexico. Bull Volcanol, 62: 20-33

Gerlach TM, McGee KA (1994) Total sulfur dioxide emissions and pre-eruption vapor saturated magma at Mount St Helens. Geophys Res Lett 21: 2833-2836

Gerlach TM, Westrich HR, Casadevall TJ, Finnegan, DL (1994) Vapor saturation and accumulation in magmas of the 1989-1990 eruption of Redoubt Volcano, Alaska. J Volc Geotherm Res 62: 317-337

Goudie AS, Middleton NJ (2001) Saharan dust storms: nature and consequences. Earth Sci Reviews 56: 179-204

Graf HF, Feichter J, Langmann B (1997) Volcanic sulphur emissions: estimates of source strength and its contribution to the global sulphate distribution. J Geophys Res 102: 10727-10738

Grattan JP, Brayshay M, Sadler J (1998) Modelling the distal impacts of past volcanic gas emissions: Evidence of Europe-wide environmental impacts from gases emitted during the eruption of the Italian and Icelandic volcanoes 1783. Quaternaire 9: 25-35

Grattan JP, Pyatt FB (1999) Volcanic eruptions dry fogs and the European palaeoenvironmental record: localized phenomena or hemispheric impacts? Global and Planetary Change 21: 173-179

Gronvold K, Larsen G, Einarsson P, Thorarinsson S, Saemundsson K (1983) The Hekla eruption 1980-81. Bull Volcanol 46: 349-363

Grove JM (1988) The Little Ice Age. Methuen, London

Guilbaud M-N, Self S, Thordarson Th, Blake S (2005) Morphology, surface structures, and emplacement of lavas produced by Laki, A.D. 1783-1784. In Manga M, Ventura G (eds), Kinematics and dynamics of lava flows: Geol Soc Am Special Paper 396: 81-72

Gurenko AA, Schmincke H-U (2000) S concentrations and its speciation in Miocene basaltic magmas north and south of Gran Canaria (Canary Islands): Constraints from glass inclusions in olivine and clinopyroxene. Geochim Cosmochim Acta 64: 2321-2337

GVN Bulletin, SEAN 09:08, 1984

GVN Bulletin, BGVN 25:02, 2000

Hall VA, Pilcher JR (2002) Late-Quaternary Icelandic tephras in Ireland and Great Britain: detection, characterization and usefulness. The Holocene, 12 (2): 223-230

Halmer MMS, Schminke HU, Graf HF (2002) The annual volcanic gas input into the atmosphere, in particular into the stratosphere: a global data set for the past 100 years. J Volc Geotherm Res 115: 511-528

Hammer CU, Clausen HB, Dansgaard W (1980) Greenland ice sheet evidence of post-glacial volcanism and its climatic impact. Nature 288: 230-235

Hansen JE, Wang WC, Lacis AA (1978) Mount Agung eruption provides test of a global climatic perturbation. Science 199: 1065-1068

Hansen JE, Lacis AA, Lee P, Wang WC (1980) Climatic effects of atmospheric aerosols. Ann NY Acad Sci 338: 575-587

Hansen J, Sato M, Ruedy R (1997) Radiative forcing and climate response. J Geophys Res 102: 6831-6864

Hansen J, Nazarenko I (2004) Soot climate forcing via snow and ice albedos. Proc Natl Acad Sci 101: 423-428

Haraldsson KO, Arnason SG, Larsen G, Eiriksson J (2002) The Hekla eruption of 2000 - The tephra fall, paper presented at 25th Nordic Geological Winter Meeting, Reykjavik

Hayakawa Y, Shirao M (1988) November 21-23, 1986 Izu-Oshima 2B lava flows and their eruption. Bull Volcanol Soc Jpn 33: s77-s91

Heliker C, Kauahikaua J, Sherrod DR, Lisowski M, Cervelli PF (2003) The rise and fall of Puu Oo cone, 1983-2002. USGS prof paper 1676: 29-51

Helz RT, Thornber CR (1987) Geothermometry of Kilauea Iki Lava Lake, Hawaii. Bull Volcanol 49: 651-668

Hernandez-Pacheco E (1909) Estudio geologico de Lanzarote y de las Isletas Canarias. Mem R Soc Esp Hist Nat, T IV

Hernandez-Pacheco E (1960) En Relacion con las grandes erupciones volcanicas del siglo XVIII y 1824 en Lanzarote. El museo Canario Las Palmas de Gran Canaria

Hoblitt RP, Wolfe EW, Scott WE, Couchman MR, Pallister JS, Javier D (1996) The preclimactic eruptions of Mount Pinatubo, June 1991. In Fire and Mud: Eruptions and lahars of Mount Pinatubo, Phillipines, (eds) CG Newhall and RS Punongbayan, Phillipine Institute of Volcanology and Seismology, Quezon City, and University Washington Press, Seattle, 457-512

Hofmann DJ, Solomon S (1989) Ozone destruction through heterogeneous chemistry following the eruption of El Chichon. J Geophys Res 94: 5029-5041

Hon K, Kauahikaua J, Denlinger R, Mackay K (1994) Emplacement and inflation of pahoehoe sheet flows: observations and measurements of active lava flows on Kilauea Volcano, Hawaii. Geol Soc Am Bull 106: 351-370

Horn S, Schmincke H-U (2000) Volatile emission during the eruption of Baitoushan Volcano (China/North Korea) ca. 969 AD. Bull Volcanol 61: 537-555

Horwell CJ, Sparks RSJ, Brewer TS, Llewellin EW, Williamson BJ (2003) Characterization of respirable volcanic ash from the Soufriere Hills volcano, Montserrat, with implications for human health hazards. Bull Volcanol 65: 346-362

Houghton BF, Wilson CJN, Pyle DM (2000) Pyroclastic fall deposits. In Encyclopedia of Volcanoes, H Sigurdsson, BF Houghton et al. (eds), academic press, San Diego, pp 555-570

Houghton BF, Wilson CJN, Fierstein J, Hildreth W (2004) Complex proximal deposition during the Plinian eruptions of 1912 at Novarupta, Alaska. Bull Volcanol 66: 95-133

Inman DL (1952) Measures for describing the size distribution of sediments. Journal of Sed Petrol, 22: 125-145

Jacoby GC, Workman KW, D'arrigo RD (1999) Laki eruption of 1783, tree rings, and disaster for northwest Alaska Inuit. Quat Sci Rev 18: 1365-1371

Jakosky BM (1986) Volcanoes, the stratosphere, and climate. J Volc Geotherm Res 28: 247-255

Jones PD, Briffa KR, Schweingruber FH (1995) Tree-ring evidence of the widespread effects of explosive volcanic eruptions. Geophys Res Lett 22: 1333-1336

Jugo PJ, Luth RW, Richards JP (2005) An experimental study of the sulfur content in basaltic melts saturated with immiscible sulfide or sulfate liquids at 1300 °C and 1.0 GPa. J Petrol 46: 783-798

Kokelaar BP (1986) Magma-water interactions in subaqeous and emergent basaltic volcanism. Bull Volcanol 48: 275-289

Koyaguchi T (1996) Volume estimation of tephra-fall deposits from the June 15, 1991, eruption of Mount Pinatubo by theoretical and geological methods. In Fire and Mud: Eruptions and lahars of Mount Pinatubo, Phillipines, (eds) CG Newhall and RS Punongbayan, Phillipine Institute of Volcanology and Seismology, Quezon City, and University Washington Press, Seattle, 513-543

Kress VC, Carmichael ISE (1991) The compressibility of silicate liquids containing Fe_2O_3 and the effect of composition, temperature, oxygen fugacity and pressure on their redox states. Contrib Mineral Petrol 99: 176-185

Krueger AJ, Walter LS, Bhartia PK, Schnetzler CC, Krotkov NA, Sprod I, Bluth GJS (1995) Volcanic sulfur dioxide measurements from the Total Ozone Mapping Spectrometer (TOMS) instruments. J Geophys Res 100: 14057-14076

Krueger AJ, Schnetzler CC, Walter LS (1996) The December 1981 eruption of Nyamuragira Volcano (Zaire) and the origin of the "mystery cloud" of early 1982. J Geophys Res 101: 15191-16196

LaMarche Jr VC, Hirschboeck KK (1984) Frost rings in trees as records of major volcanic eruptions. Nature 307: 121-126

Lacasse C (2001) Influence of climate variability on the atmospheric transport of Icelandic tephra in the subpolar North Atlantic. Global and Planetary change, 29: 31-55

Lamb HH (1970) Volcanic dust in atmosphere. Phil Trans Roy Soc A 266n 1178: 25-533

Langmuir CH, Klein EM, Plank T (1992) Petrological systematics of mid-ocean ridge basalts: Constraints on melt generation beneath ocean ridges. In Mantle flow and melt generation at mid-ocean ridges, Morgan JP, Blackman DK, Sinton JM (Eds), AGU Geophys Monogr 71, pp 183-280

Larsen G, Gudmundsson MT, Bjornsson H (1998) Eight centuries of periodic volcanism at the center of the Iceland hotspot revealed by glacier tephrostratigraphy. Geology 26: 943-946

Larsen G, Dugmore AJ, Newton AJ (1999) Geochemistry of historical age silicic tephras in Iceland. The Holocene, 9: 463-471

LeBas MJ, LeMaitre RW, Streckeisen A, Zanettin B (1986) A chemical classification of volcanic-rocks based on the total alkali silica diagram. J Petrol 27 (3): 745-750

Lipman PW, Banks NG (1987) Aa flow dynamics, Mauna Loa 1984. United States Geol Surv Prof Paper 1350: 1527-1567

Luhr JF, Carmichael ISE, Varekamp JC (1984). The 1982 eruptions of El Chichon Volcano, Chiapas, Mexico: Mineralogy and petrology of the anhydrite-bearing pumices. J Volc Geotherm Res 23: 69-108

Luhr JF (2000) The geology and petrology of Volcan San Juan (Nayarit, Mexico) and the compositionally zoned Tepic Pumice. Journal of Volc and Geotherm Res, 95: 109-156

Lundstrom CC, Hoernle K, Gill J (2003) Major and trace element and U-series disequilibria in Holocene volcanic rocks from the Canary Islands: the role and mechanism of lithospheric melting. Geochim Cosmochim Acta 67: 4153-4177

Macdonald R, McGarvie DW, Pinkerton H, Smith RL (1990) Petrogenetic evolution of the Torfajökull volcanic complex, Iceland. I. Relationship between the magma types. J Petrol, 31: 429-459

Macias JL, Arce JL, Mora JC, Espindola JM, Saucedo R (2003) A 550-year-old Plinian eruption at El Chichon Volcano, Mexico: Explosive volcanism linked to reheating of the magma reservoir. Journal of Geophys Res, 108, B12: 2569

Mandeville CW, Carey S, Sigurdsson H (1996) Magma mixing, fractional crystallization and volatile degassing during the 1883 eruption of Krakatau volcano, Indonesia. J Volc Geotherm Res 74: 243-274

Mann ME, Bradley RS, Hughes MK (1998) Global-scale temperature patterns and climate forcing over the past six centuries. Nature 392: 779-787

Mathez EA (1976) Sulfur solubility and magmatic sulfides in submarine basalt glass. J Geophys Res 81: 4269-4276

McCormick MP, Thomason LW, Trepte CR (1995) Atmospheric effects of the Mount Pinatubo eruption. Nature 373: 399-404

McPhie J, Doyle M, Allen R (1993) Volcanic textures: A guide to the interpretation of textures in volcanic rocks. Hobart (Tasmanian Govt. Printing Office)

Middleton NJ, Betzer PR, Bull PA (2001) Long-range transport of 'giant' aeolian quartz grains: linkage with discrete sedimentary sources and implications for protective particle transfer. Marine Geology 177: 411-417

Miles GM, Grainger RG, Highwood EJ (2003) Volcanic aerosols: The significance of volcanic eruption strength and frequency for climate. QJR Meteorol Soc 128: 1-999

Neumann ER, Griffin WL, Pearson NJ, O'Reilly SY (2004) The evolution of the upper mantle beneath the Canary Islands: Information from trace elements and Sr isotope ratios in minerals in mantle xenoliths. J Petrol 45: 2573-2612

Newhall CG, Self S (1982) The volcanic explosivity index (VEI): An estimate of explosivity magnitude for historic volcanism. J Geophys Res 87: 1231-1238

Ohlhorst S, Behrens H, Holtz F (2001) Compositional dependence of molar absorptivities of near-infrared OH- and H_2O bands in rhyolitic to basaltic glasses. Chem Geol, 174: 5-20

Olafsdottir R, Hoskulddon A, Gronvold K (2002) The evolution of the lava flow from the Hekla eruption 2000, paper presented at 25th Nordic Geological Winter Meeting, Reykjavik

O'Neill HStC (1987a) The quartz-fayalite-iron and quartz-fayalite-magnetite equilibria and the free energies of formation of fayalite (Fe_2SiO_4) and magnetite (Fe_3O_4). Am Mineral 72: 67-75

O'Neil HStC (1987b) The free energies of formation of NiO, CoO, Ni_2SiO_4. Am Mineral 72: 280-291

Palais JM, Sigurdsson H (1989) Petrologic evidence of volatile emissions from major historic and pre-historic volcanic eruptions. In Berger A, Dickinson RE, Kidson JW (eds) Understanding climate change. Geophys Monograph 52: 31-53

Palais JM, Taylor K, Mayewski PA, Grootes P (1991) Volcanic ash from the 1362 AD Öræfajökull eruption (Iceland) in the Greenland ice sheet. Geophys Res Lett, 18: 1241-1244

Parfitt EA, Wilson L, Neal CA (1995) Factors influencing the height of Hawaiian lava fountains: implications for the use of fountain height as an indicator of magma gas content. Bull Volcanol 57: 440-450

Perkins ME, Nash WP, Brown FH, Fleck RJ (1995) Fallout tuffs of Trapper Creek, Idaho - A record Miocene explosive volcanism in the Snake River Plain volcanic province. Geol Soc Am Bull 107: 1484-1506

Persson C (1971) Tephrochronological investigation of peat deposits in Scandinavia and the Faeroe Islands. Sveriges Geologiska Undersoekning 65 (2): 1-34

Pinto JR, Turco RP, Toon OB (1989) Self-limiting physical and chemical effects in volcanic eruption clouds. J Geophys Res 94: 11165-11174

Prata AJ, Rose WI, Self S, O'Brien DM (2004) Global, long-term Sulphur dioxide measurements from TOVS data: A new took for studying explosive volcanism and climate. In Volcanism and the Earth's atmosphere, Robock A, Oppenheimer C (eds), pp 75-92, AGU Geophys Monogr Ser 139

Prestvik T (1979) Petrology of hybrid intermediate and silicic rocks from Öræfajökull, southeast Iceland. GFF, 101: 299-308

Prestvik T (1982) Petrography, chemical characteristics and nomenclature of Öræfajökull rocks. Jokull, 32: 69-76

Prestvik T, Goldberg S, Karlsson H, Gronvold K (2001) Anomalous strontium and lead isotope signatures in the off-rift Öræfajökull central volcano in south-east Iceland evidence for enriched end member(s) of the Iceland mantle plume? Earth Planetary Sci Lett 190: 211-220

Pyle DM (1989) The thickness, volume and grain size of tephra fall deposits. Bull Volcanol, 51: 1-15

Pyle DM (1995) Assessment of the minimum volume of tephra fall deposits. Journal of Volc and Geotherm Res 69: 379-382

Pyle DM (2000) Sizes of volcanic eruptions. In Encyclopedia of Volcanoes, H Sigurdsson, BF Houghton et al. (eds), academic press, San Diego pp 263-269

Rampino MR, Self S (1982) Historic eruptions of Tambora (1815), Krakatau (1883), and Agung (1963), their stratospheric aerosols and climatic impact. Quat Res 18: 127-143

Rampino MR, Self S (1984) Sulphur-rich volcanic eruptions and stratospheric aerosols. Nature 310: 677-679

Rampino MR, Self S, Stothers RB (1988) Volcanic winters. Ann Rev Earth Planet Sci 16: 73-99

Robock A (1981) A latitudinally dependent volcanic dust veil index and its effects on climate simulations. J Volc Geotherm Res 11: 67-80

Robock A, Mao J (1995) The volcanic signal in surface temperature observations. Jour Clim 8: 1086-1103

Robock A (2000) Volcanic eruptions and climate. Rev Geophys 38: 191-219

Roeder PL, Emslie RF (1970) Olivine-liquid equilibrium. Contrib Min Petrol 29: 275-289

Roggensack K, Hervig RL, McKnight SB, Williams SN (1997) Explosive basaltic volcanism from Cerro Negro Volcano: Influence of volatiles on eruptive style. Science 277: 1639-1642

Romero R, Carrasco D, Arana V, Fernandez J (2003) A new approach to the monitoring of deformation on Lanzarote (Canary Islands): an 8-year radar perspective. Bull Volcanol 65: 1-7

Rose WI et al. (2004) The February-March 2000 eruption of Hekla, Iceland from a satellite perspective. In Volcanism and the Earth's Atmosphere, Robock A, Oppenheimer C (eds). AGU Geophys Monogr Ser 139: 107-133

Rosi M, Principe C, Vecci R (1993) The 1631 Vesuvius eruption. A reconstruction based on historical and stratigraphical data. Journal of Volc and Geotherm Res, 58: 151-182

Rossi MJ (1997) Morphology of the 1984 open-channel lava flow at Krafla volcano, Northern Iceland. Geomorph 20: 95-112

Rowe EC, Schilling JG (1979) Fluorine in Iceland and Reykjanes Ridge basalt. Nature 279: 33-37

Rowland SK Walker GPL (1987) Toothpaste lava: Characteristics and origin of a lava structural type transitional between pahoehoe and aa. Bull Volcanol 48: 631-641

Ruiz CR (1997) Cronicas documentales sobre las erupciones de Lanzarote. Fundacion Cesar Manrique, Madrid

Sato M, Hansen JE, McCormick MP, Pollack JB (1993) Stratospheric aerosol optical depths, 1850-1990. J Geophys Res 98: 22987-22994

Scaillet B, Clemente B, Evans B, Pichavant M (1998) Redox control of sulfur degassing in silicic magmas. J Geophys Res 103: 23937-23949

Scaillet B, Luhr JF, Carroll MR (2003) Petrological and volcanological constraints on volcanic sulfur emissions to the atmosphere. In Volcanism and the Earth's Atmosphere, Robock A, Oppenheimer C (eds), AGU Geophys Monogr Ser 139: 11-40

Scasso RA, Corbella H, Tiberi P (1994) Sedimentological analysis of the tephra from the 12-15 August 1991 eruption of Hudson volcano. Bull Volcanol 56: 121-132

Scuderi LA (1993) A 2000-year tree ring record of annual temperatures in the Sierra Nevada Mountains. Science 259: 14331436

Self S, Rampino MR, Newton MS, Wolff JA (1989) Volcanological study of the great Tambora eruption of 1815. Geology 12: 659-663

Self S, King AJ (1996) Petrology and sulfur and chlorine emissions of the 1963 eruption of Gunung Agung, Bali, Indonesia. Bull Volcanol 58: 263-285

Self S, Zhao J, Holasek RE, Torres RC, King AJ (1996) The atmospheric impact of the 1991 Mount Pinatubo eruption. In Fire and Mud: Eruptions and lahars of Mount Pinatubo, Phillipines, (eds) CG Newhall and RS Punongbayan, Phillipine Institute of Volcanology and Seismology, Quezon City, and University Washington Press, Seattle, 1089-1115

Self S, Keszthelyi L, Thordarson Th (1998) The importance of pahoehoe. Ann Rev Earth Planet Sci 26: 81-110

Self S, Gertisser R, Thordarson Th, Rampino MR, Wolff JA (2004) Magma volume, volatile emissions, and stratospheric aerosols from the 1815 eruption of Tambora. Geophys Res Lett 21: L20608 doi:10.1029/2004GL020925

Sharma et al. (2004) SO_2 emissions from basaltic eruptions and the excess sulfur issue. Geophys Res Lett 31: L13612 doi: 10.1029/2004GL019688

Sigurdsson H, Carey S (1989) Plinian and co-ignimbrite tephra fall from the 1815 eruption of Tambora volcano. Bull Volcanol 51: 243-270

Sigurdsson H, Carey S, Palais JM, Devine J (1990) Pre-eruption compositional gradients and mixing of andesite and dacite magma erupted from Nevado del Ruiz Volcano, Columbia in 1985. J Volc Geotherm Res 41: 127-151

Sigvaldason GE (1974) The petrology of Hekla and origin of silicic rocks in Iceland. Soc Sci Islandica V: 1-44

Simkin T, Siebert L (1994) Volcanoes of the World, 2nd edition. Geosci Press, Tucson Arizona, 349pp

Solana MC, Kilburn CRJ, Rodriguez Badiola E, Aparicio A (2004) Fast emplacement of extensive pahoehoe flow-fields: the case of the 1736 flows from Montana de las Nueces, Lanzarote. J Volc Geotherm Res 132: 189-207

Sparks RSJ, Pinkerton H (1978) Field measurements of the rheology of lava. Nature 276: 383-385

Sparks RSJ, Wilson L, Sigurdsson H (1981) The pyroclastic deposits of the 1875 eruption of Askja, Iceland. Phil Trans Royal Society of London, Series A 229: 241-273

Sparks RSJ (1986) The dimensions and dynamics of volcanic eruption columns. Bull Volcanol, 48: 3-15

Sparks RSJ, Bursik MI, Carey SN, Gilbert JS, Glaze LS, Sigurdsson H, Woods AW (1997) Volcanic plumes. JS Wiley and Sons, Chichester, pp 574

Stevenson D, Highwood EJ, Johnson CE, Collins WJ, Derwent RG (2001) Atmospheric modeling of the 1783-1784 Laki eruption. UGAMP Newsletter 2: 43-44

Stevenson DS, Johnson CE, Collins WJ, Derwent RG (2003) The tropospheric sulphur cycle and the role of volcanic SO_2. In Volcanic Degassing, Oppenheimer C, Pyle DM, Barclay J (eds) Geol Soc London Spec Pub 213: 295-305

Stevenson, JA, McGarvie DW, Smellie JL, Gilbert JS (2006) Subglacial and ice-contact volcanism at the Öræfajökull stratovolcano, Iceland. Bull Volcanol 68: 737-752

Stothers RB, Rampino MR (1983) Historic volcanism, European dry fogs, and Greenland acid precipitation, 1500 BC to AD 1500. Science 222: 411-413

Stothers RB (1984) The great Tambora eruption in 1815 and its aftermath. Science 224: 1191-1198

Stothers RB (1986) The great dry fog of 1783. Climatic Change 32: 79-89

Stothers RB, Wolff JA, Self S, Rampino MR (1986) Basaltic fissure eruptions, plume heights, and atmospheric aerosols. Geophys Res Lett 13, 8: 725-728

Stothers RB (1999) Volcanic dry fogs, climate cooling, and plague pandemics in Europe and the Middle East. Climatic Change 42: 713-723

Sugawara T (2001) Ferric iron partitioning between plagioclase and liquid: thermodynamics and petrological applications. Contrib Mineral Petrol 141: 659-686

Sumner J (1998) Formation of clastogenic lava flows during fissure eruption and scoria cone collapse: the 1986 eruption of Izu-Oshima Volcano, Eastern Japan. Bull Volcanol 60: 195-212

Sutton AJ, Elias T, Gerlach TM, Stokes JB (2001) Implications for eruptive processes as indicated by sulphur dioxide emissions from Kilauea Volcano, Hawaii, 1979-1997. J Volc Geotherm Res 108: 283-302

Swanson DA (1973) Pahoehoe flows from the 1969-1971 Mauna Ulu eruption, Kilauea Volcano, Hawaii. Geol Soc Am Bull 84: 615-626

Tabazadeh A, Turco RP (1993) Stratospheric chlorine injection by volcanic eruptions: Hydrogen chloride scavenging and implications for ozone. Science 20: 1082-1086

Tamic N, Behrens H, Holtz F (2001) The solubility of H_2O and CO_2 in rhyolitic melts in equilibrium with a mixed CO_2-H_2O fluid phase. Chem Geol, 174: 333-347

Textor C, Graf HF, Herzog M, Oberhuber JM (2003) Injection of gases into the stratosphere by explosive volcanic eruptions. J Geophys Res 108 (D19) doi: 10.1029/2002JD002987

Textor C, Graf HF, Timmreck C, Robock A (2004) Emissions from volcanoes. In Emissions of Atmospheric Trace Compounds, C Granier, P Artaxo, C Reeves (eds), Dordrecht, pp 269-303

Thomas LE, Hawksworth CJ, Van Calsteren P, Turner SP, Rogers NW (1999) Melt generation between ocean islands: A U-Th-Ra isotope study from Lanzarote in the Canary Islands. Geochim Cosmochim Acta 63, 23/24: 4081-4099

Thomason LW, Osborne MT (1992) Lidar conversion parameters derived from SAGE II extinction measurements. Geophys Res Lett 19: 1655-1658

Thorarinsson S (1958) The Öræfajökull eruption of 1362. Acta Naturalia Islandica, Vol II: no. 2

Thordarson Th, Self S (1993) The Laki (Skaftár Fires) and Grímsvötn eruptions in 1783-1785. Bull Volcanol 55: 233-263

Thordarson T, Self S, Oskarsson N, Hulsebosch T (1996) Sulphur, chlorine and fluorine degassing and atmospheric loading by the 1783-1784 AD Laki (Skaftar Fires) eruption in Iceland. Bull Volcanol 58: 205-225

Thordarson Th, Self S (1996) Sulfur, chlorine and fluorine degassing and atmospheric loading by the Roza eruption, Columbia River Basalt Group, Washington, USA. J Volc Geotherm Res 74: 49-73

Thordarson Th, Miller DJ, Larsen G, Self S, Sigurdsson H (2001) New estimates of sulfur degassing and atmospheric mass-loading by the 934 AD Eldgjá eruption, Iceland. J Volc Geotherm Res 108: 33-54

Thordarson Th, Self S (2003) Atmospheric and environmental effects of the 1783-1784 Laki eruption: A review and reassessment. J Geophys Res 108 (D1) doi: 10.1029/2001JD002042

Thordarson Th, Self S, Miller DJ, Larsen G, Vilmundardottir EG (2003) Sulphur release from flood lava eruptions in the Veidivötn, Grímsvötn and Katla volcanic systems, Iceland. In Volcanic Degassing, Oppenheimer C, Pyle DM, Barclay J (eds), Geol Soc of London Spec Pubs, 213: 103-121

Thouret JC, Juvigne E, Gourgaud A, Boivin P, Davila J (2002) Reconstruction of the AD 1600 Huaynaputina eruption based on the correlation of geologic evidence with early Spanish chronicles. J Volc Geotherm Res, 115: 529-570

Trepte CR, Viega RE, McCormick MP (1993) The poleward dispersal of Mount Pinatubo aerosol. J Geophys Res 98: 18563-18573

Twomey S (1974) Pollution and planetary albedo. Atmospheric Environment 8: 1251-1265

Wadge G (1981) The variation of magma discharge during basaltic eruptions. J Volc Geotherm Res 11:139-168

Walker GPL (1971) Grain size characteristics of pyroclastic deposits. Journal of Geology, 79: 696-714

Walker GPL (1972) Crystal concentration in ignimbrites. Contrib Mineral Petrol, 36: 135-146

Walker GPL (1980) The Taupo pumice: product of the most powerful known (ultraplinian) eruption? J Volc Geotherm Res 8: 69-94

Walker GPL (1981) Plinian eruptions and their products. Bull Volcanol, 44-2: 223-240

Walker GPL (1999) Volcanic rift zones and their intrusion swarms. J Volc Geotherm Res 94: 21-34

Wallace P, Anderson AT (2000) Volatiles in magmas. In Encyclopedia of Volcanoes, H Sigurdsson, BF Houghton et al. (eds), academic press, San Diego pp 149-170

Wallace PJ (2001) Volcanic SO_2 emissions and the abundance and distribution of exsolved gas in magma bodies. J Volc Geotherm Res 108: 85-106

Wallace PJ (2004) From mantle to atmosphere: magma degassing, explosive eruptions, and volcanic volatile budgets. In Melt inclusions in volcanic systems: methods, applications and problems; B De Vivo, RJ Bodnar (eds), Elsevier, Amsterdam pp 105-127

Wen S, Rose WI (1994) Retrieval of particle sizes and masses in volcanic clouds using AVHRR band 4 and 5. J Geophys Res 99: 5421-5431

Westrich HR, Gerlach TM (1992) Magmatic gas source for the stratospheric SO_2 cloud from the June 15, 1991 eruption of Mount Pinatubo. Geology 20: 867-870

Wiesner MG, Wetzel A, Catane SG, Listanco EL, Mirabueno HT (2004) Grain size, areal thickness distribution and controls on sedimentation of the 1991 Mount Pinatubo tephra layer in the South China Sea. Bull Volcanol, 66: 226-242

Williams SN, Self S (1983) The October 1902 Plinian eruption of Santa Maria Volcano, Guatemala. J Volc Geotherm Res, 16: 33-56

Wilson CJN, Hildreth W (1997) The Bishop Tuff: new insights from eruptive stratigraphy. J Geol 105: 407-439

Wilson L, Sparks RSJ, Huang TC, Watkins ND (1978) The control of volcanic column heights by eruption energetics and dynamics. J Geophys Res 83: 1829-1836

Wilson L Head JW (1981) Ascent and eruption of basaltic magma on the Earth and Moon. J Geophys Res 86: 2971-3001

Witham CS, Oppenheimer C (2005) Mortality in England during the 1783-84 Laki Craters eruption. Bull Volcanol 67: 15-26

Wolfe EW, Garcia MO, Jackson DB, et al. (1987) The Puu Oo eruption of Kilauea volcano, episodes 1-20, January 4, 1983 to June 8, 1984. USGS Prof Paper 1350: 471-508

Wolfe EW, Hoblitt RP (1996) Overview of the eruptions. In Fire and Mud: Eruptions and lahars of Mount Pinatubo, Phillipines, CG Newhall and RS Punongbayan (eds), Phillipine Institute of Volcanology and Seismology, Quezon City, and University Washington Press, Seattle, 1089-1115

Zhao J, Turco RP, Toon OB (1995) A model simulation of Pinatubo volcanic aerosols in the stratosphere. J Geophys Res 100: 7315-7328

Zielinski GA, Mayewski PA, Meeker LD, Whitlow S, Twickler MS, Morrison M, Meese DA, Gow AJ, Alley RB (1994) Record of volcanism since 7000 BC from the GISP2 Greenland ice core and implications for the volcano-climate system. Science 264: 948-952

Zielinski GA (1995) Stratospheric loading and optical depth estimates of explosive volcanism over the last 2100 years derived from the Greenland Ice Sheet Project 2 ice core. J Geophys Res 100 (D10): 20937-20955

Zielinski GA (2000) Use of paleo-records in determining variability within the volcanism-climate system. Quat Sci Rev 19: 417-438

Appendix A1: Supplementary information

(i) Calculation of error associated with petrologic method estimate of SO_2 release

$$M_s = M_v\,(1\text{-}W_{xtls})\,[C_{inc} - C_{matrix}] \qquad [1]$$

Percent error (2σ) associated with the petrologic method (equation 1) is calculated as follows:

M_s ± % error in M_v + % error in W_{xtls} + % error in ΔC

ΔC represents error associated with concentration of S as determined using electron microprobe analyses, this is calculated as follows:

S concentration (C) of glass inclusion = $\overline{C}_{inc} \pm \sigma_{inc}$

S concentration (C) of matrix glass = $\overline{C}_{mat} \pm \sigma_{mat}$

where $\overline{C}$ = average of all analyses; σ = 1 standard deviation

Difference = $(\overline{C}_{inc} - \overline{C}_{mat}) \pm \sqrt{\sigma_{inc}^2 + \sigma_{mat}^2} = \Delta C \pm \sigma_{\Delta C}$

(ii) Geochemistry dataset accompanying notes

Appendices A2 to A6 contain glass geochemistry (electron microprobe) and whole-rock XRF data from the following volcanic eruptions – Krafla 1984, Mauna Loa 1984, Hekla 1980, and Hekla 2000. In addition to these datasets, glass geochemistry data from Izu-Oshima 1986 is also presented.

Each dataset consists of the following:

(a) Mean matrix glass geochemistry dataset, together with mean and standard deviation (1σ), each point in this table represents an average of 5-10 spots on a matrix glass sample.

(b) Mean matrix glass data – defined as the mean original matrix glass composition. Normalized analysis represents the volatile-free mean matrix glass value (i.e. corrected for volatile content based on the total excluding volatiles). 1σ and 2σ standard deviation also shown for reference.

(c) Normalized (volatile-free) glass inclusion geochemistry dataset – this dataset also includes results from a comparison of different statistical techniques used to select inclusions that are statistically similar to the mean matrix glass composition (results shown for Krafla 1984, Mauna Loa 1984) - Euclidean distance function (*D*) (based on the method described in chapter 2), similarity coefficient (siminal), and standard deviation. The similarity coefficient (siminal) was calculated using all ten major element oxides and also using only five selected major element oxides (SiO_2, Al_2O_3, FeO, MgO, CaO) in the comparison. Siminal values need to fall within a 96% confidence level to be accepted. To compare analyses using the standard deviation, we checked each inclusion analysis to see if it falls within 2σ standard deviation of the

mean matrix glass composition. In all tables analyses shaded grey represent inclusions that are statistically similar to the mean matrix glass composition based on $D < 6.23$, siminal results are shown in the last column and analyses marked with an asterisk represent inclusions that fall within the 2σ standard deviation of the mean matrix glass composition.

(d) Original glass inclusion data shown together with mean and standard deviation (1σ)

(e) Bulk XRF whole-rock analysis

NB. We show matrix glass and glass inclusion data only for the 1986 Izu-Oshima eruption.

(iii) Electron microprobe glass standard data

This dataset contains microprobe glass standard data. The accepted value is shown for each glass standard, together with our mean value and standard deviation (2σ), n = total number of analyses. Reproducibility of the glass standard over time provides an indication of machine stability. The standard deviation is used as an estimate of relative analytical error. The following glass standards were analysed:

VG-2 (USNM-111240/52) – Basaltic glass, Juan de Fuca Ridge (Smithsonian)

JDF-D2 – Basaltic glass, Juan de Fuca Ridge (Lamont Doherty Observatory)

TB-1G – Basaltic glass (USGS)

KBT-1G – Nephelinite glass, Knippa basalt, Texas (USGS)

VG-568 (USNM-72854) – Rhyolite glass Yellowstone (Smithsonian)

KN-18 – Comenditic glass, Kenya (C. Lacasse, Rhode Island)

KE-12 – Comenditic glass, Kenya (C. Lacasse, Rhode Islands)

Appendix A2 Krafla 1984 glass geochemistry

(a) Matrix glass data

Sample	Label	SiO_2	TiO_2	Al_2O_3	FeO	MnO	MgO	CaO	Na_2O	K_2O	P_2O_5	S	Cl	F	Total
KR1 Scoria	KR01-1	49.75	2.44	12.34	16.03	0.27	5.14	9.74	2.57	0.38	0.26	0.050	0.015	0.000	99.04
KR1 Scoria	KR01-2	49.64	2.41	12.35	16.07	0.27	5.08	9.66	2.42	0.38	0.26	0.059	0.018	0.000	98.65
KR9 Scoria	KRgl1_kr9b	49.89	2.22	13.13	15.18	0.24	5.44	10.06	2.45	0.35	0.23	0.041	0.016	0.001	99.29
KR7 Scoria	KRgl1_kr7	49.85	2.37	12.45	15.38	0.26	5.16	10.14	2.36	0.37	0.24	0.040	0.017	0.003	98.68
KR8 Scoria	KRgl1_kr8a	49.66	2.38	12.60	15.59	0.25	5.08	9.94	2.44	0.38	0.26	0.054	0.017	0.003	98.69
KR2 Scoria	KRgl1_kr2	49.45	2.12	13.31	14.69	0.24	5.59	10.07	2.40	0.34	0.22	0.047	0.018	0.000	98.53
KR1 Scoria	KRgl1_kr1	49.52	2.41	12.65	15.70	0.25	5.01	9.83	2.44	0.38	0.26	0.056	0.018	0.000	98.59
KR8 Scoria	krxtl1kr8/7	50.29	2.42	12.12	15.65	0.25	4.92	10.04	2.27	0.39	0.24	0.058	0.017	0.000	98.70
KR9 Scoria	krxtl1kr9/8	48.97	2.25	12.22	15.70	0.24	5.86	10.07	2.21	0.34	0.25	0.058	0.010	0.000	98.25
KR5 Lava	krgl1kr5/	51.16	2.43	12.59	15.24	0.25	4.84	10.20	1.57	0.38	0.25	0.044	0.020	0.000	99.02
KR5 Lava	krgl1kr5a	49.85	2.34	12.45	14.99	0.25	4.73	10.18	2.31	0.38	0.27	0.043	0.015	0.000	97.85
KR4 Lava	krgl1kr4	50.10	2.23	12.88	14.63	0.23	4.76	10.13	1.77	0.36	0.23	0.043	0.012	0.000	97.41
KR4 Lava	krgl1kr4d	51.10	2.20	13.31	14.63	0.24	5.39	10.10	2.50	0.34	0.24	0.042	0.015	0.000	100.15
Average		**49.94**	**2.32**	**12.65**	**15.34**	**0.25**	**5.15**	**10.01**	**2.29**	**0.37**	**0.25**	**0.049**	**0.016**	**0.001**	**98.68**
Standard Deviation (1σ)		**0.59**	**0.10**	**0.38**	**0.48**	**0.01**	**0.32**	**0.16**	**0.28**	**0.02**	**0.01**	**0.007**	**0.003**	**0.001**	

Appendix A2 Krafla 1984 glass geochemistry

(b) Mean matrix glass data

Sample		SiO_2	TiO_2	Al_2O_3	FeO	MnO	MgO	CaO	Na_2O	K_2O	P_2O_5	S	Cl	F	Total	Total excluding volatiles
KRAFLA	Average	49.94	2.32	12.65	15.34	0.25	5.15	10.01	2.29	0.37	0.25	0.049	0.016	0.001	98.68	98.57
	Standard deviation (1σ)	0.59	0.10	0.38	0.48	0.01	0.32	0.16	0.28	0.02	0.01	0.007	0.003	0.001		
	Standard deviation (2σ)	1.18	0.21	0.76	0.96	0.02	0.64	0.33	0.56	0.04	0.03	0.014	0.006	0.002		
	Mean matrix glass normalized	50.66	2.36	12.83	15.57	0.25	5.23	10.16	2.32	0.37	0.25				100.00	

(c) Normalized glass inclusion data

Sample	Label	SiO_2	TiO_2	Al_2O_3	FeO	MnO	MgO	CaO	Na_2O	K_2O	P_2O_5	D^2	$D(2\sigma)$	$D(1\sigma)$	Total	Siminal	Siminal (5 oxide)
KR1	*KR01-11*	*50.48*	*2.12*	*13.91*	*14.43*	*0.25*	*5.12*	*10.34*	*2.70*	*0.37*	*0.27*	*23.76*	*2.44*	*4.87*	*100.00*	*94.91*	*96.14*
KR1	kr1/5	51.02	2.40	13.90	14.55	0.25	3.82	10.91	2.57	0.36	0.23	56.80	3.77	7.54	100.00	92.91	90.24
KR1	kr1/4	50.62	2.28	13.50	15.09	0.26	4.33	10.82	2.48	0.34	0.26	33.94	2.91	5.83	99.99	94.29	93.71
KR1	kr1/7	50.57	2.36	13.65	15.01	0.25	4.15	10.84	2.54	0.35	0.28	40.76	3.19	6.38	99.99	93.85	92.66
KR1	kr1/17	50.62	2.06	13.82	14.94	0.24	5.51	9.28	2.91	0.39	0.23	55.48	3.72	7.45	100.00	92.49	94.99
KR1	kr1/24	51.01	2.19	13.87	14.48	0.26	4.55	10.48	2.58	0.33	0.24	32.36	2.84	5.69	100.00	94.10	93.75
KR1	*kr1/27**	*50.31*	*2.28*	*13.43*	*15.60*	*0.25*	*4.73*	*10.04*	*2.69*	*0.40*	*0.25*	*10.06*	*1.59*	*3.17*	*100.00*	*95.93*	*96.78*
KR1	kr1/28*	50.32	2.32	13.38	15.57	0.26	4.49	10.34	2.68	0.40	0.24	14.20	1.88	3.77	100.00	94.89	95.87
KR1	kr1/30	50.51	2.34	13.22	15.66	0.28	4.38	10.29	2.67	0.38	0.27	18.23	2.13	4.27	100.00	94.40	95.73
KR1	kr1/32	50.43	2.36	13.73	15.49	0.27	3.96	10.30	2.74	0.45	0.27	46.27	3.40	6.80	100.00	91.89	93.37
KR1	kr1/33	50.67	2.45	13.53	15.39	0.24	4.05	10.18	2.82	0.42	0.23	31.78	2.82	5.64	100.00	92.56	94.18
KR8	*krxtl1kr8/4*	*49.67*	*1.85*	*16.56*	*13.14*	*0.22*	*4.57*	*10.99*	*2.49*	*0.32*	*0.19*	*212.06*	*7.28*	*14.56*	*100.00*	*86.18*	*97.95*
KR8	*krxtl1kr8/15**	*50.54*	*2.35*	*13.18*	*15.56*	*0.25*	*5.00*	*10.05*	*2.29*	*0.50*	*0.27*	*54.59*	*3.69*	*7.39*	*100.00*	*95.64*	*98.31*

Grey shading indicates statistically similar inclusions with D <6.3; analyses marked with an asterisk (*) denote inclusions within 2σ of the mean matrix glass composition; analyses in *italics* represent inclusions with a similarity coefficient >96.

Appendix A2 Krafla 1984 glass geochemistry

(d) Glass inclusion data

Sample	Label	SiO_2	TiO_2	Al_2O_3	FeO	MnO	MgO	CaO	Na_2O	K_2O	P_2O_5	S	Cl	F	Total	Total excluding volatiles
KR1	KR01-11	49.75	2.09	13.71	14.22	0.25	5.05	10.19	2.66	0.37	0.26	0.178	0.013	0.000	98.90	98.54
KR1	kr1/5	50.48	2.38	13.75	14.40	0.25	3.78	10.80	2.54	0.36	0.23	0.160	0.010	0.000	99.28	98.95
KR1	kr1/4	49.76	2.25	13.27	14.83	0.26	4.26	10.63	2.44	0.33	0.26	0.173	0.014	0.000	98.64	98.29
KR1	kr1/7	49.80	2.32	13.44	14.78	0.25	4.08	10.68	2.50	0.35	0.28	0.188	0.010	0.000	98.85	98.47
KR1	kr1/17	49.82	2.03	13.60	14.70	0.24	5.42	9.13	2.87	0.38	0.23	0.161	0.020	0.000	98.75	98.41
KR1	kr1/24	51.20	2.20	13.93	14.54	0.27	4.57	10.52	2.59	0.33	0.24	0.151	0.023	0.000	100.71	100.38
KR1	kr1/27	49.57	2.25	13.24	15.37	0.25	4.66	9.89	2.65	0.39	0.25	0.147	0.022	0.000	98.83	98.52
KR1	kr1/28	49.56	2.28	13.18	15.34	0.26	4.43	10.19	2.64	0.39	0.24	0.146	0.019	0.000	98.80	98.49
KR1	kr1/30	50.13	2.33	13.12	15.54	0.28	4.35	10.21	2.65	0.37	0.27	0.149	0.022	0.000	99.58	99.26
KR1	kr1/32	49.69	2.33	13.53	15.26	0.27	3.90	10.15	2.70	0.44	0.26	0.149	0.019	0.000	98.84	98.53
KR1	kr1/33	49.85	2.41	13.31	15.15	0.24	3.99	10.02	2.77	0.42	0.23	0.138	0.019	0.000	98.68	98.38
KR8	krxtl1kr8/4	49.51	1.84	16.51	13.10	0.22	4.56	10.95	2.48	0.32	0.19	0.184	0.015	0.000	100.06	99.68
KR8	krxtl1kr8/15	49.70	2.31	12.96	15.30	0.25	4.92	9.88	2.25	0.49	0.27	0.157	0.024	0.000	98.65	98.33
Average		**49.95**	**2.27**	**13.40**	**14.97**	**0.26**	**4.42**	**10.29**	**2.61**	**0.37**	**0.25**	**0.159**	**0.018**	**0.000**	**99.12**	
Standard Deviation (1σ)		**0.50**	**0.09**	**0.26**	**0.43**	**0.01**	**0.32**	**0.27**	**0.10**	**0.03**	**0.02**	**0.017**	**0.005**	**0.000**		

(e) XRF bulk analysis

Sample	Type	SiO_2	TiO_2	Al_2O_3	FeO	MnO	MgO	CaO	Na_2O	K_2O	P_2O_5
KR-10	1984 lava block	50.12	2.08	13.32	16.39	0.24	5.93	10.23	2.36	0.34	0.21

Appendix A3 Mauna Loa 1984 glass geochemistry

(a) Matrix glass data

Sample	SiO_2	TiO_2	Al_2O_3	FeO	MnO	MgO	CaO	Na_2O	K_2O	P_2O_5	S	Cl	F	Total
ml1-3	52.04	2.32	13.35	11.68	0.18	5.78	10.18	2.31	0.42	0.28	0.012	0.009	0.003	98.58
ml-5a	52.46	2.33	13.52	11.66	0.17	5.88	10.17	2.37	0.43	0.28	0.017	0.007	0.000	99.30
ml1-5f	51.99	2.33	13.36	11.75	0.17	5.80	10.20	2.22	0.43	0.27	0.032	0.013	0.000	98.59
ml1-5k	52.11	2.34	13.41	11.69	0.18	5.84	10.18	2.24	0.43	0.28	0.017	0.008	0.002	98.73
ml1-5p	52.06	2.34	13.38	11.64	0.18	5.81	10.17	2.38	0.42	0.28	0.014	0.005	0.008	98.69
ml1-4	51.00	2.35	13.21	11.66	0.17	5.94	10.33	2.29	0.40	0.28	0.036	0.008	0.000	97.71
ml-5b	51.28	2.36	13.32	11.73	0.18	6.01	10.28	2.30	0.42	0.26	0.010	0.008	0.000	98.16
ml-6a	50.86	2.35	13.17	12.01	0.18	6.00	10.42	2.34	0.42	0.26	0.013	0.007	0.000	98.03
ml-6g	51.24	2.35	13.31	11.73	0.17	5.99	10.30	2.33	0.43	0.29	0.010	0.007	0.000	98.16
ml2-1n	50.93	2.33	13.21	11.68	0.17	6.01	10.37	2.30	0.42	0.28	0.009	0.009	0.000	97.73
ml2-3a	50.89	2.22	13.53	11.27	0.17	6.30	10.36	2.13	0.41	0.26	0.013	0.010	0.000	97.58
ml2-3k	51.12	2.19	13.66	11.16	0.16	6.24	10.51	2.34	0.40	0.25	0.011	0.006	0.000	98.04
ml2-5h	50.72	2.34	13.24	11.53	0.17	6.10	10.26	2.31	0.42	0.28	0.020	0.008	0.000	97.42
Average	**51.44**	**2.32**	**13.36**	**11.63**	**0.17**	**5.98**	**10.29**	**2.30**	**0.42**	**0.27**	**0.016**	**0.008**	**0.001**	**98.21**
Standard Deviation (1σ)	**0.58**	**0.05**	**0.14**	**0.21**	**0.01**	**0.16**	**0.10**	**0.06**	**0.01**	**0.01**	**0.008**	**0.002**	**0.002**	

Appendix A3 Mauna Loa 1984 glass geochemistry

(b) Mean matrix glass data

Sample		SiO_2	TiO_2	Al_2O_3	FeO	MnO	MgO	CaO	Na_2O	K_2O	P_2O_5	S	Cl	F	Total	Total excluding volatiles
MLOA	Average	51.44	2.32	13.36	11.63	0.17	5.98	10.29	2.30	0.42	0.27	0.016	0.008	0.001	98.21	98.18
MLOA	Standard deviation (1σ)	0.58	0.05	0.14	0.21	0.01	0.16	0.10	0.06	0.01	0.01	0.008	0.002	0.002		
MLOA	Standard deviation (2σ)	1.16	0.10	0.28	0.42	0.02	0.32	0.20	0.12	0.02	0.02					
	Mean matrix glass normalized	52.39	2.36	13.61	11.85	0.17	6.09	10.48	2.34	0.43	0.28					

(c) Normalized glass inclusion data

Sample	Type	SiO_2	TiO_2	Al_2O_3	FeO	MnO	MgO	CaO	Na_2O	K_2O	P_2O_5	*D*	*D*(1σ)	Total	Siminal	Siminal (selected 5 oxides)
ml1-1a	85μm round	53.05	2.06	14.37	10.56	0.16	5.85	10.99	2.34	0.37	0.25	44.1	6.6	100.00	93.07	94.80
ml1-4f	*100μm t-shape clean*	*52.84*	*2.24*	*14.01*	*11.58*	*0.17*	*5.85*	*10.21*	*2.38*	*0.43*	*0.27*	*6.7*	*2.6*	*100.00*	*97.72*	*98.54*
ml1-1-a	80μm round, clean	52.74	2.04	14.44	10.38	0.17	6.27	10.98	2.34	0.38	0.26	45.4	6.7	100.00	94.14	94.75
ml1-4-a	100μm teardrop shape clean	55.01	2.15	14.12	8.35	0.14	6.29	10.97	2.32	0.40	0.24	387.8	19.7	100.00	90.58	90.89
ml1-4-e	*500μm big inc*	*52.45*	*2.28*	*14.23*	*11.29*	*0.16*	*5.94*	*10.51*	*2.45*	*0.43*	*0.25*	*38.2*	*6.2*	*100.00*	*96.36*	*97.61*
ml2-1g	*200μm elong triangle*	*52.38*	*2.30*	*13.93*	*11.70*	*0.17*	*5.75*	*10.70*	*2.36*	*0.42*	*0.27*	*18.8*	*4.3*	*100.00*	*97.95*	*97.76*
ml2-1m	30μm triangular	52.45	2.39	13.86	11.84	0.18	4.98	11.18	2.42	0.42	0.27	105.1	10.3	100.00	95.75	94.70
ml2-2e	*500μm large inc**	*52.35*	*2.42*	*13.60*	*11.83*	*0.18*	*5.97*	*10.47*	*2.45*	*0.44*	*0.29*	*9.6*	*3.1*	*100.00*	*97.94*	*99.52*
ml2-2m	*long 100μm square**	*52.08*	*2.39*	*13.70*	*11.94*	*0.17*	*6.05*	*10.50*	*2.47*	*0.44*	*0.27*	*7.2*	*2.7*	*100.00*	*98.48*	*99.43*
ml2-5a	skinny 50μm long; 1 ves	53.36	2.24	12.92	11.44	0.18	7.09	9.44	2.49	0.59	0.26	462.0	21.5	100.00	91.47	93.12
ml2-6a	80μm elong,square; 2 ves	52.90	2.53	13.52	11.10	0.18	6.36	10.12	2.49	0.49	0.30	92.0	9.6	100.00	94.72	96.87
ml2-6c	*80μm square, crack thru middle*	*51.69*	*2.29*	*13.21*	*12.08*	*0.19*	*6.80*	*10.79*	*2.25*	*0.43*	*0.28*	*46.5*	*6.8*	*100.00*	*96.32*	*96.10*
ml2-6e	*rectangle 60μm**	*52.15*	*2.40*	*13.49*	*11.84*	*0.19*	*6.31*	*10.52*	*2.36*	*0.45*	*0.30*	*17.1*	*4.1*	*100.00*	*97.06*	*98.94*
ml2-6f	*elong sausage shape, 50μm*	*52.16*	*2.41*	*13.72*	*11.89*	*0.19*	*6.09*	*10.45*	*2.33*	*0.49*	*0.27*	*43.5*	*6.6*	*100.00*	*96.93*	*99.63*
ml2-6h	v.skinny, long elong	51.88	2.28	14.77	11.33	0.17	5.70	10.72	2.48	0.43	0.24	107.2	10.4	100.00	95.48	95.63
ml2-6i	square 40μm; rim around inc	52.18	2.39	14.11	12.17	0.18	5.29	10.42	2.54	0.44	0.27	53.9	7.3	100.00	95.92	95.94
ml2-6j	*v-shape 30-40μm skinny*	*52.26*	*2.33*	*14.03*	*12.07*	*0.19*	*5.62*	*10.30*	*2.48*	*0.44*	*0.29*	*35.0*	*5.9*	*99.99*	*96.23*	*97.10*

Grey shading indicates statistically similar inclusions with D <6.3; analyses marked with an asterisk (*) denote inclusions within 2σ of the mean matrix glass composition; analyses in *italics* represent inclusions with a similarity coefficient >96.

Appendix A3 Mauna Loa 1984 glass geochemistry

(d) Glass inclusion data

Sample	Type	SiO_2	TiO_2	Al_2O_3	FeO	MnO	MgO	CaO	Na_2O	K_2O	P_2O_5	S	Cl	F	Total	Total excluding volatiles
ml1-1a	85μm round	52.11	2.02	14.11	10.37	0.16	5.75	10.79	2.30	0.36	0.25	0.129	0.003	0.001	98.49	98.22
ml1-4f	100μm t-shape clean	52.57	2.23	13.94	11.52	0.17	5.82	10.16	2.37	0.43	0.27	0.118	0.009	0.000	99.72	99.48
ml1-1-a	80μm round, clean	51.67	2.00	14.15	10.17	0.17	6.14	10.76	2.29	0.37	0.25	0.126	0.012	0.000	98.23	97.97
ml1-4-a	100μm teardrop shape clean	53.76	2.10	13.80	8.16	0.14	6.15	10.72	2.27	0.39	0.23	0.110	0.008	0.018	97.96	97.72
ml1-4-e	500μm big inc	51.46	2.24	13.96	11.08	0.16	5.83	10.31	2.40	0.42	0.25	0.091	0.009	0.000	98.30	98.11
ml2-1g	200μm elong triangle	51.62	2.27	13.73	11.53	0.17	5.67	10.55	2.33	0.41	0.27	0.121	0.008	0.000	98.79	98.54
ml2-1m	30μm triangular	51.57	2.35	13.63	11.64	0.18	4.90	10.99	2.38	0.41	0.26	0.101	0.015	0.000	98.54	98.32
ml2-2e	500μm large inc*	51.47	2.38	13.37	11.63	0.17	5.87	10.29	2.41	0.44	0.28	0.095	0.006	0.000	98.51	98.32
ml2-2m	long 100μm square*	50.85	2.34	13.38	11.66	0.17	5.91	10.25	2.41	0.43	0.26	0.096	0.005	0.000	97.84	97.64
ml2-5a	skinny 50μm long; 1 ves	52.60	2.21	12.74	11.27	0.18	6.99	9.31	2.46	0.58	0.26	0.167	0.010	0.000	98.94	98.59
ml2-6a	80μm elong,square; 2 ves	51.53	2.46	13.17	10.81	0.17	6.19	9.86	2.43	0.48	0.29	0.191	0.011	0.000	97.60	97.40
ml2-6c	80μm square, crack thru middle	50.06	2.22	12.80	11.70	0.18	6.58	10.45	2.18	0.41	0.28	0.150	0.010	0.000	97.16	96.85
ml2-6e	rectangle 60μm*	50.55	2.33	13.07	11.47	0.18	6.12	10.20	2.29	0.44	0.29	0.098	0.000	0.000	97.13	96.93
ml2-6f	elong sausage shape, 50μm	50.70	2.35	13.34	11.56	0.18	5.92	10.16	2.27	0.48	0.26	0.098	0.012	0.000	97.42	97.21
ml2-6h	v.skinny, long elong	50.99	2.24	14.51	11.14	0.17	5.60	10.53	2.43	0.43	0.24	0.087	0.007	0.000	98.46	98.28
ml2-6i	square 40μm; rim around inc	51.86	2.38	14.02	12.09	0.18	5.26	10.35	2.52	0.44	0.27	0.083	0.005	0.000	99.55	99.38
ml2-6j	v-shape 30-40μm skinny	50.96	2.27	13.68	11.77	0.18	5.48	10.04	2.41	0.43	0.29	0.091	0.007	0.000	97.71	97.52
	Average	**51.27**	**2.30**	**13.56**	**11.53**	**0.17**	**5.83**	**10.24**	**2.36**	**0.43**	**0.27**	**0.101**	**0.007**	**0.000**	**98.18**	
	Standard Deviation (1σ)	**0.61**	**0.05**	**0.30**	**0.19**	**0.01**	**0.18**	**0.14**	**0.05**	**0.02**	**0.01**	**0.011**	**0.003**	**0.000**		

(e) XRF bulk analysis

Sample	Type	SiO_2	TiO_2	Al_2O_3	FeO	MnO	MgO	CaO	Na_2O	K_2O	P_2O_5	Total
ML-1	1984 Scoria	51.70	2.06	13.84	10.95	0.17	6.91	10.45	2.33	0.39	0.23	99.04

Appendix A4 Hekla 1980 glass geochemistry

(a) Matrix glass data

Sample	Label	SiO_2	TiO_2	Al_2O_3	FeO	MnO	MgO	CaO	Na_2O	K_2O	P_2O_5	S	Cl	F	Total
HK1 Scoria	HKgl1_hk1.1	54.90	2.02	14.83	11.73	0.28	2.68	6.61	3.77	1.25	0.98	0.029	0.034	0.078	99.21
HK1 Scoria	HKglxtl1_hk1	55.65	2.09	14.82	10.79	0.27	2.62	6.68	3.88	1.40	1.00	0.027	0.032	0.069	99.34
HK1 Scoria	HKgl1_hk1.2	55.56	2.02	15.23	11.42	0.27	2.60	6.82	3.86	1.23	0.97	0.021	0.031	0.090	100.15
HK1 Scoria	HKgl1_hk1.3	54.89	2.08	14.75	11.65	0.28	2.74	6.81	3.75	1.26	1.02	0.019	0.035	0.091	99.40
HK1 Scoria	hkglxtl1hk1/2	55.93	2.07	15.19	11.44	0.28	2.96	6.72	3.02	1.19	1.04	0.061	0.052	0.062	100.07
HK1 Scoria	Hk1xtls2-1f	55.94	1.76	16.57	9.37	0.24	2.51	7.26	3.69	1.08	0.91	0.022	0.036	0.089	99.48
HK1 Scoria	hk1xtls2-3f	55.13	2.12	14.21	12.37	0.30	3.07	6.82	3.04	1.34	1.07	0.059	0.039	0.061	99.68
Average		**55.43**	**2.02**	**15.09**	**11.25**	**0.27**	**2.74**	**6.82**	**3.57**	**1.25**	**1.00**	**0.034**	**0.037**	**0.077**	**99.62**
Standard Deviation (1σ)		**0.42**	**0.11**	**0.68**	**0.88**	**0.02**	**0.19**	**0.19**	**0.35**	**0.10**	**0.05**	**0.017**	**0.007**	**0.012**	

Appendix A4 Hekla 1980 glass geochemistry

(b) Mean matrix glass data

Sample		SiO_2	TiO_2	Al_2O_3	FeO	MnO	MgO	CaO	Na_2O	K_2O	P_2O_5	S	Cl	F	Total	Total (excluding volatiles)
Hekla 1980	Average	55.43	2.02	15.09	11.25	0.27	2.74	6.82	3.57	1.25	1.00	0.034	0.037	0.077	99.62	99.44
	Standard deviation (1σ)	0.42	0.11	0.68	0.88	0.02	0.19	0.19	0.35	0.10	0.05	0.017	0.007	0.012		
	Standard deviation (2σ)	0.84	0.23	1.37	1.77	0.03	0.37	0.39	0.70	0.19	0.10	0.034	0.013	0.025		
	Mean matrix glass normalized	55.74	2.03	15.17	11.32	0.28	2.76	6.86	3.59	1.26	1.00				100.00	

(c) Normalized glass inclusion data

Sample	Type	SiO_2	TiO_2	Al_2O_3	FeO	MnO	MgO	CaO	Na_2O	K_2O	P_2O_5	D^2	$D(1\sigma)$	Total
hk1xtls-2f	round 20µm inc clean,	57.88	2.13	15.77	9.38	0.25	1.54	6.92	3.67	1.33	1.12	82.84	9.10	100.00
hkxtls-1-1e	15µm round inc	56.77	2.25	14.96	11.30	0.27	2.65	6.86	2.58	1.25	1.10	22.97	4.79	100.00
hk1xtls-5b	small 15µm inc, 2 ves at base	58.94	1.82	14.79	10.32	0.24	2.54	5.97	2.99	1.51	0.87	8.98	3.00	100.00
hk1xtls-4a	round 20µm inc, 1 ves	56.81	2.04	14.97	11.53	0.30	2.44	7.01	2.76	1.16	0.98	19.70	4.44	100.00
hk1xtls2-6d	50µm round inc, 1 ves	57.13	2.13	15.28	10.80	0.28	1.93	7.60	2.53	1.28	1.04	56.09	7.49	100.00
hk1xtls2-6b	80µm oval inc, 6 tiny ves in middle	57.25	2.17	15.34	10.62	0.28	2.07	7.49	2.50	1.29	1.01	49.18	7.01	100.00
hk1xtls2-3e	large 100µm sq inc	56.60	2.12	14.81	11.62	0.29	2.82	6.47	2.42	1.75	1.11	53.21	7.29	100.00
hk1xtls-3l*	200µm elong triangular inc, 2 ves	56.17	2.02	15.11	11.30	0.27	2.49	6.90	3.44	1.24	1.04	4.31	2.08	100.00
hk1xtls-3h	inc at edge of xtl	57.73	2.17	15.61	9.52	0.26	1.67	7.38	3.28	1.33	1.06	72.56	8.52	100.00
hk1xtls-5h	tiny round clean inc	56.72	2.17	15.13	11.18	0.31	2.29	7.34	2.52	1.26	1.08	35.56	5.96	100.00
hkxtls-1-3f	10µm across round inc 2 ves at top	58.71	1.89	14.47	10.82	0.25	2.84	5.70	2.66	1.60	1.04	111.86	10.58	100.00
hk1xtls-6b	elong inc 20µm long, 1 ves at end	56.41	2.05	14.69	11.74	0.29	2.81	6.24	2.93	1.82	1.03	53.38	7.31	100.00
hk1xtls2-4a	round 20um inc, 1 elong ves in it clean	56.34	2.13	15.36	11.32	0.29	2.91	6.09	2.97	1.57	1.03	33.92	5.82	100.00
hkxtls-1-2b	elong 20µm inc, 2 ves in middle	58.44	2.16	13.28	11.84	0.31	3.21	5.36	2.14	2.08	1.18	224.58	14.99	100.00
hk1xtls-5d	small clean oval 20µm inc	56.72	2.10	14.55	11.66	0.27	2.83	6.17	3.10	1.56	1.05	32.72	5.72	100.00
hk1xtls-3a*	oval 30µm inc 1 big	55.68	2.32	14.87	11.56	0.31	2.89	6.81	3.33	1.14	1.10	16.98	4.12	100.00
hk1xtls-2a*	elong 40µm long inc 1 ves clean	56.56	2.03	14.84	11.48	0.27	2.85	6.48	3.04	1.40	1.04	13.61	3.69	100.00
hk1xtls-2b	elong 60µm inc	56.78	2.05	14.76	11.44	0.27	2.84	6.38	3.04	1.42	1.00	18.42	4.29	100.00

(c) Normalized glass inclusion data (cont'd)

Sample	Type	SiO_2	TiO_2	Al_2O_3	FeO	MnO	MgO	CaO	Na_2O	K_2O	P_2O_5	D^2	$D(1\sigma)$	Total
hk1xtls2-4d	large inc area 80μm by 60μm	57.46	2.02	14.82	11.00	0.28	2.69	6.09	2.87	1.88	0.89	85.16	9.23	100.00
hk1xtls-1a	70μm long	60.10	1.61	15.16	9.45	0.23	2.37	5.57	3.14	1.59	0.78	216.79	14.72	100.00
hkxtls-1-2g	80μm long triangle inc 3 ves	57.25	2.11	14.19	11.76	0.28	2.91	6.39	2.44	1.54	1.13	80.21	8.96	100.00
hk1xtls2-3m*	**long 100μm elong inc 3 tiny ves at bottom crack at top**	**55.77**	**2.06**	**15.38**	**11.22**	**0.28**	**2.73**	**7.24**	**3.09**	**1.16**	**1.06**	**8.84**	**2.97**	**100.00**
hk1xtls-5a	**round inc 20μm clean**	**56.61**	**2.14**	**14.53**	**11.77**	**0.27**	**2.85**	**6.24**	**3.06**	**1.53**	**0.99**	**27.10**	**5.21**	**100.00**

Grey shading indicates statistically similar inclusions with D <6.3; analyses marked with an asterisk (*) denote inclusions within 2σ of the mean matrix glass composition.

Appendix A4 Hekla 1980 glass geochemistry

(d) Glass inclusion data

Sample	Type	SiO_2	TiO_2	Al_2O_3	FeO	MnO	MgO	CaO	Na_2O	K_2O	P_2O_5	S	Cl	F	Total	Total excluding volatiles
hk1xtls-2f	round 20µm inc clean,	58.19	2.14	15.85	9.43	0.26	1.55	6.96	3.69	1.34	1.13	0.097	0.043	0.095	100.88	100.55
hkxtls-1-1e	15µm round inc	56.32	2.23	14.84	11.21	0.27	2.63	6.81	2.56	1.24	1.10	0.097	0.047	0.073	99.52	99.21
hk1xtls-5b	small 15µm inc, 2 ves at base	57.37	1.77	14.39	10.05	0.24	2.48	5.81	2.91	1.47	0.85	0.070	0.028	0.085	97.59	97.34
hk1xtls-4a	round 20µm inc, 1 ves	56.38	2.02	14.85	11.44	0.30	2.42	6.95	2.74	1.16	0.97	0.090	0.029	0.043	99.49	99.24
hk1xtls2-6d	50µm round inc, 1 ves	56.39	2.10	15.08	10.66	0.28	1.91	7.50	2.50	1.26	1.03	0.092	0.048	0.086	99.02	98.70
hk1xtls2-6b	80µm oval inc, 6 tiny ves in middle	56.18	2.13	15.05	10.42	0.27	2.03	7.35	2.45	1.27	0.99	0.094	0.047	0.103	98.47	98.13
hk1xtls2-3e	large 100µm sq inc	55.09	2.07	14.41	11.31	0.28	2.74	6.29	2.35	1.71	1.08	0.088	0.036	0.042	97.58	97.32
hk1xtls-3l	200µm elong triangular inc, 2 ves	55.80	2.01	15.00	11.23	0.27	2.48	6.85	3.42	1.24	1.04	0.090	0.038	0.082	99.63	99.33
hk1xtls-3h	inc at edge of xtl	56.86	2.13	15.37	9.38	0.26	1.65	7.27	3.23	1.31	1.04	0.096	0.049	0.141	98.88	98.50
hk1xtls-5h	tiny round clean inc	55.65	2.12	14.85	10.97	0.30	2.25	7.20	2.47	1.23	1.06	0.103	0.043	0.049	98.40	98.10
hkxtls-1-3f	10µm across round inc 2 ves at top	57.48	1.85	14.17	10.60	0.25	2.78	5.58	2.61	1.57	1.02	0.096	0.047	0.119	98.25	97.90
hk1xtls-6b	elong inc 20µm long, 1 ves at end	55.15	2.01	14.36	11.48	0.29	2.74	6.10	2.86	1.78	1.01	0.086	0.042	0.028	98.01	97.77
hk1xtls2-4a	round 20um inc, 1 elong ves in it clean	55.32	2.09	15.08	11.11	0.28	2.85	5.98	2.92	1.54	1.01	0.085	0.059	0.079	98.50	98.19
hkxtls-1-2b	elong 20µm inc, 2 ves in middle	57.11	2.11	12.98	11.57	0.30	3.14	5.24	2.09	2.03	1.15	0.086	0.059	0.098	98.04	97.72
hk1xtls-5d	small clean oval 20µm inc	55.13	2.04	14.15	11.33	0.26	2.75	5.99	3.02	1.52	1.02	0.092	0.044	0.098	97.52	97.20
hk1xtls-3a	oval 30µm inc 1 big	55.96	2.33	14.94	11.62	0.31	2.90	6.85	3.35	1.15	1.11	0.096	0.041	0.132	100.87	100.51
hk1xtls-2a	elong 40µm long inc 1 ves clean	55.63	2.00	14.60	11.29	0.27	2.80	6.38	3.00	1.38	1.03	0.091	0.047	0.095	98.70	98.37
hk1xtls-2b	elong 60µm inc	56.09	2.03	14.58	11.30	0.27	2.81	6.31	3.01	1.41	0.99	0.094	0.042	0.055	99.07	98.79
hk1xtls2-4d	large inc area 80µm by 60µm	55.71	1.96	14.37	10.67	0.27	2.61	5.91	2.78	1.82	0.86	0.077	0.046	0.083	97.23	96.95
hk1xtls-1a	70µm long	59.09	1.59	14.90	9.29	0.23	2.33	5.48	3.09	1.57	0.76	0.058	0.032	0.121	98.58	98.31
hkxtls-1-2g	80µm long triangle inc 3 ves	55.91	2.06	13.86	11.49	0.28	2.84	6.24	2.39	1.50	1.10	0.091	0.045	0.101	98.00	97.67
k1xtls2-3m	long 100µm elong inc 3 tiny ves at bottom crack at top	54.94	2.03	15.15	11.06	0.27	2.69	7.14	3.04	1.15	1.05	0.098	0.033	0.048	98.78	98.51
hk1xtls-5a	round inc 20µm clean	54.88	2.08	14.09	11.41	0.26	2.76	6.05	2.97	1.48	0.96	0.094	0.039	0.022	97.20	96.95
Average		**55.79**	**2.06**	**14.71**	**11.17**	**0.27**	**2.65**	**6.53**	**2.95**	**1.33**	**1.01**	**0.091**	**0.041**	**0.072**	**98.77**	
Standard Deviation (1σ)		**0.68**	**0.13**	**0.34**	**0.38**	**0.02**	**0.19**	**0.47**	**0.26**	**0.15**	**0.07**	**0.008**	**0.008**	**0.029**		

(e) XRF bulk analysis

Sample	Type	SiO_2	TiO_2	Al_2O_3	FeO	MnO	MgO	CaO	Na_2O	K_2O	P_2O_5	Total
HK-1	1980 scoria	54.30	2.04	14.50	13.03	0.27	2.89	6.77	3.82	1.26	0.10	98.98

Appendix A5 Hekla 2000 glass geochemistry

(a) Matrix glass data

Sample	Label	SiO_2	TiO_2	Al_2O_3	FeO	MnO	MgO	CaO	Na_2O	K_2O	P_2O_5	S	Cl	F	Total
HK2 Scoria	hkglxtl1_hk2	55.31	2.04	14.91	11.16	0.27	2.78	6.69	3.51	1.28	1.00	0.031	0.034	0.066	99.11
HK2 Scoria	hkgl1_hk2	55.24	2.08	14.90	11.58	0.27	2.77	6.75	3.72	1.24	1.02	0.039	0.036	0.098	99.76
HK2 Scoria	b2hk2gl/1	55.18	2.02	14.91	11.43	0.27	2.66	6.78	3.71	1.21	0.99	0.024	0.035	0.091	99.33
HK2 Scoria	b2hk2gl/8	54.86	2.04	14.68	11.55	0.27	2.75	6.78	3.53	1.27	1.00	0.028	0.035	0.068	98.88
HK2 Scoria	hk2xtl-4c	55.15	2.32	12.28	14.42	0.35	2.55	6.15	2.76	1.74	1.27	0.043	0.057	0.128	99.26
HK2 Scoria	Hk2xtls2-5j	56.68	2.11	15.07	11.72	0.26	2.63	6.96	4.09	1.03	0.99	0.024	0.036	0.000	101.64
HK2 Scoria	HKxtls-1-4o	56.62	2.06	15.10	11.46	0.28	2.71	6.81	3.34	1.22	1.04	0.031	0.034	0.052	100.79
Average		**55.58**	**2.10**	**14.55**	**11.90**	**0.28**	**2.69**	**6.70**	**3.52**	**1.28**	**1.04**	**0.031**	**0.038**	**0.072**	**99.82**
Standard Deviation (1σ)		**0.69**	**0.10**	**0.94**	**1.04**	**0.03**	**0.08**	**0.24**	**0.38**	**0.20**	**0.09**	**0.007**	**0.008**	**0.037**	

Appendix A5 Hekla 2000 glass geochemistry

Sample		SiO_2	TiO_2	Al_2O_3	FeO	MnO	MgO	CaO	Na_2O	K_2O	P_2O_5	S	Cl	F	Total	Total excluding volatiles
Hekla 2000	Average	55.58	2.10	14.55	11.90	0.28	2.69	6.70	3.52	1.28	1.04	0.031	0.038	0.072	99.82	99.66
	Standard deviation (1σ)	0.69	0.10	0.94	1.04	0.03	0.08	0.24	0.38	0.20	0.09	0.007	0.008	0.037		
	Standard deviation (2σ)	1.38	0.19	1.87	2.08	0.05	0.15	0.48	0.76	0.40	0.19	0.013	0.015	0.075		
	Mean matrix glass normalized	55.77	2.10	14.60	11.94	0.28	2.70	6.73	3.54	1.29	1.05				100.00	

(c) Normalized glass inclusion data

Sample	Type	SiO_2	TiO_2	Al_2O_3	FeO	MnO	MgO	CaO	Na_2O	K_2O	P_2O_5	D^2	D (1σ)	Total
hk2xtl_1d*	oval inc clean 25µm	56.33	1.99	14.97	11.51	0.29	2.49	6.82	3.42	1.15	1.04	10.64	3.26	100.00
hk2xtl_1f	long inc 10µm across	56.62	2.19	15.24	10.62	0.28	1.74	7.38	3.55	1.25	1.12	169.91	13.03	100.00
hk2xtl_1g	small round inc	56.79	2.08	15.30	9.99	0.26	1.51	8.11	3.63	1.32	1.02	281.41	16.78	100.00
hk2xtl_1j*	large 60 µm inc 10-12 small vesicles in it	56.75	2.08	15.30	10.67	0.29	1.87	7.19	3.52	1.29	1.04	123.62	11.12	100.00
hk2xtl-3a	oval inc 40 µm across 1 ves	59.37	1.56	14.98	9.86	0.23	2.57	5.59	3.33	1.63	0.88	100.23	10.01	100.00
hk2xtl-3bc	clean elongate inc	58.41	1.56	16.04	9.33	0.23	2.40	6.25	3.53	1.40	0.85	83.42	9.13	100.00
hk2xtl-4b	v small round clean inc 20 µm across	57.12	2.20	13.46	12.12	0.30	3.19	5.59	2.88	1.99	1.14	85.90	9.27	99.99
hk2xtl-6a	tiny 10 µm round 2 ves in inc	56.88	2.27	13.21	12.08	0.28	2.99	6.12	3.55	1.48	1.15	29.58	5.44	100.00
hk2xtl-6h	long l-shaped inc	56.54	1.65	17.09	9.45	0.23	2.18	7.19	3.70	1.20	0.78	97.79	9.89	100.00
hk2xtl-6n	100 µm clean elongate inc	55.19	2.02	14.93	11.69	0.29	2.03	7.58	3.98	1.28	1.01	91.85	9.58	100.00
hk2xtls2-1a	very tiny 10µm inc 1 big ves in it	57.68	2.21	15.64	9.41	0.26	1.23	7.90	3.10	1.39	1.19	412.50	20.31	100.00
hk2xtls2-1b	round 15µm inc 1 ves	56.81	1.53	18.06	8.24	0.20	1.90	7.68	3.71	1.08	0.80	205.44	14.33	100.00
hk2xtls2-1e*	small oval inc	56.28	2.32	14.80	11.34	0.28	2.76	6.65	3.32	1.20	1.05	7.21	2.68	100.00
hk2xtls2-2a	elong triangle inc small 1 ves at top 15µm long few um wide	56.05	2.49	11.53	14.39	0.36	3.26	5.87	2.47	2.26	1.30	145.47	12.06	99.99
hk2xtls2-2e	elong 90µm long inc 10µm wide 1 ves at end	57.36	2.03	14.46	11.40	0.27	2.91	6.01	2.96	1.58	1.02	27.33	5.23	100.00
hk2xtls2-3f*	40µm inc	57.52	1.95	14.87	10.88	0.27	2.62	6.33	3.19	1.48	0.89	18.82	4.34	100.00
hk2xtls2-3h	100µm long inc	57.82	1.89	15.04	10.63	0.26	2.73	6.22	3.16	1.34	0.91	23.88	4.89	100.00
hk2xtls2-3j*	80µm oval 2 ves in it	57.71	1.95	14.88	10.82	0.27	2.67	6.30	3.13	1.40	0.87	20.49	4.53	100.00
hk2xtls2-5b	triangle inc 50µm across 5 small ves v.near to xtal edge	58.94	2.08	13.03	11.96	0.28	3.10	5.32	2.50	1.81	0.97	100.44	10.02	100.00
hk2xtls2-5d	25µm long inc 2 ves	58.03	1.95	14.95	10.68	0.25	2.65	6.09	3.04	1.44	0.91	27.91	5.28	100.00
hk2xtls2-5h	round 20µm across clean inc 1 ves in it	57.67	1.99	14.65	11.04	0.26	2.89	5.99	2.93	1.60	0.98	31.18	5.58	100.00
hkxtls-1-4a	oval 50µm across inc clean 1 ves at base	56.90	2.09	14.90	11.66	0.30	2.30	7.42	2.23	1.18	1.03	51.57	7.18	100.00
hkxtls-1-4h*	50µm oval inc clean	56.75	2.10	14.70	11.61	0.29	2.83	6.54	2.58	1.46	1.12	13.45	3.67	100.00
hkxtls-1-5h	50µm oval inc 2 ves at top rim around inc	57.73	1.92	15.09	11.02	0.28	2.76	6.13	2.60	1.50	0.97	27.00	5.20	99.99
hkxtls-1-5k	sq inc 2 ves 30-40µm across	57.21	2.03	14.97	11.14	0.28	2.76	6.49	2.65	1.47	1.00	13.61	3.69	100.00

Grey shading indicates statistically similar inclusions with D <6.3; analyses marked with an asterisk (*) denote inclusions within 2σ of the mean matrix glass composition.

Appendix A5 Hekla 2000 glass geochemistry

(d) Glass inclusion data

Sample	Type	SiO_2	TiO_2	Al_2O_3	FeO	MnO	MgO	CaO	Na_2O	K_2O	P_2O_5	S	Cl	F	Total	Total excluding volatiles
hk2xtl_1d	oval inc clean 25µm	56.58	2.00	15.04	11.56	0.29	2.50	6.85	3.44	1.16	1.05	0.102	0.040	0.091	100.79	100.45
hk2xtl_1f	long inc 10µm across	55.84	2.16	15.03	10.48	0.28	1.71	7.28	3.50	1.24	1.10	0.108	0.046	0.029	98.90	98.61
hk2xtl_1g	small round inc	56.79	2.08	15.30	9.99	0.26	1.51	8.11	3.63	1.32	1.02	0.110	0.048	0.156	100.43	100.00
hk2xtl_1j	large 60 µm inc 10-12 small vesicles in it	56.83	2.08	15.32	10.68	0.29	1.88	7.20	3.53	1.30	1.04	0.101	0.046	0.078	100.46	100.14
hk2xtl-3a	oval inc 40 µm across 1 ves	58.83	1.54	14.84	9.77	0.22	2.55	5.54	3.30	1.62	0.87	0.072	0.048	0.071	99.35	99.09
hk2xtl-3bc	clean elongate inc	58.04	1.55	15.94	9.27	0.23	2.38	6.21	3.51	1.39	0.84	0.064	0.044	0.088	99.62	99.36
hk2xtl-4b	v small round clean inc 20 µm across	55.56	2.14	13.10	11.79	0.29	3.10	5.44	2.80	1.94	1.11	0.090	0.046	0.090	97.58	97.27
hk2xtl-6a	tiny 10 µm round 2 ves in inc	55.77	2.23	12.95	11.84	0.28	2.93	6.00	3.48	1.45	1.12	0.112	0.045	0.070	98.39	98.05
hk2xtl-6h	long l-shaped inc	56.33	1.64	17.03	9.41	0.23	2.17	7.16	3.68	1.19	0.78	0.074	0.032	0.069	99.87	99.62
hk2xtl-6n	100 µm clean elongate inc	56.20	2.05	15.20	11.90	0.29	2.07	7.72	4.05	1.30	1.03	0.101	0.048	0.122	102.19	101.82
hk2xtls2-1a	very tiny 10µm inc 1 big ves in it	55.80	2.14	15.13	9.10	0.25	1.19	7.65	3.00	1.34	1.15	0.100	0.042	0.133	97.13	96.75
hk2xtls2-1b	round 15µm inc 1 ves	55.42	1.49	17.62	8.04	0.19	1.86	7.49	3.62	1.05	0.78	0.059	0.031	0.143	97.86	97.56
hk2xtls2-1e	small oval inc	56.47	2.33	14.85	11.38	0.28	2.77	6.67	3.33	1.21	1.05	0.095	0.034	0.083	100.64	100.33
hk2xtls2-2a	elong triangle inc small 1 ves at top 15µm long	54.19	2.41	11.15	13.91	0.35	3.15	5.68	2.39	2.18	1.26	0.107	0.061	0.165	97.12	96.68
hk2xtls2-2e	elong 90µm long inc 10µm wide 1 ves at end	56.94	2.02	14.35	11.32	0.27	2.89	5.97	2.93	1.57	1.01	0.084	0.053	0.082	99.57	99.27
hk2xtls2-3f	40µm inc	57.16	1.94	14.78	10.81	0.27	2.61	6.29	3.17	1.47	0.88	0.085	0.046	0.000	99.59	99.37
hk2xtls2-3h	100µm long inc	57.75	1.89	15.02	10.62	0.26	2.73	6.21	3.16	1.34	0.91	0.087	0.048	0.050	100.15	99.88
hk2xtls2-3j	80µm oval 2 ves in it	57.32	1.94	14.78	10.74	0.27	2.66	6.25	3.11	1.39	0.86	0.087	0.035	0.021	99.55	99.32
hk2xtls2-5b	triangle inc 50µm across 5 small ves v.near to xtal edge	57.75	2.04	12.77	11.72	0.28	3.04	5.22	2.45	1.78	0.95	0.091	0.059	0.106	98.34	97.99
hk2xtls2-5d	25µm long inc 2 ves	57.55	1.93	14.82	10.60	0.25	2.63	6.04	3.01	1.43	0.91	0.088	0.039	0.096	99.48	99.17
hk2xtls2-5h	round 20µm across clean inc 1 ves in it	57.33	1.97	14.56	10.98	0.26	2.88	5.96	2.91	1.59	0.98	0.085	0.043	0.056	99.69	99.42
hkxtls-1-4a	oval 50µm across inc clean 1 ves at base	55.89	2.06	14.63	11.45	0.29	2.26	7.28	2.19	1.16	1.01	0.096	0.041	0.109	98.56	98.22
hkxtls-1-4h	50µm oval inc clean	54.88	2.03	14.22	11.23	0.29	2.74	6.32	2.50	1.41	1.09	0.096	0.041	0.090	97.02	96.69
hkxtls-1-5h	50µm oval inc 2 ves at top rim around inc	57.11	1.90	14.93	10.90	0.27	2.73	6.07	2.57	1.48	0.96	0.078	0.038	0.107	99.23	98.93
hkxtls-1-5k	sq inc 2 ves 30-40µm across	55.96	1.99	14.65	10.90	0.28	2.70	6.35	2.59	1.44	0.98	0.082	0.042	0.062	98.08	97.81
Average		**56.73**	**2.01**	**14.58**	**11.07**	**0.27**	**2.73**	**6.25**	**3.02**	**1.41**	**0.98**	**0.090**	**0.042**	**0.067**	**99.35**	
Standard Deviation (1σ)		**0.81**	**0.13**	**0.55**	**0.38**	**0.01**	**0.12**	**0.27**	**0.32**	**0.12**	**0.08**	**0.009**	**0.005**	**0.030**		

(e) XRF bulk analysis

Sample	Type	SiO_2	TiO_2	Al_2O_3	FeO	MnO	MgO	CaO	Na_2O	K_2O	P_2O_5	Total
HK-2	2000 scoria	54.45	2.04	14.57	13.04	0.28	2.91	6.80	3.91	1.27	1.00	100.26

Appendix A6 Izu-Oshima 1986 glass geochemistry

Sample	SiO_2	TiO_2	Al_2O_3	FeO	MnO	MgO	CaO	Na_2O	K_2O	P_2O_5	S	Cl	F	Total
870923-2-1	54.02	1.45	13.59	14.89	0.24	4.39	9.57	0.80	0.49	0.11	0.001	0.047	-0.026	99.60
870923-2-2	53.63	1.33	13.54	14.39	0.23	4.53	9.64	1.89	0.46	0.10	0.004	0.035	-0.043	99.76
870923-2-3	53.52	1.23	12.46	14.72	0.26	6.71	9.06	1.40	0.42	0.09	0.003	0.033	-0.013	99.89
870923-2-4	54.03	1.35	13.71	14.26	0.24	4.32	9.65	1.94	0.49	0.09	0.005	0.041	-0.069	100.12
870923-2-5	53.75	1.34	13.68	14.34	0.24	4.55	9.54	1.71	0.46	0.09	0.008	0.037	-0.070	99.76
870923-2-6	54.97	1.32	9.84	17.03	0.30	7.78	7.61	0.67	0.42	0.10	0.003	0.035	-0.098	100.08
870923-2-7	53.27	1.21	10.89	15.82	0.28	7.98	8.68	0.72	0.38	0.08	0.003	0.034	-0.056	99.34
870923-2-9	56.61	1.67	12.54	15.63	0.25	3.19	8.44	0.64	0.61	0.13	0.006	0.040	-0.108	99.76
870923-2-10	54.16	1.43	13.49	14.72	0.24	4.31	9.52	1.35	0.49	0.11	0.005	0.030	-0.140	99.86
Average	53.82	1.34	13.38	14.48	0.24	4.88	9.48	1.66	0.46	0.10	0.005	0.04	-0.07	99.87
Standard Deviation (1σ)	0.24	0.07	0.47	0.20	0.01	0.92	0.22	0.24	0.03	0.01	0.002	0.004	0.042	
Standard Dev (2σ)	0.48	0.13	0.93	0.39	0.02	1.83	0.44	0.49	0.05	0.01	0.003	0.007	0.084	
Mean matrix glass normalized	53.91	1.34	13.40	14.51	0.24	4.89	9.50	1.66	0.46	0.10				100.00

(b) Glass inclusion data

Sample	Type	SiO_2	TiO_2	Al_2O_3	FeO	MnO	MgO	CaO	Na_2O	K_2O	P_2O_5	S	Cl	F	Total
870923-1-1	20um across oval inc 2 ves at end	52.91	1.24	14.41	13.90	0.23	4.71	9.48	0.59	0.44	0.08	0.040	0.055	b.d.	98.11
870923-1-4	30um across teardrop inc	51.81	1.26	13.87	15.45	0.26	5.50	10.37	1.57	0.25	0.08	0.059	0.022	b.d.	100.55

Appendix A7 Electron microprobe glass standard dataset

Name	SiO_2	TiO_2	Al_2O_3	FeO	MnO	MgO	CaO	Na_2O	K_2O	P_2O_5	S	Cl	F	Total
Accepted Value VG2	*50.81*	*1.85*	*14.06*	*11.84*	*0.22*	*6.71*	*11.12*	*2.62*	*0.19*	*0.20*	*n.a.*	*n.a.*	*n.a.*	*99.86*
This study VG-2 (n = 270)	50.76	1.85	13.96	11.78	0.21	6.70	11.01	2.64	0.20	0.23	0.147	0.032	b.d.	99.52
Standard Deviation (2σ)	0.35	0.02	0.05	0.07	0.01	0.05	0.09	0.03	0.01	0.01	0.005	0.004	0.002	
Accepted Value JDF-D2	*50.80*	*1.89*	*13.80*	*12.17*	*0.22*	*6.83*	*10.80*	*2.77*	*0.22*	*0.23*	*n.a.*	*n.a.*	*n.a.*	*99.72*
This study JDF-D2 (n = 200)	50.47	1.91	13.88	12.15	0.19	6.84	10.71	2.75	0.22	0.23	0.150	0.037	b.d.	99.53
Standard Deviation (2σ)	0.36	0.02	0.06	0.06	0.01	0.09	0.11	0.03	0.01	0.02	0.005	0.004	0.007	
Accepted Value KN-18	*74.60*	*0.18*	*10.53*	*3.45*	*0.06*	*0.00*	*0.15*	*5.68*	*4.39*	*0.00*	*n.a.*	*0.370*	*0.640*	*100.05*
This study KN-18 (n = 110)	74.70	0.17	10.48	3.49	0.06	0.01	0.14	5.46	4.42	0.00	0.004	0.355	0.667	99.96
Standard Deviation (2σ)	0.34	0.01	0.05	0.02	0.01	0.00	0.06	0.08	0.02	0.01	0.002	0.009	0.093	
Accepted Value KE-12	70.30	0.33	7.62	8.36	0.26	<0.01	0.35	7.28	4.27	<0.01	b.d.	0.330	0.440	99.54
This study KE-12 (n = 55)	70.30	0.31	7.51	8.41	0.30	0.01	0.36	6.98	4.29	0.02	0.000	0.292	0.385	99.17
Standard Deviation (2σ)	0.73	0.01	0.15	0.05	0.01	0.01	0.01	0.03	0.07	0.01	0.000	0.021	0.034	
Accepted Value TB-1G	*54.22*	*0.85*	*16.68*	*9.05*	*0.18*	*3.64*	*6.87*	*3.20*	*4.37*	*0.59*	*n.a.*	*n.a.*	*n.a.*	*99.65*
This study TB-1G (n = 135)	53.52	0.84	16.36	9.24	0.17	3.48	6.81	3.19	4.45	0.61	0.010	0.015	0.040	98.73
Standard Deviation (2σ)	0.49	0.01	0.11	0.17	0.01	0.03	0.05	0.03	0.03	0.02	0.010	0.004	0.026	
Accepted value KBT-1G	*37.94*	*3.78*	*9.96*	*11.76*	*0.20*	*14.85*	*12.58*	*3.15*	*1.15*	*0.82*	*n.a.*	*n.a.*	*n.a.*	*96.19*
This study KBT-1G (n = 80)	38.02	3.80	10.08	11.70	0.19	14.84	12.56	3.06	1.12	0.86	0.000	0.001	0.066	*96.30*
Standard Deviation (2σ)	0.20	0.02	0.06	0.02	0.01	0.14	0.05	0.05	0.02	0.04	0.000	0.001	0.030	
Accepted value VG-568	*76.71*	*0.12*	*12.06*	*1.23*	*0.03*	*<0.1*	*0.50*	*3.75*	*4.89*	*<0.01*	*b.d.*	*0.130*		*99.59*
This study VG-568 (n = 130)	76.62	0.10	11.97	1.20	0.04	0.02	0.49	3.73	4.94	0.01	0.000	0.124	0.153	*99.40*
Standard Deviation (2σ)	0.87	0.01	0.12	0.02	0.01	0.00	0.01	0.09	0.02	0.01	0.000	0.013	0.034	

Glass standard accepted values are shown in italics, n = number of analyses, b.d. = below microprobe detection limit, n.a. = not analysed.

Appendix B1: Supplementary information

Appendix B contains data associated with chapter 3 (Öræfajökull 1362).

Appendix B2 is a list of all Öræfajökull sample locations.

The complete Öræfajökull 1362 glass (major element and volatiles) and mineral geochemistry dataset is listed in appendix B3-B6. Glass composition data is listed for each of the major eruptive units (*A-D*) and sub-units. Each analysis listed in the matrix glass dataset represents an average of 3-10 spots on an area of pumice matrix glass or on small fragments or shards of glass. Glass and mineral compositional data for the mafic pumice samples (banded pumice and grey pumice) is also reported here.

Mineral formulas are calculated using cation data as follows:

Plagioclase feldspar: formula based on 8 oxygens; An = Ca/(Ca+Na+K), Ab = Na/(Ca+Na+K), Or = K/(Ca+Na+K).

Clinopyroxene: formula based on 6 oxygens; Wo = Ca/(Ca+Mg+Fe), En = Mg/(Ca+Mg+Fe), Fs = Fe/(Ca+Mg+Fe).

Olivine: formula based on 4 oxygens; Fo = Mg/(Mg+Fe).

Appendix B2 Öræfajökull 1362 sample locations

Location	Description
Ö-1	Old ruined farm just off Highway 1; 2-3 steep patches of deposit on hillside
Ö -2	Near Hof, bank on north side of Hvalvörtugil (also Öldur), at stream ~0.7 km north of Highway 1
Ö-3	Small section beyond Hof – deposit all reworked
Ö-4	Gljúfursá (small stream) north of Highway 1 near Hofnes farm
Ö-5	Múlagyofar Valley of Highway 1
Ö-6	Partial section in peat bog of Highway 1
Ö-7	On path to Svartiföss waterfall above Skeidara
Ö-8	Patch of deposit on hilltop above Svartiföss
Ö-9	Bölti, above end of Sveinafallsjökull
Ö-10	Hnapavellir, small pit bu Highway 1
Ö-11	Ingolfshöfdi
Ö-12	Small section at start of Laki road
Ö-13	Near Stigajökull, way above location 10

Appendix B3 Öræfajökull 1362 glass geochemistry

(a) Unit A_2 matrix glass data

Sample	Description	SiO_2	TiO_2	Al_2O_3	FeO	MnO	MgO	CaO	Na_2O	K_2O	P_2O_5	S	Cl	F	Total
O206-1-2	glass shard	73.17	0.28	13.30	3.55	0.13	0.02	1.21	4.98	3.44	0.02	n/a	n/a	n/a	100.10
O206-1-3a	glass shard	72.26	0.23	13.12	3.28	0.15	0.00	1.03	4.96	3.51	0.00	0.008	0.196	0.059	98.80
O206-2-1a	glass shard	73.39	0.28	12.91	3.32	0.11	0.00	0.99	4.94	3.40	0.00	0.004	0.211	0.062	99.61
O206-2-3a	glass shard	74.11	0.23	13.22	3.30	0.12	0.02	1.02	5.04	3.57	0.02	0.002	0.206	0.064	100.92
O206-2-4	glass shard	74.06	0.23	13.35	3.31	0.11	0.01	1.00	5.09	3.52	0.01	n/a	n/a	n/a	100.66
O206-2-4a	glass shard	73.66	0.25	13.19	3.38	0.11	0.01	1.01	5.36	3.57	0.00	0.001	0.194	0.208	100.93
O206-2-5a	glass shard	74.22	0.26	13.27	3.20	0.13	0.01	0.95	5.13	3.48	0.00	0.000	0.216	0.103	100.97
O206-2-6	glass shard	73.74	0.26	13.33	3.28	0.10	0.03	1.07	5.00	3.43	0.02	n/a	n/a	n/a	100.25
Average		**73.57**	**0.25**	**13.21**	**3.33**	**0.12**	**0.01**	**1.04**	**5.06**	**3.49**	**0.01**	**0.002**	**0.128**	**0.062**	**100.28**
Standard Deviation (1σ)		**0.60**	**0.02**	**0.13**	**0.10**	**0.01**	**0.01**	**0.07**	**0.13**	**0.06**	**0.01**	**0.003**	**0.008**	**0.057**	

(b) Unit B_1 basaltic glass shards

Sample	Description	SiO_2	TiO_2	Al_2O_3	FeO	MnO	MgO	CaO	Na_2O	K_2O	P_2O_5	S	Cl	F	Total
O205-a	basaltic glass shard	48.83	2.93	12.97	14.23	0.21	5.18	9.86	2.69	0.45	0.310	0.107	0.015	0.000	97.89
O205-b	basaltic glass shard	48.08	2.57	13.31	13.13	0.20	5.76	10.67	2.51	0.37	0.270	0.069	0.012	0.000	97.02
O205-c	basaltic glass shard	48.98	2.98	13.19	14.08	0.23	5.17	9.87	2.75	0.45	0.371	0.057	0.023	0.000	98.21
O205-d	basaltic glass shard	48.79	2.67	13.24	13.67	0.23	5.22	9.95	2.70	0.44	0.306	0.061	0.018	0.000	97.35

Appendix B3 Öræfajökull 1362 glass geochemistry

(b) Unit B_1 matrix glass data

Sample	Description	SiO_2	TiO_2	Al_2O_3	FeO	MnO	MgO	CaO	Na_2O	K_2O	P_2O_5	S	Cl	F	Total
o205-1	glass shard	74.05	0.24	13.67	3.42	0.10	0.00	1.00	3.96	3.52	0.018	0.006	0.160	0.136	100.27
o205-2	glass shard	73.44	0.24	13.59	3.39	0.11	0.01	1.02	3.87	3.52	0.015	0.008	0.210	0.025	99.45
o205-3	glass shard	73.79	0.22	13.78	3.35	0.08	0.01	0.98	3.87	3.53	0.016	0.002	0.186	0.061	99.88
o205-4	glass shard	73.38	0.25	13.63	3.37	0.10	0.01	0.98	3.82	3.55	0.029	0.002	0.192	0.065	99.37
o205-5	glass shard	72.49	0.24	13.26	3.71	0.10	0.01	1.28	5.06	3.00	0.022	0.004	0.146	0.061	99.38
o205-6	glass shard	73.24	0.24	13.51	3.31	0.09	0.01	0.94	3.98	3.54	0.000	0.000	0.190	0.099	99.15
o205-7	glass shard	74.24	0.24	13.91	3.34	0.08	0.01	0.97	4.01	3.50	0.011	0.003	0.170	0.075	100.55
o205-8	glass shard	73.00	0.23	13.66	3.40	0.08	0.00	0.98	3.91	3.50	0.013	0.000	0.182	0.088	99.04
o205-9	glass shard	73.54	0.24	13.58	3.38	0.09	0.01	0.98	3.79	3.46	0.021	0.005	0.166	0.068	99.32
o205-10	glass shard	71.17	0.25	13.09	4.60	0.16	0.01	1.82	4.19	4.35	0.006	0.001	0.191	0.264	100.11
o205-11	glass shard	73.36	0.25	13.66	3.37	0.10	0.01	0.98	3.88	3.64	0.023	0.001	0.186	0.030	99.48
o205-12	glass shard	73.96	0.24	13.92	3.44	0.10	0.01	1.00	3.91	3.48	0.000	0.000	0.185	0.092	100.33
o205-13	glass shard	72.22	0.24	13.72	3.37	0.09	0.01	1.01	3.68	3.49	0.016	0.001	0.188	0.126	98.15
o205-14	glass shard	73.22	0.23	13.60	3.40	0.12	0.01	1.00	4.55	3.41	0.011	0.007	0.195	0.100	99.84
o205-15	glass shard	72.59	0.23	13.38	3.31	0.11	0.01	0.97	4.02	3.42	0.015	0.000	0.180	0.040	98.27

Appendix B3 Öræfajökull 1362 glass geochemistry

(c) Unit B_2 matrix glass data

Sample	Description	SiO_2	TiO_2	Al_2O_3	FeO	MnO	MgO	CaO	Na_2O	K_2O	P_2O_5	S	Cl	F	Total
O204-1a	glass shard	73.63	0.24	13.00	3.35	0.10	0.01	0.98	5.25	3.65	0.01	0.011	0.185	0.061	100.49
O204-2a	glass shard	72.55	0.27	12.78	3.37	0.13	0.01	1.00	5.15	3.63	0.02	0.003	0.193	0.066	99.17
O204-3a	glass shard	73.33	0.26	12.96	3.43	0.12	0.03	0.98	5.23	3.74	0.00	0.000	0.191	0.120	100.37
O204-4a	glass shard	71.97	0.26	12.91	3.49	0.08	0.00	0.80	5.48	3.50	0.03	0.004	0.199	0.014	98.74
O204-5a	glass shard	72.11	0.20	12.90	3.38	0.11	0.00	0.99	5.16	3.70	0.00	0.000	0.191	0.080	98.82
O204-6a	glass shard	73.21	0.27	13.14	3.31	0.11	0.00	1.01	5.18	3.47	0.05	0.010	0.175	0.130	100.06
O204-7a	glass shard	73.42	0.28	13.05	3.36	0.12	0.02	1.02	5.04	3.51	0.02	0.004	0.191	0.026	100.06
O204-8a	glass shard	72.92	0.23	12.82	3.39	0.09	0.01	1.00	5.19	3.50	0.01	0.004	0.184	0.105	99.46
O204-9a	glass shard	73.33	0.26	13.09	3.36	0.11	0.01	1.06	5.14	3.52	0.02	0.009	0.179	0.082	100.16
O204-10a	glass shard	73.41	0.25	12.90	3.37	0.15	0.01	1.01	5.29	3.77	0.01	0.009	0.177	0.066	100.43
O11-02-1	glass shard	72.10	0.23	13.38	3.33	0.10	0.02	1.00	4.42	3.67	0.012	0.000	0.203	0.079	98.54
O11-02-2	glass shard	72.85	0.22	13.18	3.20	0.08	0.01	0.89	4.84	3.57	0.000	0.004	0.184	0.166	99.19
O11-02-3	glass shard	71.95	0.22	13.42	2.97	0.08	0.00	0.78	5.76	3.19	0.005	0.006	0.144	0.070	98.59
O11-02-4	glass shard	72.73	0.24	13.38	3.44	0.09	0.01	0.97	4.91	3.53	0.008	0.001	0.196	0.071	99.56
O11-02-6	glass shard	71.82	0.23	13.39	3.36	0.10	0.01	0.96	5.68	3.54	0.000	0.001	0.178	0.004	99.39
O11-02-9	glass shard	73.63	0.24	13.55	3.37	0.11	0.01	0.98	5.03	3.31	0.000	0.004	0.176	0.127	100.53
O11-02-10	glass shard	72.12	0.23	13.12	3.30	0.09	0.01	0.99	4.29	3.65	0.012	0.007	0.211	0.028	98.08
O11-02-11	glass shard	72.36	0.23	13.24	3.32	0.10	0.02	0.97	4.58	3.56	0.008	0.000	0.196	0.022	98.61
O11-02-12	glass shard	68.91	0.25	12.39	5.62	0.18	0.03	3.06	5.78	2.40	0.000	0.004	0.123	0.000	98.75
O11-02-13	glass shard	72.12	0.23	13.24	3.34	0.11	0.01	0.99	4.69	3.41	0.015	0.005	0.168	0.101	98.43
O11-02-14	glass shard	73.23	0.23	13.53	3.37	0.10	0.00	0.98	4.58	3.67	0.013	0.003	0.192	0.037	99.93

Appendix B3 Öræfajökull 1362 glass geochemistry

(d) Unit B_3 matrix glass data

Sample	Description	SiO_2	TiO_2	Al_2O_3	FeO	MnO	MgO	CaO	Na_2O	K_2O	P_2O_5	S	Cl	F	Total
O1303-2-2	glass shard	71.76	0.25	13.29	3.26	0.13	0.02	0.98	5.01	3.34	0.01	0.010	0.216	0.224	98.50
O1303-2-3a	glass shard	71.05	0.26	13.14	3.31	0.11	0.02	1.00	4.96	3.68	0.01	0.003	0.206	0.123	97.87
O1303-2-4a	glass shard	71.96	0.25	13.12	3.39	0.09	0.03	0.98	5.03	3.76	0.01	0.002	0.187	0.145	99.06
O1303-2-5	glass shard	72.10	0.24	13.09	3.37	0.11	0.01	0.98	5.05	3.37	0.04	0.005	0.203	0.095	98.66
O1303-3-4	glass shard	72.14	0.26	13.07	3.29	0.14	0.02	0.99	5.01	3.39	0.01	0.003	0.209	0.045	98.56
O1303-1-1a	glass shard	70.95	0.23	12.94	3.28	0.13	0.00	0.96	5.14	3.43	0.00	0.009	0.199	0.148	97.40
O1303-1-4a	glass shard	70.76	0.27	12.99	3.35	0.11	0.01	0.96	5.05	3.40	0.01	0.006	0.210	0.137	97.26
O1303-1-5a	glass shard	70.76	0.27	12.99	3.26	0.11	0.01	0.94	5.03	3.35	0.00	0.000	0.204	0.096	97.02
O1303-1-6	glass shard	71.61	0.24	12.92	3.32	0.12	0.01	0.97	5.00	3.37	0.01	0.000	0.204	0.096	97.86
O1303-1-7a	glass shard	71.01	0.25	12.97	3.30	0.11	0.01	1.01	4.99	3.39	0.00	0.013	0.194	0.048	97.30
O1303-1-9a	glass shard	71.42	0.25	13.08	3.35	0.09	0.01	0.99	5.07	3.41	0.01	0.009	0.217	0.087	98.00

Appendix B3 Öræfajökull 1362 glass geochemistry

(e) Unit *C* matrix glass data

Sample	Description	SiO_2	TiO_2	Al_2O_3	FeO	MnO	MgO	CaO	Na_2O	K_2O	P_2O_5	S	Cl	F	Total
o902-1-2a	matrix glass in pumice	71.84	0.23	12.98	3.24	0.12	0.01	0.99	4.98	3.39	0.02	0.009	0.206	0.162	98.18
o902-1-3a	matrix glass in pumice	72.60	0.23	13.19	3.33	0.08	0.00	0.96	5.08	3.39	0.03	0.006	0.215	0.096	99.22
o902-1-4a	matrix glass in pumice	72.80	0.24	13.10	3.29	0.09	0.02	0.92	4.92	3.40	0.00	0.008	0.223	0.138	99.15
o902-1-5a	matrix glass in pumice	72.43	0.22	13.33	3.27	0.09	0.02	0.97	5.16	3.48	0.00	0.006	0.205	0.109	99.29
o902-2-5a	matrix glass attached to xtl	72.31	0.25	13.05	3.22	0.11	0.00	0.97	5.03	3.37	0.00	0.005	0.209	0.111	98.64
o902-2-16a	matrix glass attached to xtl	72.37	0.24	13.17	3.82	0.12	0.03	1.01	4.93	3.40	0.00	0.010	0.204	0.035	99.35
o401b-1	glass shard	71.77	0.25	13.49	3.31	0.09	0.01	0.99	4.97	3.34	0.01	0.006	0.202	0.149	98.28
o401b-3	glass shard	71.59	0.23	13.49	3.29	0.10	0.02	0.97	4.96	3.36	0.00	0.005	0.205	0.159	98.10
o401b-4	glass shard	71.17	0.23	13.30	3.22	0.11	0.01	0.98	5.14	3.38	0.00	0.001	0.203	0.164	97.50
o401b-1-6	glass shard	71.88	0.24	13.50	3.30	0.10	0.01	0.97	5.02	3.40	0.00	0.003	0.201	0.154	98.44
o401b-1-7	glass shard	72.11	0.24	13.49	3.30	0.10	0.01	0.98	5.00	3.35	0.00	0.002	0.199	0.119	98.52
o401b-3-4	matrix glass attached to xtl	71.43	0.24	13.42	3.24	0.10	0.01	0.93	4.73	3.40	0.00	0.006	0.195	0.159	97.87
o401b-3-10	matrix glass attached to xtl	71.54	0.25	13.60	3.26	0.09	0.01	0.96	4.97	3.38	0.00	0.004	0.204	0.149	98.01
O401c-9	glass shard	72.57	0.24	13.06	3.28	0.11	0.00	0.95	5.00	3.49	0.00	0.007	0.212	0.036	98.95
O401-x-4a	glass shard	72.75	0.20	13.24	3.95	0.11	0.00	0.99	4.89	3.25	0.00	0.009	0.216	0.024	99.63
O401-x-6a	matrix glass attached to xtl	72.20	0.21	12.93	3.14	0.10	0.02	0.96	5.16	3.33	0.00	0.009	0.211	0.134	98.41
O9-02-1	matrix glass in pumice	72.52	0.23	13.08	3.36	0.12	0.01	0.98	5.29	3.39	0.02	0.008	0.207	0.151	99.36
O9-02-4	matrix glass in pumice	72.24	0.27	12.88	3.41	0.12	0.01	0.95	5.06	3.42	0.02	0.006	0.224	0.096	98.71
O9-02-6	matrix glass in pumice	72.35	0.24	13.09	3.34	0.10	0.02	0.98	5.26	3.39	0.01	0.008	0.200	0.079	99.05
O9-02-8a	matrix glass in pumice	72.70	0.26	13.13	3.37	0.11	0.02	0.96	5.14	3.31	0.00	0.011	0.198	0.025	99.25
O9-02-20	matrix glass attached to xtl	71.57	0.22	12.82	3.82	0.13	0.01	0.97	5.04	3.54	0.02	0.008	0.195	0.078	98.42
O401-1a	glass shard	72.81	0.24	13.08	3.32	0.12	0.01	1.06	4.82	3.44	0.00	0.003	0.222	0.100	99.22
O401-2a	glass shard	72.99	0.24	12.87	3.27	0.10	0.01	1.04	4.73	3.35	0.05	0.000	0.228	0.061	98.93
O401-3a	glass shard	72.08	0.24	13.02	3.27	0.11	0.01	1.00	4.87	3.36	0.03	0.006	0.211	0.064	98.27
O401-5a	glass shard	72.45	0.26	13.06	3.24	0.11	0.00	1.01	5.00	3.41	0.00	0.010	0.220	0.093	98.87
O401-6a	glass shard	72.43	0.24	12.84	3.20	0.13	0.01	0.95	4.73	3.44	0.04	0.004	0.213	0.000	98.21
O401-7a	glass shard	72.98	0.21	13.13	3.30	0.11	0.00	0.99	4.78	3.30	0.02	0.007	0.229	0.084	99.15
O401-8a	glass shard	72.35	0.28	12.81	3.19	0.11	0.01	0.98	4.61	3.37	0.02	0.009	0.217	0.076	98.03
O401-9a	glass shard	73.36	0.26	12.89	3.24	0.12	0.02	1.01	4.91	3.43	0.03	0.000	0.228	0.138	99.63
O401-10a	glass shard	72.89	0.26	13.00	3.36	0.12	0.01	1.01	4.85	3.43	0.03	0.002	0.210	0.088	99.25
Average		**72.30**	**0.24**	**13.13**	**3.34**	**0.11**	**0.01**	**0.98**	**4.97**	**3.39**	**0.01**	**0.006**	**0.210**	**0.101**	**98.73**
Standard Deviation (1σ)		**0.52**	**0.02**	**0.22**	**0.19**	**0.01**	**0.01**	**0.03**	**0.16**	**0.06**	**0.01**	**0.003**	**0.010**	**0.046**	

Appendix B3 Öræfajökull 1362 glass geochemistry

(f) Unit *D* matrix glass data

Sample	Description	SiO_2	TiO_2	Al_2O_3	FeO	MnO	MgO	CaO	Na_2O	K_2O	P_2O_5	S	Cl	F	Total
O1301-2a	matrix glass in elongate pumice	73.22	0.27	13.15	3.32	0.12	0.02	1.03	4.78	3.35	0.04	0.003	0.217	0.050	99.56
O1301-3	matrix glass in elongate pumice	73.95	0.26	13.29	3.26	0.12	0.01	1.03	4.97	3.31	0.00	0.007	0.215	0.074	100.49
O1301-4a	matrix glass in pumice	73.88	0.24	13.16	3.30	0.12	0.02	1.01	4.83	3.33	0.04	0.006	0.215	0.095	100.24
O1301-5a	matrix glass in pumice	73.73	0.23	13.29	3.24	0.12	0.00	1.00	4.78	3.36	0.00	0.000	0.223	0.081	100.07
O1301-6a	matrix glass in pumice	73.26	0.25	13.09	3.20	0.13	0.00	1.03	4.88	3.43	0.02	0.000	0.212	0.074	99.57
O1301-7	matrix glass in pumice	72.37	0.25	12.88	3.32	0.10	0.01	1.01	4.86	3.44	0.02	0.009	0.214	0.080	98.56
O1301-9a	matrix glass in pumice	73.94	0.27	13.07	3.28	0.12	0.00	1.05	4.96	3.40	0.00	0.008	0.221	0.083	100.41
O1301-10a	glass shard	73.37	0.25	12.96	3.25	0.15	0.00	1.04	4.88	3.42	0.01	0.006	0.198	0.101	99.63
O1301-2-1a	glass shard	72.60	0.23	13.11	3.38	0.10	0.00	1.00	4.78	3.29	0.02	0.009	0.204	0.049	98.78
O1301-2-2a	glass shard	72.30	0.22	12.70	3.23	0.08	0.02	1.02	4.79	3.32	0.02	0.006	0.213	0.081	98.02
O1301-2-4a	glass shard	73.57	0.30	12.93	3.29	0.11	0.01	0.97	4.76	3.41	0.03	0.003	0.215	0.073	99.67
O1301-2-5a	glass shard	72.69	0.27	12.87	3.25	0.13	0.00	0.97	4.89	3.47	0.00	0.015	0.198	0.068	98.83
O1301-2-6a	glass shard	72.30	0.24	13.17	3.24	0.10	0.00	1.02	4.95	3.40	0.01	0.009	0.212	0.107	98.75
O1301-2-7a	glass shard	72.63	0.24	12.87	3.25	0.12	0.02	1.01	4.72	3.38	0.00	0.001	0.212	0.085	98.54
O1301-2-8	glass shard	71.32	0.22	12.75	3.22	0.12	0.02	1.04	4.74	3.39	0.02	0.009	0.213	0.022	97.08
O1301-2-9	glass shard	71.62	0.25	12.83	3.36	0.13	0.01	1.02	4.63	3.31	0.03	0.000	0.216	0.093	97.49
O1301-2-10a	glass shard	71.58	0.25	12.96	3.30	0.10	0.01	1.02	4.85	3.33	0.04	0.007	0.217	0.047	97.71
Average		**72.84**	**0.25**	**13.00**	**3.28**	**0.12**	**0.01**	**1.01**	**4.83**	**3.37**	**0.02**	**0.006**	**0.213**	**0.074**	**99.02**
Std Dev		**0.83**	**0.02**	**0.17**	**0.05**	**0.02**	**0.01**	**0.02**	**0.09**	**0.05**	**0.01**	**0.004**	**0.007**	**0.021**	

Appendix B3 Öræfajökull 1362 glass geochemistry

(g) Glass inclusion data

Sample	Description	SiO_2	TiO_2	Al_2O_3	FeO	MnO	MgO	CaO	Na_2O	K_2O	P_2O_5	S	Cl	F	Total
orae01-6a	small round 40μm across inc	71.60	0.23	13.44	4.22	0.14	0.01	1.03	4.13	3.26	0.01	0.002	0.198	0.090	98.08
orae01-6g	oval inc small oxide on one end	70.97	0.23	13.28	4.11	0.12	0.02	0.98	4.25	3.41	0.01	0.006	0.191	0.015	97.39
orae01-6j	**clean oval 60μm across**	**71.41**	**0.15**	**13.44**	**3.73**	**0.12**	**0.01**	**1.05**	**4.82**	**3.30**	**0.01**	**0.013**	**0.216**	**0.083**	**98.36**
orae01-3a	elongate 50μm long inc	70.61	0.25	13.19	4.24	0.13	0.03	1.51	4.18	3.22	0.01	0.005	0.219	0.070	97.37
orae01-3f	round inc small vesicle on edge	71.37	0.26	13.37	4.31	0.14	0.01	1.02	4.78	3.47	0.00	0.005	0.197	0.041	98.98
orae01-3j	oval inc 60μm across small oxide on edge	72.45	0.22	13.59	3.94	0.12	0.02	1.02	4.73	3.24	0.00	0.004	0.217	0.074	99.63
o902-2-1a	40μm across round inc clean	71.85	0.22	13.16	3.82	0.09	0.01	0.89	5.72	3.39	0.00	0.007	0.214	0.190	99.55
o902-2-3a	100μm long elongate oval inc	71.76	0.24	13.04	3.28	0.14	0.02	1.05	5.04	3.39	0.00	0.008	0.207	0.071	98.26
o902-2-6a	semi-circle shaped inc 100μm across oxide xtl @ end	71.70	0.21	12.94	3.57	0.10	0.00	0.94	5.11	3.71	0.00	0.010	0.210	0.084	98.58
o902-2-8	figure of 8 shaped inc 200μm long, small crack @ edge	73.20	0.23	13.27	3.27	0.10	0.00	0.93	4.26	3.47	0.01	0.002	0.218	0.090	98.72
o902-2-13a	110μm long elongate oval inc	71.87	0.18	13.28	3.87	0.10	0.00	0.94	5.02	3.39	0.04	0.008	0.207	0.050	98.98
o902-2-14	50μm across round inc in same xtl as inc -o902-2-13	72.79	0.23	13.24	3.92	0.11	0.00	0.93	4.65	3.50	0.00	0.014	0.207	0.043	99.64
o902-2-15a	250μm long skinny inc	71.67	0.23	13.14	3.97	0.13	0.01	0.94	4.85	3.44	0.01	0.010	0.203	0.062	98.68
O401z-9-a	**60 μm across clean inc**	**72.45**	**0.21**	**13.04**	**3.53**	**0.09**	**0.00**	**0.92**	**5.00**	**3.36**	**0.04**	**0.019**	**0.225**	**0.038**	**98.92**
O401-x-4a	50μm across perfect round clean inc	71.33	0.21	13.20	3.89	0.12	0.00	0.94	4.960	3.420	0.041	0.01	0.23	0.1	98.45
O401xtls-9	inclusion	71.87	0.21	13.08	4.10	0.13	0.01	0.92	5.153	3.393	0.006	0.01	0.21	0.174	99.28
O9-02-12a	**inclusion**	**70.98**	**0.24**	**12.82**	**3.24**	**0.10**	**0.02**	**0.95**	**5.171**	**3.329**	**0.008**	**0.02**	**0.199**	**0.062**	**97.13**
O9-06-1a	elongate 70μm long inc	71.37	0.23	12.87	3.25	0.11	0.00	0.81	5.16	3.406	0.025	0.009	0.20	0.063	97.51
O9-06-2a	perfect round clean inc 60μm across	71.17	0.23	13.09	3.81	0.13	0.00	0.95	5.08	3.433	0.019	0.011	0.20	0.063	98.19
O9-06-3a	200μm long elongate inc w/ bump at top end	71.82	0.23	13.15	3.70	0.12	0.02	0.96	5.15	3.388	0.000	0.014	0.23	0.024	98.79
O10-2a-1a	200μm long elongate inc	70.97	0.24	12.98	3.69	0.10	0.02	0.90	5.22	3.505	0.047	0.012	0.20	0.071	97.94
O10-2a-2a	**60μm across triangular inc**	**71.14**	**0.24**	**12.97**	**3.39**	**0.11**	**0.01**	**0.89**	**5.18**	**3.331**	**0.042**	**0.024**	**0.22**	**0.019**	**97.55**
O10-2a-3a	**v.skinny 300μm long inc in same xtl as -2**	**71.25**	**0.24**	**12.81**	**3.34**	**0.12**	**0.00**	**0.90**	**5.09**	**3.378**	**0.029**	**0.013**	**0.20**	**0.081**	**97.46**
O10-2a-4a	**half moon shape inc 50μm across oxides on edge**	**71.21**	**0.24**	**12.98**	**3.66**	**0.13**	**0.03**	**0.93**	**5.10**	**3.410**	**0.051**	**0.023**	**0.18**	**0.111**	**98.06**
O9-02-9a	**100μm long figure of 8 shape inc crack on edge**	**71.81**	**0.25**	**13.01**	**3.39**	**0.13**	**0.00**	**0.87**	**5.02**	**3.887**	**0.000**	**0.017**	**0.20**	**0.024**	**98.44**
O9-02-12a	80μm across oval inc 2 ves. at edge	70.96	0.25	12.98	3.88	0.11	0.01	1.03	5.11	3.460	0.000	0.012	0.20	0.017	98.01
O9-02-14a	80μm long clean semi-circle shape inc oxide on edge	70.90	0.23	12.93	3.66	0.15	0.01	0.94	5.03	3.410	0.007	0.011	0.22	0.067	97.55
O9-02-16a	round clean inc 30μm across	71.47	0.24	12.96	3.80	0.14	0.00	0.95	5.10	3.334	0.010	0.015	0.19	0.127	98.32
O9-02-18a	150μm long clean skinny oval inc	71.14	0.25	12.84	4.01	0.13	0.00	1.01	5.14	3.420	0.037	0.012	0.19	0.028	98.23
O9-02-21a	round clean inc	71.38	0.23	12.91	3.91	0.13	0.01	0.92	5.02	3.475	0.002	0.011	0.19	0.15	98.34
O9-02-22a	round clean inc w/ tiny bubble at base	70.88	0.24	12.94	3.89	0.14	0.00	0.92	4.96	3.707	0.014	0.010	0.21	0.105	98.02
Average		**71.47**	**0.24**	**12.94**	**3.43**	**0.11**	**0.01**	**0.91**	**5.09**	**3.45**	**0.03**	**0.019**	**0.204**	**0.056**	**97.93**
Standard Deviation (1σ)		**0.26**	**0.02**	**0.12**	**0.26**	**0.01**	**0.01**	**0.07**	**0.06**	**0.18**	**0.02**	**0.004**	**0.014**	**0.036**	

Shaded analyses indicate glass inclusions selected for petrologic method calculation (see chapter 3 (section 3.11 for more information).

Appendix B3 Öræfajökull 1362 glass geochemistry

(h) Distal ash glass data														
Sample	**Description**	**SiO_2**	**TiO_2**	**Al_2O_3**	**FeO**	**MnO**	**MgO**	**CaO**	**Na_2O**	**K_2O**	**P_2O_5**	**S**	**Cl**	**F**	**Total**
o1362-1	glass shard	73.61	0.23	13.72	3.38	0.09	0.01	0.99	4.01	3.39	0.001	0.006	0.203	0.000	99.66
o1362-2	glass shard	72.82	0.23	13.48	3.37	0.10	0.01	1.00	4.15	3.39	0.006	0.005	0.219	0.063	98.84
o1362-3	glass shard	72.75	0.23	13.45	3.27	0.11	0.00	0.96	4.05	3.28	0.011	0.003	0.214	0.081	98.40
o1362-4	glass shard	72.30	0.24	13.34	3.29	0.09	0.01	0.96	4.13	3.35	0.003	0.005	0.205	0.097	98.01
Average		**72.87**	**0.23**	**13.50**	**3.33**	**0.10**	**0.01**	**0.98**	**4.09**	**3.36**	**0.01**	**0.005**	**0.210**	**0.060**	**98.73**
Standard Deviation (1σ)		**0.47**	**0.00**	**0.14**	**0.05**	**0.01**	**0.00**	**0.02**	**0.06**	**0.05**	**0.00**	**0.001**	**0.007**	**0.037**	

Ö1362 distal ash location - 15 km N of Vatnajokull at Sauda, 1.5 cm thick tephra layer (sample provided by G. Larsen, 2001)

Appendix B3 Öræfajökull 1362 glass geochemistry

(i) Banded pumice glass data

Sample	Description	SiO_2	TiO_2	Al_2O_3	FeO	MnO	MgO	CaO	Na_2O	K_2O	P_2O_5	S	Cl	F	Total
O2-03-1	glass shard	71.34	0.24	13.63	3.32	0.10	0.01	0.97	4.60	3.43	0.00	0.00	0.19	0.16	98.0
O2-03-2	glass shard	72.05	0.24	13.70	3.46	0.11	0.02	1.02	4.77	3.39	0.00	0.01	0.20	0.17	99.1
O2-03-3	glass shard	71.88	0.36	13.60	3.51	0.10	0.03	1.07	4.54	3.33	0.00	0.00	0.18	0.10	98.7
O2-03-4	glass shard	71.19	0.21	15.24	2.79	0.08	0.02	1.28	5.84	2.91	0.00	0.00	0.16	0.15	99.9
O2-03-5	glass shard	71.97	0.25	13.64	3.49	0.10	0.04	0.99	4.61	3.39	0.00	0.00	0.19	0.11	98.8
O2-03-6	glass shard	70.81	0.22	14.51	3.02	0.10	0.01	1.19	5.51	2.99	0.00	0.00	0.17	0.08	98.6
O2-03-7	glass shard	71.26	0.24	13.47	3.40	0.10	0.04	1.01	4.80	3.36	0.01	0.00	0.19	0.17	98.0
O2-03-8	glass shard	71.56	0.25	13.76	3.37	0.11	0.01	1.00	4.67	3.41	0.01	0.00	0.20	0.11	98.5
O2-03-9	glass shard	71.07	0.24	13.61	3.37	0.10	0.02	1.01	4.65	3.44	0.00	0.01	0.20	0.12	97.9
O2-03-11	glass shard	72.61	0.25	13.73	3.54	0.11	0.01	1.06	4.68	3.43	0.00	0.00	0.20	0.17	99.8
O2-03-12	glass shard	72.38	0.26	13.66	3.43	0.10	0.02	1.01	4.61	3.38	0.00	0.00	0.18	0.15	99.2
O2-03-13	glass shard	73.05	0.24	13.70	3.44	0.10	0.01	0.98	4.81	3.37	0.00	0.01	0.21	0.07	100.0
O2-03-14	glass shard	72.63	0.26	13.82	3.31	0.11	0.01	0.99	4.49	3.39	0.00	0.00	0.20	0.13	99.3
O2-03-15	glass shard	71.68	0.25	13.61	3.61	0.11	0.07	1.06	4.67	3.18	0.00	0.01	0.19	0.15	98.6
O2-03-16	glass shard	72.41	0.24	13.64	3.46	0.09	0.04	1.02	4.70	3.38	0.00	0.00	0.20	0.18	99.4
O2-03-17	glass shard	72.57	0.25	13.66	3.34	0.11	0.01	1.00	4.52	3.47	0.00	0.01	0.20	0.13	99.3
O2-03-18	glass shard	70.96	0.22	14.16	3.22	0.10	0.02	0.95	4.55	3.30	0.00	0.01	0.20	0.16	97.9
O2-03-19	glass shard	72.88	0.23	13.73	3.40	0.09	0.02	0.99	4.72	3.42	0.00	0.00	0.19	0.07	99.7
O10-04matic-2	glass shard	59.83	0.26	13.29	12.52	0.61	0.28	7.34	6.71	0.83	0.02	n.a.	n.a.	n.a.	101.67
O10-04matic-3	glass shard	61.09	0.94	11.74	12.97	0.52	0.21	6.06	5.18	2.17	0.05	n.a.	n.a.	n.a.	100.92

Appendix B3 Öræfajökull 1362 glass geochemistry

(j) Grey pumice glass data

Sample	Description	SiO_2	TiO_2	Al_2O_3	FeO	MnO	MgO	CaO	Na_2O	K_2O	P_2O_5	S	Cl	F	Total
o405-3-3	matrix glass in pumice	55.74	1.85	13.63	12.14	0.34	2.84	10.14	4.79	0.80	0.78	0.13	0.04	0.06	101.4
o405-3-5	matrix glass in pumice	55.66	1.29	16.34	10.34	0.33	2.44	10.21	5.77	0.38	0.41	0.03	0.01	0.02	101.3
O405-II-4	matrix glass in pumice	50.38	3.18	12.76	14.47	0.23	4.86	8.91	2.81	0.52	0.39	n/a	n/a	n/a	98.5
O405-II-5	matrix glass in pumice	50.43	1.89	13.37	12.87	0.20	6.67	11.10	2.41	0.20	0.18	n/a	n/a	n/a	99.3
O405-II-12	matrix glass in pumice	50.14	1.78	13.49	12.80	0.22	6.46	11.14	2.35	0.21	0.16	n/a	n/a	n/a	98.8
O405-II-13	matrix glass in pumice	50.23	1.84	13.63	12.83	0.22	6.58	10.81	2.42	0.23	0.17	n/a	n/a	n/a	99.0
O405-II-14	matrix glass in pumice	50.26	1.90	13.35	13.04	0.21	6.50	10.85	2.48	0.21	0.19	n/a	n/a	n/a	99.0
O405-II-15	matrix glass in pumice	50.17	1.83	13.47	12.73	0.23	6.56	10.78	2.40	0.23	0.18	n/a	n/a	n/a	98.6

Appendix B5 Öræfajökull 1362 mineral geochemistry

(k) Feldspar data (rhyolite pumice)

Sample	SiO_2	Al_2O_3	FeO	MgO	CaO	Na_2O	K_2O	Total	Ab	An	Or	An/An+Ab
O9-02-5-rim	64.35	20.73	0.23	0.00	2.54	9.69	0.95	98.52	82.7	12.0	5.3	0.13
O9-02-6	64.29	21.20	0.24	0.00	3.00	9.45	0.82	99.02	81.1	14.2	4.6	0.15
O9-02-7	65.89	21.52	0.26	0.00	2.79	9.63	0.91	101.03	81.8	13.1	5.1	0.14
O9-02-7a	64.18	21.14	0.24	0.01	3.06	9.16	0.86	98.68	80.2	14.8	5.0	0.16
O9-02-7b	64.75	21.74	0.23	0.00	3.40	9.21	0.78	100.18	79.4	16.2	4.4	0.17
O9-02-8	65.95	21.76	0.24	0.00	2.87	10.00	0.86	101.69	82.3	13.1	4.7	0.14
o902-1-1	64.52	21.81	0.22	0.00	3.29	9.10	0.82	99.77	79.4	15.9	4.7	0.17
o902-1-1a	64.16	21.79	0.24	0.00	3.22	9.12	0.84	99.39	79.6	15.5	4.8	0.16
O401c-1-xtl-rim	62.83	21.91	0.34	0.00	4.03	8.42	0.82	98.38	75.3	19.9	4.8	0.21
O401c-1-xtl-core	62.72	22.01	0.34	0.00	4.02	8.35	0.79	98.24	75.3	20.0	4.7	0.21
O401c-2-xtl	62.62	22.25	0.36	0.00	4.34	8.13	0.82	98.56	73.5	21.7	4.9	0.23
O401c-3-xtl-rim	65.06	21.08	0.23	0.00	2.84	8.88	0.91	99.03	80.4	14.2	5.4	0.15
O401c-3-xtl-core	64.50	21.09	0.26	0.00	2.81	8.99	0.99	98.64	80.3	13.9	5.8	0.15
O401c-6-xtl-rim	64.22	21.17	0.24	0.00	2.91	8.84	0.90	98.32	80.1	14.6	5.4	0.15
O401c-6-xtl-core	64.69	22.01	0.25	0.00	3.50	8.71	0.73	99.94	78.3	17.4	4.3	0.18
O401z-1-xtl-rim	63.80	21.21	0.24	0.00	2.97	8.92	0.85	98.04	80.2	14.8	5.0	0.16
O401z-1-xtl-core	64.86	21.60	0.25	0.00	3.11	8.99	0.84	99.68	79.8	15.3	4.9	0.16

(k) Feldspar data (rhyolite pumice) (cont'd)

Sample	SiO_2	Al_2O_3	FeO	MgO	CaO	Na_2O	K_2O	Total	Ab	An	Or	An/An+Ab
O401z-2-xtl-rim	64.66	20.84	0.25	0.00	2.82	8.79	0.87	98.27	80.5	14.3	5.2	0.15
O401z-2-xtl-core	64.52	21.05	0.24	0.00	2.81	9.08	0.87	98.59	81.0	13.9	5.1	0.15
O401z-3-xtl-rim	65.23	21.38	0.23	0.00	2.88	9.05	0.88	99.66	80.7	14.2	5.2	0.15
O401z-3-xtl-core	64.93	21.14	0.24	0.00	2.74	9.15	0.90	99.09	81.3	13.5	5.3	0.14
O401z-4-xtl-rim	63.81	21.19	0.23	0.00	3.12	9.03	0.84	98.27	79.9	15.3	4.9	0.16
O401z-4-xtl-core	64.37	21.38	0.24	0.00	2.98	9.04	0.85	98.88	80.4	14.6	5.0	0.15
O401z-5-xtl-rim	64.06	21.70	0.25	0.00	3.35	8.87	0.78	99.03	79.0	16.5	4.6	0.17
O401z-5-xtl-core	64.34	21.05	0.26	0.00	2.76	9.15	0.89	98.49	81.3	13.5	5.2	0.14
O401z-12-xtl-rim	64.48	21.08	0.26	0.01	2.82	8.83	0.88	98.36	80.5	14.2	5.3	0.15
O401z-14-xtl-rim	65.33	21.35	0.24	0.00	2.73	9.14	0.90	99.71	81.3	13.4	5.3	0.14
O401z-14-xtl-core	64.66	21.57	0.25	0.00	3.14	9.00	0.82	99.46	79.8	15.4	4.8	0.16

Appendix B5 Öræfajökull 1362 mineral geochemistry

(l) Olivine data (rhyolite pumice)

Sample	SiO_2	FeO	MnO	MgO	CaO	NiO	Cr_2O_3	Total	Fo	Fa
O401xtls-3c	29.27	66.64	2.61	0.69	0.50	0.00	0.00	99.73	1.8	98.2
O401xtls-5c	29.00	66.25	2.67	0.70	0.53	0.00	0.00	99.20	1.9	98.2
O9-02-2	29.02	66.48	2.67	0.68	0.50	0.01	0.00	99.39	1.8	98.2
O9-02-9c	28.26	66.58	2.66	0.70	0.47	0.01	0.01	98.71	1.8	98.2
O9-02-14	29.00	66.54	2.66	0.71	0.51	0.01	0.00	99.45	1.9	98.1
O9-02-16	29.19	66.64	2.66	0.72	0.54	0.00	0.01	99.80	1.9	98.1
O9-02-18	28.84	66.16	2.70	0.68	0.53	0.00	0.02	98.99	1.8	98.2
O401c-7-xtl-rim	29.88	66.25	2.62	0.70	0.47	0.00	0.00	99.97	1.9	98.2
O401c-7-xtl-core	29.23	66.20	2.64	0.67	0.48	0.00	0.00	99.32	1.8	98.2
O401z-8-xtl-rim	30.07	66.54	2.63	0.72	0.49	0.01	0.02	100.51	1.9	98.1
O401z-8-xtl-core	29.15	66.39	2.64	0.70	0.48	0.00	0.01	99.41	1.8	98.2
O401z-9-xtl-rim	28.86	66.51	2.63	0.71	0.48	0.00	0.00	99.24	1.9	98.1
O401z-9-xtl-core	29.38	65.97	2.65	0.70	0.48	0.00	0.00	99.19	1.9	98.1
O401z-10-xtl-rim	29.25	66.54	2.67	0.71	0.45	0.00	0.00	99.67	1.9	98.1
O401z-10-xtl-core	29.17	66.51	2.68	0.65	0.49	0.01	0.01	99.55	1.7	98.3
O401-xtls-1c	29.36	66.66	2.64	0.71	0.50	0.00	0.01	99.94	1.9	98.1
O401-xtls-3c	29.26	66.67	2.67	0.73	0.48	0.01	0.00	99.88	1.9	98.1

Appendix B5 Öræfajökull 1362 mineral geochemistry

(m) Pyroxene data (rhyolite pumice)

Sample	SiO_2	TiO_2	Al_2O_3	FeO	MnO	MgO	CaO	Na_2O	Total	En	Fs	Wo	En/(En+Fs)
O9-02-15	47.20	0.54	0.72	29.45	1.15	1.48	18.88	0.36	99.78	4.7	52.3	43.0	0.08
O9-02-17	47.08	0.46	0.56	29.29	1.07	1.21	19.51	0.32	99.53	3.8	51.9	44.3	0.07
O9-02-19	47.49	0.46	0.57	29.62	1.13	1.00	19.48	0.37	100.12	3.2	52.6	44.3	0.06
O9-02-20	46.94	0.43	0.54	29.24	1.06	0.99	19.56	0.36	99.15	3.2	52.2	44.7	0.06
O401c-4-xtl-rim	47.05	0.43	0.51	28.31	0.99	1.51	19.30	0.33	98.54	4.8	50.8	44.4	0.09
O401c-4-xtl-core	48.77	0.51	1.17	24.17	0.88	4.01	19.32	0.41	99.28	12.8	43.1	44.1	0.23
O401c-5-xtl-rim	48.02	0.42	0.51	28.78	1.05	1.21	19.56	0.30	99.83	3.9	51.4	44.8	0.07
O401c-5-xtl-core	48.05	0.40	0.47	28.75	1.03	1.14	19.47	0.34	99.67	3.7	51.6	44.8	0.07
O401z-6-xtl-rim	48.10	0.41	0.49	28.93	1.03	1.22	19.45	0.31	99.95	3.9	51.6	44.5	0.07
O401z-6-xtl-core	47.61	0.42	0.46	28.96	1.02	1.13	19.26	0.32	99.17	3.6	52.0	44.3	0.07
O401z-7-xtl-rim	47.11	0.41	0.50	29.08	1.03	1.07	19.30	0.33	98.85	3.4	52.2	44.4	0.06
O401z-7-xtl-core	47.31	0.45	0.52	29.29	1.03	1.23	19.07	0.34	99.24	3.9	52.4	43.7	0.07
O401z-11-xtl-rim	46.27	0.41	0.52	28.97	1.03	1.18	19.07	0.32	97.77	3.8	52.2	44.0	0.07
O401z-11-xtl-core	47.84	0.42	0.52	28.81	1.02	1.39	19.10	0.31	99.43	4.4	51.7	43.9	0.08
O401z-13-xtl-rim	46.43	0.41	0.50	29.05	1.07	1.14	19.17	0.31	98.09	3.7	52.2	44.1	0.07
O401z-13-xtl-core	47.26	0.39	0.48	28.99	1.01	1.10	19.12	0.31	98.68	3.5	52.3	44.2	0.06
O401-xtls-2c	48.02	0.67	0.83	29.91	1.08	0.67	19.21	0.36	100.79	2.1	53.7	44.2	0.04

Appendix B5 Öræfajökull 1362 mineral geochemistry

(n) Fe-Ti oxide data (rhyolite pumice)

Sample	Description	SiO_2	TiO_2	Al_2O_3	FeO	MnO	MgO	CaO	Cr_2O_3	Total	Oxide Pairs for QUILF	Mg/Mn (Bacon &Hirschmann (1988))	Log (Mg/Mn)
o902-2-2	Ti-Magnetite inclusion	0.03	22.97	0.64	71.76	1.03	0.04	0.01	n/a	96.48	2	0.04	-1.43
o902-2-4	Ilmenite xtl	0.00	49.13	0.03	47.30	1.31	0.07	0.04	n/a	97.89	2	0.06	-1.25
o902-2-12	Ilmenite xtl	0.17	49.68	0.04	46.64	1.34	0.05	0.00	n/a	97.94	1	0.04	-1.40
o401b-35	Ti-Magnetite inclusion	0.12	24.03	0.66	71.82	1.04	0.03	0.01	n/a	97.72	1	0.03	-1.48
orae01-2-a	Magnetite xtl	0.04	23.30	0.66	71.24	1.04	0.04	0.00	0.000	96.31	3	0.04	-1.41
orae01-2-b	Ilmenite inc	0.00	49.96	0.05	46.85	1.31	0.07	0.06	0.000	98.30	3	0.05	-1.30
orae01-2-e	Ilmenite inc	0.00	49.86	0.03	46.44	1.32	0.08	0.10	0.023	97.86	4	0.06	-1.19
orae01-2-f	Magnetite inc	0.08	23.59	0.78	69.91	1.06	0.06	0.24	0.017	95.73	4	0.05	-1.28
orae01-5-k	Ilmenite inc	0.00	49.54	0.04	46.23	1.36	0.05	0.03	0.000	97.25	5	0.04	-1.41
orae01-5-l	Magnetite inc	0.03	23.31	0.69	69.65	1.04	0.03	0.00	0.000	94.75	5	0.03	-1.51
O902-1	Magnetite inc	0.04	22.46	0.68	70.40	1.02	0.03	0.09	0.000	94.72	9	0.03	-1.53
O902-2	Ilmenite xtl	0.00	49.14	0.04	46.00	1.32	0.08	0.02	0.000	96.60	9	0.06	-1.21
O902-4	Magnetite inc	0.04	23.62	0.65	68.90	1.07	0.05	0.15	0.027	94.49	10	0.05	-1.32
O902-5	Ilmenite xtl	0.04	47.67	0.05	43.97	1.29	0.08	2.41	0.000	95.49	10	0.06	-1.23
O902-6	Ilmenite xtl	0.00	49.34	0.05	46.07	1.35	0.08	0.01	0.005	96.90	11	0.06	-1.23
O902-7	Magnetite inc	0.03	23.61	0.80	69.32	1.07	0.19	0.09	0.000	95.11	11	0.18	-0.74
O902-8	Magnetite inc	0.03	24.69	0.80	68.86	1.09	0.21	0.07	0.008	95.76	12	0.19	-0.72
O902-10	Ilmenite xtl	0.00	49.16	0.06	46.27	1.33	0.07	0.05	0.000	96.92	12	0.05	-1.27
O902-11	Ilmenite xtl	0.00	49.45	0.02	46.14	1.35	0.09	0.02	0.005	97.07	13	0.07	-1.17
O902-12	Ilmenite xtl	0.00	49.39	0.05	46.34	1.33	0.08	0.02	0.013	97.22	14	0.06	-1.23
O902-13	Ilmenite xtl	0.00	49.03	0.04	46.26	1.31	0.05	0.03	0.016	96.74	15	0.04	-1.40
O902-15	Ilmenite inc	0.00	49.18	0.04	46.27	1.34	0.07	0.03	0.001	96.92	16	0.05	-1.31
O902-16	Ilmenite inc	0.00	48.72	0.05	46.01	1.32	0.09	0.22	0.000	96.40	6	0.07	-1.18
O902-17	Magnetite inc	0.03	23.78	0.69	68.98	1.04	0.04	0.07	0.004	94.64	6	0.04	-1.39
O902-18	Ilmenite inc	0.00	49.15	0.03	46.16	1.33	0.05	0.06	0.006	96.80	22	0.04	-1.39
O902-19	Magnetite inc	0.00	23.59	0.67	69.70	1.08	0.04	0.00	0.037	95.12	13	0.04	-1.39

(n) Fe-Ti oxide data (rhyolite pumice) (cont'd)

Sample	Description	SiO_2	TiO_2	Al_2O_3	FeO	MnO	MgO	CaO	Cr_2O_3	Total	Oxide Pairs for QUILF	Mg/Mn (Bacon &Hirschmann (1988))	Log (Mg/Mn)
O902-20	Magnetite inc	0.03	23.14	0.65	70.29	1.02	0.04	0.00	0.000	95.16	14	0.04	-1.43
O902-21	Magnetite inc	0.03	23.99	0.74	69.20	1.02	0.07	0.05	0.000	95.09	15	0.07	-1.18
O902-22	Ilmenite inc	0.00	48.75	0.04	45.92	1.30	0.10	0.07	0.000	96.17	17	0.07	-1.13
O902-23	Magnetite inc	0.07	23.30	0.60	69.00	1.03	0.05	0.14	0.000	94.18	16	0.05	-1.28
O902-24	Magnetite inc	0.09	21.96	0.64	69.12	1.03	0.05	0.21	0.034	93.12	17	0.04	-1.35
O902-25	Magnetite inc	0.05	23.97	0.67	69.56	1.04	0.06	0.00	0.013	95.37	18	0.06	-1.22
O902-26	Magnetite xtl	0.12	20.81	0.86	70.28	1.12	0.14	0.00	0.009	93.33	19	0.12	-0.91
O902-27	Magnetite xtl	0.11	21.09	0.82	69.92	1.02	0.16	0.03	0.009	93.15	20	0.15	-0.81
O902-29	Ilmenite xtl	0.00	50.08	0.02	45.89	1.35	0.07	0.00	0.017	97.43	18	0.05	-1.29
O902-30	Ilmenite xtl	0.00	49.00	0.04	46.08	1.29	0.09	0.01	0.040	96.53	19	0.07	-1.18
O902-31	Ilmenite xtl	0.00	49.65	0.04	46.42	1.31	0.07	0.09	0.002	97.59	20	0.05	-1.26
O902-32	Ilmenite xtl	0.00	48.94	0.03	46.49	1.31	0.08	0.02	0.000	96.87	21	0.06	-1.19
O902-33	Magnetite xtl	0.04	23.32	0.67	70.04	1.04	0.06	0.00	0.020	95.18	21	0.05	-1.26
O902-34	Magnetite xtl	0.02	23.63	0.66	69.46	1.05	0.04	0.00	0.001	94.86	22	0.04	-1.43
o206-1	Ilmenite xtl	0.00	49.18	0.04	46.05	1.32	0.06	0.01	0.008	96.67	8	0.05	-1.32
o206-7	Magnetite xtl	0.28	20.70	1.67	68.61	0.90	0.04	0.30	0.103	92.60	8	0.04	-1.35
o206-5	Ilmenite xtl	0.00	48.88	0.04	45.85	1.28	0.06	0.20	0.005	96.32	23	0.05	-1.31
o206-6	Magnetite xtl	0.05	24.53	1.03	67.11	1.08	0.00	0.17	0.033	94.00	23	0.00	-3.03
o206-14	Ilmenite xtl	0.00	49.05	0.11	45.95	1.28	0.08	0.05	0.014	96.53	7	0.06	-1.22
o206-15	Magnetite xtl	0.07	22.90	0.67	69.61	1.13	0.05	0.04	0.013	94.47	7	0.04	-1.35

Appendix B6 Öræfajökull 1362 mafic mineral geochemistry

(o) Feldspar data (banded pumice)

Sample	Description	SiO_2	Al_2O_3	FeO	MgO	CaO	Na_2O	K_2O	Total	Ab	An	Or	An/An+Ab
O1004-mafic-1	large xtl - fsp	62.23	22.07	0.31	0.00	4.79	8.46	0.49	98.38	74.0	23.2	2.8	0.24
O1004-mafic-2	large xtl - fsp	62.95	22.01	0.34	0.00	4.63	8.49	0.50	98.95	74.6	22.5	2.9	0.23
O203M-5	feldspar	54.09	19.86	9.41	0.66	5.27	6.73	0.37	96.85	68.1	29.5	2.5	0.30
O203-11-9	feldspar xtl	51.15	30.69	0.67	0.23	14.53	2.93	0.04	100.29	26.7	73.1	0.2	0.73

(p) Pyroxene data (banded pumice)

Sample	Description	SiO_2	TiO_2	Al_2O_3	FeO	MnO	MgO	CaO	Na_2O	Total	En	Fs	Wo	En/En+Fs
O1004-mafic-3	large xtl - pyx	47.03	0.69	0.92	27.03	1.23	2.72	19.96	0.31	99.94	8.4	47.1	44.5	0.15
O1004-mafic-4	large xtl - pyx	48.72	0.66	1.09	24.01	1.10	5.27	19.66	0.37	100.89	16.0	41.0	43.0	0.28
O1004-mafic-5	large xtl - pyx	47.23	0.79	1.08	27.27	1.18	2.43	19.94	0.33	100.28	7.6	47.7	44.7	0.14
O203M-3	pyroxene - augite xtl	48.50	0.96	1.66	18.31	0.71	9.82	18.35	0.28	98.66	29.5	30.9	39.6	0.49
O203M-7	pyroxene - augite xtl	48.93	1.11	4.00	19.46	0.71	7.04	16.63	1.55	100.00	23.5	36.5	40.0	0.39
O203M-9	pyroxene - augite xtl	51.76	1.25	3.67	20.29	0.68	4.57	14.35	1.72	99.11	17.4	43.3	39.3	0.29
O203M-10	pyroxene - augite xtl	47.66	1.18	2.24	20.73	0.78	7.33	17.91	0.44	98.65	23.0	36.5	40.4	0.39

(q) Olivine data (banded pumice)

Name	Description	SiO_2	FeO	MnO	MgO	CaO	NiO	Cr_2O_3	Total	Fo	Fa
O203M-4	olivine xtl	33.95	55.66	1.80	4.20	0.66	0.001	0.000	99.67	11.9	88.1

(r) Other mineral data (banded pumice)

Name	Type	SiO_2	TiO_2	Al_2O_3	FeO	MnO	MgO	CaO	Na_2O	K_2O	P_2O_5	NiO	Cr_2O_3	Total
O203M-1	apatite xtl?	0.16	0.00	0.00	0.54	0.08	0.15	54.32	0.02	0.00	43.05	0.000	0.000	98.32
O203M-2	apatite xtl?	0.12	0.01	0.00	0.52	0.09	0.18	54.97	0.03	0.00	42.71	0.000	0.000	98.63

Appendix B6 Öræfajökull 1362 mafic mineral geochemistry

(s) Feldspar data (grey pumice)

Sample	Description	SiO_2	Al_2O_3	FeO	MgO	CaO	Na_2O	K_2O	Total	Ab	An	Or	An/An+Ab
O405M-3	250um across phenocryst size xtl - fsp	55.85	25.55	0.49	0.06	8.85	6.45	0.21	97.54	56.2	42.6	1.2	0.43
O405M-4	250um across phenocryst size xtl - fsp	54.03	26.68	0.42	0.04	10.33	5.59	0.16	97.33	49.0	50.1	0.9	0.51
O405M-6	250um across phenocryst size xtl - fsp	53.63	26.87	0.42	0.04	10.43	5.56	0.15	97.14	48.7	50.4	0.9	0.51
O405M-7	xtl in mixed grey/white pumice clast - fsp	45.39	31.70	0.72	0.09	17.06	1.83	0.05	96.88	16.2	83.5	0.3	0.84
O405M-8	feldpsar xtl	55.91	26.32	0.44	0.03	9.68	6.05	0.20	98.67	52.5	46.4	1.1	0.47
O405M-10	feldpsar xtl	55.70	25.71	0.65	0.06	9.29	6.17	0.22	97.89	53.9	44.8	1.3	0.45
O405M-12	feldpsar xtl	55.84	25.79	0.60	0.04	9.11	6.36	0.22	98.06	55.1	43.6	1.3	0.44
O405M-14	feldpsar xtl	65.35	20.18	0.08	0.00	1.59	10.70	0.14	98.04	91.7	7.5	0.8	0.08
o405mafic-1	feldspar xtl	60.42	24.56	1.08	0.07	7.01	6.90	0.56	100.76	61.9	34.8	3.3	0.36
o405mafic-2	feldspar xtl	65.81	18.98	1.60	0.07	3.88	7.26	1.63	100.17	69.3	20.5	10.2	0.23
o405mafic-4	feldspar xtl	60.89	25.08	0.63	0.03	6.32	7.76	0.44	101.30	67.2	30.3	2.5	0.31
o405mafic-5	feldspar xtl	61.83	24.29	0.47	0.02	5.41	7.98	0.49	100.55	70.7	26.5	2.9	0.27
o405mafic-17	feldspar xtl	66.56	21.76	0.82	0.02	3.53	7.61	1.10	101.55	74.0	19.0	7.0	0.20
o405mafic-18	feldspar xtl	63.24	24.04	1.05	0.02	5.05	7.98	0.62	102.68	71.4	25.0	3.7	0.26
o405mafic-19	feldspar xtl	63.22	23.69	1.91	0.05	4.95	8.13	0.65	103.21	72.0	24.2	3.8	0.25
o405mafic-20	feldspar xtl	62.12	23.58	0.42	0.02	5.16	8.12	0.59	100.30	71.5	25.1	3.4	0.26
o405mafic-23	feldspar xtl	63.58	23.25	0.72	0.03	5.44	7.81	0.78	102.21	68.9	26.5	4.5	0.28
o405mafic-24	feldspar xtl	58.58	26.68	0.61	0.05	8.57	6.62	0.26	101.48	57.4	41.1	1.5	0.42
o405mafic-25	feldspar xtl	59.53	19.22	4.95	1.51	8.22	6.88	0.52	101.67	58.5	38.6	2.9	0.40
O405-M-18	feldspar lath	55.34	25.91	1.09	0.15	9.32	5.77	0.33	98.07	51.8	46.2	2.0	0.47
O405-M-19	feldspar lath	48.33	31.79	0.74	0.12	15.55	2.36	0.06	99.02	21.5	78.2	0.4	0.78

(t) Pyroxene data (grey pumice)

Sample	Description	SiO_2	TiO_2	Al_2O_3	FeO	MnO	MgO	CaO	Na_2O	Total	En	Fs	Wo	En/En+Fs
O405M-2	pyroxene - augite xtl	47.79	1.54	2.99	15.45	0.49	10.60	19.48	0.40	98.77	31.9	26.1	42.1	0.55
O405M-9	pyroxene - augite xtl	48.21	2.27	3.25	19.70	0.66	8.09	15.89	1.04	99.50	26.5	36.2	37.4	0.42
O405M-11	pyroxene - augite xtl	48.19	1.65	3.05	16.51	0.57	9.89	18.01	0.57	98.59	30.8	28.9	40.3	0.52
o405mafic-21	pyroxene xtl	48.46	2.21	4.36	16.81	0.56	9.46	18.72	0.67	101.41	29.3	29.2	41.6	0.50
O203-II-10	pyroxene xtl twinned?	51.70	0.92	4.16	7.97	0.20	16.27	18.62	0.23	100.28	47.7	13.1	39.2	0.78

Appendix C1: Supplementary information

Appendix C contains data associated with Chapter 4 (Lanzarote 1730-36).

Appendix C2 is a list of all sample locations.

FTIR data, temperature, and oxygen fugacity calculation data is listed in appendix C3. In the FTIR dataset, corresponding inclusion/matrix glass S, Cl, K_2O values are also shown for reference. The olivine-liquid equilibrium data calculated using the Kress and Carmichael calibration is also listed here.

The complete Lanzarote glass (major element and volatiles) and mineral geochemistry dataset is listed in appendix C4. Glass composition data (matrix glasses and glass inclusions) is listed for each eruptive episode. Each analysis listed in the matrix glass dataset represents an average of 3-10 spots on either an area of scoria matrix glass, lava matrix glass. Cation totals of mineral analyses are also listed (appendix C5).

Each dataset consists of the following:

(a) Matrix glass data

(b) Glass inclusion data

(c) Glass inclusion host crystal data

(d) Other crystal data

(e) Inclusion S (C_o) calculation data – this is the predicted S composition calculated using the K_2O, TiO_2, P_2O_5 content of matrix glass (refer to chapter 4 text on S/*I* ratios for more information). The mean value calculated using this proxy method provides the pre-eruptive S concentration for use in the petrologic method (see

chapter 4). Note that the predicted S table for the phase IV lava sample is calculated using a slightly different method (refer to chapter 4).

Mean and standard deviation (2σ) values for matrix glass analyses from each of the eruptive episodes are also shown for reference – this data also provides an indication of relative analytical error.

Appendix C2 Lanzarote sample locations

Location	Description
LZ-1	Small side road behind village of Tenesar; phase I episode 2 distal lavas
LZ-2	SE side of main Mancha Blanca coastal road, west of Tenesar; phase V episode 2 distal lavas
LZ-3	Eastern side of Caldera de los Cuervos; phase I proximal lavas & fallout
LZ-4	Caldera de los Cuervos cone; phase I episode 1 cone deposits & lavas
LZ-5	Western end of Caldera de los Cuervos cone, margin between Cuervos and older cone; phase I lava
LZ-6	Outskirts of Arrecife; phase V episode 1 distal lavas
LZ-7	Outskirts of La Asomeda; phase V episode 1 lava (Puerto del Carmen finger)
LZ-8	Camino Bilbao, in front of Montana Diama; phase I episode 1 fallout
LZ-9	Small quarry in La Geria, on margin of La Geria vineyard; phase I fallout
LZ-10	Rim of Santa Catalina cone; phase I episode 2 cone deposits
LZ-11	South flank of Santa Catalina; phase I & II fallout and lavas
LZ-12	Main SW road into Timanfaya National Park; phase II lavas & phase IV fallout
LZ-13	Punta del Volcan, just past Playa del Janubio; phase III episode 2 coastal lavas
LZ-14	Coastal track at El Golfo; phase III episode 1 lavas
LZ-15	Farm at the back of El Golfo; phase III episode 1 vents
LZ-16	Small track leading towards Timanfaya National Park of main El Golfo-Yaiza highway; phase III episode 3 distal lavas
LZ-17	Small track in national park leading up to NNE crater of Pico Partido; phase I episode 2 & phase II proximal lavas & fallout

Appendix C3 Fourier Transform Infra Red (FTIR) data (Lanzarote glass inclusions and matrix glasses)

(a) Glass inclusions

Sample	Unit	Absorbance	Thickness (cm)	Density (g/L)	εH_2O	H_2O (wt%)	S	Cl	K_2O	H_2O/K_2O
LZ-3-02-17a	Phase I Episode 1	0.308	0.00632	2850	63	0.489	0.228	0.198	1.46	0.34
LZ-3-02-10	Phase I Episode 1	0.284	0.01323	2840	63	0.216	0.169	0.149	1.30	0.17
LZ-3-02-16b	Phase I Episode 1	0.054	0.01323	2850	63	0.041	0.079	0.093	1.41	0.03
LZ-3-04-4	Phase I Episode 2	0.226	0.02309	2810	63	0.100	0.099	0.100	0.94	0.11
LZ-3-04-2	Phase I Episode 2	0.265	0.02309	2820	63	0.116	0.112	0.131	0.82	0.14
LZ-3-04-3	Phase I Episode 2	0.272	0.02309	2820	63	0.119	0.106	0.127	0.90	0.13

(b) Matrix glasses

Sample	Unit	Absorbance	Thickness (cm)	Density (g/L)	εH_2O	H_2O (wt%)	S	Cl	K_2O	H_2O/K_2O
LZ-3-02-3	Phase I Episode 1	0.074	0.01923	2850	63	0.039	0.019	0.047	1.54	0.03
LZ-3-02-20	Phase I Episode 1	0.05	0.01923	2840	63	0.026	0.014	0.035	1.41	0.02
LZ-3-04-e	Phase I Episode 2	0.108	0.02103	2820	63	0.052	0.011	0.048	0.86	0.06
LZ-11-02-1-6	Phase II	0.139	0.01904	2780	63	0.075	0.016	0.032	1.06	0.07
LZ-11-02-12	Phase II	0.093	0.01904	2820	63	0.050	0.014	0.022	0.87	0.06

H_2O is calculated using Beers Law [$c = MA/pd\varepsilon \times 100$, where c is the species concentration, M is the molecular weight (18.02 for total H_2O, A is the absorbance, d is the room temperature density of the glass (g/l), ρ is the sample thickness (cm) and ε is the molar absorption coefficient ($l\ mol^{-1}cm^{-1}$). Sample thickness was measured using a Mitutoyo Digimatic Indicator, to a precision of 3 microns. Glass density, based on major element glass composition was calculated using the MELTS software and extrapolated to obtain density at room temperature. Molar absorption coefficient for H_2O is 63 $lmol^{-1}cm^{-1}$ Dixon et al. 1995).

Appendix C3 Oxygen fugacity and temperature calculation data

(a) Oxygen fugacity calculation data

Phase/Episode	*X*Fe (olivine)	*X*Mg (olivine)	*X*Al (spinel)	*X*Mg (spinel)	XFe^{3+} (spinel)	*X*Cr (spinel)	XFe^{3+} (spinel)	*X*Ti (spinel)	Mg#	Cr#
LZ-8-02-22/23 (I,1)	0.22	1.787	0.875	0.572	0.421	0.947	0.176	0.001	0.58	0.52
LZ-3-02-21R/22 (I,1)	0.258	1.748	1.12	0.351	0.651	0.612	0.244	0.012	0.35	0.35
LZ-3-02-23/24R (I,1)	0.231	1.754	0.877	0.534	0.48	0.934	0.141	0.024	0.53	0.52
LZ-3-02-27/28 (I,1)	0.276	1.723	0.378	0.492	0.552	1.255	0.259	0.054	0.47	0.77
LZ-5-01-10c (I,2)	0.233	1.782	0.88	0.544	0.464	0.981	0.104	0.018	0.54	0.53
LZ-5-01-11c (I,2)	0.291	1.689	0.873	0.464	0.544	0.981	0.108	0.019	0.46	0.53
LZ-5-01-4c/9c (I,2)	0.363	1.624	0.811	0.633	0.36	1.045	0.143	0	0.64	0.56
LZ-11-02-2 (II)	0.212	1.808	0.913	0.663	0.343	0.972	0.088	0.013	0.66	0.52
LZ-11-02-1c/d (II)	0.33	1.692	0.875	0.689	0.317	0.762	0.336	0.014	0.68	0.47
LZ-14-01-1 (III,1)	0.312	1.664	0.656	0.483	0.578	0.882	0.322	0.07	0.46	0.57
LZ-16-01-21c/22c (III,3)	0.339	1.638	0.736	0.539	0.496	0.98	0.2	0.042	0.52	0.57
LZ-12-01-1c (IV)	0.269	1.743	0.587	0.614	0.492	0.699	0.488	0.113	0.56	0.54
LZ-12-02-1c (IV lava)	0.269	1.743	0.817	0.588	0.412	0.998	0.172	0.007	0.59	0.55
LZ-6-01-2 (V,1)	0.331	1.636	0.316	1.391	0.361	0.561	1.049	0.037	0.79	0.64
LZ-2-01-1c (V,2)	0.225	1.779	0.976	0.656	0.344	0.83	0.183	0.005	0.66	0.46
LZ-3-01-6/6c (V,2)	0.315	1.668	0.843	0.557	0.484	0.842	0.22	0.048	0.54	0.50

(a) Oxygen fugacity calculation data (cont'd)

Phase/Episode	$X Fe_{sp}$ (Fe/Fe+Mg)	$X Fe^{3+}_{sp}$ ($Fe^{3+}/Fe^{3+}+Al^{3+}Cr^{3+}$)	$X Fe^{2+}_{sp}$ ($Fe^{2+}/Fe^{2+}+Mg$)	$X Al_{sp}$ (Al/Al+Cr+Fe^{3+})
LZ-8-02-22/23 (I,1)	0.110	0.088	0.424	0.438
LZ-3-02-21R/22 (I,1)	0.129	0.123	0.650	0.567
LZ-3-02-23/24R (I,1)	0.116	0.072	0.473	0.449
LZ-3-02-27/28 (I,1)	0.138	0.137	0.529	0.200
LZ-5-01-10c (I,2)	0.116	0.053	0.460	0.448
LZ-5-01-11c (I,2)	0.147	0.055	0.540	0.445
LZ-5-01-4c/9c (I,2)	0.183	0.072	0.363	0.406
LZ-11-02-2 (II)	0.105	0.045	0.341	0.463
LZ-11-02-1c/d (II)	0.163	0.170	0.315	0.443
LZ-14-01-1 (III,1)	0.158	0.173	0.545	0.353
LZ-16-01-21c/22c (III,3)	0.171	0.104	0.479	0.384
LZ-12-01-1c (IV)	0.134	0.275	0.445	0.331
LZ-12-02-1c (IV lava)	0.134	0.087	0.412	0.411
LZ-6-01-2 (V,1)	0.168	0.545	0.206	0.164
LZ-2-01-1c (V,2)	0.112	0.092	0.344	0.491
LZ-3-01-6/6c (V,2)	0.159	0.115	0.465	0.443

(a) Oxygen fugacity calculation data (cont'd)

Sample	Pressure (GPa)	*R*	*T* (K)	$\Delta\log f_{O_2}$ (FMQ)	T (°C)	FMQ buffer value	NNO buffer value	log fO2	ΔNNO
LZ-8-02-22/23 (I,1)	1	8.3145	1439.05	1.12	1166.1	-8.2	-7.8	-7.1	0.7
LZ-3-02-21R/22 (I,1)	1	8.3145	1445.68	1.97	1172.7	-8.1	-7.7	-6.1	1.6
LZ-3-02-23/24R (I,1)	1	8.3145	1412.76	0.76	1139.8	-8.5	-8.1	-7.7	0.3
LZ-3-02-27/28 (I,1)	1	8.3145	1412.74	1.30	1139.7	-8.5	-8.1	-7.2	0.9
LZ-5-01-10c (I,2)	1	8.3145	1444.62	0.20	1171.6	-8.1	-7.7	-7.9	-0.2
LZ-5-01-11c (I,2)	1	8.3145	1444.62	-0.10	1171.6	-8.1	-7.7	-8.2	-0.5
LZ-5-01-4c/9c (I,2)	1	8.3145	1432.81	-0.48	1159.8	-8.3	-7.9	-8.7	-0.9
LZ-5-01-10c (I,2)	1	8.3145	1432.81	-0.48	1159.8	-8.3	-7.9	-8.7	-0.9
LZ-11-02-2 (II)	1	8.3145	1427.21	-0.12	1154.2	-8.3	-7.9	-8.4	-0.5
LZ-11-02-1c/d (II)	1	8.3145	1437.53	1.18	1164.5	-8.2	-7.8	-7.0	0.8
LZ-14-01-1 (III,1)	1	8.3145	1453.07	1.62	1180.1	-8.0	-7.6	-6.4	1.2
LZ-16-01-21c/22c (III,3)	1	8.3145	1442.15	0.51	1169.2	-8.2	-7.7	-7.6	0.1
LZ-12-01-1c (IV)	1	8.3145	1416.62	2.56	1143.6	-8.5	-8.0	-5.9	2.1
LZ-12-02-1c (IV lava)	1	8.3145	1439.94	0.60	1166.9	-8.2	-7.8	-7.6	0.2
LZ-6-01-2 (V,1)	1	8.3145	1408.22	2.46	1135.2	-8.6	-8.1	-6.1	2.0
LZ-2-01-1c (V,2)	1	8.3145	1394.41	1.05	1121.4	-8.7	-8.3	-7.7	0.6
LZ-3-01-6/6c (V,2)	1	8.3145	1410.37	0.90	1137.4	-8.5	-8.1	-7.6	0.5

**R* = gas constant. NNO and FMQ buffer values calculated using method described in Chapter 4.

Appendix C3 Temperature calculation data

(b) Temperature data			
Phase/Episode	**wt% MgO (glass)**	T_{MgO} (°C)	T(°C) (Langmuir)
LZ-8-01-22/23 (I,1)	6.06	1135.8	1166.1
LZ-3-02-21C/22 (I,1)	6.06	1135.8	1172.7
LZ-3-02-23/24C (I,1)	6.02	1135.0	1139.8
LZ-3-02-27/28 (I,1)	5.99	1134.4	1139.7
LZ-5-01-q (I,2)	6.63	1147.3	1171.6
LZ-5-01-11c (I,2)	6.47	1144.0	1171.6
LZ-5-01-4c/9c (I,2)	6.21	1138.8	1159.8
LZ-5-01-10c (I,2)	6.28	1140.2	1159.8
LZ-11-02-2 (II)	6.17	1138.0	1154.2
LZ-11-02-1c/d (II)	6.14	1137.4	1164.5
LZ-14-01-1 (III,1)	6.86	1151.9	1180.1
LZ-16-01-21c/22c (III,3)	6.33	1141.2	1169.2
LZ-16-01-6c (III,3)	6.08	1136.2	1162.1
LZ-12-01-1c (IV)	5.72	1129.0	1143.6
LZ-12-02-3c (IV lava)	7.06	1155.9	1175.1
LZ-12-02-1c (IV lava)	6.91	1152.9	1166.9
LZ-6-01-2 (V,1)	5.48	1124.1	1135.2
LZ-2-01-1c (V,2)	5.96	1133.8	1121.4

Appendix C3 Olivine-liquid equilibrium dataset

(c) Olivine-Liquid equilibrium (Kress and Carmichael) data

		HOST OLIVINE CRYSTAL					GLASS INCLUSION				
Phase	**Sample**	**Fe^{2+}olv**	**Mg olv**	**Fe^{2+}/Mg olv**	**Fe^{2+}/Mg liq**	**K_D**	**Fe^{2+}/Mg liq (K&C)**	**K_D(K&C)**	**Fe^{2+}/Fe^{3+} ratio**	**wt% Fe_2O_3**	**wt% FeO**
I,1	LZ-8-01-6a	0.296	1.703	0.174	0.991	0.18	0.642	0.27	0.272	4.18	6.92
I,1	LZ-8-01-24	0.264	1.73	0.153	1.076	0.14	0.691	0.22	0.269	4.11	6.87
I,1	LZ-8-01-1a	0.278	1.72	0.162	0.999	0.16	0.651	0.25	0.267	4.11	6.92
I,1	LZ-8-01-2a	0.278	1.72	0.162	1.144	0.14	0.742	0.22	0.271	4.34	7.22
I,1	LZ-8-01-26	0.268	1.729	0.155	1.016	0.15	0.661	0.23	0.268	4.26	7.14
I,1	LZ-8-01-19	0.296	1.703	0.174	1.075	0.16	0.697	0.25	0.271	4.18	6.94
I,1	LZ-3-02-4a	0.313	1.689	0.185	1.063	0.17	0.578	0.32	0.420	5.59	5.98
I,1	LZ-3-02-10	0.311	1.684	0.185	1.056	0.17	0.571	0.32	0.424	5.38	5.71
I,1	LZ-3-02-10a	0.311	1.684	0.185	0.957	0.19	0.517	0.36	0.426	5.29	5.58
I,1	LZ-3-02-13a	0.256	1.758	0.146	1.112	0.13	0.604	0.24	0.421	5.62	6.01
I,1	LZ-3-02-16b	0.184	1.823	0.101	1.030	0.10	0.562	0.18	0.416	5.58	6.03
I,1	LZ-3-02-17a	0.184	1.823	0.101	1.034	0.10	0.564	0.18	0.416	5.57	6.02
I,1	LZ-3-02-26a	0.223	1.793	0.124	1.149	0.11	0.626	0.20	0.417	5.36	5.78
I,1	LZ-5-02-a	0.250	1.713	0.146	1.247	0.12	0.684	0.21	0.412	5.59	6.11
I,2	LZ-10-01-6b	0.282	1.729	0.163	0.961	0.17	0.705	0.23	0.182	3.13	7.76
I,2	LZ-10-01-6d	0.282	1.729	0.163	0.955	0.17	0.703	0.23	0.180	3.11	7.79
I,2	LZ-10-01-7b	0.282	1.729	0.163	0.988	0.17	0.725	0.22	0.181	3.14	7.83
I,2	LZ-10-01-8a	0.282	1.729	0.163	1.033	0.16	0.759	0.21	0.181	3.13	7.79
I,2	LZ-10-01-9a	0.282	1.729	0.163	0.984	0.17	0.722	0.23	0.181	3.15	7.83
I,2	LZ-10-01-14a	0.282	1.729	0.163	1.002	0.16	0.736	0.22	0.181	3.13	7.79
I,2	LZ-11-04-4	0.385	1.629	0.236	1.035	0.23	0.786	0.30	0.159	2.93	8.28
I,2	LZ-11-04-9a	0.318	1.695	0.188	1.387	0.14	0.972	0.19	0.159	3.06	8.65
I,2	LZ-11-04-1a	0.322	1.696	0.190	1.263	0.15	0.960	0.20	0.158	3.05	8.67
I,2	LZ-3-04-2	0.314	1.674	0.188	1.041	0.18	0.773	0.24	0.174	3.15	8.15
I,2	LZ-3-04-3	0.321	1.668	0.192	1.017	0.19	0.749	0.26	0.179	3.19	8.01
I,2	LZ-3-04-4	0.273	1.727	0.158	0.947	0.17	0.697	0.23	0.180	3.08	7.72
II	LZ-11-01-2a	0.212	1.807	0.117	0.996	0.12	0.688	0.17	0.225	3.66	7.33
II	LZ-11-02-1a	0.33	1.692	0.195	1.026	0.19	0.713	0.27	0.219	3.81	7.81
II	LZ-11-02-18a	0.304	1.695	0.179	0.995	0.18	0.635	0.28	0.215	3.71	7.76
II	LZ-11-02-11a	0.33	1.692	0.195	0.908	0.21	0.692	0.28	0.219	3.75	7.72
II	LZ-11-02-14a	0.312	1.692	0.184	1.044	0.18	0.728	0.25	0.217	3.71	7.68
II	LZ-11-02-2a	0.296	1.707	0.173	1.012	0.17	0.699	0.25	0.224	3.83	7.69

(c) Olivine-Liquid equilibrium (Kress and Carmichael) data

		HOST OLIVINE CRYSTAL					GLASS INCLUSION				
Phase	**Sample**	**Fe^{2+}olv**	**Mg olv**	**Fe^{2+}/Mg olv**	**Fe^{2+}/Mg liq**	**K_D**	**Fe^{2+}/Mg liq (K&C)**	**K_D(K&C)**	**Fe^{2+}/Fe^{3+} ratio**	**wt% Fe_2O_3**	**wt% FeO**
III,1	LZ-15-01-25a	0.294	1.695	0.173	0.907	0.19	0.596	0.29	0.261	4.11	7.09
III,1	LZ-15-01-29a	0.294	1.695	0.173	1.005	0.17	0.659	0.26	0.263	3.98	6.81
III,1	LZ-15-01-16a	0.291	1.701	0.171	0.998	0.17	0.656	0.26	0.260	4.10	7.09
III,1	LZ-15-01-20a	0.303	1.703	0.178	1.059	0.17	0.694	0.26	0.263	4.13	7.05
III,1	LZ-15-01-21a	0.351	1.604	0.219	0.986	0.22	0.649	0.34	0.261	4.05	6.98
III,1	LZ-14-01-1a	0.307	1.671	0.184	1.054	0.17	0.695	0.26	0.258	4.03	7.02
III,1	LZ-14-01-1-5a	0.305	1.688	0.181	0.898	0.20	0.589	0.31	0.262	4.20	7.20
III,1	LZ-14-01-2a	0.312	1.697	0.184	0.948	0.19	0.630	0.29	0.253	4.01	7.14
III,1	LZ-14-01-5a	0.301	1.679	0.179	0.912	0.20	0.604	0.30	0.255	4.14	7.30
III,1	LZ-14-01-7a	0.301	1.679	0.179	0.984	0.18	0.655	0.27	0.252	4.04	7.22
III,2	LZ-13-01-7a	0.331	1.71	0.194	1.058	0.18	0.734	0.26	0.220	4.58	9.35
III,2	LZ-13-01-10a	0.341	1.639	0.208	1.071	0.19	0.744	0.28	0.220	4.58	9.36
III,2	LZ-13-01-12a	0.351	1.633	0.215	1.098	0.20	0.761	0.28	0.221	4.61	9.36
III,2	LZ-13-01-17a	0.354	1.595	0.222	1.180	0.19	0.810	0.27	0.229	4.49	8.84
III,2	LZ-13-01-22a	0.354	1.595	0.222	1.169	0.19	0.800	0.28	0.231	4.56	8.88
III,3	LZ-16-01-10a	0.228	1.755	0.130	0.976	0.13	0.709	0.18	0.188	3.24	7.76
III,3	LZ-16-01-22a	0.339	1.638	0.207	0.937	0.22	0.684	0.30	0.186	3.18	7.72
III,3	LZ-16-01-3a	0.389	1.616	0.241	0.945	0.25	0.684	0.35	0.191	3.36	7.91
III,3	LZ-16-01-7a	0.322	1.68	0.192	0.918	0.21	0.664	0.29	0.192	3.33	7.79
III,3	LZ-16-01-8a	0.322	1.68	0.192	1.014	0.19	0.733	0.26	0.191	3.38	7.95
IV	LZ-12-01-1a	0.306	1.689	0.181	1.055	0.17	0.579	0.31	0.411	5.39	5.91
IV	LZ-12-01-4a	0.33	1.675	0.197	1.015	0.19	0.562	0.35	0.403	5.09	5.69
IV	LZ-12-01-6a	0.297	1.701	0.175	0.981	0.18	0.543	0.32	0.404	5.22	5.81
IV	LZ-12-01-28	0.316	1.669	0.189	1.123	0.17	0.615	0.31	0.413	5.29	5.76
IV	LZ-12-01-1-7	0.304	1.685	0.180	1.085	0.17	0.598	0.30	0.408	5.29	5.84
IV-lava	LZ-12-02-5a	0.21	1.776	0.118	0.987	0.12	0.659	0.18	0.249	4.38	7.89
IV-lava	LZ-12-02-9a	0.28	1.721	0.163	0.988	0.16	0.664	0.25	0.244	4.51	8.32
IV-lava	LZ-12-02-10a	0.28	1.721	0.163	0.947	0.17	0.635	0.26	0.246	4.32	7.91
IV-lava	LZ-12-02-14a	0.253	1.76	0.144	0.968	0.15	0.647	0.22	0.248	4.39	7.97
IV-lava	LZ-12-02-16a	0.253	1.76	0.144	0.944	0.15	0.633	0.23	0.246	4.35	7.97

(c) Olivine-Liquid equilibrium (Kress and Carmichael) data

		HOST OLIVINE CRYSTAL					GLASS INCLUSION				
Phase	**Sample**	**Fe^{2+}olv**	**Mg olv**	**Fe^{2+}/Mg olv**	**Fe^{2+}/Mg liq**	**K_D**	**Fe^{2+}/Mg liq (K&C)**	**K_D(K&C)**	**Fe^{2+}/Fe^{3+} ratio**	**wt% Fe_2O_3**	**wt% FeO**
V,1	LZ-6-01-1a	0.444	1.517	0.293	1.069	0.27	0.768	0.38	0.196	3.24	7.43
V,1	LZ-6-01-1b	0.444	1.517	0.293	1.135	0.26	0.813	0.36	0.198	3.31	7.52
V,1	LZ-6-01-5a	0.283	1.689	0.168	1.037	0.16	0.593	0.28	0.375	4.80	5.76
V,1	LZ-6-01a-8a	0.379	1.588	0.239	1.075	0.22	0.771	0.31	0.197	3.30	7.53
V,1	LZ-6-01a-9a	0.43	1.536	0.280	1.121	0.25	0.805	0.35	0.197	3.39	7.75
V,1	LZ-7-01-7b	0.416	1.554	0.268	1.173	0.23	0.833	0.32	0.205	3.37	7.42
V,1	LZ-7-01-8a	0.428	1.548	0.276	1.158	0.24	0.826	0.33	0.201	3.53	7.89
V,1	LZ-7-01-9b	0.337	1.641	0.205	1.158	0.18	0.659	0.31	0.379	5.16	6.13
V,2	LZ-2-01-1a	0.225	1.778	0.127	1.031	0.12	0.561	0.23	0.419	5.55	5.96
V,2	LZ-2-01-6a	0.266	1.727	0.154	1.009	0.15	0.548	0.28	0.421	5.61	6.00
V,2	LZ-2-01-9a	0.264	1.739	0.152	1.108	0.14	0.592	0.26	0.436	5.77	5.96
V,2	LZ-2-01-12a	0.27	1.721	0.157	1.113	0.14	0.602	0.26	0.425	5.82	6.17
V,2	LZ-2-01-12d	0.27	1.721	0.157	1.050	0.15	0.574	0.27	0.415	5.74	6.23
V,2	LZ-3-01-20a	0.292	1.708	0.171	1.075	0.16	0.598	0.29	0.399	5.31	5.99
V,2	LZ-3-01-a-1a	0.293	1.704	0.172	1.131	0.15	0.617	0.28	0.416	5.70	6.16
V,2	LZ-3-01-1a	0.23	1.77	0.130	1.124	0.12	0.638	0.20	0.382	5.42	6.40

*Fe^{2+}/Mg_{liq} (K&C) and K_D (K&C) indicate values calculated following correction of inclusion data to include Fe_2O_3. Calculation of ferric-ferrous iron ratios based on Kress and Carmichael (1991)

Appendix C4 Phase I Episode 1 (Caldera de los Cuervos)

(a) Phase I Episode 1 Matrix glass data

Sample	Type	SiO_2	TiO_2	Al_2O_3	FeO	MnO	MgO	CaO	Na_2O	K_2O	P_2O_5	S	Cl	F	Total
LZ-8-01-9	mtx gls attached to xtl LZ-8-01-6c	44.86	3.02	14.51	10.61	0.18	5.90	12.46	4.23	1.19	1.08	0.010	0.069	0.034	98.16
LZ-8-01-16	Gls in scoria frag	44.78	3.00	14.99	10.78	0.18	5.11	11.59	4.61	1.31	1.15	0.013	0.077	0.061	97.65
LZ-5-02-1	xtl-free matrix gls shard in scoria frag	45.12	3.57	15.18	11.35	0.18	5.02	11.59	4.22	1.83	1.15	0.018	0.070	0.054	99.38
LZ-5-02-6	matrix gls shard some larger olv xtls	44.63	3.55	15.49	11.51	0.19	4.93	11.01	4.40	1.90	1.15	0.020	0.079	0.053	98.62
LZ-5-02-11	gls in scoria frag	44.55	3.61	15.34	11.41	0.17	4.99	11.14	4.38	1.91	1.12	0.025	0.080	0.057	98.55
LZ-5-02-16	gls in scoria frag	44.08	3.70	15.08	11.39	0.18	5.10	11.85	4.06	1.81	1.07	0.017	0.074	0.042	98.47
LZ-5-02-21	matrix gls attached to oliv xtl	44.26	3.62	15.07	11.44	0.19	5.02	11.48	4.15	1.87	1.11	0.025	0.082	0.018	98.35
LZ-5-02-26	matrix gls in scoria frag	44.50	3.61	15.45	11.43	0.20	5.23	11.47	4.29	1.86	1.09	0.020	0.077	0.020	98.88
LZ-5-02-31	matrix gls in scoria frag	45.33	3.71	13.29	10.50	0.17	6.14	12.65	3.19	1.33	0.81	0.016	0.050	0.033	98.98
LZ-8-01-1	matrix gls in scoria frag	46.54	2.89	14.53	10.73	0.19	5.37	12.06	3.98	1.21	1.18	0.012	0.073	0.030	98.78
LZ-5-02-b	matrix glass	45.14	3.62	14.86	11.01	0.17	5.49	12.26	3.82	1.75	1.10	0.019	0.067	0.000	99.30
LZ-5-02-c	matrix glass	44.80	3.56	15.13	11.53	0.18	5.63	11.41	4.05	1.81	1.20	0.027	0.077	0.012	99.42
LZ-5-02-d	matrix glass	45.38	3.66	15.55	12.10	0.19	5.13	10.47	4.60	2.07	1.33	0.021	0.039	0.053	100.60
LZ-5-02-e	matrix glass	45.36	3.56	15.56	11.50	0.20	5.56	11.03	4.42	1.90	1.13	0.023	0.038	0.051	100.32
LZ-8-01-3	matrix gls in scoria frag	45.18	3.60	15.41	11.71	0.19	5.77	10.97	4.36	1.92	1.22	0.014	0.022	0.039	100.41
LZ-3-02-1	matrix glass in scoria	44.635	3.59	14.75	10.51	0.16	5.91	12.83	4.05	1.49	0.98	0.015	0.056	0.124	99.10
LZ-3-02-2	matrix glass in scoria	44.617	3.52	15.45	10.93	0.18	5.38	11.51	4.38	1.67	1.12	0.017	0.028	0.034	98.82
LZ-3-02-3	matrix glass in scoria	44.351	3.52	15.48	10.89	0.17	5.20	12.26	4.27	1.54	1.04	0.019	0.047	0.212	98.99
LZ-3-02-6	matrix glass in Pele's tear	44.66	3.26	14.63	10.50	0.19	5.85	12.53	4.21	1.39	1.07	0.016	0.064	0.001	98.36
LZ-3-02-7	matrix glass in Pele's tear	44.62	3.58	15.26	10.99	0.19	5.49	11.93	4.01	1.42	0.99	0.018	0.054	0.042	98.59
LZ-3-02-12	matrix glass attached to xtl	44.47	3.55	14.68	10.90	0.16	5.51	12.07	4.04	1.36	1.06	0.013	0.066	0.152	98.04
LZ-3-02-14	matrix glass attached to xtl	44.73	3.36	14.78	10.96	0.16	5.46	12.03	4.07	1.40	0.99	0.015	0.070	0.000	98.01
LZ-3-02-20	matrix glass attached to xtl	44.57	3.40	14.90	10.56	0.17	5.55	12.47	4.05	1.41	0.95	0.014	0.035	0.033	98.10
LZ-3-02-06	xtl-free matrix glass	44.20	3.20	14.57	10.98	0.16	5.65	12.44	4.21	1.42	1.02	0.013	0.066	0.070	98.00

(b) Phase I episode 1 glass inclusion data

Sample	Type	SiO_2	TiO_2	Al_2O_3	FeO	MnO	MgO	CaO	Na_2O	K_2O	P_2O_5	S	Cl	F	Total
LZ-8-01-6a	35µm across rounded triangle inc	45.27	2.97	14.24	10.69	0.18	6.05	12.90	4.00	1.21	1.05	0.055	0.081	0.188	98.87
LZ-8-01-24	**100µm long boot shape inc crack on edge**	**45.36**	**3.06**	**14.94**	**10.57**	**0.17**	**5.58**	**12.27**	**4.25**	**1.29**	**1.03**	**0.095**	**0.076**	**0.119**	**98.81**
LZ-8-01-1a	40µm across teardrop shape inc	44.06	3.24	14.97	10.61	0.16	5.96	12.12	4.14	1.35	0.99	0.209	0.114	0.010	97.94
LZ-8-01-2a	elongate teardrop shape inc	44.72	3.23	14.21	11.13	0.16	5.46	12.20	4.26	1.37	0.99	0.256	0.156	0.041	98.18
LZ-8-01-26	50µm across rectangle inc	44.96	3.08	14.22	10.98	0.18	6.06	12.42	4.07	1.30	1.00	0.164	0.177	0.054	98.67
LZ-8-01-19	80µm long thin elongate inc in same xtl as inc -6a	45.08	3.08	14.74	10.70	0.17	5.58	12.50	4.30	1.19	1.07	0.142	0.170	0.112	98.82
LZ-3-02-4a	20um across small square inc	45.04	3.50	14.75	11.01	0.16	5.81	12.64	4.10	1.25	0.98	0.265	0.190	0.212	99.89
LZ-3-02-10	20um across clean round inc	44.82	3.36	14.47	10.56	0.17	5.61	12.40	4.06	1.30	0.86	0.169	0.149	0.033	97.97
LZ-3-02-10a	**25um across oval inc**	**44.95**	**3.426**	**14.45**	**10.34**	**0.15**	**6.06**	**12.16**	**4.17**	**1.46**	**1.00**	**0.193**	**0.180**	**0.141**	**98.68**
LZ-3-02-13a	20um long rectangle inc	44.42	3.37	14.70	11.06	0.17	5.58	12.54	3.97	1.43	0.89	0.065	0.079	0.000	98.27
LZ-3-02-16b	**40um long thin clean inc**	**44.75**	**3.52**	**15.02**	**11.06**	**0.18**	**6.02**	**12.43**	**4.03**	**1.41**	**0.95**	**0.079**	**0.093**	**0.032**	**99.56**
LZ-3-02-17a	**20um across tiny round inc**	**44.99**	**3.47**	**15.09**	**11.04**	**0.14**	**5.99**	**12.29**	**4.10**	**1.46**	**0.96**	**0.228**	**0.198**	**0.134**	**100.09**
LZ-3-02-26a	45um long square inc	45.80	3.18	14.62	10.61	0.14	5.18	12.19	3.92	1.38	0.85	0.086	0.088	0.013	98.00
LZ-5-02-a	40µm round clean inc	45.01	3.66	15.12	11.14	0.19	5.01	11.46	4.08	1.86	1.14	0.056	0.091	0.046	98.86

Shaded analyses indicate glass inclusions used in temperature calculations.

(c) Phase I episode 1 host crystal data

Sample	Sample Type	SiO_2	TiO_2	Al_2O_3	FeO	MnO	MgO	CaO	Na_2O	K_2O	P_2O_5	NiO	Cr_2O_3	Total	Fo	Fa
LZ-8-01-6c	host xtl of inc LZ-8-01-6a, 19	38.91	0.00	0.02	13.32	0.18	45.86	0.23	0.01	0.00	0.00	0.37	0.05	98.95	86.0	14.0
LZ-8-01-24c	host xtl of inc LZ-8-01-24	38.77	0.02	0.03	14.58	0.19	44.50	0.24	0.01	0.00	0.01	0.32	0.03	98.70	84.5	15.5
LZ-8-01-2c	host xtl of inc LZ-8-01-1a, 2a	38.20	0.05	0.03	17.90	0.26	42.52	0.30	0.01	0.00	0.05	0.19	0.06	99.55	80.9	19.1
LZ-8-01-26C	host xtl of inc LZ-8-01-26	39.23	0.00	0.04	15.14	0.18	45.33	0.20	0.00	0.00	0.02	0.36	0.04	100.54	84.2	15.8
LZ-3-02-4c	host xtl of inc LZ-3-02-4a	38.86	0.01	0.04	15.25	0.21	45.04	0.22	0.00	0.00	0.00	0.29	0.04	99.98	84.0	16.0
LZ-3-02-10c	host xtl of inc LZ-3-02-10, 10a	39.71	0.03	0.04	14.99	0.21	44.83	0.25	0.01	0.00	0.04	0.26	0.07	100.44	84.2	15.8
LZ-3-02-13c	host xtl of inc LZ-3-02-13a	39.36	0.07	0.02	15.20	0.24	44.36	0.34	0.01	0.01	0.05	0.24	0.06	99.95	83.9	16.1
LZ-3-02-16c	host xtl of inc LZ-3-02-16a, 17a	40.18	0.00	0.02	13.20	0.15	46.92	0.12	0.00	0.00	0.00	0.40	0.01	100.99	86.4	13.6
LZ-3-02-26c	host xtl of inc LZ-3-02-26a	38.91	0.00	0.02	13.32	0.18	45.86	0.23	0.01	0.00	0.00	0.37	0.05	98.95	86.0	14.0
LZ-5-02-c	oliv host xtl of inc LZ-5-02-a	38.77	0.02	0.03	14.58	0.19	44.50	0.24	0.01	0.00	0.01	0.32	0.03	98.70	84.5	15.5

(d) Phase I episode 1 other crystal data

Sample	Sample Type	SiO_2	TiO_2	Al_2O_3	FeO	MnO	MgO	CaO	Na_2O	K_2O	P_2O_5	NiO	Cr_2O_3	Total
LZ-8-01-22	Cr-spinel inc in oliv xtl	0.00	0.05	23.95	23.03	0.32	12.38	0.00	0.00	0.01	0.00	0.16	38.67	98.57
LZ-8-01-23	olivine xtl of Cr-spinel inc LZ-8-01-22	40.08	0.00	0.02	10.70	0.15	48.65	0.14	0.03	0.00	0.00	0.41	0.02	100.18
LZ-3-02-21C	oliv xtl core	39.45	0.00	0.00	12.20	0.19	47.29	0.02	0.00	0.00	0.00	0.31	0.00	99.47
LZ-3-02-21R	oliv xtl rim	39.33	0.01	0.00	12.24	0.19	46.53	0.00	0.01	0.00	0.00	0.32	0.01	98.64
LZ-3-02-22	Cr-spinel xtl on edge of oliv xtl LZ-3-02-21C	0.00	0.51	30.62	34.47	0.38	7.59	0.01	0.00	0.00	0.03	0.21	24.94	98.76
LZ-3-02-23	Cr-spinel xtl on edge of oliv xtl LZ-3-02-24	0.00	1.02	23.85	23.80	0.35	11.49	0.01	0.02	0.00	0.02	0.17	37.88	98.60
LZ-3-02-24R	oliv xtl rim	40.08	0.00	0.00	11.09	0.17	47.46	0.12	0.00	0.00	0.01	0.35	0.03	99.30
LZ-3-02-24C	oliv xtl core	40.27	0.00	0.00	11.47	0.18	47.55	0.18	0.00	0.00	0.01	0.37	0.00	100.02
LZ-3-02-25C	oliv xtl core	40.42	0.00	0.01	8.98	0.14	49.45	0.03	0.00	0.00	0.01	0.42	0.01	99.47
LZ-3-02-25R	oliv xtl rim	40.53	0.01	0.00	9.14	0.14	49.02	0.02	0.00	0.00	0.00	0.41	0.01	99.28
LZ-3-02-27	Cr-spinel inc in oliv xtl LZ-3-02-28	0.07	2.13	9.50	28.74	0.36	9.79	0.11	0.01	0.02	0.00	0.12	47.09	97.95
LZ-3-02-28	oliv xtl core	39.51	0.00	0.00	13.14	0.19	46.06	0.26	0.01	0.00	0.00	0.24	0.09	99.50

Shaded analyses indicate olivine/cr-spinel pairs used in oxygen fugacity calculations.

(e) Phase I episode 1 Predicted S concentration			
Sample	**Method 1 (K_2O/TiO_2)**	**Method 2 (P_2O_5/TiO_2)**	**Method 3 (constant S/TiO_2)**
	wt% S_{inc} (predicted)	**wt% S_{inc} (predicted)**	**wt% S_{inc} (predicted)**
LZ-8-01-9	0.230	0.216	0.211
LZ-8-01-16	0.240	0.229	0.210
LZ-5-02-1	0.311	0.350	0.250
LZ-5-02-6	0.316	0.362	0.248
LZ-5-02-11	0.319	0.371	0.253
LZ-5-02-16	0.314	0.362	0.259
LZ-5-02-21	0.316	0.365	0.254
LZ-5-02-26	0.315	0.365	0.252
LZ-5-02-31	0.271	0.291	0.260
LZ-8-01-1	0.226	0.204	0.202
LZ-5-02-b	0.305	0.344	0.253
LZ-5-02-c	0.308	0.338	0.249
LZ-5-02-d	0.335	0.373	0.256
LZ-5-02-e	0.316	0.366	0.249
LZ-8-01-3	0.320	0.359	0.252
LZ-3-02-1	0.281	0.305	0.251
LZ-3-02-2	0.294	0.321	0.246
LZ-3-02-3	0.282	0.305	0.246
LZ-3-02-6	0.258	0.264	0.228
LZ-3-02-7	0.274	0.288	0.251
LZ-3-02-12	0.267	0.268	0.249
LZ-3-02-14	0.263	0.278	0.235
LZ-3-02-20	0.266	0.286	0.238
LZ-3-02-06	0.258	0.273	0.224
Average	**0.287**	**0.312**	**0.243**
Standard Deviation (2σ)	**0.031**	**0.051**	**0.016**

Appendix C4 Phase I Episode 2 (Santa Catalina/Pico Partido)

(a) Phase I episode 2 matrix glass data

Sample	Type	SiO_2	TiO_2	Al_2O_3	FeO	MnO	MgO	CaO	Na_2O	K_2O	P_2O_5	S	Cl	F	Total
LZ-10-01-2	matrix glass in scoria	48.38	2.78	14.42	10.29	0.15	6.21	10.69	3.64	0.90	0.55	0.020	0.043	0.041	98.12
LZ-10-01-17	matrix glass in scoria	48.39	2.80	14.23	10.47	0.13	6.16	10.70	3.65	0.90	0.51	0.018	0.031	0.077	98.07
LZ-11-04-1	matrix glass	48.96	3.41	14.09	11.93	0.18	5.28	10.12	2.63	1.10	0.81	0.012	0.059	0.184	98.78
LZ-11-04-5	matrix glass	47.31	3.29	16.02	11.50	0.18	5.05	10.90	2.49	1.05	0.80	0.013	0.037	0.010	98.66
LZ-11-04-8	matrix glass	48.73	3.45	13.94	12.06	0.17	5.13	10.94	2.43	1.01	0.79	0.015	0.064	0.108	98.83
LZ-11-04-10	mtx gls in scoria frag w/ xtl LZ-11-04-9c	49.69	3.38	14.46	11.92	0.18	5.33	10.41	2.13	0.99	0.81	0.017	0.049	0.067	99.42
LZ-11-04-18	matrix glass	49.32	3.37	14.22	11.72	0.16	5.33	10.20	1.96	1.03	0.84	0.013	0.045	0.163	98.36
LZ-11-04-21	matrix glass	49.06	3.38	14.25	11.31	0.16	5.23	10.22	2.09	1.06	0.87	0.012	0.056	0.068	97.77
LZ-3-04-e	matrix glass	48.76	3.42	13.91	10.63	0.16	5.49	10.98	2.92	0.86	0.80	0.011	0.048	0.019	98.00
LZ-3-04-d	matrix glass	47.97	3.35	14.11	11.30	0.15	5.99	10.61	2.83	1.04	0.74	0.010	0.049	0.026	98.18
LZ-11-04-1	mtx gls	48.96	3.41	14.09	11.93	0.18	5.28	10.12	2.63	1.10	0.81	0.012	0.059	0.184	98.79
LZ-11-04-5	mtx gls	47.31	3.29	16.02	11.50	0.18	5.05	9.90	2.49	1.05	0.80	0.013	0.037	0.010	97.67
LZ-11-04-8	mtx gls	48.73	3.45	13.94	12.06	0.17	5.13	9.94	2.43	1.01	0.79	0.015	0.064	0.108	97.85
LZ-11-04-10	mtx gls in scoria frag w/ xtl LZ-11-04-9c	49.69	3.38	14.46	11.92	0.18	5.33	10.41	2.13	0.99	0.81	0.010	0.049	0.067	99.42
LZ-11-04-18	mtx gls	49.32	3.37	14.22	11.72	0.16	5.33	10.20	1.96	1.03	0.84	0.013	0.045	0.163	98.36
LZ-11-04-21	mtx gls	49.06	3.38	14.25	11.31	0.16	5.23	10.22	2.09	1.06	0.87	0.012	0.056	0.068	97.77
LZ-5-01-2	matrix glass in lava	48.61	2.80	14.11	9.90	0.14	6.63	11.14	3.29	0.98	0.54	0.008	0.045	0.023	98.22
LZ-5-01-3	matrix glass in lava	48.32	3.30	14.27	9.91	0.16	6.47	10.80	3.77	0.58	0.88	0.011	0.052	0.033	98.54
LZ-5-01-5	matrix glass in lava	48.83	3.12	14.56	9.82	0.15	6.09	9.97	3.51	1.04	0.79	0.009	0.055	0.150	98.09
LZ-5-01-6	matrix glass in lava	48.25	3.14	14.69	10.85	0.16	6.17	9.66	3.73	1.12	0.80	0.009	0.056	0.008	98.63
LZ-5-01-7	matrix glass in lava	48.30	3.04	14.80	9.99	0.14	6.21	10.28	3.84	0.94	0.76	0.009	0.032	0.000	98.34
LZ-5-01-1-x	matrix glass in lava	48.82	2.92	14.18	10.08	0.16	6.22	10.56	3.53	0.92	0.61	0.008	0.035	0.019	98.06
LZ-5-01-2-x	matrix glass in lava	49.17	2.98	14.25	10.13	0.17	6.16	10.54	3.47	0.96	0.71	0.010	0.021	0.000	98.57
LZ-5-01-6-x	matrix glass in lava	49.27	3.02	14.28	10.38	0.16	6.28	10.79	3.57	0.86	0.69	0.010	0.035	0.019	99.36
LZ-5-01-8-x	matrix glass in lava	49.17	3.05	14.17	9.99	0.15	6.00	10.52	3.65	0.88	0.59	0.012	0.059	0.021	98.26

Phase I episode 2 distal lava matrix glass data

Sample	Type	SiO_2	TiO_2	Al_2O_3	FeO	MnO	MgO	CaO	Na_2O	K_2O	P_2O_5	S	Cl	F	Total
LZ-1-01-2	matrix glass in lava	49.29	2.96	13.99	10.41	0.19	5.96	11.02	3.60	0.90	0.51	0.009	0.025	0.059	98.92
LZ-1-01-3	matrix glass in lava	48.96	2.76	14.16	10.35	0.14	5.99	10.70	3.58	0.88	0.50	0.008	0.018	0.071	98.12
LZ-1-01-4	matrix glass in lava	49.23	2.76	13.64	10.25	0.19	6.35	11.06	3.69	0.92	0.54	0.009	0.028	0.070	98.74
LZ-1-01-5	matrix glass in lava	48.58	2.88	14.13	10.38	0.22	6.30	10.63	3.61	0.86	0.47	0.007	0.015	0.049	98.13
LZ-1-01-7	matrix glass in lava	48.63	2.92	13.93	10.42	0.17	6.05	10.81	3.64	0.86	0.49	0.008	0.044	0.059	98.03

(b) Phase I episode 2 glass inclusion data

Sample	Type	SiO_2	TiO_2	Al_2O_3	FeO	MnO	MgO	CaO	Na_2O	K_2O	P_2O_5	S	Cl	F	Total
LZ-10-01-6b	120 μm across, clean L shape inc	48.01	2.81	14.47	10.59	0.15	6.18	10.97	3.69	0.92	0.51	0.210	0.194	0.221	98.64
LZ-10-01-6d	80 μm across clean oval shape inc	47.98	2.74	14.67	10.59	0.16	6.22	10.87	3.64	0.88	0.51	0.084	0.161	0.000	98.41
LZ-10-01-7b	100μm long, clean boot shape inc	47.96	2.80	14.34	10.67	0.15	6.06	10.93	3.61	0.89	0.47	0.075	0.073	0.001	98.00
LZ-10-01-8a	35 μm across round inc	48.10	2.84	14.69	10.61	0.15	5.76	11.04	3.61	0.88	0.47	0.065	0.070	0.000	98.24
LZ-10-01-9a	40 μm across oval inc	47.98	2.83	14.35	10.67	0.15	6.08	10.88	3.72	0.89	0.50	0.074	0.660	0.000	98.16
LZ-10-01-14a	20 μm across L shape inc w/ bulbous end	48.09	2.71	14.02	10.61	0.15	5.94	10.84	3.62	0.85	0.48	0.097	0.065	0.089	97.55
LZ-11-04-4	40μm across rounded triangle shape inc	48.72	2.82	14.38	10.91	0.18	5.91	10.53	1.79	0.97	0.59	0.076	0.071	0.161	97.11
LZ-11-04-9a	100μm long clean square inc w/ bulbous end	48.48	3.03	15.32	11.40	0.17	4.99	10.87	1.89	1.02	0.74	0.145	0.066	0.052	98.17
LZ-11-04-1a	40μm across triangle shape inc	47.49	2.93	15.95	11.42	0.16	5.07	10.87	1.99	0.96	0.71	0.196	0.184	0.176	98.11
LZ-3-04-2	50μm across oval inc	48.36	3.22	14.75	10.99	0.14	5.92	11.06	3.18	0.82	0.85	0.112	0.131	0.098	99.63
LZ-3-04-3	30μm long rectangle inc	47.99	3.00	14.00	10.88	0.18	6.00	10.91	3.44	0.90	0.79	0.106	0.127	0.099	98.42
LZ-3-04-4	40μm across round, clean inc	49.11	2.88	14.17	10.49	0.20	6.21	11.02	3.40	0.94	0.60	0.099	0.100	0.112	99.33

Phase I episode 2 host crystal data

Sample	Sample Type	SiO_2	TiO_2	Al_2O_3	FeO	MnO	MgO	CaO	Na_2O	K_2O	P_2O_5	NiO	Cr_2O_3	Total	Fo	Fa
LZ-10-01-6c-core	host xtl of inc LZ-10-01-6,7,8,9,14	38.91	0.00	0.02	13.32	0.18	45.86	0.23	0.01	0.00	0.00	0.37	0.05	98.95	86.0	14.0
LZ-10-01-6c-rim	host xtl of inc LZ-10-01-6,7,8,9,14	38.77	0.02	0.03	14.58	0.19	44.50	0.24	0.01	0.00	0.01	0.32	0.03	98.70	84.5	15.5
LZ-11-04-xtl-4	host xtl of inc LZ-11-04-4	38.20	0.05	0.03	17.90	0.26	42.52	0.30	0.01	0.00	0.05	0.19	0.06	99.55	80.9	19.1
LZ-11-04-xtl-9c	host xtl of inc LZ-11-04-9a	39.23	0.00	0.04	15.14	0.18	45.33	0.20	0.00	0.00	0.02	0.36	0.04	100.54	84.2	15.8
LZ-11-04-1c	host xtl of inc LZ-11-04-1a	38.86	0.01	0.04	15.25	0.21	45.04	0.22	0.00	0.00	0.00	0.29	0.04	99.98	84.0	16.0
LZ-3-04-2c	host xtl of inc LZ-3-02-2a	39.71	0.03	0.04	14.99	0.21	44.83	0.25	0.01	0.00	0.04	0.26	0.07	100.44	84.2	15.8
LZ-3-04-3c	host xtl of inc LZ-3-02-3a	39.36	0.07	0.02	15.20	0.24	44.36	0.34	0.01	0.01	0.05	0.24	0.06	99.95	83.9	16.1
LZ-3-04-4c	host xtl of inc LZ-3-02-4a	40.18	0.00	0.02	13.20	0.15	46.92	0.12	0.00	0.00	0.00	0.40	0.01	100.99	86.4	13.6

Phase I episode 2 other crystal data														
Sample	**Sample Type**	**SiO_2**	**TiO_2**	**Al_2O_3**	**FeO**	**MnO**	**MgO**	**CaO**	**Na_2O**	**K_2O**	**P_2O_5**	**NiO**	**Cr_2O_3**	**Total**
LZ-1-01-oxide	Fe-Ti oxide xtl	1.31	20.81	3.11	64.98	0.46	3.58	0.25	0.07	0.18	0.05	0.06	0.05	94.91
LZ-1-01-2c rim	oliv xtl (xeno?) rim	41.38	0.01	0.00	8.40	0.13	50.22	0.01	0.00	0.00	0.00	0.42	0.02	100.60
LZ-1-01-2c core	oliv xtl (xeno?) core	41.65	0.00	0.01	8.24	0.13	50.26	0.01	0.00	0.00	0.00	0.41	0.00	100.71
LZ-1-01-1c rim	oliv xtl (xeno?) rim	41.32	0.01	0.00	9.43	0.13	49.48	0.02	0.00	0.01	0.00	0.40	0.00	100.81
LZ-1-01-1c core	oliv xtl (xeno?) core	41.73	0.01	0.02	8.24	0.11	50.31	0.01	0.00	0.00	0.00	0.42	0.01	100.86
LZ-5-01-q-ol	oliv xtl	40.92	0.02	0.08	14.08	0.18	45.87	0.21	0.00	0.01	0.04	0.37	0.05	101.82
LZ-5-01-4c	**cr-spinel inclusion in xtl LZ-5-01-9c**	**0.03**	**0.01**	**22.65**	**19.83**	**0.26**	**13.99**	**0.00**	**0.03**	**0.00**	**0.00**	**0.17**	**43.54**	**100.50**
LZ-5-01-9c	**olivine xtl**	**37.33**	**0.04**	**0.05**	**19.13**	**0.32**	**41.64**	**0.18**	**0.01**	**0.00**	**0.14**	**0.11**	**0.03**	**98.98**
LZ-5-01-10c-crsp	**cr-spinel inclusion**	**0.02**	**0.78**	**24.49**	**22.26**	**0.37**	**11.98**	**0.00**	**0.01**	**0.00**	**0.00**	**0.15**	**40.68**	**100.75**
LZ-5-01-10c	**olivine xtl**	**39.53**	**0.00**	**0.03**	**11.21**	**0.19**	**48.05**	**0.21**	**0.00**	**0.00**	**0.00**	**0.37**	**0.02**	**99.61**
LZ-5-01-11c	**olivine xtl**	**40.45**	**0.00**	**0.00**	**14.06**	**0.16**	**45.76**	**0.24**	**0.00**	**0.01**	**0.01**	**0.37**	**0.02**	**101.07**
LZ-5-01-11c-crsp	**cr-spinel inclusion**	**0.01**	**0.82**	**23.79**	**25.01**	**0.45**	**9.99**	**0.00**	**0.01**	**0.00**	**0.00**	**0.15**	**39.83**	**100.07**
LZ-5-01-13c	olivine xtl	39.87	0.00	0.00	8.91	0.13	49.94	0.05	0.00	0.00	0.00	0.39	0.00	99.28
LZ-5-01-8c-rim	pyx xtl rim	46.81	2.47	4.79	6.54	0.09	13.90	22.86	0.47	0.00	0.01	0.01	0.04	97.98
LZ-5-01-8c-core	pyx xtl core	45.60	3.62	6.71	6.83	0.12	12.96	22.81	0.55	0.00	0.04	0.01	0.02	99.27

Shaded analyses indicate olivine/cr-spinel pairs used in oxygen fugacity calculations.

(e) Phase I episode 2 Predicted S concentration			
Sample	**Method 1 (K_2O/TiO_2)**	**Method 2 (P_2O_5/TiO_2)**	**Method 3 (constant S/TiO_2)**
	wt% S_{inc} (predicted)	**wt% S_{inc} (predicted)**	**wt% S_{inc} (predicted)**
LZ-10-01-2	0.194	0.200	0.195
LZ-10-01-17	0.195	0.203	0.196
LZ-11-04-1	0.238	0.235	0.239
LZ-11-04-5	0.229	0.223	0.230
LZ-11-04-8	0.231	0.218	0.241
LZ-11-04-10	0.227	0.211	0.236
LZ-11-04-18	0.230	0.216	0.236
LZ-11-04-21	0.233	0.220	0.236
LZ-3-04-e	0.217	0.184	0.239
LZ-3-04-d	0.230	0.226	0.235
LZ-11-04-1	0.238	0.235	0.239
LZ-11-04-5	0.229	0.223	0.230
LZ-11-04-8	0.231	0.218	0.241
LZ-11-04-10	0.227	0.211	0.236
LZ-11-04-18	0.230	0.216	0.236
LZ-11-04-21	0.233	0.220	0.236
LZ-5-01-2	0.202	0.220	0.196
LZ-5-01-3	0.186	0.119	0.231
LZ-5-01-5	0.221	0.218	0.219
LZ-5-01-6	0.229	0.234	0.220
LZ-5-01-7	0.208	0.197	0.213
LZ-5-01-1-x	0.202	0.203	0.204
LZ-5-01-2-x	0.208	0.205	0.209
LZ-5-01-6-x	0.200	0.185	0.211
Average	**0.219**	**0.209**	**0.225**
Standard Deviation (2σ)	**0.016**	**0.021**	**0.017**

Appendix C4 Phase II (Montanas del Senalo)

(a) Phase II matrix glass data

Sample	Type	SiO_2	TiO_2	Al_2O_3	FeO	MnO	MgO	CaO	Na_2O	K_2O	P_2O_5	S	Cl	F	Total
LZ-11-01-4	matrix glass in lava	50.28	3.02	12.34	10.63	0.17	6.46	10.86	3.53	0.80	0.42	0.009	0.049	0.071	98.64
LZ-11-02-9	mtx gls in small 'Pele's tear' frag	51.72	2.80	13.93	10.28	0.16	5.97	9.91	3.44	0.71	0.38	0.010	0.016	0.000	99.30
LZ-11-02-10	mtx gls in small 'Pele's tear' frag	51.72	2.77	14.05	10.21	0.15	5.90	9.93	3.34	0.74	0.36	0.010	0.017	0.000	99.19
LZ-11-02-11	mtx gls in small 'Pele's tear' frag	50.69	2.77	13.85	10.28	0.15	5.94	9.90	3.31	0.75	0.39	0.009	0.024	0.031	98.08
LZ-11-02-12	mtx gls in small 'Pele's tear' frag	51.25	2.73	14.05	10.21	0.15	5.98	10.00	3.36	0.87	0.36	0.014	0.022	0.000	98.99
LZ-11-02-13	mtx gls in small 'Pele's tear' frag	51.28	2.81	13.91	10.29	0.16	5.93	9.94	3.38	0.73	0.37	0.013	0.013	0.000	98.82
LZ-11-02-1-1	mtx gls in scoria frag, frag quite xtallized	48.41	3.31	13.62	11.93	0.18	5.55	9.89	3.88	1.04	0.73	0.015	0.047	0.062	98.65
LZ-11-02-1-6	mtx gls in scoria frag, frag quite xtallized	48.79	3.30	13.48	11.90	0.18	5.42	10.17	3.80	1.06	0.72	0.016	0.032	0.031	98.89
LZ-11-02-1-11	mtx gls in scoria frag, gls xtl-free	47.90	3.35	13.37	12.21	0.17	5.40	9.83	3.88	1.09	0.75	0.011	0.042	0.032	98.03
LZ-11-02-2-1	mtx gls in scoria frag, mostly fsp xtls in gdmass	48.00	3.26	12.91	11.60	0.17	5.90	10.74	3.44	1.00	0.70	0.013	0.040	0.038	97.81
LZ-11-02-2-6	mtx gls in scoria frag, 'clean' gls	48.01	3.49	12.91	12.42	0.18	5.34	9.95	3.68	1.10	0.75	0.013	0.033	0.035	97.91
LZ-11-02-2-15	mtx gls in scoria	47.98	3.36	13.45	12.17	0.18	5.30	9.76	3.73	1.08	0.76	0.014	0.037	0.043	97.86

(b) Phase II glass inclusion data

Sample	Type	SiO_2	TiO_2	Al_2O_3	FeO	MnO	MgO	CaO	Na_2O	K_2O	P_2O_5	S	Cl	F	Total
LZ-11-01-2a	20 µm across, clean round inc	49.42	3.21	12.56	10.62	0.14	5.98	11.12	3.44	0.86	0.45	0.087	0.098	0.101	98.09
LZ-11-02-1a	**10µm across tiny round inc**	**47.72**	**3.64**	**13.85**	**11.23**	**0.15**	**6.14**	**10.73**	**3.70**	**0.95**	**0.57**	**0.103**	**0.092**	**0.037**	**98.91**
LZ-11-02-18a	15µm across tiny round inc	48.47	2.53	14.03	11.10	0.17	6.86	10.46	3.64	0.83	0.57	0.084	0.790	0.093	99.62
LZ-11-02-11a	20µm across small, clean teardrop shape inc	48.06	3.24	13.97	11.10	0.16	6.26	11.01	3.41	1.05	0.69	0.209	0.132	0.010	99.30
LZ-11-02-14a	20µm across small square inc	48.03	3.22	14.04	11.02	0.15	5.92	11.02	3.40	0.88	0.69	0.210	0.177	0.021	98.78
LZ-11-02-2a	**elongate teardrop shape inc w/ thin end**	**48.12**	**3.23**	**13.31**	**11.13**	**0.16**	**6.17**	**11.20**	**3.62**	**0.93**	**0.62**	**0.083**	**0.088**	**0.041**	**98.70**

Shaded analyses indicate glass inclusions used in temperature calculations.

(c) Phase II host crystal data

Sample	Sample Type	SiO_2	TiO_2	Al_2O_3	FeO	MnO	MgO	CaO	Na_2O	K_2O	P_2O_5	NiO	Cr_2O_3	Total	Fo	Fa
LZ-11-01-2c-core	host xtl of inc LZ-11-01-2a	39.41	0.00	0.00	10.14	0.14	48.53	0.13	0.01	0.00	0.00	0.260	0.000	98.507	89.5	10.5
LZ-11-01-2c-rim	host xtl of inc LZ-11-01-2a	38.26	0.01	0.04	16.13	0.20	43.38	0.19	0.01	0.01	0.01	0.278	0.041	98.558	82.7	17.3
LZ-11-02-18c	host xtl of inc LZ-11-02-18a	39.85	0.00	0.05	14.62	0.17	45.76	0.19	0.01	0.00	0.03	0.407	0.038	101.12	84.8	15.2
LZ-11-02-1c	host xtl of inc LZ-11-02-1a, 11a	38.36	0.04	0.05	15.46	0.20	44.53	0.26	0.02	0.00	0.07	0.269	0.028	99.30	83.7	16.3
LZ-11-02-14c	hose xtl of inc LZ-11-02-14a	39.62	0.00	0.03	14.94	0.21	45.45	0.22	0.00	0.00	0.02	0.29	0.011	100.78	84.4	15.6
LZ-11-02-2c	host xtl of inc LZ-11-02-2a	39.55	0.02	0.05	14.17	0.20	45.84	0.24	0.00	0.00	0.02	0.29	0.083	100.47	85.2	14.8

(d) Phase II other crystal data

Sample	Sample Type	SiO_2	TiO_2	Al_2O_3	FeO	MnO	MgO	CaO	Na_2O	K_2O	P_2O_5	NiO	Cr_2O_3	Total
LZ-11-02-2-crsp	Cr-spinel inc in oliv xtl LZ-11-02-1cc	0.02	0.59	25.81	17.19	0.25	14.82	0.00	0.02	0.00	0.02	0.132	40.923	99.759
LZ-11-02-1cc	oliv xtl core	40.75	0.02	0.00	8.23	0.14	50.31	0.05	0.01	0.00	0.00	0.39	0.044	99.95
LZ-11-02-1d	Cr-spinel inc in oliv xtl LZ-11-02-1c	3.14	0.07	5.65	24.18	0.36	10.94	0.50	0.24	0.11	0.01	0.15	54.001	99.36
LZ-11-02-1c	oliv xtl core	38.36	0.04	0.05	15.46	0.20	44.53	0.26	0.02	0.00	0.07	0.269	0.028	99.30
LZ-11-02-05	Fe-Ti oxide xtl in mtx gls	0.33	13.47	1.76	1.28	73.78	3.41	0.45	0.08	0.03	0.03	0.017	0.041	94.662

Shaded analyses indicate olivine/cr-spinel pairs used in oxygen fugacity calculations.

(e) Phase II Predicted S concentration			
Sample	**Method 1 (K_2O/TiO_2)**	**Method 2 (P_2O_5/TiO_2)**	**Method 3 (constant S/TiO_2)**
	wt% S_{inc} (predicted)	**wt% S_{inc} (predicted)**	**wt% S_{inc} (predicted)**
LZ-11-01-4	0.195	0.191	0.211
LZ-11-02-9	0.178	0.171	0.196
LZ-11-02-10	0.179	0.178	0.194
LZ-11-02-11	0.180	0.178	0.194
LZ-11-02-12	0.189	0.209	0.191
LZ-11-02-13	0.180	0.176	0.196
LZ-11-02-1-1	0.228	0.226	0.232
LZ-11-02-1-6	0.230	0.231	0.231
LZ-11-02-1-11	0.234	0.237	0.234
LZ-11-02-2-1	0.223	0.219	0.228
LZ-11-02-2-6	0.242	0.242	0.245
LZ-11-02-2-15	0.234	0.234	0.235
Average	**0.208**	**0.208**	**0.216**
Standard Deviation (2σ)	**0.025**	**0.026**	**0.020**

Appendix C4 Phase III Episode 1 (Volcan do el Quemado)

(a) Phase III episode 1 matrix glass data

Sample	Type	SiO_2	TiO_2	Al_2O_3	FeO	MnO	MgO	CaO	Na_2O	K_2O	P_2O_5	S	Cl	F	Total
LZ-15-01-1	matrix glass	49.12	2.81	14.90	10.35	0.16	5.94	10.73	3.74	0.92	0.56	0.080	0.032	0.000	99.27
LZ-15-01-2	matrix glass	48.07	2.82	14.35	10.56	0.16	6.41	10.54	3.79	0.92	0.58	0.078	0.043	0.088	98.34
LZ-15-01-3	matrix glass	48.35	2.77	14.44	10.39	0.14	6.36	10.65	3.61	0.90	0.59	0.011	0.027	0.000	98.25
LZ-15-01-2	matrix glass in scoria	48.34	2.71	14.40	10.39	0.16	6.45	10.55	3.58	0.87	0.52	0.014	0.041	0.020	98.04
LZ-15-01-4	matrix glass attached to xtl	48.43	2.80	14.44	10.26	0.16	6.05	10.88	3.55	0.93	0.54	0.018	0.034	0.000	98.09
LZ-15-01-5	matrix glass attached to xtl	48.16	2.90	14.30	10.54	0.16	5.98	10.62	3.59	0.99	0.58	0.013	0.031	0.080	97.94
LZ-15-01-7	matrix glass in Pele's tear	47.94	2.80	14.31	10.39	0.15	6.27	10.64	3.68	0.92	0.56	0.012	0.046	0.116	97.83
LZ-15-01-8	matrix glass in Pele's tear	47.88	2.86	14.36	10.38	0.18	6.54	10.68	3.69	0.87	0.52	0.013	0.032	0.020	98.02
LZ-15-01-3	matrix glass in Pele's tear	48.17	2.81	14.54	10.42	0.15	6.48	10.64	3.60	0.87	0.54	0.015	0.041	0.091	98.35
LZ-15-01-5	matrix glass in scoria	47.83	2.76	14.36	10.44	0.15	6.42	10.61	3.76	0.91	0.54	0.012	0.033	0.138	97.95
LZ-15-01-6	matrix glass in scoria	47.65	2.80	14.45	10.44	0.16	6.48	10.79	3.74	0.92	0.51	0.012	0.042	0.087	98.07
LZ-15-01-12	matrix glass in scoria	47.35	2.70	14.58	10.34	0.15	6.14	10.75	3.69	0.93	0.55	0.014	0.036	0.121	97.35
LZ-15-01-13	matrix glass in scoria	47.83	2.75	14.65	10.25	0.15	6.36	10.70	3.76	0.93	0.50	0.013	0.044	0.087	98.02
LZ-15-01-14	matrix glass in scoria	48.04	2.77	14.60	10.54	0.15	6.32	10.60	3.70	0.87	0.51	0.011	0.032	0.095	98.23
LZ-15-01-20	matrix glass in Pele's tear	48.46	2.77	14.49	10.32	0.15	6.43	10.51	3.71	0.88	0.49	0.011	0.039	0.093	98.36
LZ-15-01-4	matrix glass in 'bubbly' scoria fragment	49.31	2.80	14.54	10.55	0.16	6.43	10.61	3.72	0.88	0.53	0.011	0.041	0.062	99.63
LZ-15-01-6	matrix glass in angular xtl-free shard	49.28	2.74	14.57	10.51	0.15	6.54	10.58	3.70	0.86	0.54	0.009	0.033	0.000	99.51
LZ-15-01-10	matrix glass in scoria fragment	49.13	2.78	14.55	10.52	0.15	6.48	10.56	3.69	0.92	0.53	0.012	0.050	0.000	99.39
LZ-15-01-15	matrix glass in glass shard	48.90	2.86	14.54	10.70	0.16	6.43	10.61	3.75	0.90	0.48	0.010	0.043	0.000	99.39
LZ-15-01-18	matrix glass in glass shard	48.86	2.78	14.28	10.50	0.16	6.46	10.62	3.69	0.88	0.53	0.011	0.035	0.218	99.01
LZ-15-01-22	matrix glass	48.84	2.81	14.46	10.55	0.14	6.39	10.59	3.71	0.88	0.55	0.010	0.038	0.059	99.01
LZ-14-01-1-2	matrix glass in lava	49.21	2.80	14.39	10.98	0.12	6.53	10.49	3.57	0.81	0.51	0.013	0.038	0.016	99.48
LZ-14-01-1-7	matrix glass in lava	48.60	2.89	13.99	10.84	0.18	6.34	10.62	3.45	0.88	0.52	0.009	0.025	0.104	98.45
LZ-14-01-5	matrix glass in lava	50.22	2.81	14.11	10.94	0.11	6.36	10.65	3.32	0.92	0.48	0.017	0.011	0.012	99.96
LZ-14-01-13	matrix glass in lava	50.64	2.80	14.12	10.81	0.15	6.23	10.32	3.37	0.80	0.53	0.031	0.022	0.024	99.85

(b) Phase III episode 1 glass inclusion data

Sample	Type	SiO_2	TiO_2	Al_2O_3	FeO	MnO	MgO	CaO	Na_2O	K_2O	P_2O_5	S	Cl	F	Total
LZ-15-01-25a	50μm across elongate inc	48.05	2.49	14.95	10.79	0.13	6.67	11.35	3.60	0.76	0.48	0.135	0.107	0.272	99.78
LZ-15-01-29a	saucer shape inc ~30 μm across	49.26	2.73	16.12	10.39	0.11	5.80	10.67	4.15	1.03	0.57	0.030	0.042	0.038	100.92
LZ-15-01-16a	20 μm across round clean inc	48.69	2.86	14.44	10.78	0.16	6.06	10.77	3.66	0.86	0.49	0.125	0.092	0.091	99.08
LZ-15-01-20a	25 μm across round inc, small crack on side	48.56	2.73	14.73	10.76	0.15	5.70	11.24	3.67	0.81	0.51	0.067	0.100	0.074	99.11
LZ-15-01-21a	40μm across elongate diamond-shape inc	48.48	2.76	14.46	10.62	0.16	6.04	10.67	3.73	0.84	0.52	0.019	0.037	0.099	98.42
LZ-14-01-1a	40 μm across triangle inc	48.46	2.94	15.25	10.65	0.11	5.67	11.07	3.47	0.88	0.55	0.069	0.074	0.022	99.22
LZ-14-01-1-5a	**35 μm across round inc 1 bubble near base**	**48.91**	**2.50**	**14.21**	**10.98**	**0.16**	**6.86**	**11.07**	**3.66**	**0.90**	**0.50**	**0.073**	**0.125**	**0.032**	**99.98**
LZ-14-01-2a	35 μm across diamond shape inc	50.51	2.77	14.12	10.75	0.12	6.36	10.44	3.45	0.76	0.59	0.127	0.182	0.449	100.63
LZ-14-01-5a	40 μm long, ½ moon shape inc	49.52	2.69	13.76	11.02	0.18	6.78	10.43	3.53	0.80	0.50	0.123	0.099	0.070	99.50
LZ-14-01-7a	small 20μm across round inc	49.42	2.59	13.95	10.86	0.13	6.19	10.28	3.40	0.74	0.54	0.061	0.071	0.016	98.25

Shaded analyses indicate glass inclusions used in temperature calculations.

(c) Phase III episode 1 host crystal data

Sample	Sample Type	SiO_2	TiO_2	Al_2O_3	FeO	MnO	MgO	CaO	Na_2O	K_2O	P_2O_5	NiO	Cr_2O_3	Total	Fo	Fa
LZ-15-01-25c	host xtl of incs LZ-15-01-25a, 29a	39.88	0.01	0.04	14.10	0.20	45.56	0.19	0.00	0.00	0.01	0.360	0.060	100.41	85.2	14.8
LZ-15-01-16c	host xtl of LZ-15-01-16a	39.94	0.02	0.04	13.98	0.18	45.85	0.22	0.02	0.00	0.02	0.32	0.06	100.64	85.4	14.6
LZ-15-01-20c	host xtl of inc LZ-15-01-20a	39.19	0.02	0.02	14.40	0.17	45.36	0.25	0.00	0.01	0.01	0.33	0.04	99.79	84.9	15.1
LZ-15-01-21c	host xtl of LZ-15-01-21a	40.01	0.17	0.02	16.72	0.23	42.80	0.56	0.02	0.04	0.05	0.23	0.05	100.88	82.0	18.0
LZ-14-01-1c	host xtl of inc LZ-14-01-1a	40.20	0.01	0.05	14.75	0.18	45.02	0.22	0.02	0.00	0.01	0.330	0.060	100.85	84.5	15.5
LZ-14-01-1-5c	host xtl of inc LZ-14-01-5a	39.92	0.01	0.04	14.64	0.18	45.48	0.19	0.01	0.01	0.00	0.35	0.06	100.88	84.7	15.3
LZ-14-01-2c	host xtl of inc LZ-14-01-2a	39.00	0.00	0.01	14.76	0.22	45.06	0.24	0.00	0.00	0.01	0.310	0.060	99.67	84.5	15.5
LZ-14-01-7c	host xtl of inc LZ-14-01-5a; 7a	39.96	0.02	0.03	14.38	0.18	44.98	0.22	0.00	0.01	0.00	0.340	0.020	100.14	84.8	15.2

(d) Phase III episode 1 other crystal data

Sample	Sample Type	SiO_2	TiO_2	Al_2O_3	FeO	MnO	MgO	CaO	Na_2O	K_2O	P_2O_5	NiO	Cr_2O_3	Total
LZ-15-01-9c-crsp	Fe-Ti oxide? Inc	5.94	13.30	7.05	59.16	0.33	7.92	2.38	0.13	0.00	0.01	0.16	1.32	97.70
LZ-15-01-9c-core	olivine xtl	39.44	0.03	0.03	14.01	0.21	46.24	0.24	0.00	0.00	0.06	0.29	0.06	100.61
LZ-14-01-1-crsp	**cr-spinel inclusion**	**0.45**	**2.89**	**17.31**	**33.47**	**0.32**	**10.07**	**0.14**	**0.01**	**0.00**	**0.00**	**0.20**	**34.71**	**99.56**
LZ-14-01-1-oliv	**olivine xtl core**	**40.53**	**0.02**	**0.05**	**15.07**	**0.21**	**45.12**	**0.22**	**0.01**	**0.00**	**0.04**	**0.29**	**0.04**	**101.61**

Shaded analyses indicate olivine/cr-spinel pairs used in oxygen fugacity calculations.

(e) Phase III episode 1 predicted S concentration			
Sample	**Method 1 (K_2O/TiO_2) wt% S_{inc} (predicted)**	**Method 2 (P_2O_5/TiO_2) wt% S_{inc} (predicted)**	**Method 3 (constant S/TiO_2) wt% S_{inc} (predicted)**
LZ-15-01-1	0.198	0.199	0.197
LZ-15-01-2	0.199	0.200	0.197
LZ-15-01-3	0.194	0.193	0.194
LZ-15-01-2	0.189	0.191	0.190
LZ-15-01-4	0.199	0.204	0.196
LZ-15-01-5	0.210	0.215	0.203
LZ-15-01-7	0.198	0.200	0.196
LZ-15-01-8	0.193	0.193	0.200
LZ-15-01-3	0.191	0.190	0.197
LZ-15-01-5	0.195	0.198	0.193
LZ-15-01-6	0.197	0.203	0.196
LZ-15-01-12	0.196	0.201	0.189
LZ-15-01-13	0.198	0.205	0.192
LZ-15-01-14	0.190	0.191	0.194
LZ-15-01-20	0.192	0.196	0.194
LZ-15-01-4	0.192	0.193	0.196
LZ-15-01-6	0.188	0.188	0.192
LZ-15-01-10	0.198	0.203	0.195
LZ-15-01-15	0.197	0.202	0.200
LZ-15-01-18	0.192	0.193	0.194
LZ-15-01-22	0.192	0.191	0.196
LZ-14-01-1-2	0.183	0.179	0.196
LZ-14-01-1-7	0.195	0.195	0.202
LZ-14-01-5	0.198	0.206	0.197
LZ-14-01-13	0.182	0.176	0.196
Average	**0.194**	**0.196**	**0.196**
Standard Deviation (2σ)	**0.006**	**0.008**	**0.003**

Appendix C4 Phase III episode 2 (Montana Rajada)

(a) Phase III episode 2 matrix glass data

Sample	Type	SiO_2	TiO_2	Al_2O_3	FeO	MnO	MgO	CaO	Na_2O	K_2O	P_2O_5	S	Cl	F	Total
LZ-13-01-2	matrix glass in lava	44.38	3.41	14.67	13.29	0.21	7.05	10.60	3.27	0.89	0.40	0.010	0.050	0.100	98.33
LZ-13-01-3	matrix glass in lava	45.06	3.52	14.44	13.31	0.21	6.98	10.16	3.22	0.92	0.42	0.010	0.045	0.099	98.39
LZ-13-01-4	matrix glass in lava	44.86	3.66	14.87	13.24	0.19	6.96	10.42	3.24	0.90	0.44	0.012	0.029	0.088	98.91
LZ-13-01-6	matrix glass in lava	47.55	3.00	13.68	12.86	0.19	6.57	10.92	3.16	0.81	0.84	0.012	0.026	0.082	99.70

(b) Phase III episode 2 glass inclusion data

Sample	Type	SiO_2	TiO_2	Al_2O_3	FeO	MnO	MgO	CaO	Na_2O	K_2O	P_2O_5	S	Cl	F	Total
LZ-13-01-7a	40 µm across Y shape inc	44.57	3.64	14.44	13.47	0.20	7.14	10.21	3.19	0.96	0.38	0.087	0.095	0.099	98.48
LZ-13-01-10a	50 µm across round, clean inc	45.01	3.70	14.81	13.48	0.22	7.06	10.41	3.14	0.98	0.36	0.106	0.110	0.013	99.40
LZ-13-01-12a	40 µm long, thin rectangle inc	44.99	3.62	14.72	13.51	0.18	6.90	10.38	3.28	0.92	0.44	0.128	0.119	0.090	99.28
LZ-13-01-17a	60 µm across round inc	48.09	2.72	12.97	12.88	0.15	6.12	11.00	3.00	0.69	0.21	0.170	0.166	0.094	98.26
LZ-13-01-22a	35 µm across oval inc	48.87	2.66	13.09	12.98	0.19	6.23	11.19	3.11	0.77	0.29	0.098	0.054	0.061	99.59

(c) Phase III episode 2 host crystal data

Sample	Sample Type	SiO_2	TiO_2	Al_2O_3	FeO	MnO	MgO	CaO	Na_2O	K_2O	P_2O_5	NiO	Cr_2O_3	Total	Fo	Fa
LZ-13-01-7c	host xtl of inc LZ-13-01-7a	38.03	0.03	0.02	15.49	0.20	44.91	0.15	0.00	0.00	0.03	0.255	0.008	99.12	83.8	16.2
LZ-13-01-10c	host xtl of inc LZ-13-01-10a	39.14	0.03	0.02	15.99	0.18	43.06	0.22	0.00	0.01	0.01	0.36	0.04	99.06	82.8	17.2
LZ-13-01-12c	host xtl of inc LZ-13-01-12a	39.06	0.01	0.00	16.44	0.22	42.87	0.19	0.01	0.00	0.01	0.314	0.07	99.19	82.3	17.7
LZ-13-01-17c	host xtl of inc LZ-13-01-17a; 22a	40.01	0.00	0.01	16.68	0.20	42.14	0.20	0.01	0.00	0.00	0.3	0.05	99.60	81.8	18.2

(e) Phase III episode 2 predicted S concentration

	Method 1 (K_2O/TiO_2)	Method 2 (P_2O_5/TiO_2)	Method 3 (constant S/TiO_2)
	wt% S_{inc} (predicted)	wt% S_{inc} (predicted)	wt% S_{inc} (predicted)
LZ-13-01-2	0.219	0.218	0.239
LZ-13-01-3	0.226	0.224	0.246
LZ-13-01-4	0.230	0.219	0.256
LZ-13-01-6	0.195	0.164	0.210
Average	**0.218**	**0.206**	**0.238**
Standard Deviation (2σ)	**0.014**	**0.025**	**0.017**

Appendix C4 Phase III episode 3 (Calderas Quemadas)

(a) Phase III episode 3 matrix glass data

Sample	Type	SiO_2	TiO_2	Al_2O_3	FeO	MnO	MgO	CaO	Na_2O	K_2O	P_2O_5	S	Cl	F	Total
LZ-16-01-1b	matrix glass	49.79	2.50	13.74	10.54	0.17	6.23	10.46	2.76	0.80	0.36	0.009	0.028	0.091	97.48
LZ-16-01-4b	matrix glass	49.56	2.55	12.92	10.83	0.13	6.35	10.58	2.74	0.84	0.36	0.012	0.069	0.121	97.06
LZ-16-01-12	matrix glass	50.89	2.30	12.99	10.96	0.14	5.90	10.27	3.58	0.88	0.59	0.010	0.045	0.153	98.70
LZ-16-01-14	matrix glass	49.47	2.34	13.07	10.71	0.16	6.18	10.83	3.53	0.86	0.40	0.011	0.023	0.163	97.75

(b) Phase III episode 3 glass inclusion data

Sample	Type	SiO_2	TiO_2	Al_2O_3	FeO	MnO	MgO	CaO	Na_2O	K_2O	P_2O_5	S	Cl	F	Total
LZ-16-01-10a	40µm long diamond shape inc	49.84	2.46	13.24	10.68	0.16	6.14	10.47	3.12	0.85	0.41	0.070	0.958	0.162	98.56
LZ-16-01-22a	**20 µm across small round inc**	**50.19**	**2.54**	**13.41**	**10.58**	**0.12**	**6.33**	**10.38**	**3.09**	**0.75**	**0.38**	**0.087**	**0.098**	**0.028**	**97.97**
LZ-16-01-3a	20 µm across rectangular inc, ves. in corner	49.07	2.67	13.33	10.93	0.12	6.49	10.42	3.52	0.87	0.41	0.043	0.113	0.066	98.05
LZ-16-01-7a	**20 µm across small round inc**	**48.50**	**2.46**	**13.21**	**10.79**	**0.11**	**6.59**	**10.57**	**3.44**	**0.86**	**0.48**	**0.109**	**0.104**	**0.071**	**97.29**
LZ-16-01-8a	30 µm across triangular inc	49.13	2.39	12.93	10.99	0.12	6.08	10.20	3.54	0.91	0.56	0.134	0.145	0.099	97.22

Shaded analyses indicate glass inclusions used in temperature calculations.

(c) Phase III episode 3 host crystal data

Sample	Sample Type	SiO_2	TiO_2	Al_2O_3	FeO	MnO	MgO	CaO	Na_2O	K_2O	P_2O_5	NiO	Cr_2O_3	Total	Fo	Fa
LZ-16-01-10c	host xtl of inc LZ-16-01-10a	40.68	0.00	0.03	11.07	0.13	47.84	0.09	0.02	0.01	0.00	0.38	0.02	100.25	88.5	11.5
LZ-16-01-22c	host xtl of inc LZ-16-01-22a	39.98	0.02	0.03	16.16	0.20	43.83	0.24	0.01	0.01	0.01	0.28	0.04	100.80	82.9	17.1
LZ-16-01-3c-rim	host xtl of inc LZ-16-01-3a	38.67	0.03	0.02	18.23	0.22	42.46	0.26	0.01	0.00	0.02	0.24	0.02	100.19	80.6	19.4
LZ-16-01-6c	host xtl of inc LZ-16-01-7a, -8a	38.79	0.01	0.02	15.11	0.19	44.19	0.24	0.00	0.01	0.03	0.31	0.05	98.95	83.9	16.1

(d) Phase III episode 3 other crystal data

Sample	Sample Type	SiO_2	TiO_2	Al_2O_3	FeO	MnO	MgO	CaO	Na_2O	K_2O	P_2O_5	NiO	Cr_2O_3	Total
LZ-16-01-1c-core	olivine xtl core	38.79	0.00	0.00	12.99	0.19	46.35	0.18	0.03	0.00	0.00	0.36	0.01	98.91
LZ-16-01-1c-rim	olivine xtl rim	39.22	0.00	0.01	12.87	0.17	46.38	0.21	0.01	0.00	0.01	0.36	0.04	99.29
LZ-16-01-2c	olivine xtl	38.99	0.00	0.00	10.61	0.17	47.82	0.04	0.00	0.00	0.00	0.32	0.00	97.94
LZ-16-01-21c-crsp	**cr-spinel inclusion in oliv xtl LZ-16-01-22c**	**0.02**	**1.73**	**19.28**	**25.71**	**0.26**	**11.16**	**0.01**	**0.03**	**0.01**	**0.00**	**0.06**	**38.26**	**99.94**
LZ-16-01-22c	**oliv host for cr-sp inc LZ-16-01-21c-crsp**	**39.98**	**0.02**	**0.03**	**16.16**	**0.20**	**43.83**	**0.24**	**0.01**	**0.01**	**0.01**	**0.28**	**0.04**	**100.80**
LZ-16-01-6c	oliv host for cr-sp inc LZ-16-01-6c	38.79	0.01	0.02	15.11	0.19	44.19	0.24	0.00	0.01	0.03	0.31	0.05	98.95
LZ-16-01-4c	oliv xtl	39.86	0.01	0.00	14.56	0.18	45.28	0.16	0.00	0.00	0.00	0.30	0.04	100.40

Shaded analyses indicate olivine/cr-spinel pairs used in oxygen fugacity calculations.

(e) Phase III episode 3 predicted S concentration			
	Method 1 (K_2O/TiO_2)	**Method 2 (P_2O_5/TiO_2)**	**Method 3 (constant S/TiO_2)**
	wt% S_{inc} (predicted)	**wt% S_{inc} (predicted)**	**wt% S_{inc} (predicted)**
LZ-16-01-1b	0.219	0.218	0.239
LZ-16-01-4b	0.226	0.224	0.246
LZ-16-01-12	0.230	0.219	0.256
LZ-16-01-14	0.195	0.164	0.210
Average	**0.218**	**0.206**	**0.238**
Standard Deviation (2σ)	**0.014**	**0.025**	**0.017**

Appendix C4 Phase IV (Montana del Fuego)

Phase IV matrix glass data

Sample	Type	SiO_2	TiO_2	Al_2O_3	FeO	MnO	MgO	CaO	Na_2O	K_2O	P_2O_5	S	Cl	F	Total
LZ-12-01-2	mtx gls in scoria frag	48.56	3.33	14.36	10.85	0.17	5.86	10.29	3.31	1.06	0.49	0.014	0.021	0.064	98.38
LZ-12-01-3	mtx gls in scoria frag	48.61	3.35	14.16	10.62	0.18	5.88	10.32	3.49	1.00	0.49	0.013	0.032	0.000	98.15
LZ-12-01-8	mtx gls in scoria frag	48.43	3.33	14.24	10.64	0.16	5.93	10.38	3.48	1.06	0.47	0.015	0.020	0.022	98.16
LZ-12-01-9	mtx gls in scoria frag	48.13	3.38	14.17	10.83	0.17	5.82	10.41	3.51	1.00	0.49	0.012	0.043	0.043	98.01
LZ-12-01-12	mtx gls in scoria frag	47.98	3.32	14.29	10.93	0.19	5.90	10.37	3.47	1.04	0.53	0.014	0.036	0.062	98.13
LZ-12-01-1	mtx gls in scoria frag	48.91	3.42	14.35	10.37	0.16	5.72	10.37	3.59	1.04	0.45	0.012	0.029	0.000	98.43
LZ-12-01-8	mtx gls in scoria frag	48.79	3.41	14.19	10.39	0.15	5.67	10.35	3.71	1.05	0.49	0.012	0.045	0.071	98.33
LZ-12-01-9	mtx gls in scoria frag	48.12	3.41	14.25	10.28	0.15	5.67	10.33	3.57	1.11	0.44	0.012	0.031	0.040	97.43
LZ-12-01-15	mtx gls in scoria frag	48.02	3.44	14.38	10.38	0.15	5.68	10.36	3.68	1.11	0.49	0.012	0.035	0.000	97.73
LZ-12-01-25	mtx gls	48.24	3.42	14.13	10.41	0.18	5.63	10.39	3.63	1.10	0.49	0.011	0.039	0.000	97.68
LZ-12-01-29	mtx gls in scoria frag w/ xtl LZ-12-01-28c	48.15	3.31	14.08	9.83	0.13	5.50	9.74	5.10	1.22	0.49	0.009	0.028	0.000	97.18
LZ-12-01-35	mtx gls in scoria frag	48.16	3.43	14.20	10.35	0.16	5.73	10.32	3.60	1.13	0.45	0.010	0.030	0.000	97.57

(b) Phase IV glass inclusion data

Sample	Type	SiO_2	TiO_2	Al_2O_3	FeO	MnO	MgO	CaO	Na_2O	K_2O	P_2O_5	S	Cl	F	Total
LZ-12-01-1a	30 μm across square inc	48.23	3.32	14.19	10.76	0.15	5.72	10.88	3.62	1.02	0.46	0.086	0.108	0.098	98.64
LZ-12-01-4a	35μm across clean oval inc	49.44	3.31	14.15	10.28	0.16	5.68	11.02	3.15	0.92	0.56	0.228	0.185	0.107	99.19
LZ-12-01-6a	30μm long L-shape inc	48.59	3.25	14.11	10.51	0.16	6.01	11.26	3.07	0.97	0.19	0.116	0.091	0.122	98.45
LZ-12-01-28	25μm across square inc	47.22	3.26	14.61	10.51	0.16	5.25	10.91	3.67	0.99	0.48	0.064	0.090	0.172	97.37
LZ-12-01-1-7	40μm across semi-square inc, crack on edge	48.63	3.36	14.50	10.61	0.16	5.48	10.58	3.68	1.05	0.48	0.094	0.101	0.025	98.74

(c) Phase IV host crystal data

Sample	Sample Type	SiO_2	TiO_2	Al_2O_3	FeO	MnO	MgO	CaO	Na_2O	K_2O	P_2O_5	NiO	Cr_2O_3	Total	Fo	Fa
LZ-12-01-1c	host xtl of inc LZ-12-01-1a	38.20	0.02	0.02	15.44	0.19	44.72	0.23	0.00	0.00	0.02	0.294	0.05	99.18	83.8	16.2
LZ-12-02-4c	host xtl of inc LZ-12-02-4a	37.39	0.03	0.02	16.10	0.21	43.58	0.23	0.01	0.00	0.00	0.297	0.02	97.89	82.8	17.2
LZ-12-02-3c	host xtl of inc LZ-12-02-6a	38.24	0.00	0.01	14.06	0.15	45.16	0.16	0.01	0.00	0.02	0.402	0.07	98.28	85.1	14.9
LZ-12-01-28c	host xtl of inc LZ-12-01-28	38.52	0.03	0.04	15.01	0.19	44.44	0.27	0.01	0.00	0.01	0.307	0.07	98.88	84.1	15.9
LZ-12-01-1-7c	oliv host xtl of inc LZ-12-01-1-7	39.29	0.02	0.03	14.39	0.22	45.69	0.18	0.01	0.00	0.03	0.412	0.08	100.34	85.0	15.0

(d) Phase IV other crystal data

Sample	Sample Type	SiO_2	TiO_2	Al_2O_3	FeO	MnO	MgO	CaO	Na_2O	K_2O	P_2O_5	NiO	Cr_2O_3	Total
LZ-12-01-f	cr-spinel inclusion	0.20	4.73	15.70	36.94	0.28	12.97	0.10	0.00	0.00	0.01	0.249	27.85	99.03
LZ-12-01-fc	olivine xtl	38.68	0.05	0.05	16.21	0.21	44.02	0.30	0.01	0.01	0.04	0.266	0.12	99.94
LZ-12-01-jc	olivine xtl	37.62	0.02	0.03	15.69	0.19	44.26	0.27	0.00	0.00	0.01	0.274	0.05	98.41
LZ-12-01-xtl-1R	oliv xtl rim	39.31	0.04	0.39	15.40	0.21	44.15	0.29	0.01	0.01	0.02	0.300	0.06	100.17
LZ-12-01-xtl-1C	oliv xtl core	39.03	0.04	0.03	14.89	0.21	44.93	0.23	0.02	0.00	0.01	0.326	0.09	99.80
LZ-12-01-xtl-23-3	oliv xtl core (traverse)	36.62	0.04	0.02	23.13	0.32	38.14	0.32	0.01	0.00	0.03	0.196	0.00	98.82
LZ-12-01-xtl-23-4	oliv xtl opposite rim (traverse)	36.74	0.03	0.02	23.08	0.33	38.16	0.30	0.00	0.00	0.02	0.191	0.01	98.87
LZ-12-01-xtl-27	Fe-Ti oxide inc on edge of oliv	0.05	18.16	3.97	63.15	0.37	6.08	0.16	0.01	0.00	0.00	0.206	2.77	94.94

Shaded analyses indicate olivine/cr-spinel pairs used in oxygen fugacity calculations.

(e) Phase IV predicted S concentration			
Sample	**Method 1 (K_2O/TiO_2) wt% S_{inc} (predicted)**	**Method 2 (P_2O_5/TiO_2) wt% S_{inc} (predicted)**	**Method 3 (constant S/TiO_2) wt% S_{inc} (predicted)**
LZ-12-01-2	0.231	0.251	0.233
LZ-12-01-3	0.227	0.237	0.235
LZ-12-01-8	0.231	0.252	0.233
LZ-12-01-9	0.228	0.237	0.237
LZ-12-01-12	0.229	0.243	0.232
LZ-12-01-1	0.233	0.251	0.239
LZ-12-01-8	0.234	0.250	0.239
LZ-12-01-9	0.238	0.267	0.239
LZ-12-01-15	0.240	0.264	0.241
LZ-12-01-25	0.238	0.261	0.239
LZ-12-01-29	0.245	0.289	0.232
LZ-12-01-35	0.241	0.272	0.240
Average	**0.235**	**0.256**	**0.237**
Standard Deviation (2σ)	**0.006**	**0.015**	**0.003**

Appendix C4 Phase IV lava (Montana del Fuego)

(a) Phase IV lava matrix glass data

Sample	Type	SiO_2	TiO_2	Al_2O_3	FeO	MnO	MgO	CaO	Na_2O	K_2O	P_2O_5	S	Cl	F	Total
LZ-12-02-a	matrix glass	49.17	1.29	12.57	12.18	0.18	7.00	11.87	3.23	0.98	0.23	0.009	0.036	0.000	98.75
LZ-12-02-b	matrix glass	49.91	1.46	13.06	12.24	0.16	7.66	10.88	2.98	1.06	0.27	0.010	0.049	0.000	99.73
LZ-12-02-2	matrix glass in lava	49.88	1.51	13.06	12.49	0.14	6.64	11.10	3.14	1.02	0.26	0.011	0.014	0.000	99.27
LZ-12-02-3	matrix glass in lava	50.02	1.51	12.76	12.61	0.19	7.39	11.56	3.16	0.92	0.29	0.009	0.012	0.011	100.44
LZ-12-02-4	matrix glass in lava	50.05	1.36	13.01	12.23	0.20	6.84	11.22	2.99	0.94	0.21	0.010	0.038	0.000	99.10
LZ-12-02-6	matrix glass in lava	49.94	1.59	12.20	12.41	0.14	6.66	10.79	3.15	1.04	0.22	0.011	0.019	0.029	98.20
LZ-12-02-7	matrix glass in lava	49.20	1.54	12.84	12.48	0.15	6.97	10.99	3.07	0.94	0.29	0.009	0.031	0.012	98.53
LZ-12-02-8	matrix glass in lava	49.02	1.56	13.07	12.53	0.17	6.88	11.04	3.23	1.01	0.24	0.012	0.011	0.000	98.77
LZ-12-02-13	matrix glass in lava	50.49	1.61	13.43	12.45	0.16	6.80	11.55	2.71	0.93	0.27	0.018	0.012	0.000	100.43
LZ-12-02-2	matrix glass	51.92	1.29	12.29	11.93	0.09	6.52	11.49	3.37	1.03	0.24	0.009	0.002	0.000	100.18
LZ-12-02-3	matrix glass	48.84	1.28	12.94	12.10	0.15	6.85	11.57	2.91	0.95	0.27	0.009	0.050	0.106	98.03
LZ-12-02-4	matrix glass	48.76	1.72	12.72	12.14	0.14	6.91	11.15	2.96	1.06	0.33	0.007	0.134	0.183	98.21
LZ-12-02-b	matrix glass	47.99	1.68	13.08	12.25	0.18	6.98	11.19	3.08	0.99	0.30	0.011	0.034	0.087	97.85

(b) Phase IV lava glass inclusion data

Sample	Type	SiO_2	TiO_2	Al_2O_3	FeO	MnO	MgO	CaO	Na_2O	K_2O	P_2O_5	S	Cl	F	Total
LZ-12-02-5a	30 um across round inc	49.98	1.49	12.66	11.83	0.15	6.72	10.81	3.28	0.98	0.25	0.072	0.612	0.049	98.88
LZ-12-02-9a	small oval inc	48.26	1.48	13.12	12.38	0.21	7.03	11.02	3.05	0.94	0.32	0.098	0.097	0.094	98.10
LZ-12-02-10a	35 um across long oval inc	48.87	1.42	13.03	11.80	0.19	6.99	10.96	3.01	0.93	0.31	0.114	0.091	0.099	97.81
LZ-12-02-14a	**40um across square inc**	**50.06**	**1.50**	**12.96**	**11.92**	**0.16**	**6.91**	**10.89**	**3.22**	**0.99**	**0.26**	**0.184**	**0.160**	**0.044**	**99.26**
LZ-12-02-16a	**50um across semi-circle inc**	**49.91**	**1.44**	**12.99**	**11.88**	**0.19**	**7.06**	**10.84**	**3.16**	**0.92**	**0.32**	**0.146**	**0.109**	**0.100**	**99.07**

Shaded analyses indicate glass inclusions used in temperature calculations.

(c) Phase IV lava host crystal data

Sample	Sample Type	SiO_2	TiO_2	Al_2O_3	FeO	MnO	MgO	CaO	Na_2O	K_2O	P_2O_5	NiO	Cr_2O_3	Total	Fo	Fa
LZ-12-02-5c	host xtl of inc LZ-12-02-5a	39.56	0.00	0.01	12.03	0.18	47.60	0.06	0.01	0.00	0.01	0.36	0.00	99.82	87.6	12.4
LZ-12-02-9c	host xtl of inc LZ-12-02-9c; 10c	38.66	0.01	0.00	13.06	0.20	46.96	0.14	0.01	0.00	0.00	0.34	0.06	99.44	86.5	13.5
LZ-12-02-14c	host xtl of inc LZ-12-02-14a; 16a	39.67	0.01	0.00	12.21	0.20	47.56	0.18	0.00	0.00	0.01	0.36	0.04	100.24	87.4	12.6

(d) Phase IV lava other crystal data

Sample	Sample Type	SiO_2	TiO_2	Al_2O_3	FeO	MnO	MgO	CaO	Na_2O	K_2O	P_2O_5	NiO	Cr_2O_3	Total
LZ-12-02-1c-crsp	cr-spinel inclusion	0.03	0.29	22.55	22.69	0.25	12.84	0.00	0.01	0.00	0.00	0.19	41.05	99.90
LZ-12-02-1c-core	olivine xtl core	39.30	0.00	0.01	12.83	0.16	46.57	0.12	0.00	0.00	0.00	0.35	0.02	99.36
LZ-12-02-1c-rim	olivine xtl rim	39.39	0.01	0.00	13.50	0.17	46.23	0.13	0.03	0.01	0.00	0.35	0.03	99.85
LZ-12-02-3c	olivine xtl core	38.92	0.02	0.05	15.38	0.18	43.82	0.22	0.00	0.00	0.04	0.292	0.057	98.981
LZ-12-02-2oliv	olivine xtl	38.88	0.01	0.02	15.22	0.18	44.24	0.26	0.00	0.00	0.02	0.19	0.02	99.04

Shaded analyses indicate olivine/cr-spinel pairs used in oxygen fugacity calculations.

(e) Phase IV lava predicted S concentration

Sample	Method 1 ($S/K_2O = 0.186$)	Method 2 ($S/P_2O_5 = 0.708$)	Method 3 ($S/TiO_2 = 0.123$)
	wt% S_{inc} (predicted)	wt% S_{inc} (predicted)	wt% S_{inc} (predicted)
LZ-12-02-a	0.182	0.162	0.159
LZ-12-02-b	0.197	0.191	0.180
LZ-12-02-2	0.190	0.184	0.186
LZ-12-02-3	0.171	0.205	0.186
LZ-12-02-4	0.175	0.149	0.167
LZ-12-02-6	0.193	0.156	0.196
LZ-12-02-7	0.175	0.205	0.189
LZ-12-02-8	0.188	0.170	0.192
LZ-12-02-13	0.173	0.191	0.198
LZ-12-02-2	0.192	0.173	0.159
LZ-12-02-3	0.177	0.191	0.157
LZ-12-02-4	0.197	0.234	0.212
LZ-12-02-b	0.184	0.212	0.207
Average	**0.184**	**0.186**	**0.184**
Standard Deviation (2σ)	**0.009**	**0.023**	**0.017**

NB. See chapter 4 for details on predicted S calculation for phase IV lava sample.

Appendix C4 Phase V episode 1 (Montana de las Nueces)

(a) Phase V episode 1 matrix glass data

Sample	Type	SiO_2	TiO_2	Al_2O_3	FeO	MnO	MgO	CaO	Na_2O	K_2O	P_2O_5	S	Cl	F	Total
LZ-7-01-2	matrix glass in lava	52.31	3.09	12.99	10.43	0.19	5.17	9.80	3.16	0.76	0.41	0.012	0.030	0.000	98.35
LZ-7-01-4	matrix glass in lava	51.52	3.15	13.34	10.63	0.15	5.06	9.54	3.29	0.82	0.48	0.017	0.053	0.044	98.09
LZ-7-01-11	matrix glass in lava	52.77	3.06	12.98	10.57	0.12	5.01	9.40	3.36	0.76	0.49	0.009	0.043	0.171	98.74
Distal lava															
LZ-6-01-a	matrix glass in lava	52.52	3.14	13.57	10.66	0.14	5.34	9.38	3.35	0.81	0.43	0.006	0.017	0.004	99.37
LZ-6-01-b	matrix glass in lava	52.52	3.12	13.54	10.70	0.15	5.32	9.32	3.22	0.83	0.43	0.008	0.018	0.000	99.18
LZ-6-01-d	matrix glass in lava	52.26	3.08	13.59	10.73	0.16	5.34	9.39	3.30	0.81	0.39	0.009	0.026	0.109	99.19
LZ-6-01-e	matrix glass in lava	52.44	3.11	13.59	10.89	0.17	5.29	9.41	3.30	0.83	0.42	0.008	0.032	0.033	99.52
LZ-6-01-g	matrix glass in lava	52.65	3.18	13.53	10.74	0.14	5.30	9.29	3.26	0.82	0.44	0.009	0.017	0.000	99.39
LZ-6-01-6	matrix glass in lava	52.33	3.12	13.50	10.58	0.14	5.47	9.29	3.30	0.85	0.38	0.009	0.011	0.000	98.98
LZ-6-01-9	matrix glass in lava	52.65	3.14	13.44	10.51	0.15	5.18	9.54	3.42	0.78	0.37	0.008	0.017	0.042	99.25
LZ-6-01-11	matrix glass in lava	52.36	3.12	13.77	10.54	0.18	5.41	9.40	3.27	0.79	0.44	0.008	0.027	0.000	99.31
LZ-6-01-12	matrix glass in lava	51.95	3.16	13.66	10.58	0.15	5.32	9.41	3.29	0.83	0.40	0.011	0.043	0.000	98.79
LZ-6-01a-4	matrix glass in lava	52.32	3.17	13.60	10.73	0.16	5.36	9.28	3.36	0.90	0.40	0.008	0.025	0.061	99.36
LZ-6-01a-5	matrix glass in lava	52.36	3.12	13.61	10.59	0.15	5.44	9.38	3.32	0.81	0.41	0.007	0.026	0.000	99.22
LZ-6-01a-10	matrix glass in lava	52.44	3.13	13.41	10.82	0.15	5.24	9.53	3.35	0.91	0.43	0.010	0.031	0.000	99.44
LZ-6-01a-11	matrix glass in lava	52.23	3.07	13.55	10.72	0.15	5.37	9.46	3.36	0.83	0.41	0.008	0.028	0.000	99.19

(b) Phase V episode 1 glass inclusion data

Sample	Type	SiO_2	TiO_2	Al_2O_3	FeO	MnO	MgO	CaO	Na_2O	K_2O	P_2O_5	S	Cl	F	Total
LZ-6-01-1a	small oval inc	51.94	3.11	14.23	10.35	0.14	5.43	9.76	3.10	0.70	0.36	0.071	0.099	0.022	99.30
LZ-6-01-1b	small oval inc	51.31	3.11	13.80	10.50	0.14	5.19	9.55	3.22	0.75	0.40	0.063	0.122	0.000	98.15
LZ-6-01-5a	40 µm across L-shape inc	51.89	3.20	13.55	10.08	0.16	5.45	9.74	3.23	0.84	0.48	0.075	0.085	0.035	98.82
LZ-6-01a-8a	**small square inc**	**51.71**	**3.20**	**14.16**	**10.50**	**0.15**	**5.48**	**9.58**	**3.21**	**0.81**	**0.44**	**0.081**	**0.111**	**0.026**	**99.43**
LZ-6-01a-9a	small round inc	52.26	3.18	13.60	10.80	0.16	5.40	9.29	3.27	0.86	0.42	0.070	0.103	0.047	99.37
LZ-7-01-7b	small v-shape inc	51.99	2.97	13.09	10.46	0.12	5.00	9.54	3.48	0.90	0.51	0.090	0.134	0.089	98.37
LZ-7-01-8a	40 µm long thin oval inc	51.46	3.06	12.79	11.07	0.15	5.36	9.62	3.30	0.86	0.43	0.067	0.090	0.059	98.31
LZ-7-01-9b	small square inc	52.32	3.11	13.13	10.78	0.11	5.22	10.10	3.36	0.74	0.41	0.149	0.074	0.064	99.57

Shaded analyses indicate glass inclusions used in temperature calculations.

(c) Phase V episode 1 host crystal data

Sample	Sample Type	SiO_2	TiO_2	Al_2O_3	FeO	MnO	MgO	CaO	Na_2O	K_2O	P_2O_5	NiO	Cr_2O_3	Total	Fo	Fa
LZ-6-01-1c	host xtl of inc LZ-6-01-1a; 1b	39.30	0.02	0.03	20.68	0.26	39.65	0.31	0.00	0.00	0.06	0.221	0.039	100.571	77.4	22.6
LZ-6-01-5c-core	host xtl of inc LZ-6-01-5a - core	40.56	0.01	0.03	13.67	0.21	45.75	0.26	0.01	0.00	0.02	0.252	0.017	100.797	85.6	14.4
LZ-6-01-5c-rim	host xtl of inc LZ-6-01-5a - rim	40.46	0.01	0.03	15.28	0.20	44.46	0.35	0.01	0.01	0.01	0.281	0.101	101.184	83.8	16.2
LZ-6-01a-8c	host xtl of inc LZ-6-01a-8a	39.47	0.00	0.24	17.85	0.22	41.98	0.24	0.01	0.00	0.01	0.313	0.016	100.354	80.7	19.3
LZ-6-01a-9c	host xtl of inc LZ-6-01a-9a	39.08	0.02	0.06	19.98	0.25	40.04	0.28	0.00	0.00	0.03	0.230	0.032	100.003	78.1	21.9
LZ-7-01-7c	host xtl of inc LZ-7-01-7b	39.27	0.03	0.01	19.42	0.23	40.70	0.31	0.00	0.00	0.00	0.192	0.022	100.183	78.9	21.1
LZ-7-01-8c	host xtl of inc LZ-7-01-8a	39.06	0.03	0.02	19.93	0.25	40.47	0.27	0.01	0.00	0.06	0.204	0.013	100.309	78.4	21.7
LZ-7-01-9c	host xtl of inc LZ-7-01-9b	39.75	0.02	0.04	16.05	0.20	43.80	0.24	0.01	0.00	0.06	0.309	0.081	100.567	83.0	17.1

(d) Phase V episode 1 other crystal data

Sample	Sample Type	SiO_2	TiO_2	Al_2O_3	FeO	MnO	MgO	CaO	Na_2O	K_2O	P_2O_5	NiO	Cr_2O_3	Total
LZ-6-01-xtl-a	olivine xtl core	39.36	0.01	0.03	19.69	0.24	40.86	0.28	0.00	0.00	0.06	0.210	0.030	100.768
LZ-6-01-xtl-c	olivine xtl core	39.76	0.02	0.03	18.65	0.21	41.70	0.21	0.01	0.00	0.02	0.266	0.040	100.924
LZ-6-01-xtl-d	olivine xtl core	40.21	0.01	0.02	16.12	0.21	43.72	0.22	0.00	0.00	0.00	0.319	0.061	100.882
LZ-6-01-xtl-e	olivine xtl core	39.19	0.03	0.02	16.87	0.20	43.20	0.21	0.03	0.00	0.06	0.309	0.067	100.201
LZ-7-01-6c	olivine xtl core	39.06	0.01	0.02	17.92	0.20	42.59	0.20	0.02	0.00	0.02	0.288	0.064	100.379
LZ-6-01-2-crsp	**cr-spinel inc in olivine xtl**	**19.92**	**1.49**	**8.13**	**24.97**	**0.24**	**28.30**	**0.20**	**0.04**	**0.02**	**0.02**	**0.24**	**21.54**	**105.11**
LZ-6-01-2-oliv	**olivine xtl w/ cr-spinel inc**	**40.46**	**0.00**	**0.03**	**15.94**	**0.21**	**44.13**	**0.23**	**0.01**	**0.00**	**0.02**	**0.32**	**0.06**	**101.40**

Shaded analyses indicate olivine/cr-spinel pairs used in oxygen fugacity calculations.

(e) Phase I episode 1 Predicted S concentration			
Sample	**Method 1 (K_2O/TiO_2)**	**Method 2 (P_2O_5/TiO_2)**	**Method 3 (constant S/TiO_2)**
	wt% S_{inc} (predicted)	**wt% S_{inc} (predicted)**	**wt% S_{inc} (predicted)**
LZ-7-01-2	0.194	0.183	0.216
LZ-7-01-4	0.202	0.193	0.221
LZ-7-01-11	0.193	0.177	0.214
Distal lava			
LZ-6-01-a	0.200	0.193	0.220
LZ-6-01-b	0.202	0.198	0.219
LZ-6-01-d	0.198	0.196	0.215
LZ-6-01-e	0.202	0.200	0.218
LZ-6-01-g	0.204	0.196	0.223
LZ-6-01-6	0.204	0.208	0.218
LZ-6-01-9	0.198	0.191	0.220
LZ-6-01-11	0.198	0.188	0.218
LZ-6-01-12	0.203	0.201	0.221
LZ-6-01a-4	0.210	0.217	0.222
LZ-6-01a-5	0.200	0.194	0.218
LZ-6-01a-10	0.209	0.218	0.219
LZ-6-01a-11	0.200	0.200	0.215
Average	**0.238**	**0.231**	**0.259**
Standard Deviation (2σ)	**0.005**	**0.011**	**0.002**

Appendix C4 Phase V episode 2 (Montana Colorada)

(a) Phase V episode 2 matrix glass data

Sample	Type	SiO_2	TiO_2	Al_2O_3	FeO	MnO	MgO	CaO	Na_2O	K_2O	P_2O_5	S	Cl	F	Total
LZ-3-01-5	matrix glass in tephra	50.06	2.31	13.60	11.86	0.15	5.71	10.59	2.97	0.86	0.28	0.014	0.055	0.104	98.55
LZ-3-01-10	matrix glass attached to xtl	50.06	2.66	14.78	10.56	0.15	5.82	10.82	3.60	0.72	0.43	0.010	0.027	0.000	99.64
LZ-3-01-a-2	matrix glass shard	45.69	3.68	15.18	11.86	0.18	5.74	10.77	3.65	1.02	1.03	0.017	0.072	0.000	98.89
LZ-3-01-a-3	matrix glass shard	45.19	3.77	15.23	11.57	0.18	5.73	10.98	3.52	1.04	1.04	0.016	0.075	0.175	98.50
LZ-3-01-a-7	matrix glass shard	45.25	3.77	14.91	11.09	0.19	5.42	11.44	3.62	1.18	0.96	0.018	0.076	0.086	98.00
LZ-3-01-a-8	matrix glass shard	45.40	3.80	15.00	11.21	0.19	5.77	11.91	3.28	1.14	1.04	0.020	0.071	0.013	98.84
LZ-3-01-a-9	matrix glass shard	45.00	3.51	14.64	11.18	0.16	5.54	12.98	3.33	1.26	0.96	0.020	0.079	0.126	98.78
LZ-3-01-b	xtl-free matrix glass	45.64	3.36	14.98	11.09	0.16	5.90	11.80	3.59	1.34	0.69	0.011	0.057	0.000	98.61
LZ-3-01-f	matrix glass in scoria fragment	51.56	2.69	15.50	10.22	0.13	5.39	9.86	3.09	0.70	0.40	0.019	0.038	0.035	99.62
LZ-3-01-g	matrix glass in scoria fragment	47.46	3.06	14.89	11.15	0.13	5.83	10.65	3.01	1.08	0.63	0.016	0.040	0.065	98.01
LZ-3-01-j	matrix glass in scoria fragment	51.02	2.59	15.25	10.52	0.14	5.28	9.92	3.15	0.70	0.41	0.012	0.063	0.032	99.08
LZ-3-01-4	matrix glass in scoria fragment	45.71	3.45	14.87	11.12	0.16	5.84	11.76	3.29	1.20	0.70	0.015	0.061	0.172	98.35
LZ-3-01-5	matrix glass in scoria fragment	45.10	3.41	14.99	11.07	0.16	5.76	11.76	3.50	1.39	0.71	0.017	0.060	0.212	98.13
Distal lava															
LZ-2-01-17	matrix glass in lava	50.85	2.25	13.67	11.41	0.10	5.43	10.81	2.98	0.82	0.24	0.012	0.024	0.000	98.60
LZ-2-01-2	matrix glass in lava	50.60	2.51	13.45	11.36	0.18	5.14	11.00	2.74	0.80	0.26	0.008	0.044	0.010	98.10
LZ-2-01-3	matrix glass in lava	50.10	2.46	13.57	11.28	0.19	5.51	11.17	2.84	0.78	0.24	0.008	0.048	0.013	98.21

(b) Phase V episode 2 glass inclusion data

Sample	Type	SiO_2	TiO_2	Al_2O_3	FeO	MnO	MgO	CaO	Na_2O	K_2O	P_2O_5	S	Cl	F	Total
LZ-2-01-1a	70μm long clean sq inc	50.96	2.23	13.78	10.96	0.12	5.96	10.56	2.75	0.72	0.28	0.047	0.137	0.098	98.60
LZ-2-01-6a	small 30 μm across rectangular inc	49.96	2.14	14.00	11.05	0.11	6.14	10.30	3.02	0.74	0.29	0.043	0.129	0.082	98.00
LZ-2-01-9a	30 μm across bulb shape inc	50.85	2.08	13.24	11.16	0.09	5.65	10.78	3.17	0.72	0.26	0.068	0.081	0.066	98.21
LZ-2-01-12a	30 μm across clean triangular inc	50.02	2.27	13.52	11.41	0.13	5.75	10.66	2.89	0.79	0.27	0.071	0.125	0.104	98.01
LZ-2-01-12d	30 μm across oval inc	50.36	2.04	13.76	11.40	0.13	6.09	10.35	2.75	0.80	0.28	0.053	0.074	0.117	98.20
LZ-3-01-20a	small, clean round inc	49.42	2.68	14.47	10.77	0.16	5.62	10.88	3.42	0.86	0.50	0.079	0.132	0.241	99.23
LZ-3-01-a-1a	50μm across clean, flat, oval inc	45.53	3.25	14.74	11.29	0.20	5.60	11.49	3.69	1.06	0.68	0.138	0.101	0.277	98.05
LZ-3-01-1a	25 μm across small round inc	50.25	2.65	14.23	11.28	0.11	5.63	10.90	2.96	0.57	0.30	0.056	0.071	0.024	99.03

Shaded analyses indicate glass inclusions used in temperature calculations.

(c) Phase V episode 2 host crystal data

Sample	Sample Type	SiO_2	TiO_2	Al_2O_3	FeO	MnO	MgO	CaO	Na_2O	K_2O	P_2O_5	NiO	Cr_2O_3	Total	Fo	Fa
LZ-2-01-1c-core	host xtl of inc LZ-2-01-1a	40.11	0.00	0.00	10.90	0.17	48.28	0.16	0.01	0.00	0.00	0.30	0.00	99.92	88.8	11.2
LZ-2-01-1c-rim	host xtl of inc LZ-2-01-1a	39.61	0.01	0.02	10.96	0.17	48.27	0.16	0.01	0.00	0.00	0.30	0.03	99.54	88.7	11.3
LZ-2-01-6c	host xtl of inc LZ-2-01-6a	38.48	0.00	0.02	12.64	0.17	47.45	0.14	0.02	0.00	0.00	0.38	0.04	99.34	87.0	13.0
LZ-2-01-9c	host xtl of inc LZ-2-01-9a	38.42	0.00	0.03	12.58	0.16	47.44	0.15	0.00	0.00	0.00	0.31	0.04	99.14	87.1	13.0
LZ-2-01-12c	host xtl of inc LZ-2-01-12a, 12d	38.33	0.00	0.01	12.94	0.17	46.18	0.20	0.00	0.00	0.01	0.28	0.06	98.17	86.4	13.6
LZ-3-01-20c	host xtl of inc LZ-3-01-20a	39.47	0.01	0.00	13.88	0.16	45.60	0.22	0.00	0.00	0.02	0.32	0.06	99.74	85.4	14.6
LZ-3-01-a-1c	host xtl of inc LZ-3-01-a-1a	38.95	0.01	0.04	14.00	0.19	45.59	0.19	0.02	0.00	0.03	0.29	0.05	99.35	85.3	14.7
LZ-3-01-1c	host xtl of inc LZ-3-01-1a	40.55	0.00	0.00	11.24	0.13	48.47	0.08	0.00	0.00	0.04	0.41	0.01	100.94	88.5	11.5

(d) Phase V episode 2 other crystal data

Sample	Sample Type	SiO_2	TiO_2	Al_2O_3	FeO	MnO	MgO	CaO	Na_2O	K_2O	P_2O_5	NiO	Cr_2O_3	Total
LZ-2-01-1c-crsp	cr-spinel inc in oliv xtl	1.04	0.23	27.48	20.92	0.22	14.59	0.01	0.13	0.11	0.00	0.16	34.82	99.70
LZ-2-01-1c-core	oliv host of cr-sp inc LZ-2-01-1c	40.11	0.00	0.00	10.90	0.17	48.28	0.16	0.01	0.00	0.00	0.30	0.00	99.92
LZ-3-01-k-c-core	olivine xtl core	40.90	0.00	0.00	8.41	0.12	50.94	0.02	0.00	0.02	0.00	0.43	0.00	100.82
LZ-3-01-k-c-rim	olivine xtl rim	41.21	0.01	0.01	8.34	0.12	50.43	0.01	0.00	0.00	0.00	0.40	0.01	100.53
LZ-2-01-10c	olivine xtl	37.96	0.00	0.01	13.84	0.14	45.91	0.17	0.00	0.01	0.01	0.38	0.02	98.45
LZ-2-01-10c-crsp	cr-spinel inc in oliv xtl	0.29	1.46	31.54	22.31	0.23	8.93	0.11	0.05	0.03	0.00	0.22	28.24	93.43
LZ-3-01-6	cr-spinel inclusion	1.38	2.01	22.69	26.68	0.26	11.85	0.17	0.17	0.06	0.01	0.27	33.78	99.33
LZ-3-01-6c	olivine xtl	38.80	0.03	0.04	15.03	0.18	44.71	0.24	0.02	0.00	0.01	0.41	0.08	99.54

Shaded analyses indicate olivine/cr-spinel pairs used in oxygen fugacity calculations.

(e) Phase V episode 2 Predicted S concentration			
Sample	**Method 1 (K_2O/TiO_2)**	**Method 2 (P_2O_5/TiO_2)**	**Method 3 (constant S/TiO_2)**
	wt% S_{inc} (predicted)	**wt% S_{inc} (predicted)**	**wt% S_{inc} (predicted)**
LZ-3-01-5	0.172	0.209	0.162
LZ-3-01-10	0.173	0.168	0.186
LZ-3-01-a-2	0.242	0.206	0.258
LZ-3-01-a-3	0.247	0.212	0.264
LZ-3-01-a-7	0.260	0.246	0.264
LZ-3-01-a-8	0.257	0.232	0.266
LZ-3-01-a-9	0.257	0.257	0.246
LZ-3-01-b	0.258	0.297	0.235
LZ-3-01-f	0.173	0.166	0.188
LZ-3-01-g	0.222	0.239	0.214
LZ-3-01-j	0.168	0.163	0.181
LZ-3-01-4	0.248	0.267	0.241
LZ-3-01-5	0.264	0.306	0.238
Distal lava			
LZ-2-01-17	0.166	0.203	0.158
LZ-2-01-2	0.174	0.198	0.176
LZ-2-01-3	0.170	0.195	0.172
Average	**0.216**	**0.223**	**0.216**
Standard Deviation (2σ)	**0.041**	**0.042**	**0.039**

Appendix C5 Mineral cation data

Sample/Analysis	Cation Total	Spinel Mg# or Mg_{sl}	Spinel Cr# or Fe^{3+}_{sl}	Mg#
Phase I, Episode 1				
LZ-8-01-6c	3.009	1.70	0.30	0.85
LZ-8-01-24c	3.005	1.73	0.26	0.87
LZ-8-01-2c	3.007	1.72	0.28	0.86
LZ-8-01-26C	3.008	1.73	0.27	0.87
LZ-3-02-4c	3.011	1.69	0.31	0.84
LZ-3-02-10c	3.007	1.68	0.31	0.84
LZ-3-02-13c	3.014	1.76	0.26	0.87
LZ-3-02-16c	3.010	1.82	0.18	0.91
LZ-3-02-26c	3.014	1.79	0.22	0.89
LZ-5-02-c	2.988	1.71	0.25	0.87
LZ-8-01-22	3.000	0.58	0.52	-
LZ-8-01-23	3.013	1.79	0.22	0.89
LZ-3-02-21C	3.014	1.76	0.26	0.87
LZ-3-02-21R	3.009	1.75	0.26	0.87
LZ-3-02-22	3.000	0.35	0.35	-
LZ-3-02-23	3.000	0.53	0.52	-
LZ-3-02-24R	3.003	1.76	0.23	0.88
LZ-3-02-24C	3.004	1.75	0.24	0.88
LZ-3-02-25C	3.001	1.80	0.19	0.91
LZ-3-02-25R	3.005	1.81	0.19	0.91
LZ-3-02-27	3.000	0.47	0.77	-
LZ-3-02-28	3.008	1.72	0.28	0.86
Phase I, Episode 2				
LZ-10-01-6c-core	3.015	1.73	0.28	0.86
LZ-10-01-6c-rim	3.011	1.69	0.31	0.84
LZ-11-04-xtl-4	3.017	1.63	0.39	0.81
LZ-11-04-xtl-9c	3.015	1.70	0.32	0.84
LZ-11-04-1c	3.017	1.70	0.32	0.84
LZ-3-04-2c	3.003	1.67	0.31	0.84
LZ-3-04-3c	3.005	1.67	0.32	0.84
LZ-3-04-4c	3.007	1.73	0.27	0.86
LZ-1-01-oxide	-	-	-	-
LZ-1-01-2c rim	2.997	1.81	0.17	0.91
LZ-1-01-2c core	2.994	1.81	0.17	0.92
LZ-1-01-1c rim	2.997	1.79	0.19	0.90

Sample/Analysis	Cation Total	Spinel Mg# or Mg_{sp}	Spinel Cr# or Fe^{2+}_{sp}	Mg#
LZ-1-01-1c core	2.993	1.81	0.17	0.92
LZ-5-01-q-ol	2.993	1.68	0.29	0.85
LZ-5-01-4c	3.000	0.64	0.56	-
LZ-5-01-9c	3.026	1.62	0.42	0.80
LZ-5-01-10c-crsp	3.000	0.54	0.53	-
LZ-5-01-10c	3.016	1.78	0.23	0.88
LZ-5-01-11c	2.999	1.69	0.29	0.85
LZ-5-01-11c-crsp	3.000	0.46	0.53	-
LZ-5-01-13c	3.016	1.84	0.18	0.91
Phase II				
LZ-11-01-2c-core	3.016	1.81	0.21	0.89
LZ-11-01-2c-rim	3.014	1.66	0.35	0.83
LZ-11-02-18c	3.009	1.70	0.30	0.85
LZ-11-02-1c	3.021	1.69	0.33	0.84
LZ-11-02-14c	3.010	1.69	0.31	0.84
LZ-11-02-2c	3.010	1.71	0.30	0.85
LZ-11-02-2-crsp	3.000	0.66	0.69	-
LZ-11-02-1cc	3.005	1.83	0.17	0.92
LZ-11-02-1d	3.000	0.52	0.47	-
LZ-11-02-1c	3.021	1.69	0.33	0.84
LZ-11-02-05	-	-	-	-
Phase III, episode 1				
LZ-15-01-25c	3.003	1.695	0.294	0.85
LZ-15-01-16c	3.005	1.70	0.291	0.85
LZ-15-01-20c	3.012	1.70	0.303	0.85
LZ-15-01-21c	2.991	1.60	0.351	0.82
LZ-14-01-1c	2.998	1.67	0.307	0.84
LZ-14-01-1-5c	3.005	1.69	3.050	0.36
LZ-14-01-2c	3.014	1.70	0.312	0.84
LZ-14-01-7c	2.999	1.68	0.301	0.85
LZ-15-01-9c-crsp	-	-	-	-
LZ-15-01-9c-core	3.015	1.72	0.292	0.85
LZ-14-01-1-crsp	3.000	0.46	0.574	-
LZ-14-01-1-oliv	2.996	1.66	0.312	0.84
Phase III episode 2				
LZ-13-01-7c	3.028	1.71	0.331	0.84
LZ-13-01-10c	2.999	1.64	0.341	0.83

Sample/Analysis	Cation Total	Spinel Mg# or Mg_{ul}	Spinel Cr# or Fe^{2+}_{ul}	Mg#
LZ-13-01-12c	3.001	1.63	0.351	0.82
LZ-13-01-17c	2.983	1.60	0.354	0.82
Phase III, episode 3				
LZ-16-01-10c	2.999	1.76	0.228	0.89
LZ-16-01-22c	2.997	1.64	0.339	0.83
LZ-16-01-3c-rim	3.012	1.62	0.389	0.81
LZ-16-01-6c	3.010	1.68	0.322	0.84
LZ-16-01-1c-core	3.020	1.75	0.28	0.86
LZ-16-01-1c-rim	3.013	1.74	0.27	0.87
LZ-16-01-2c	3.017	1.80	0.22	0.89
LZ-16-01-21c-crsp	3.000	0.52	0.57	
LZ-16-01-22c	2.997	1.64	0.34	0.83
LZ-16-01-6c	3.010	1.68	0.32	0.84
LZ-16-01-4c	3.003	1.69	0.30	0.85
Phase IV				
LZ-12-01-1c	3.006	1.69	0.31	0.85
LZ-12-02-4c	3.012	1.68	0.33	0.84
LZ-12-02-3c	3.008	1.70	0.30	0.85
LZ-12-01-28c	3.002	1.67	0.32	0.84
LZ-12-01-1-7c	3.005	1.69	0.30	0.85
LZ-12-01-f	3.000	0.56	0.54	-
LZ-12-01-fc	3.003	1.65	0.34	0.83
LZ-12-01-jc	3.003	1.66	0.33	0.83
LZ-12-01-xtl-1R	3.006	1.65	0.33	0.83
LZ-12-01-xtl-1C	3.000	1.67	0.31	0.84
LZ-12-01-xtl-23-3	3.001	1.55	0.44	0.78
LZ-12-01-xtl-23-4	2.995	1.51	0.46	0.77
LZ-12-01-xtl-27	-	-	-	-
Phase IV lava				
LZ-12-02-5c	3.000	1.78	0.21	0.89
LZ-12-02-9c	3.009	1.72	0.28	0.86
LZ-12-02-14c	3.015	1.76	0.25	0.87
LZ-12-02-1c-crsp	3.000	0.59	0.55	-
LZ-12-02-1c-core	3.013	1.74	0.27	0.87
LZ-12-02-1c-rim	3.012	1.73	0.28	0.86
LZ-12-02-3c	3.006	1.67	0.33	0.84
LZ-12-02-2oliv	3.009	1.68	0.32	0.84

Sample/Analysis	Cation Total	Spinel Mg# or Mg_{ol}	Spinel Cr# or Fe^{2+}_{ol}	Mg#
Phase V episode 1				
LZ-6-01-1c	2.990	1.52	0.44	0.77
LZ-6-01-5c-core	2.995	1.69	0.28	0.86
LZ-6-01-5c-rim	2.993	1.65	0.32	0.84
LZ-6-01a-8c	2.995	1.58	0.38	0.81
LZ-6-01a-9c	2.993	1.54	0.43	0.78
LZ-7-01-7c	2.994	1.55	0.42	0.79
LZ-7-01-8c	2.997	1.55	0.43	0.78
LZ-7-01-9c	2.999	1.64	0.34	0.83
LZ-6-01-xtl-a	2.996	1.55	0.42	0.79
LZ-6-01-xtl-c	2.993	1.57	0.40	0.80
LZ-6-01-xtl-d	2.993	1.63	0.34	0.83
LZ-6-01-xtl-e	3.005	1.63	0.36	0.82
LZ-7-01-6c	3.006	1.61	0.38	0.81
LZ-6-01-2-crsp	3.000	0.60	0.60	-
LZ-6-01-2-oliv	2.993	1.64	0.33	0.83
Phase V episode 2				
LZ-2-01-1c-core	3.009	1.78	0.23	0.89
LZ-2-01-1c-rim	3.015	1.79	0.23	0.89
LZ-2-01-6c	3.005	1.73	0.26	0.87
LZ-2-01-9c	3.009	1.74	0.26	0.87
LZ-2-01-12c	3.004	1.72	0.27	0.86
LZ-3-01-20c	3.008	1.71	0.29	0.85
LZ-3-01-a-1c	3.008	1.70	0.29	0.85
LZ-3-01-1c	3.007	1.77	0.23	0.89
LZ-2-01-1c-crsp	3.000	0.66	0.46	-
LZ-2-01-1c-core	3.009	1.78	0.23	0.89
LZ-3-01-k-c-core	3.010	1.84	0.17	0.92
LZ-3-01-k-c-rim	3.001	1.82	0.17	0.92
LZ-2-01-10c	3.006	1.71	0.29	0.86
LZ-2-01-10c-crsp	3.000	0.42	0.38	-
LZ-3-01-6	3.000	0.54	0.50	-
LZ-3-01-6c	3.002	1.67	0.32	0.84